Quantum Vlasov Theory of Mie Oscillations in Metal Clusters: A Self-Consistent Approach to Quantum Surface Effects in Nanoparticles

Von der Fakultät für Mathematik, Informatik und Naturwissenschaften der RWTH Aachen University zur Erlangung des akademischen Grades eines Doktors der Naturwissenschaften genehmigte Dissertation

vorgelegt von

Amir El-Khawaldeh, M.Sc. RWTH

aus Aachen

Berichter: Univ.-Prof. Dr. rer. nat. Hans-Jörg Kull
Univ.-Prof. Dr. rer. nat. Dieter Bauer

Tag der mündlichen Prüfung: 09. Mai 2018

Supervisor

Prof. Dr. Hans-Jörg Kull
Institute for Theory of Statistical Physics
Laser Physics Group
RWTH Aachen University

Abstract

The electron dynamics in metal clusters is studied in the framework of the quantum Vlasov theory. The Vlasov theory describes equilibria and excitations in ideal plasmas by a self-consistent field approach. It is applied to the spherical jellium model of atomic clusters with an emphasis on quantum-size effects in nanometer-sized clusters. A proper understanding of the spill-out-induced surface effects of the Mie plasmon is one of the major goals of this work. For this purpose, the Vlasov model is treated by theoretical and numerical methods both in the linear and nonlinear regime of free and laser-driven cluster excitations.

Linear electrostatic cluster excitations are treated in a multistream-Vlasov and in a reduced single-state Vlasov model. In the framework of the single-state model, the damping of the Mie plasmon can be explained by a mode conversion process from surface to volume plasmons due to surface scattering. Increasing the number of representative states in the multistream approach, it is shown that the residual volume plasmons are damped by single-particle excitations (Landau damping). Reference calculations are performed for specific Na clusters with the multistream and the more common density-functional theory approach. The plasmon damping rate in the multistream model shows good quantitative agreement with the damping rate obtained by the single-state model, which indicates the importance of mode conversion for the plasmon decay. The damping rate shows a characteristic scaling with the inverse cluster radius. In addition, the resonance frequency is redshifted with respect to the Mie frequency especially for small clusters. By further including exchange-correlation corrections, close agreement of the damping rate coefficient with previous experimental and numerical results can be achieved.

Linear electromagnetic cluster excitations are treated in the single-state model. Resonance absorption of clusters is investigated at the critical density where the light frequency equals the plasma frequency. In this framework, the well-known theory of resonance absorption is generalized from plane to spherical surfaces with variable angles of incidence and light polarizations along the surface.

As a preparatory study for nonlinear electrostatic cluster excitations, the nonresonant collisionless absorption (Brunel mechanism) of thin foils is investigated. Brunel's scaling can be confirmed for thick foils in the present quantum regime. However, the energy absorption shows a clear signature of quantum-size effects for thin foils due to the spill-out effect of the electron density. The main result is an increase of Brunel's scaling exponent for thin foils.

Nonlinear electrostatic cluster excitations are investigated for spherical Na clusters. The nonlinear Mie oscillation is studied based on an impulsive excitation of the cluster. For moderate perturbations, the resonance position of the Mie plasmon is blueshifted with respect to the linear result. In addition, the plasmon linewidth decreases. For sufficiently large perturbations, dynamical deformation effects are observed, which lead to a splitting of the Mie resonance. This splitting can be explained by a coupling of the cluster dipole moment to the quadrupole field induced by the electron cloud exterior to the cluster region. The residual excitations in the interior region of the cluster are characterized by local density fluctuations on the timescale of the plasma period. The interaction of clusters with femtosecond laser pulses is studied for peak intensities up to $10^{14}\mathrm{W/cm}^2$. Nonlinear plasma-wave generation at the cluster surface can be observed, which appears in the presence of strong laser-induced polarization fields. The acceleration of plasma waves through the cluster results in enhanced outer ionization close to the cluster poles. Recombinations of emitted electron wave packets result in fast density oscillations on the attosecond scale.

Zusammenfassung

Die Elektronendynamik in metallischen Atomclustern wird im Rahmen der Quanten-Vlasov-Theorie untersucht. Die Vlasov-Theorie beschreibt Gleichgewichte und Anregungen in idealen Plasmen mithilfe selbstkonsistenter Felder und wird in dieser Arbeit auf das sphärische Jellium-Modell der Atomcluster angewandt. Hierbei liegt der Schwerpunkt auf Quanteneffekten in Nanometer großen Clustern. Eines der Hauptziele dieser Arbeit ist die Einordnung der Quantenoberflächeneffekte des Mie-Plasmons, die mit dem Spill-Out-Effekt der Elektronendichte verknüpft sind. Dafür wird das Vlasov-Modell im Rahmen theoretischer und numerischer Methoden sowohl im linearen als auch im nichtlinearen Regime behandelt.

Lineare elektrostatische Clusteranregungen werden im Vielstrom-Vlasov-Modell und in einem Einzustand-Vlasov-Modell behandelt. Im Einzustandmodell kann die Dämpfung des Mie-Plasmons mit einer Konversion von Oberflächen- in Volumenplasmonen erklärt werden, die durch Oberflächenstreuung hervorgerufen wird. Unter Erhöhung der Anzahl repräsentativer Zustände im Vielstrom-Modell wird gezeigt, dass das Volumenplasmon in Einteilchenanregungen zerfällt (Landau-Dämpfung). Rechnungen für Na-Cluster werden im Vielstrommodell und mithilfe der Dichtefunktionaltheorie durchgeführt. Die Dämpfungsrate im Vielstrom-Modell ist in guter Übereinstimmung mit der des Einzustandmodells. Dies zeigt die Relevanz der Modenkonversion für den Zerfall des Mie-Plasmons. Die Dämpfungsrate zeigt eine charakteristische Skalierung mit dem inversen Clusterradius. Zusätzlich ist die Resonanzfrequenz für kleine Cluster rotverschoben. Unter Berücksichtigung von Austausch-Korrelations-Korrekturen ergibt sich eine gute Übereinstimmung der Dämpfungsrate mit experimentellen und theoretischen Referenzergebnissen.

Lineare elektromagnetische Clusteranregungen werden im Rahmen des Einzustandmodells behandelt. Das Ziel der Untersuchung ist die Analyse der Resonanzabsorption von Clustern an der kritischen Dichte, wobei die Theorie der Resonanzabsorption von ebenen Flächen auf sphärische Oberflächen mit variablem Einfallswinkel und variablen Lichtpolarisationen entlang der Oberfläche verallgemeinert wird.

Als Vorstudie für nichtlineare elektrostatische Clusteranregungen wird die nichtresonante stoßfreie Absorption (Brunel-Mechanismus) von dünnen Schichten untersucht. Die Brunel'sche Skalierung kann für dicke Schichten im Quantenregime bestätigt werden. Für dünne Schichten zeigen sich Quanteneffekte, die durch den Spill-Out-Effekt hervorgerufen werden. Das Resultat ist eine Erhöhung des Brunel'schen Skalierungsexponenten für dünne Schichten.

Nichtlineare elektrostatische Clusteranregungen sphärischer Na-Cluster werden untersucht. Für moderate Störungen ist die Resonanzposition des Mie-Plasmons in Bezug auf die lineare Resonanz blauverschoben. Zusätzlich verringert sich die Dämpfungsrate. Für hinreichend große Störungen werden dynamische Deformationseffekte beobachtet, die zu einer Aufspaltung der Mie-Resonanz führen. Diese Aufspaltung kann durch die Kopplung des Cluster-Dipolmoments an das Quadrupolfeld der Elektronenwolke außerhalb des Clusters erklärt werden. Die Wechselwirkung von Clustern mit Femtosekunden-Laserpulsen wird für Laserintensitäten bis $10^{14}\mathrm{W/cm}^2$ untersucht. An der Clusteroberfläche kann die Erzeugung von nichtlinearen Plasmawellen beobachtet werden, die in starken laserinduzierten Polarisationsfeldern entstehen. Die Beschleunigung der Plasmawellen durch das Cluster resultiert in der äußeren Ionisation des Clusters nahe der Pole. Rekombinationen von emittierten Elektronenwellenpaketen führen zu schnellen Dichteoszillationen auf der Attosekundenskala.

Contents

Chapter 1

Introduction

Atomic clusters are aggregates of atoms typically containing a few tens up to a few million atoms [1], which fill the gap between atoms or molecules and bulk matter. Their first observation has been made back in the 1940s [2] based on mass spectrometric investigations of small carbon clusters consisting of up to 15 atoms.

Clusters have received broad attention in the study of laser-matter interaction. Since cluster densities are typically of the same order of magnitude as in solids, while energy transport losses are absent, clusters can be used to couple high laser energies to matter rather efficiently. The interaction of clusters with high-intensity laser fields leads to inner ionization of the cluster, which can cause a dense plasma state together with high electron temperatures [3]. As a result of the inner ionization, large space charges can be generated which lead to an expansion of the cluster. Thermal and Coulomb explosions of clusters can act as sources for highly energetic particles. Kinetic energies up to 500keV were measured for electrons [4, 5] and 1MeV for ions [6].

One further aspect of the laser-cluster interaction is the excitation of the collective dipole oscillation, known as Mie plasmon, which is related to the bound electron motion in the electric field of the cluster ions. In practice, it can be excited resonantly during the cluster expansion that is accompanied by a reduction of the electron density [7]. On a theoretical basis, the Mie plasmon can be described rather simply by considering the response of a small dielectric sphere in a homogeneous time-dependent electric field [8]. This description is based on an early work by Lord Rayleigh [9]. For a free electron gas, this yields the resonance frequency $\omega_M = \omega_p/\sqrt{3}$, where $\omega_p = \sqrt{4\pi n_0 e^2/m_e}$ is the plasma frequency, e the elementary charge in Gaussian cgs units and m_e the electron mass. This frequency is known as the Mie frequency. The corresponding problem for spheres of arbitrary size has been treated by Mie with a full account to the electromagnetic (EM) radiation field [10].

Various physical mechanism are known to drive the relaxation of the Mie plasmon. Collisional damping is related to electron-ion collisions in the cluster. The corresponding collision frequency is independent of the cluster radius and decreases with increasing temperature [11–13]. In larger clusters, radiation damping becomes relevant that is related to the energy loss of the collective electron motion through radiation emission [14]. Furthermore, Landau damping is a collisionless mechanism related to an energy transfer of the collective electron motion to single-particle excitations [15, 16] that can also be observed in homogeneous systems [17]. Nonlinear laser-cluster interactions lead to additional collisionless damping effects like e.g. harmonic generation and outer

ionization of the cluster [18–20]. In smaller clusters, the dipole motion is significantly influenced by the surface due the interaction of the cluster electrons with the nonharmonic restoring force in the region exterior to the cluster. This effect is commonly interpreted as surface scattering [21, 22]. It leads to a characteristic $1/R$-contribution to the total plasmon linewidth Γ, which is frequently written in the form

$$\Gamma = A\frac{v_F}{R}, \tag{1.0.1}$$

where v_F is the Fermi velocity, R the cluster radius and A a constant of order unity. In recent experiments on free isolated Ag [23] and Au clusters [24], the A-parameter has been determined as $A = 0.25$. Apart from the plasmon relaxation, surface scattering leads to a modification of the plasmon frequency. It is a common result of experiments on the Mie resonance of alkali metal clusters that the plasmon frequency is redshifted with respect to ω_M [13]. In contrast to alkali metal clusters, the inverse trend can be observed for noble metal clusters. It has been found experimentally for Ag clusters in the gas phase that the Mie resonance is blueshifted [25], which has been attributed to the reduced s-d screening interaction in the outer region of the Ag particles.

In the earliest stages of cluster research, various classical models have been developed to account for surface scattering, e.g. free-path models with isotropic [21, 26] and diffuse scattering [27] at the cluster boundary. The mean free path of the electrons obtained in [27] has been reproduced in a recent kinetic approach based on classical particle dynamics [28]. The first quantum-mechanical treatment of the plasmon relaxation in metal clusters goes back to Kawabata and Kubo [29] who considered the linear cluster response of quantized electron states confined to a sphere of radius R.

However, if the cluster size approaches the nanoscale, quantum confinement becomes relevant [30], which leads to the so-called spill-out effect of the electron density. The spill-out effect describes the occurrence of a nonvanishing electron density outside the cluster. It is a pure quantum-mechanical effect in degenerate electron gases with temperatures below the Fermi energy. In this regime of cluster sizes, a proper quantum-mechanical description is necessary to account for the details of the electron distribution at the cluster surface which are decisive for the damping mechanism of surface scattering.

With the trend to higher and higher computer performances, quantum-theoretical cluster studies have made great progress since the 1980s. In this framework, electron equilibria in clusters have been calculated based on various quantum models. Standard approaches rely on the density functional theory (DFT) [31], the Hartree-Fock method [32] or the Thomas-Fermi method [12, 33]. In particular, the spherical jellium approximation for the ion background has proven to show good results for alkali metal clusters with closed subshells [34–37]. In this model, the ion background is spread homogeneously over a sphere of radius R. Apart from spherically symmetric cluster equilibria with closed subshells, equilibria of small deformed clusters are well-known [38–40].

In the 1980s, the cluster response has been widely treated in linear approximations. Particular attention has been paid to the plasmon linewidth through various approaches based on the random-phase approximation (RPA) [41, 42] and corresponding

semiclassical approximations [43]. These results have been reviewed and extended in a later work by Tran Thoai and Ekardt [44]. More advanced self-consistent approaches based on the time-dependent local-density approximation (TDLDA) [31] have lead to great insight into the absorption spectra of small metal clusters [45] and their size dependencies [15] as well as basic cluster excitations [45, 46].

Based on the invention of the chirped pulse amplification technique [47] in the mid-1980s, nonlinear cluster response became experimentally accessible through the interaction of clusters with high-intensity laser fields [48]. Another possibility to generate highly excited cluster states relies on scattering of low-energetic charged ion beams in cluster media [49]. An overview on major phenomena in the nonlinear response of metal clusters can be found in [18, 50, 51].

The quantum-theoretical study of nonlinear phenomena in small metal clusters has been extensively performed in TDLDA [50] with applications to e.g. plasmon-enhanced emission [52] and field amplification [53] or the nonlinear dipole response [16, 54].

Apart from quantum-theoretical treatments, classical particle-in-cell (PIC) methods [18, 51, 55–57] are well-established for larger clusters where a classical treatment is reasonable. In this framework, various laser-driven phenomena such as electron emission through resonant energy absorption [58] or nonlinear resonance absorption [59] have been studied. In a later work, PIC simulations were improved by microscopic PIC methods [60, 61] with an emphasis on bulk collisions, surface collisions and radiation damping in laser-driven clusters. In this framework, attosecond plasma-wave dynamics has been observed, which is generated by recollisions of electrons at the cluster surface. Furthermore, semiclassical methods such as the Thomas-Fermi-Vlasov model [12] have been applied to the study of laser-driven clusters with attention to the plasmon-enhanced energy aborption and Coulomb explosions. It is mentioned that collective phenomena in nanometer-sized clusters have also been adressed in the strongly-coupled regime based on classical molecular dynamics [62].

In this thesis, metallic atomic clusters with delocalized electrons are described in the high-density and low-temperature regime, where the main focus is put on the spherical jellium approximation. The cluster electrons are treated as an ideal or weakly coupled quantum plasma. A common approach to the description of ideal quantum plasmas is based on the self-consistent quantum Vlasov theory for the single-particle density operator [63]. In this framework, exchange and correlation effects are neglected. Most generally, the quantum Vlasov theory can be derived from the Bogoliubov–Born–Green–Kirkwood–Yvon (BBGKY) hierarchy [64–69]. This hierarchy describes the time evolution of reduced statistical operators. Based on a discretization of the single-particle density operator, the quantum Vlasov theory can be transformed into a multistream model in which the plasma electrons are described by a finite set of representative single-particle states interacting via a self-consistent potential. The multistream model allows for a computationally efficient treatment of quantum plasmas and is closely related to the quasiparticle concept in classical PIC simulations [55]. It has been widely applied to homogeneous quantum plasmas in one dimension [17, 63, 70].

Particular attention is paid to quantum-sized clusters with diameters of a few nanometers. Here, an electrostatic treatment is reasonable. The underlying model is also gen-

eralized to the EM regime to account for radiative effects [14] in clusters with diameters larger than a few tens of nanometers. Apart from the treatment of three-dimensional clusters, reference calculations are performed for foils in a one-dimensional geometry.

The present thesis is devoted to the treatment of cluster excitations with an emphasis on freely propagating and driven collective excitations both in the linear and nonlinear regime. One important type of cluster excitation is the surface plasmon, which corresponds to a collective excitation of the electron density in the surface area of the cluster. They are accompanied by an excitation of the cluster multipole moments [10], e.g. the dipole moment that is associated with the Mie plasmon. In contrast, volume plasmons are eigenmodes of the electron density in the interior region of the cluster [71–73]. The main focus is put on the dynamics of the Mie plasmon in nanometer-sized clusters where quantum-size effects become decisive. The damping of the Mie plasmon is analyzed in the linear and nonlinear regime of cluster excitations with particular attention to the underlying damping mechanism, the residual cluster excitations and the size dependence of the damping rate. While the decay of the Mie plasmon has been mostly analyzed on the basis of the dipole spectrum [15, 45, 54], it is intended to provide a time-resolved analysis of the Mie oscillation by considering in addition the evolution of the cluster density. This study aims to characterize in more detail how the residual cluster excitations emerge from the interaction of the cluster electrons with the surface. Since the single-particle properties of the electron system can be controlled by the number of representative states taken into account in the multistream model, the present analysis allows for a study of collective excitations and how they are influenced by an increasingly large number of single-particle excitations [15, 16].

Besides the study of elementary cluster excitations, two collective absorption mechanisms are analyzed for clusters irradiated by an external laser field. On the one hand, the resonance absorption [74–76] of laser light at a diffuse metal surface and on the other hand the well-known Brunel mechanism, also known as vacuum heating, which describes the nonresonant collisionless energy absorption at a sharp metal surface [77–80]. In contrast to resonance absorption at diffuse surfaces, the Brunel mechanism is a nonlinear mechanism that is closely related to outer ionization [19]. The Brunel mechanism is treated for thin foils on the nanometer scale with particular attention to the quantum-size effects of the absorption mechanism. The resonance absorption is studied for spherical clusters with radii larger than 40nm. It has been treated already for plane surfaces and p-polarized light [74–76].

This thesis is divided as follow: In Chapter 2, the theoretical framework is reviewed. Subsequently, the equilibrium states of the electron system are calculated in Chapter 3, which define the initial state of the electron system in dynamical cluster simulations. Here, particular attention is paid to the surface region of the equilibrium density which is decisive for the decay of the surface plasmon resonance in the quantum-size regime. Many-electron equilibria of Na clusters are treated in the Vlasov model with a full account to the electronic degrees of freedom. These Na clusters act as reference examples for simple metal clusters. In addition, the reduced single-state Vlasov model (SSVM) is introduced, which describes the cluster electrons in terms of a single representative state, thereby taking into account only the collective degrees of freedom. In Chapter 4, electrostatic cluster excitations are treated by linear perturbation theory. Calculations are performed for Na clusters and within the SSVM. The influence of the electronic

details on the damping mechanism of the Mie plasmon and the corresponding damping rate is investigated. The transition of the surface plasmon into collective volume modes (volume plasmons) [81] and single-particle excitations is studied based on the time-resolved evolution of the electron density. Furthermore, the size dependence of the damping rate is studied. Subsequent to the analysis of cluster excitations in the quantum-size regime, the SSVM is generalized to the EM regime in Chapter 5 with a full account to the EM radiation field. Here, the focus is put on the linear light scattering and light absorption by clusters which are irradiated by a plane EM wave. For this purpose, the absorption and scattering cross sections are evaluated based on the self-consistent fields of the EM SSVM. Simulation results for the cross sections and damping rates of the Mie plasmon are compared with those of the classical Mie theory. As a major application of the EM SSVM, resonance absorption of clusters with a diffuse surface profile of the background ions is studied for cluster radii larger than 40nm. In Chapter 7, the nonlinear laser-driven dynamics of thin foils is investigated with an emphasis on the Brunel mechanism. The absorbed laser energy is studied as a function of the laser field strength for various foil thicknesses. Quantum-size corrections to the classical Brunel theory are calculated [82], which are interpreted in more detail. After having considered foils in a one-dimensional geometry, finally the focus is put again on spherical clusters in Chapter 7. The nonlinear dynamics of free and and laser-driven cluster excitations is studied for Na clusters on the nanoscale. The excitation of the free Mie oscillation is generated by an impulsive excitation of the cluster electrons. By studying the cluster response as a function of the initial momentum, nonlinear effects of the Mie oscillation are analyzed. The damping mechanism of the Mie oscillation as well es the residual cluster excitations are studied based on the evolution of the electron density. The corresponding results are compared with the results of the linear calculations performed in the framework of this thesis. Apart from the treatment of free Mie oscillations, the interaction of clusters with few-cycle femtosecond laser pulses is studied.

Finally, it is noted that throughout this thesis dimensional quantities are defined in terms of Gaussian cgs units.

Chapter 2

Theoretical Framework

In this chapter, the theoretical framework of this thesis is described in more detail, which is based on a quantum-statistical description of the cluster electrons in the Fermi-degenerate regime. Section 2.1 consists of two parts. First, the concept of reduced statistical operators is introduced in Subsection 2.1.1 [66]. Subsequently, the quantum BBGKY hierarchy [64] is derived, which corresponds to a chain of equations describing the time evolution of reduced statistical operators. Based on the BBGKY hierarchy, the quantum Vlasov equation is derived in Section 2.2, which is a kinetic equation for the single-particle statistical operator in the collisionless regime. By introducing a multistream ansatz for the single-particle statistical operator, the electron system can be described by a finite set of single-particle wave functions in a self-consistent potential. This approach forms the basis of the present theoretical analysis of cluster dynamics. Therefore, the basic assumptions of the Vlasov approach are discussed. Finally, the corresponding dimensionless equations are formulated in Section 2.3 by using plasma units. These dimensionless equations form the basis for numerical simulations.

2.1 BBGKY Hierarchy

2.1.1 Reduced Statistical Operators

In this subsection, the concept of reduced statistical operators is introduced. The statistical properties of a quantum N-particle system are in general fully described by the N-particle statistical operator

$$\rho_N = \sum_k w_k |\Psi_k\rangle\langle\Psi_k|. \tag{2.1.1}$$

Here, the many-particle ensemble states $|\Psi_k\rangle$ are occupied with probability w_k. The ensemble average $\langle A\rangle$ of a N-particle observable A can be calculated based on the statistical operator (2.1.1) by the expression

$$\langle A\rangle = \mathrm{Tr}\{A\rho_N\}, \tag{2.1.2}$$

where the trace denoted by Tr has to be taken over the full N-particle Hilbert space. In the following, S-particle observables are introduced which have the form

$$A_S = \sum_{i_1<i_2\ldots<i_S} A_{i_1,i_2\ldots,i_S}. \tag{2.1.3}$$

Here, $A_{i_1,i_2\ldots i_S}$ is an operator which acts only on the single-particle Hilbert spaces i_1 up to i_S. Now, it is demonstrated that the ensemble average $\langle A_S\rangle$ can be evaluated with the help of an S-particle density operator ρ_S. For this purpose, the trace in (2.1.2) is evaluated based on a product basis of orthonormal single-particle states,

$$|\alpha_1\alpha_2\ldots\alpha_N\rangle = |\alpha_1\rangle\otimes|\alpha_2\rangle\otimes\ldots\otimes|\alpha_N\rangle, \quad \langle\alpha'|\alpha\rangle = \delta_{\alpha\alpha'}. \tag{2.1.4}$$

The corresponding completeness relation reads

$$\mathbb{1} = \sum_{\alpha_1\alpha_2\cdots\alpha_N} |\alpha_1\alpha_2\ldots\alpha_N\rangle\langle\alpha_1\alpha_2\ldots\alpha_N|, \tag{2.1.5}$$

where $\mathbb{1}$ denotes the identity operator. Due to the indistinguishability of the particles, the matrix elements of the statistical operator with respect to the product states (2.1.4) is preserved under any arbitrary permutation σ of the single-particle states,

$$\langle\alpha_1\alpha_2\ldots\alpha_N|\rho_N|\beta_1\beta_2\ldots\beta_N\rangle = \langle\alpha_{\sigma(1)}\alpha_{\sigma(2)}\ldots\alpha_{\sigma(N)}|\rho_N|\beta_{\sigma(1)}\beta_{\sigma(2)}\ldots\beta_{\sigma(N)}\rangle. \tag{2.1.6}$$

By using this symmetry and the completeness relation (2.1.5), the following equality holds:

$$\begin{aligned}
&\mathrm{Tr}\left\{A_{\sigma(i_1),\sigma(i_2)\ldots\sigma(i_N)}\,\rho_N\right\}\\
&= \sum_{\substack{\alpha_1,\alpha_2\ldots\alpha_N\\ \beta_1,\beta_2\ldots\beta_N}} \langle\alpha_1\ldots\alpha_N|A_{\sigma(i_1),\ldots\sigma(i_N)}|\beta_1\ldots\beta_N\rangle\langle\beta_1\ldots\beta_N|\rho_N|\alpha_1\ldots\alpha_N\rangle\\
&= \sum_{\substack{\alpha_1,\alpha_2\ldots\alpha_N\\ \beta_1,\beta_2\ldots\beta_N}} \langle\alpha_{\sigma(1)}\ldots\alpha_{\sigma(N)}|A_{i_1,\ldots i_N}|\beta_{\sigma(1)}\ldots\beta_{\sigma(N)}\rangle\langle\beta_1\ldots\beta_N|\rho_N|\alpha_1\ldots\alpha_N\rangle\\
&= \sum_{\substack{\alpha_1,\alpha_2\ldots\alpha_N\\ \beta_1,\beta_2\ldots\beta_N}} \langle\alpha_{\sigma(1)}\ldots\alpha_{\sigma(N)}|A_{i_1,\ldots i_N}|\beta_{\sigma(1)}\ldots\beta_{\sigma(N)}\rangle\langle\beta_{\sigma(1)}\ldots\beta_{\sigma(N)}|\rho_N|\alpha_{\sigma(1)}\ldots\alpha_{\sigma(N)}\rangle\\
&= \mathrm{Tr}\left\{A_{i_1,i_2\ldots i_N}\,\rho_N\right\}.
\end{aligned} \tag{2.1.7}$$

In conclusion, each summand in (2.1.3) gives rise to the same contribution to the ensemble average $\langle A_S\rangle$. The number of ways of picking S unordered outcomes from N possibilities is given by the binomial coefficient

$$\binom{N}{S} = \frac{N!}{S!(N-S)!}. \tag{2.1.8}$$

Then, the ensemble average can be written as

$$\langle A\rangle = \frac{1}{S!}\,\mathrm{Tr}_{1,2,\ldots,S}\{A_{1,2,\ldots,S}\,\rho_S\}, \tag{2.1.9}$$

where the S-particle density operator ρ_S is defined by

$$\rho_S = \frac{N!}{(N-S)!} \operatorname*{Tr}_{(S+1),\ldots,N} \rho_N. \tag{2.1.10}$$

In (2.1.9), the partial trace is taken over the first S single-particle Hilbert spaces. Then, ρ_S can be obtained from (2.1.9) by partially tracing out $N-S$ single-particle Hilbert spaces.

2.1.2 Hierarchy of Equations for Reduced Statistical Operators

As demonstrated in the previous subsection, ensemble averages of S-particle observables can be calculated based on the S-particle statistical operator ρ_S. This approach requires the calculation of ρ_S as a function of time. In this section, the BBGKY hierarchy is derived which describes the time evolution of the operators ρ_S. First, it was derived for the reduced phase space distribution functions of a classical N-particle system [65]. Later, it was generalized to quantum systems [64]. In the following, it is described how the equation of motion of ρ_S can be derived based on the von Neumann equation

$$i\hbar\partial_t \rho_N = [H, \rho_N] \tag{2.1.11}$$

for the N-particle statistical operator, where H is the many-body Hamiltonian of the N-particle system.

Now, consider a system of N electrons of mass m_e. In this thesis, the main focus is put on the electrostatic regime of the electron-electron interaction with Coulomb interactions of the form

$$V_{i,j} = \frac{e^2}{|\boldsymbol{r}_i - \boldsymbol{r}_j|}. \tag{2.1.12}$$

Here, e is the elementary charge. Then, the many-body Hamiltonian H has the form

$$H = \sum_{i=1}^{N} \left(\frac{p_i^2}{2m_e} + V_i \right) + \sum_{1 \le i < j \le N} V_{i,j}, \tag{2.1.13}$$

where V_i denotes a general single-particle potential. For the further evaluation of (2.1.11), it is convenient to split H into three parts:

$$H = H_S + H_{N-S} + V_{S,N-S} \tag{2.1.14}$$

$$.H_S = \sum_{i=1}^{S} \left(\frac{p_i^2}{2m_e} + V_i \right) + \sum_{1 \le i < j \le S} V_{i,j}, \tag{2.1.15}$$

$$H_{N-S} = \sum_{i=S+1}^{N} \left(\frac{p_i^2}{2m_e} + V_i \right) + \sum_{S+1 \le i < j \le N} V_{i,j}, \tag{2.1.16}$$

$$V_{S,N-S} = \sum_{i=1}^{S} \sum_{j=S+1}^{N} V_{i,j}. \tag{2.1.17}$$

In this representation, the electron system is divided into two systems consisting of S and $(N-S)$ electrons. The Hamiltonian H_S describes the Hamiltonian of the S-

particle system. The operator $V_{S,N-S}$ takes into account the interaction between the two particle systems.

The equation of motion of ρ_S can be obtained by taking the partial trace of both sides of (2.1.11) with respect to the $(N-S)$-particle system. Then, the following equation holds:

$$i\hbar\partial_t\rho_S = [H_S,\rho_S] + \frac{N!}{(N-S)!}\operatorname*{Tr}_{(S+1),\dots,N}\Big([V_{S,N-S},\rho_N] + [H_{N-S},\rho_N]\Big). \tag{2.1.18}$$

Here, the definition (2.1.10) of ρ_S was introduced. The third summand vanishes, since the following equality holds:

$$\begin{aligned}
&\operatorname*{Tr}_{(S+1),\dots,N} H_{N-S}\,\rho_N \\
&= \sum_{\substack{\alpha_{S+1}\cdots\alpha_N \\ \beta_{S+1},\cdots\beta_N}} \langle\alpha_{S+1}\dots\alpha_N|H_{N-S}|\beta_{S+1}\dots\beta_N\rangle\langle\beta_{S+1}\dots\beta_N|\rho_N|\alpha_{S+1}\dots\alpha_N\rangle \\
&= \sum_{\substack{\alpha_{S+1}\cdots\alpha_N \\ \beta_{S+1},\cdots\beta_N}} \langle\beta_{S+1}\dots\beta_N|\rho_N|\alpha_{S+1}\dots\alpha_N\rangle\langle\alpha_{S+1}\dots\alpha_N|H_{N-S}|\beta_{S+1}\dots\beta_N\rangle \\
&= \operatorname*{Tr}_{(S+1)\dots N} \rho_N\,H_{N-S}.
\end{aligned} \tag{2.1.19}$$

Here, the completeness relation (2.1.5) of the single-particle states was taken into account together with the fact that the operator H_{N-S} acts only on the $(N-S)$-particle system. Furthermore, it was used that the matrix elements $\langle\alpha_{S+1}\dots\alpha_N|H_{N-S}|\beta_{S+1}\dots\beta_N\rangle$ are just real numbers.

By using (2.1.17), the second summand of (2.1.18) can be written as follows:

$$\begin{aligned}
I &\equiv \operatorname*{Tr}_{(S+1),\dots,N} V_{S,N-S}\,\rho_N \\
&= \sum_{\substack{\alpha_{S+1}\cdots\alpha_N \\ \beta_1,\beta_2\dots\beta_N}} \langle\alpha_{S+1}\dots\alpha_N|V_{S,N-S}|\beta_1\dots\beta_N\rangle\langle\beta_1\dots\beta_N|\rho_N|\alpha_{S+1}\dots\alpha_N\rangle \\
&= \sum_{\substack{\alpha_{S+1}\cdots\alpha_N \\ \beta_1,\beta_2\dots\beta_N}} \sum_{i=1}^{S}\sum_{j=S+1}^{N} \langle\alpha_{S+1}\dots\alpha_N|V_{i,j}|\beta_1\dots\beta_N\rangle\langle\beta_1\dots\beta_N|\rho_N|\alpha_{S+1}\dots\alpha_N\rangle.
\end{aligned} \tag{2.1.20}$$

In (2.1.20), the operator $V_{i,j}$ couples a particle j of the $(N-S)$-particle to a particle i of the S-particle system. Therefore, the following relation holds:

$$\langle\alpha_{S+1}\dots\alpha_N|V_{i,j}|\beta_1\dots\beta_N\rangle = \langle\alpha_j|V_{i,j}|\beta_j\rangle \prod_{\substack{j'=S+1 \\ j'\neq j}}^{N} \delta_{\alpha_{j'}\beta_{j'}}\,|\beta_1\dots\beta_S\rangle. \tag{2.1.21}$$

It should be noted that $\langle\alpha_j|V_{i,j}|\beta_j\rangle$ is an operator which acts on particle space i of the S-particle system. With this result, (2.1.20) yields

$$\begin{aligned}
I = \sum_{\substack{\alpha_{S+1}\cdots\alpha_N \\ \beta_1,\beta_2\dots\beta_S}} \sum_{i=1}^{S}\sum_{j=S+1}^{N}\sum_{\beta_j} \left(\langle\alpha_j|V_{i,j}|\beta_j\rangle\right)|\beta_1\dots\beta_S\rangle \\
\times\langle\beta_1\dots\beta_S\alpha_{S+1}\dots\alpha_{j-1}\beta_j\alpha_{j+1}\dots\alpha_N|\rho_N|\alpha_{S+1}\dots\alpha_N\rangle.
\end{aligned} \tag{2.1.22}$$

In the next step, the symmetry property (2.1.6) is used to exchange the states $\beta_j \leftrightarrow \alpha_{S+1}$ and $\alpha_j \leftrightarrow \alpha_{S+1}$ in the matrix elements of ρ_N. Subsequently, one can rename the summation variables by making the replacement $j \leftrightarrow S+1$. Finally, one ends up with

$$\begin{aligned} I &= \sum_{\substack{\alpha_{S+1} \\ \beta_1,\beta_2\ldots\beta_{S+1}}} \sum_{i=1}^{S} \sum_{j=S+1}^{N} \langle \alpha_{S+1}|V_{i,S+1}|\beta_1\ldots\beta_{S+1}\rangle\langle\beta_1\ldots\beta_{S+1}|\underset{(S+2)\ldots N}{\mathrm{Tr}}\rho_N|\alpha_{S+1}\rangle \\ &= (N-S)\underset{S+1}{\mathrm{Tr}}\left\{\sum_{i=1}^{S} V_{i,S+1}\underset{(S+2)\ldots N}{\mathrm{Tr}}\rho_N\right\} = \frac{(N-S)!}{N!}\underset{S+1}{\mathrm{Tr}}\left\{\sum_{i=1}^{S} V_{i,S+1}\,\rho_{S+1}\right\} \end{aligned} \tag{2.1.23}$$

In the last step, the definition (2.1.10) of ρ_{S+1} was introduced. This relation can be introduced in (2.1.18) to obtain the following equation of motion of ρ_S:

$$i\hbar\partial_t\rho_S = [H_S,\rho_S] + \underset{S+1}{\mathrm{Tr}}\sum_{i=1}^{S}[V_{i,S+1},\rho_{S+1}]. \tag{2.1.24}$$

This result corresponds to a chain of equations for the reduced statistical operators of a N-particle system. To solve the BBGKY hierarchy (2.1.24) exactly, one would first have to solve the von Neumann equation for ρ_N. This result could then be used to obtain successively all operators ρ_S with $S < N$ based on (2.1.24). In conclusion, the exact treatment of the electron system via reduced statistical operators is not a simplification, since the solution of the von Neumann equation is not feasible even for a few-electron system. Therefore, one has to make further assumptions in order to truncate the hierarchy at a certain level.

2.2 Quantum Vlasov Equation

In this section, the quantum Vlasov equation is derived, which forms the basis of the present theoretical approach. Furthermore, it is intended to describe the basic assumptions of the underlying model.

In this work, one is frequently interested in the time evolution of single-particle quantities like the average energy or position of a single electron. According to the last section, averages of single-particle observables can be calculated based on the single-particle statistical operator ρ_1. By using (2.1.24), the time evolution of ρ_1 is governed by the equation

$$i\hbar\partial_t\rho_1 = [H_1,\rho_1] + \underset{2}{\mathrm{Tr}}[V_{1,2},\rho_2]. \tag{2.2.1}$$

In the present work, the focus is put on the quantum collisionless regime of the electron dynamics. Furthermore, exchange effects are neglected. More general approaches including correlation and exchange effects can be found in [31, 83–85]. Further approaches are discussed at the end of this section. To quantify the relevance of electron-electron collisions for the description of the electron system, one commonly introduces the coupling parameter $\Gamma = E_{int}/E_{kin}$ [86]. Here, E_{kin} and E_{int} are characteristic values of the kinetic energy and the interaction energy of the electrons. For a quantum system, E_{kin} is given by the Fermi energy $E_F = (\hbar^2/(2m_e))(3\pi^2 n)^{2/3}$, where n is the electron density. The interaction energy can be estimated by the Coulomb energy

$E_{int} = e^2/d$ of two electrons at the mean distance $d = n^{-1/3}$. Then, the coupling parameter reads

$$\Gamma = \frac{2m_e e^2}{\hbar^2 (3\pi^2)^{2/3}} \frac{1}{n^{1/3}} \sim \frac{1}{n^{1/3}}. \tag{2.2.2}$$

This relation shows that in the limit of high densities Γ becomes small, where the interaction energy of the electrons is small compared with the kinetic energy. For $\Gamma \ll 1$, collisions are less effective and electron-electron correlation effects can be neglected. In this framework, the two-particle statistical operator ρ_2 factorizes

$$\rho_2 = \rho_1 \otimes \rho_1 \tag{2.2.3}$$

and the BBGKY hierarchy can be truncated at the single-particle level $S = 1$. Based on approximation (2.2.3), the interaction term of (2.2.1) yields

$$\operatorname*{Tr}_2 V_{1,2}\, \rho_2 = V_{eff}\, \rho_1, \qquad V_{eff} = \operatorname*{Tr}_2 V_{1,2}\, \rho_1. \tag{2.2.4}$$

Here, an effective potential V_{eff} was introduced which is discussed below in more detail. With (2.2.4), the equation of motion of $\rho_1(t)$ reads

$$i\hbar \partial_t \rho_1 = [H_{eff}, \rho_1], \quad H_{eff} = \frac{p^2}{2m} + V_1 + V_{eff}, \quad V_{eff} = \operatorname*{Tr}_2 V_{12}\, \rho_1. \tag{2.2.5}$$

This equation has the same structure as the von Neumann equation, but with an effective single-particle Hamiltonian H_{eff}. It is known as quantum Vlasov equation and corresponds to the quantum-mechanical analog of the classical Vlasov equation describing the time evolution of the single-particle phase space distribution function [65].

In this thesis, the electron system is described by a statistical ensemble of N_s single-particle states $|\varphi_k(t)\rangle$, where w_k denotes the probability of occupancy of state $|\varphi_k(t)\rangle$. Here, the focus is put on a description at temperatur $T = 0$. Therefore, all states are equally occupied and the weights w_k are replaced by $w_k = w = 1/N_s$. Based on this ansatz, the single-particle statistical operator has the following form:

$$\rho_1(t) = w \sum_{k=1}^{N_s} |\varphi_k(t)\rangle\langle\varphi_k(t)|, \quad \langle\varphi_k|\varphi_k\rangle = 1. \tag{2.2.6}$$

Each wave function $\varphi_k(\boldsymbol{r}, t)$ associated with state $|\varphi_k(t)\rangle$ generates a probability current. The total probability current is then given by the ensemble average of all these contributions. In this sense, the approach (2.2.6) is called a multistream model. Multistream models have been widely used in classical [55] and quantum plasma physics [63, 70, 87, 88]. In the following, the states $|\varphi_k(t)\rangle$ will be called representative states since they represent the single-particle properties of the electron system rather than having a microscopic interpretation. With (2.1.9), they can be used to calculate the average $\langle A_1\rangle$ of a single-particle observable A_1 according to the following expression:

$$\langle A_1\rangle(t) = w \sum_{k=1}^{N_s} \langle\varphi_k(t)|A_1|\varphi_k(t)\rangle. \tag{2.2.7}$$

With ansatz (2.2.6), the effective potential (2.2.4) can be written in a clearer form as

follows:

$$\begin{aligned} V_{eff}(\boldsymbol{r},t) &= -e\int\limits_{\mathbb{R}^3}\frac{\rho_e(\boldsymbol{r'},t)}{|\boldsymbol{r}-\boldsymbol{r'}|}d^3r', \quad \rho_e(\boldsymbol{r},t) = -e\sum_{k=1}^{N_s} w\,|\varphi_k|^2(\boldsymbol{r},t), \\ \Delta\phi_e(\boldsymbol{r},t) &= -4\pi\rho_e(\boldsymbol{r},t), \qquad\qquad V_{eff}(\boldsymbol{r},t) = -e\,\phi_e(\boldsymbol{r},t). \end{aligned} \tag{2.2.8}$$

Here ρ_e is the average charge density of the electrons. In this sense, V_{eff} describes the interaction of a single electron with a mean electrostatic potential that is determined self-consistently by the average charge density of all electrons. In contrast to the bare coulomb interaction which accounts for electron-electron collisions, V_{eff} describes only the long-range component of the electron-electron interaction.

Now, the potential energy V_1 in the Vlasov equation (2.2.5) is specified in more detail for the present case of an atomic cluster. Here, V_1 consists of two contributions of the form $V_1(\boldsymbol{r},t) = V_{ei}(\boldsymbol{r}) + V_{ext}(\boldsymbol{r},t)$. The first contribution $V_{ei} = -e\phi_{ion}$ is associated with the electron-ion interaction energy, where $\phi_{ion}(\boldsymbol{r})$ is the potential generated by the ions. In this thesis, the ion system is treated as a spatially fixed charge distribution $\rho_{ion}(\boldsymbol{r})$. This approximation relies on the fact that the mass m_i of an ion is much larger than the mass m_e of an electron. The ratio of the ion and electron plasma periods defining the characteristic timescales of the collective motion is given by $T_{p,e}/T_{p,i} = \sqrt{m_e/m_i}$. Therefore, the electron dynamics takes place at a much shorter timescale in comparison with the timescale of the ions. The potential ϕ_{ion} can be combined with ϕ_e as $\phi = \phi_e + \phi_{ion}$. Then, ϕ is the total internal potential generated by the ions and the electrons. The second contribution $V_{ext} = -e\phi_{ext}$ to V_1 describes the interaction of an electron with an external potential $\phi_{ext}(\boldsymbol{r},t)$, e.g. generated by a laser field or an external charge distribution.

In order to calculate the time evolution of single-particle quantities based on (2.2.7), it is convenient to rewrite the Vlasov equation (2.2.5) in terms of a system of equations describing the time evolution of the wave functions $\varphi_k(\boldsymbol{r},t)$ and the self-consistent potential $\phi(\boldsymbol{r},t)$. By introducing the momentum operator $\boldsymbol{p} = -i\hbar\nabla$, the resulting Vlasov-Poisson system is given by

$$i\hbar\partial_t\varphi_k = \left[-\frac{\hbar^2}{2m_e}\Delta - e\phi - e\phi_{ext}\right]\varphi_k, \tag{2.2.9a}$$

$$\Delta\phi = 4\pi e\sum_{k=1}^{N_s} w\,|\varphi_k|^2 - 4\pi\rho_{ion}. \tag{2.2.9b}$$

Here, $\hbar$ is the reduced Planck constant. In this representation, the time evolution of each wave function φ_k is governed by a Schrödinger equation with a time-dependent potential ϕ. The potential ϕ has to be calculated self-consistently based on Poisson's equation with the average charge density of the electrons. The Vlasov-Poisson system (2.2.9) forms the basis of this thesis and will be applied to both the linear and nonlinear regime of cluster excitations.

It should be noted that (2.2.9) is closely related to the well-known Hartree-theory. The Hartree theory is based on the Rayleigh–Ritz method and can be derived by minimizing the energy functional with respect a product state of single-particle wave functions. Both models differ slightly since the self-energy interaction term in Poisson's equation

Quantity	Symbol	Unit
Density	n^*	n_0
Charge	q^*	e
Time	t^*	$1/\omega_p$
Energy	E^*	$\hbar\omega_p$
Length	l^*	$\sqrt{\hbar/(m_e\omega_p)}$
Mass	m^*	m_e
Angular momentum	L^*	$\hbar$
Frequency	ω^*	ω_p
Volume	V^*	$l^{*\,3}$
Velocity	v^*	$l^*/\,t^*$
Momentum	p^*	$m^*l^*/\,t^*$
Wave function	φ^*	$1/\sqrt{V^*}$
Probability current	j^*	$n^*p^*/\,m^*$
Scalar potential	ϕ^*	$E^*/\,q^*$
Vector potential	A^*	$E^*/\,q^*$
Electric field	$\mathcal{E}^*$	$E^*/\,(q^*l^*)$
Magnetic field	$\mathcal{B}^*$	$E^*/\,(q^*l^*)$
Force	F^*	$E^*/\,l^*$
Energy flux	S^*	$n^*\,l^*E^*/\,t^*$
Power	P^*	$n^*\,V^*E^*/\,t^*$

Table 2.3.1: Table of plasma units used in this thesis.

(2.2.9b) is not included within the Hartree theory. A further self-consistent field approach including exchange interaction is the Hartree-Fock method, which describes the exchange interaction in terms of non-local exchange potentials generated by the overlap of two individual single-particle states [89]. A more simplified description including both exchange and correlation effects can be achieved in the framework of DFT, where exchange and correlation effects are modeled by a local exchange-correlation potential $\phi_{xc}(\boldsymbol{r}, t)$, e.g. in local-density approximation (LDA) [90]. In Section (3.4), cluster equilibria within the present Vlasov approach will be compared with previous DFT results. These results were reproduced by adding ϕ_{xc} to ϕ in (2.2.9a). Then, the equations (2.2.9) agree with the well-known Kohn-Sham equations of DFT [91].

2.3 Dimensionless Equations

In this thesis, the main focus is put on the jellium approximation of the background ions. Here, the ions with charge state Z and particle density n_0/Z are considered to

n_0	$2.65 \cdot 10^{28}/\mathrm{m}^3$
ω_p	$9.19 \cdot 10^{15}$ Hz
E^*	6.05 eV
l^*	1.12 Å
t^*	0.11 fs

Table 2.3.2: Fundamental plasma units for Na with Bulk Wigner-Seitz radius $r_s = 3.93\, a_B$.

be distributed homogeneously over a sphere of radius R and volume $V_{ion} = (4/3)\pi R^3$. Then, the ion charge density reads

$$\rho_{ion}(\boldsymbol{r}) = e n_0 \theta(R - r). \tag{2.3.1}$$

A more general description of the ion distribution in terms of a Fermi function with a smooth surface profile can be found in Subsection 5.2.2.

For the numerical evaluation of the basic equations (2.2.9), dimensionless variables are introduced. Here, it is convenient to introduce plasma units for a plasma with density n_0 and plasma frequency $\omega_p = \sqrt{4\pi n_0 e^2/m_e}$. A list of plasma units that are used throughout this thesis is given in Table 2.3.1. *As not otherwise stated, all quantities in the following chapters are given in terms of these units.* The first five listed quantities form the basis of the present unit system from which all other listed units can be deduced. They are commonly introduced for a harmonic oscillator with frequency $\omega = \omega_p$. Since ω_p depends on the density n_0, the units (2.3.1) have the same dependency. They are chosen for the numerical evaluation since n_0 and all other constants besides the cluster radius R and the number of representative states N_s can be eliminated from the underlying equations. To get an estimate of the fundamental plasma units for simple metals, they were evaluated for sodium with Bulk Wigner-Seitz radius $r_s = 3.93\, a_B$ [92]. The numerical values are given in Table 2.3.2.

Another unit system frequently used in cluster simulations is the atomic unit system. For the comparison with the corresponding results, it is convenient to express the radius R_{at} in atomic units by the radius R_{pl} in plasma units. The corresponding relation is given by

$$R_{at} = C \left(\frac{r_s}{a_B}\right)^{\frac{3}{4}} R_{pl}, \quad C = \frac{1}{\sqrt[4]{3}} \approx 0.76, \tag{2.3.2}$$

where, $r_s = (3/4\pi n_0)^{1/3}$ denotes the Wigner-Seitz radius and a_B the Bohr radius.

Finally, the plasma units (2.3.1) are used to transform the basic equations (2.2.9) into the following dimensionless Vlasov-Poisson system:

$$i\partial_t \varphi_k = \left[-\frac{1}{2}\Delta - \phi - \phi_{ext}\right] \varphi_k, \tag{2.3.3a}$$

$$\Delta\phi = \sum_{k=1}^{N_s} w\, |\varphi_k|^2 - \theta(R - r). \tag{2.3.3b}$$

It is important to notice that the states φ_k have been renormalized to the value V_{ion} in the dimensionless equations (2.3.3). Therefore, from now on, one has $\langle\varphi_k|\varphi_k\rangle = V_{ion}$.

Chapter 3

Spherical Cluster Equilibria

This chapter incorporates results that have been pre-published in [81].

Prior to the perturbation of the cluster, the electron system is assumed to be in or close to the equilibrium state. Therefore, it is necessary to consider equilibria of the Vlasov-Poisson system (2.3.3). Electron equilibria have been obtained in cluster simulations based on various models. Standard approaches rely on DFT [31], the Hartree-Fock method [32] or the Thomas-Fermi method [12, 33].

In Section 3.1, the basic method for the solution of the single-particle time-independent Schrödinger equation is introduced, which is based on the concept of imaginary time propagation [93]. Subsequently, the equilibrium equations for the Vlasov-Poisson system are introduced in Section 3.2. Here, the equilibrium wave functions are characterized in more detail and the basic quantum numbers of the electron system are introduced. In Section 3.3, equilibrium results are presented for many-electron equilibria of Na clusters, which act as reference examples for simple metal clusters in this work. In Section 3.4, the SSVM is introduced, which corresponds to a reduced Vlasov model with one representative electron state. The spill-out region of the electron density is of particular importance for the description of plasmon damping. Therefore, a more detailed analysis of the surface region of the equilibrium density is provided. It is demonstrated that the SSVM is capable of describing the spill-out region of Na clusters to a very good approximation. For the interpretation of the SSVM results, comparison is made between the SSVM and many-electron Vlasov-equilibria of Na clusters. To investigate the effect of exchange and correlation interactions on the spill-out density, further comparison is made with previous DFT results [31].

3.1 Relaxation Method

The relaxation method is an iterative method to calculate the stationary states of a quantum system. In the following, this method is motivated for a single-particle system with Hamiltonian $H = T + V$, where T is the kinetic energy operator and V an arbitrary, time-independent potential. The basic problem to be solved is the eigenvalue problem

$$H\,|\psi_n\rangle = \epsilon_n\,|\psi_n\rangle, \quad \langle\psi_i|\psi_j\rangle = \delta_{ij}, \quad n = 1, 2, \ldots \tag{3.1.1}$$

for the stationary bound states $|\psi_n\rangle$ and the eigenvalues $\epsilon_1 < \epsilon_2 < \ldots$ of the Hamiltonian. Instead of solving the equation (3.1.1) directly, the relaxation method is based on a solution of the Schrödinger equation with an imaginary time variable $t = -i\tau$ ($\tau \in \mathbb{R}$),

$$-\partial_\tau |\psi(\tau)\rangle = H|\psi(\tau)\rangle. \tag{3.1.2}$$

For $V = 0$, this equation has the same form as a diffusion equation, e.g. the heat conduction equation.

For the motivation of the relaxation method, it is convenient to expand the solution $|\psi(\tau)\rangle$ in terms of eigenfunctions $|\psi_n\rangle$ of H. Let the expansion of the initial wave function be given by

$$|\psi(0)\rangle = \sum_n c_n |\psi_n\rangle, \quad c_n \in \mathbb{C}. \tag{3.1.3}$$

Then, the solution of (3.1.2) reads

$$|\psi(\tau)\rangle = \sum_n e^{-\epsilon_n \tau} c_n |\psi_n\rangle. \tag{3.1.4}$$

Each summand in (3.1.4) decays exponentially as a function of τ. Now, it is assumed that $|\psi_i\rangle$ is the energetically lowest-lying state which contributes to the expansion (3.1.3), where $c_n = 0$ for $n < i$. Then, all summands in (3.1.4) decay faster than the one, which corresponds to $|\psi_i\rangle$. In conclusion, the solution $|\psi(\tau)\rangle$ is proportional to $|\psi_i\rangle$ for $\tau \to \infty$. This demonstration shows that the solution of (3.1.2) can be used to calculate successively the stationary states of H for time-independent potentials. In the following subsection, the concept of imaginary time propagation is generalized to the Vlasov-Poisson system (2.3.3) with a self-consistent interaction potential and multiple electron states.

3.2 Equilibrium Equations

In the following, the equilibrium equations of the Vlasov-Poisson system (2.3.3) are introduced. The equilibrium is characterized by a set of stationary wave functions $\varphi_k^{(0)}(\boldsymbol{r})$, which correspond to a time-independent electron density $n^{(0)}(\boldsymbol{r})$. The stationary wave functions and the time-independent self-consistent potential $\phi^{(0)}(\boldsymbol{r})$ are determined by the following system of equations:

$$H^{(0)}\varphi_k^{(0)} = \epsilon_k \varphi_k^{(0)}, \quad H^{(0)} = -\frac{1}{2}\Delta - \phi^{(0)}, \tag{3.2.1a}$$

$$\Delta\phi^{(0)} = n^{(0)} - \theta(R - r), \quad n^{(0)} = w \sum_{k=1}^{N_s} |\varphi_k^{(0)}|^2. \tag{3.2.1b}$$

Stationary states are orthogonal,

$$\int_{\mathbb{R}^3} \varphi_k^{(0)\,*} \varphi_{k'}^{(0)}\, d^3r = \delta_{kk'} V_{ion}. \tag{3.2.2}$$

Their time evolution is given by

$$\varphi_k(\boldsymbol{r},t) = \varphi_k^{(0)}(\boldsymbol{r})\, e^{-i\epsilon_k t}. \tag{3.2.3}$$

In this chapter, the focus is put on clusters with a spherically symmetric density $n^{(0)}$ and a corresponding spherically symmetric potential $\phi^{(0)}$. Based on assumption, the commutator relations

$$\left[L^2, H^{(0)}\right] = \left[L_z, H^{(0)}\right] = 0 \tag{3.2.4}$$

hold for the angular momentum operator $\boldsymbol{L}$. Therefore, the states $\varphi_k^{(0)}$ can be classified according to angular momentum quantum numbers l and m. In addition, a third quantum number n is introduced to characterize the single-particle energies for fixed values of l and m. In summary, equilibrium states are characterized by three quantum numbers (nlm), where a stationary wave function can be written as a product of a radial part $R_{nl}(r)$ and the spherical harmonic $Y_{lm}(\theta,\phi)$,

$$\begin{aligned} \varphi_{nlm}^{(0)}(\boldsymbol{r}) &= R_{nl}(r)\, Y_{lm}(\theta,\phi), \\ L^2\, Y_{lm} &= l(l+1)\, Y_{lm}, \\ L_z\, Y_{lm} &= m\, Y_{lm}. \end{aligned} \tag{3.2.5}$$

In the present plasma unit system, the angular momentum is measured in units of $\hbar$.

Spherical symmetry of $n^{(0)}$ requires that all subshells for fixed values of n and l are completely filled. Then, spherical symmetry follows from the addition theorem

$$\sum_{m=-l}^{l} |Y_{lm}|^2 = \frac{2l+1}{4\pi} \tag{3.2.6}$$

and the resulting system of equations for the radial parts R_{nl} read

$$-\left[\frac{1}{2}\Delta_l + \phi^{(0)}\right] R_{nl} = \epsilon_{nl} R_{nl}, \tag{3.2.7a}$$

$$\Delta_r\, \phi^{(0)} = \sum_{l,n} w\, \frac{2l+1}{4\pi}\, |R_{nl}|^2 - \theta(R-r), \tag{3.2.7b}$$

where

$$\Delta_l = \Delta_r - \frac{l(l+1)}{r^2}. \tag{3.2.8}$$

Here, it was taken into account that the Laplacian

$$\Delta = \Delta_r - \frac{L^2}{r^2}, \quad \Delta_r = \frac{1}{r^2}\partial_r r^2 \partial_r \tag{3.2.9}$$

is diagonal with respect to the spherical harmonics (SH), $\Delta Y_{lm} = Y_{lm}\Delta_l$. With the ansatz (3.2.5), the eigenvalues ϵ_{nl} are independent of the quantum number m and the degree of degeneracy of the eigenvalue ϵ_{nl} is given by $2l+1$.

Due to (3.2.5), the orthogonality of stationary states φ_{nlm} for different values of l respectively m is achieved based on the orthogonality of SH. In contrast, the radial

parts R_{nl} for one value of l have to fulfill the orthogonality relation

$$\langle R_{nl}|R_{n'l}\rangle \equiv \int_0^\infty R_{nl}^*(r)\, R_{n'l}(r) r^2 dr = V_{ion}\delta_{nn'} \tag{3.2.10}$$

in order to provide orthogonality of the functions φ_{nlm}.

To determine the equilibrium quantum numbers for a given number of representative states N_s, one has to assign to each electron state quantum numbers (nlm). There are many possible configurations for a given value of N_s. To obtain the ground state, one has to choose the configuration which minimizes the total energy. Let l_{max} be the highest occupied l-number. Then, for each quantum number l, there is a set of N_l occupied states with different n-numbers $n = 1, 2 \ldots, N_l$ and a set of $2l+1$ occupied states with different m-numbers $m = 0, \pm 1, \ldots, \pm l$. Alltogether, the number of electron states can be written as

$$N_s = \sum_{l=0}^{l_{max}} (2l+1) N_l. \tag{3.2.11}$$

In summary, an equilibrium with N_s states is uniquely characterized by the parameters l_{max} and N_l.

For the calculation of the equilibrium states according to (3.2.7), a relaxation method [93] is chosen, which was motivated in subsection 3.1. In the following, it is briefly described how this method can be generalized to the present self-consistent theory.

Since equilibrium wave functions can be classified according to the quantum numbers l and m, an ansatz of the form

$$\tilde{\varphi}_{nlm}(\boldsymbol{r}, t) = N_{nl}(r, t) Y_{lm}(\theta, \phi) \tag{3.2.12}$$

is chosen for the time-dependent single-particle states. Then, the Vlasov-Poisson system (2.3.3) reduces to a set of equations for the radial wave functions N_{nl}, which are solved in imaginary time $t = -i\tau$,

$$\begin{aligned} -\partial_\tau N_{nl} &= -\left[\frac{1}{2}\Delta_l + \phi\right] N_{nl}, \\ \Delta_r \phi &= \sum_{l,n} w \frac{2l+1}{4\pi} |N_{nl}|^2 - \theta(R-r). \end{aligned} \tag{3.2.13}$$

There are two main differences to the single-particle eigenvalue problem of subsection 3.1. On the one hand, the presence of a potential, which depends on the wave functions itself. On the other hand, the presence of multiple electron wave functions. Since the imaginary time propagation does not conserve the norm of a wave function, it is necessary to renormalize the wave functions N_{nl} after each time step $\Delta\tau$ of wave-propagation in order to stick to the subspace of neutrally charged clusters. Otherwise, the self-consistent potential would be generated by an electron-ion system with nonzero charge under time propagation and the wave functions would be driven away from the equilibrium state of a neutral cluster.

Furthermore, one has to take into account that the orthogonality of two wave functions $\tilde{\varphi}_{nlm}(\boldsymbol{r},\tau)$ and $\tilde{\varphi}_{n'l'm'}(\boldsymbol{r},\tau)$ under imaginary time propagation is only guaranteed if $l \neq l'$ and $m \neq m'$ due to the ansatz (3.2.12) and the orthogonality of SH. Therefore, one has to orthogonalize all N_l radial parts $N_{nl}(r,\tau)$ for each value of l after each time step $\Delta\tau$ in addition to the renormalization process. Test calculations were carried out which confirmed that a Gram-Schmidt orthonormalization [94] is sufficient to achieve convergence of the present imaginary time method. It covers both the orthogonalization and the renormalization of the wave functions.

By starting with orthonormal wave functions N_{nl} at time $\tau_i = i\Delta\tau$, the propagation over one time step $\Delta\tau$ according to (3.2.13) results in nonorthonormal wave functions N'_{nl}. Subsequently, the following Gram-Schmidt procedure is used to calculate orthonormal functions N_{nl} at time τ_{i+1} based on the functions N'_{nl} in two steps.

Orthogonalization:

$$\begin{aligned} &k = 1 && M_1 = N_1, \\ &k = 2,\ldots,N_l && M_k = N'_k - \sum_{j=1}^{k-1} M_j \frac{\langle M_j | N'_k \rangle}{\langle M_j | M_j \rangle}. \end{aligned} \tag{3.2.14}$$

Normalization:

$$k = 1,\ldots,N_l \qquad \tilde{N}_k = V_{ion} \frac{M_k}{\sqrt{\langle M_k | M_k \rangle}}.$$

The index k was introduced to count all N_l radial wave functions for a given number l.

Finally, one iteration step of the imaginary time method consists of two parts. The initial data of each step consists of a set of orthonormal wave functions N_{nl}, which fulfill the orthogonality relation (3.2.10). First, these functions are propagated based on (3.2.13) over a time step $\Delta\tau$. In the second step, all functions N'_{nl} for one l are orthonormalized based on (3.2.14). The resulting functions N_{nl} are used as initial functions for the next iteration step. The iteration process is repeated until the desired degree of convergence is achieved. The time propagation of the functions N_{nl} is done by the Crank-Nicolson finite-difference method [95, 96] on a radial grid. The potential ϕ is calculated on the same grid by using central differences [97] and LU decomposition [98].

Test calculations showed that the convergence behavior of the present method is not significantly influenced by the choice of the initial radial functions $N_{nl}(r,0)$. In particular, initial functions of the form

$$N_{nl}(r,0) \sim \exp\Big(-(r-r_l)^2\Big), \quad r_l = \frac{l}{l_{max}} R \tag{3.2.15}$$

lead to satisfactory results. A rather important parameter of the relaxation method is the time step $\Delta\tau$. This parameter has to be chosen sufficiently small to achieve

convergence. The upper bound $\Delta\tau_{max}$ for which the method converges strongly depends on the size of the cluster. It turns out that the parameter $\Delta\tau_{max}$ decreases as a function of the cluster radius R. In particular, a value of $\Delta\tau_{max} \approx 10^{-1}$ can be used for $R = 20$, while one needs $\Delta\tau_{max} \approx 10^{-4}$ for $R = 400$. In the following two subsections, the relaxation method is applied to calculate electron equilibria for different values of N_s in the present Vlasov model.

3.3 Multistream Na Cluster

In this subsection, results for the equilibrium states of Na clusters are presented, which have a well-known equilibrium state [31]. In section 4.4, these Na clusters are treated as reference examples for simple metal clusters with a full account to the electronic details. In the present Vlasov model, this means that each representative state of the single-particle ensemble is associated with one electron of the cluster. Due to the spin degeneracy, always two electrons can be assigned to a single spatial wave function. One therefore requires $N_s = N_e/2$ electron states to describe the many-electron system, where N_e is the number of electrons.

In the present jellium model, the negative electron charge is neutralized by a positive charge, which is distributed homogeneously over a sphere of radius R. By using the definition

$$n_0 = \left(\frac{4}{3}\pi r_s^3\right)^{-1} \tag{3.3.1}$$

of the Wigner-Seitz radius r_s and the condition $n_0 = N_e/V_{ion}$ for neutrally charged clusters, the radius can alternatively be written as

$$R = N_e^{1/3} r_s. \tag{3.3.2}$$

This relation determines the cluster radius for a neutral system with bulk Wigner-Seitz radius r_s and a given number of electrons. The bulk Wigner-Seitz radius of Na is given by $r_s = 3.93\, a_B$ [92]. Here, a_B is the Bohr radius.

In the following, equilibria of differently sized Na clusters are presented. The electron configurations for different cluster radii are taken from [31]. They are given in Appendix A.1 using the compact notation as defined in Subsection 3.2. The largest cluster consists of $N_e = 198$ electrons, which gives rise to a cluster radius of $R = 10.8$ in the present plasma units and $R_{at} = 22.9$ in atomic units. These numerical values correspond to a cluster radius of 1.2nm. The electron configuration of this cluster is shown in Table 3.3.1 using the common spectroscopic notation of atomic physics.
For the Na cluster, the sequence of electron orbitals representing the order of filling of electron states up to $N_e = 198$ is given by

$$1s^2\ 1p^6\ 1d^{10}\ 2s^2\ 1f^{14}\ 2p^6\ 1g^{18}\ 2d^{10}\ 1h^{22}\ 3s^2\ 2f^{14}\ 1i^{26}\ 3p^6\ 1k^{30}\ 2g^{18}\ 3d^{10}\ 4s^2.$$

Now, the structure of the equilibrium density is analyzed. Figure 3.3.1 shows the equilibrium densities for different cluster radii. Besides the total electron density $n^{(0)}(r)$,

l	N_l	$n=1$	$n=2$	$n=3$	$n=4$
0	4	s^2 (1)	s^2 (9)	s^2 (14)	s^2 (17)
1	3	p^6 (2)	p^6 (10)	p^6 (15)	
2	3	d^{10} (3)	d^{10} (11)	d^{10} (16)	
3	2	f^{14} (4)	f^{14} (12)		
4	2	g^{18} (5)	g^{18} (13)		
5	1	h^{22} (6)			
6	1	i^{26} (7)			
7	1	k^{30} (8)			

Table 3.3.1: Electron configuration of a Na cluster with $R = 10.8$ and N_e=198. The numbers in the round brackets denote the subshell numbering in figures.

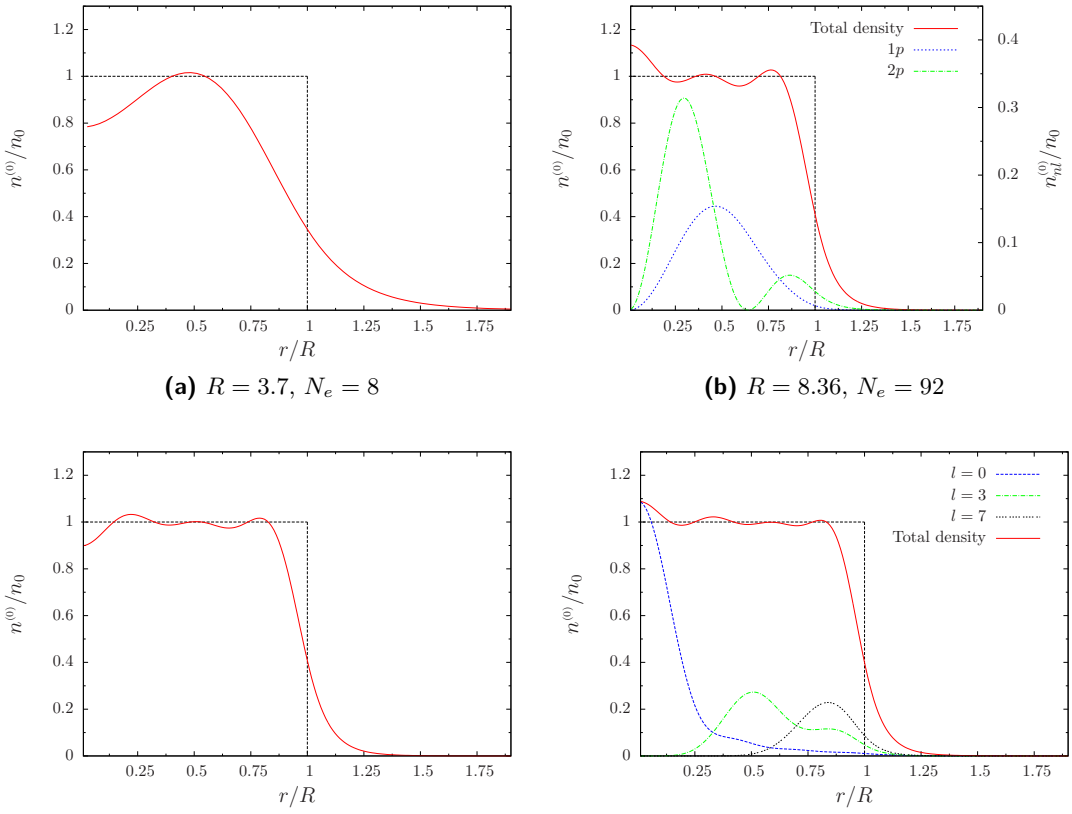

(a) $R = 3.7$, $N_e = 8$ **(b)** $R = 8.36$, $N_e = 92$

(c) $R = 9.57$, $N_e = 138$ **(d)** $R = 10.8$, $N_e = 198$

Figure 3.3.1: Equilibrium densities $n^{(0)}(r)$ of Na clusters in the Vlasov model. Results are shown for different cluster radii R. It is shown that $n^{(0)}(r)$ becomes smoother inside the cluster as R increases. Furthermore, one recognizes the spill-out effect of the electron density at the cluster surface. In (d), the densities $n_l^{(0)}(r)$ of electrons with a specific angular momentum l are shown. It is visible that the electron system exhibits a shell structure. In (b), the subshell densities $n_{nl}^{(0)}(r)$ of the $1p$ and $2p$ electrons are plotted to illustrate the effect of the quantum number n on the function profile of the electron states.

the electron densities $n_l^{(0)}(r)$ of electrons with a specific angular momentum l are plotted,

$$n_l^{(0)}(r) = w \sum_{n=1}^{N_l} \frac{2l+1}{4\pi} |R_{nl}|^2. \tag{3.3.3}$$

As shown, the cluster equilibrium exhibits a shell structure [37]. Electrons with higher angular momentum are located closer to the cluster surface. For the smallest cluster with $N_e = 8$ electrons, the density varies significantly inside the cluster. This variation becomes less pronounced as the cluster size increases. In particular, the density of the largest cluster shows a slight oscillation around the step function $n_{cl}(r) = \theta(R - r)$, which represents the classical electron density at $T = 0$. Here, the maximum deviation from the classical result is given by less than 10%.

Now, the focus is put on the behavior at the cluster surface. As visible, the electron density does not strictly vanish at the cluster boundary. It rather decays exponentially outside the cluster. This behavior, known as the spill-out effect, is a pure quantum-mechanical effect at $T = 0$. In the case of a classical system, the spill out is a thermal effect which depends on T and which vanishes at $T = 0$. For a quantum system, the spill-out effect is essentially independent of the temperature for $T \lesssim \epsilon_F$, where ϵ_F is the Fermi energy. It leads to an effective lack of electrons on the inner side of the cluster surface. The resulting positive surface charge is screened by electrons inside the cluster, which leads to a local maximum of the electron density close to the cluster surface (see Fig. 3.3.1).

3.4 Single-State Vlasov Model

A large computational simplification can be gained by a reduction of the number of representative electron states in comparison to the cluster calculations of the previous subsection with $N_s = N_e/2$ and a full account to the electronic details. In particular, this subsection introduces a numerically feasible model, the SSVM. The SSVM corresponds to a simplified Vlasov model with only one representative state ($N_s = 1$). Within the SSVM, the equilibrium is described by one spherically symmetric wave function $\varphi_{100}^{(0)}(r) = R_{10}(r)Y_{00}$, which corresponds to equilibrium quantum numbers $n = 1$ and $l = m = 0$.

First, the equilibrium properties of this model are discussed. In Fig. (3.4.1), the equilibrium densities $n^{(0)}(r)$ of the SSVM are plotted for a large cluster with $R = 250$ and a small cluster with $R = 10$. In addition, the self-consistent potentials $\phi^{(0)}(r)$ in the equilibrium state are shown. One recognizes that the equilibrium density is very close to the classical result inside the cluster. The main difference to the classical result is a broadening of the electron density at the cluster surface, which is related to the spill-out effect. One recognizes that the density spill-out strongly depends on the size of the cluster. It becomes significant for small clusters. Here, electrons are weakly bound to the cluster and can penetrate the cluster surface into the vacuum region. The broadening of the electron density with a sharp local maximum close to the cluster surface leads to an inhomogeneous surface potential with a pronounced local minimum. This minimum generates the binding and is a well-known feature of an electron gas at

l	$n=1$	$n=2$
0	-0.4924	-0.3033
1	-0.4231	-0.1685
2	-0.3378	-0.0443
3	-0.2362	
4	-0.1208	

(a) $R = 7.56,\ N_e = 68$

l	$n=1$	$n=2$	$n=3$
0	-0.4827	-0.3081	-0.0765
1	-0.4139	-0.2063	
2	-0.3329	-0.0961	
3	-0.2418		
4	-0.1415		
5	-0.0334		

(b) $R = 8.36,\ N_e = 92$

l	$n=1$	$n=2$	$n=3$
0	-0.4984	-0.3582	-0.1614
1	-0.4489	-0.2755	-0.0562
2	-0.3870	-0.1841	
3	-0.3149	-0.0857	
4	-0.2338		
5	-0.1445		
6	-0.0479		

(c) $R = 9.57,\ N_e = 138$

l	$n=1$	$n=2$	$n=3$	$n=4$
0	-0.5179	-0.4028	-0.2376	-0.0382
1	-0.4828	-0.3354	-0.1434	
2	-0.4355	-0.2603	-0.0497	
3	-0.3785	-0.1775		
4	-0.3130	-0.0885		
5	-0.2396			
6	-0.1591			
7	-0.0718			

(d) $R = 10.8,\ N_e = 198$

Table 3.3.2: Energy eigenvalues ϵ_{nl} for Na clusters of various size. The degeneracy of the eigenvalue ϵ_{nl} is given by $2(2l+1)$ corresponding to two opposite spin directions and $2l+1$ m-values for each subshell with quantum numbers n and l. The numerical values are calculated with a spatial grid constant of $\Delta r = 0.1$.

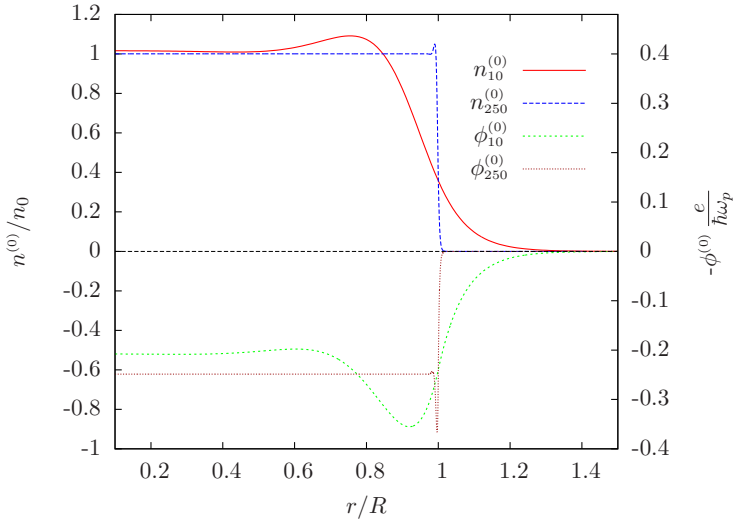

Figure 3.4.1: Equilibrium densities $n^{(0)}(r)$ of atomic clusters in the single-state Vlasov model. Results are shown for cluster radii $R = 250$ and $R = 10$. In addition, the corresponding self-consistent potentials $\phi^{(0)}(r)$ are plotted. One can see that the spill-out effect becomes pronounced for small clusters. The broadening of the electron density close to the cluster surface leads to an inhomogeneous surface potential.

the surface of a metal [99]. As the cluster size increases, the minimum becomes sharper and the electrons effectively see a potential that is close to that of a finite potential well. Moreover, the relative number of spill-out electrons is strongly reduced for large clusters and the density approaches the classical behavior of a homogeneous sphere.

In the following, the equilibrium density of the SSVM is compared with the results of the previous subsection for the many-electron Vlasov equilibria of sodium clusters. In addition, comparison will be made with previous DFT calculations for sodium clusters. The DFT results are recalculations of the work of Ekardt [31] for the same parameters. The difference to the present Vlasov calculations is an additional exchange-correlation potential ϕ_{xc} in LDA, which is taken from Gunnarson and Lundqvist [90]. The DFT results are reproduced by adding ϕ_{xc} to the self-consistent potential ϕ in (2.3.3a). In [90], the function ϕ_{xc} is given in terms of atomic units. Transforming ϕ_{xc} into the present plasma units (see Table 2.3.1) yields

$$\phi_{xc}(\boldsymbol{r},t) = \frac{1}{2}\frac{E_H}{\hbar\omega_p}\left(\frac{1.222\, n_0^{1/3}\, a_B}{r_s(\boldsymbol{r},t)} + 0.0666 \ln\left(1 + \frac{1.767\, n_0^{1/3}\, a_B}{r_s(\boldsymbol{r},t)}\right)\right). \tag{3.4.1}$$

Here, $E_H \approx 27.2\text{eV}$ is the Hartree energy. The position-dependent Wigner-Seitz radius $r_s(\boldsymbol{r},t)$ is determined by the electron density as follows:

$$r_s(\boldsymbol{r},t) = \left(\frac{3}{4\pi}\right)^{1/3} n^{-1/3}(\boldsymbol{r},t). \tag{3.4.2}$$

For the comparison, a Na cluster of radius $R = 10.8$ is considered. The corresponding plasma parameters for the evaluation of (3.4.1) are given in Table 2.3.2. Figure 3.4.2

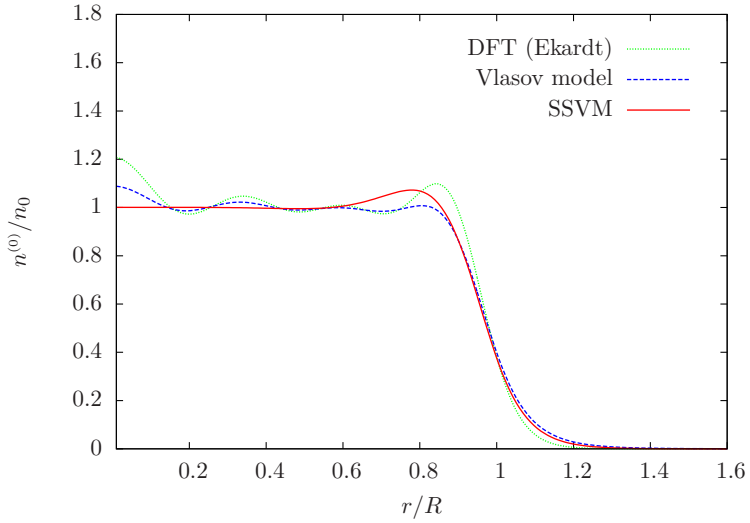

Figure 3.4.2: Equilibrium density $n^{(0)}(r)$ of a Na cluster ($N_e = 198$, $R = 10.8$). The DFT result was first calculated by Ekardt [31] with the exchange-correlation potential introduced by Gunnarsson and Lundqvist [90]. It is compared to the present Vlasov model, neglecting exchange-correlation effects, and with the single-state Vlasov model (SSVM). The density of the spill-out electrons can be rather accurately described by the single-state approach.

shows the equilibrium density $n^{(0)}(r)$ of the reference Na cluster as well as the equilibrium density in the SSVM. In addition, to investigate qualitatively how exchange and correlation effects modify the equilibrium state, the DFT result for the electron density in LDA is plotted. It is clearly visible that the SSVM does not account for electronic details in the cluster, in particular for the oscillations of the electron density. However, as it will be shown in Subsection 4.2, the spill-out region of the electron density is of particular importance for the dynamics of the Mie plasmon. Figure 3.4.2 shows that the SSVM leads to a very good approximation of the Vlasov result in the spill-out region. Furthermore, the inclusion of exchange and correlation effects modifies the spill-out region only weakly. Therefore, the close agreement of the density profiles in the spill-out region indicates that the SSVM is a good starting point for the analysis of the surface plasmon resonance.

Chapter 4

Linear Theory of Electrostatic Cluster Excitations

This chapter incorporates results that have been pre-published in [81]. *These results were partly presented at the twenty fifth and twenty sixth annual International Laser Physics Workshop (LPHYS'16,LPHYS'17) by the author of this thesis.*

The following chapter is devoted to the linear dynamics of atomic clusters in the quantum-size regime of particle diameters of a few nanometers. One important type of cluster excitation is the surface plasmon resonance, which corresponds to a collective excitation of the electron density in the surface area of the cluster. Since surface plasmons are accompanied by an excitation of the cluster multipole moments, in particular the cluster dipole moment, they couple to an external light wave. Therefore, they are of particular importance for the understanding of the optical properties of atomic clusters. In particular, the interaction of typical laser light with nanometer-sized clusters leads to an excitation of the Mie plasmon [7], which is related to the collective dipole oscillation of the cluster electrons in the electric field of the background ions. A rather simple theoretical treatment of the Mie oscillation goes back to Lord Rayleigh, who considered a small dielectric sphere in a homogeneous time-dependent electric field [9]. This approach yields the resonance condition $\epsilon(\omega) + 2 = 0$ for the Mie plasmon, where $\epsilon(\omega)$ is the dielectric function of the sphere. By introducing the dielectric function $\epsilon(\omega) = 1 - \omega_p^2/\omega^2$ of a free electron gas, the resonance frequency becomes $\omega = \omega_p/\sqrt{3}$, which corresponds to the Mie frequency. The more complete Mie theory applies to light scattering by dielectric spheres of arbitrary size with a full account to the EM radiation field [10]. In small clusters, as treated in this chapter, the motion of the cluster electrons is significantly influenced by the surface of the cluster. In particular, for cluster sizes on the nanometer scale, a proper quantum-mechanical description of the plasmon dynamics requires a consistent treatment of the quantum-mechanical spill-out effect of the electron density (see Section 3). It has been demonstrated experimentally that surface effects in nanometer-sized clusters lead to a damping of the Mie oscillation [21, 23, 100]. The corresponding damping mechanism is generally known as surface scattering. Further experiments have shown that the resonance frequency of the Mie oscillation is shifted with respect to ω_M depending on the cluster material and temperature [25, 101–104]. The surface-induced damping of the Mie plasmon has been widely studied also on a theoretical basis. Most of this work has been based on the RPA [41, 42] and corresponding semi-classical approximations [43], the TDLDA [15, 45, 46, 105] and classical free-path models with isotropic [26] and diffuse scattering

[27] at the cluster boundary. The major results [41, 43] have been reviewed and extended in a later work by Tran Thoai and Ekardt [44]. It is a common feature of most theoretical models that the full width at half maximum Γ of the plasmon resonance curve can be written in the form

$$\Gamma = A\frac{v_F}{R}, \tag{4.0.1}$$

where v_F is the Fermi velocity, R the cluster radius and A a constant of order unity which depends on the model considered. Some characteristic values for the parameter A can be found in [100]. The plasmon linewidth Γ has been the subject of various experiments under different conditions. While early experimental data of Kreibig [21] on Ag particles embedded in glass were consistent with the isotropic free-path consideration [26] ($A = 1$), later experiments [106] with embedded Ag particles were in good agreement with the corrected RPA result $A = 0.38$ [44]. More advanced TDLDA calculations of Ag particles in an embedding material with dielectric constant ϵ_m [105] lead to a slightly smaller value of $A \approx 0.28$ for free isolated particles ($\epsilon_m = 1$). This parameter is close to the value of $A = 0.25$ measured in more recent experiments of free isolated Ag [23] and Au clusters [24].

In this chapter, atomic cluster excitations are studied by linear perturbation theory on the basis of the underlying Vlasov-Poisson system (2.3.3). This electrostatic treatment is reasonable since the effect of radiation emission becomes small in nanometer-sized clusters [14]. In the framework of linear perturbation theory, the cluster is assumed to be close to the equilibrium state, which was introduced in Section 3. In Section 4.1, the basic equations of the perturbation theory are derived. In order to interpret the surface effects of the plasmon dynamics systematically, an equation of motion for the time evolution of the center of mass (c.m.) is derived in Section 4.2. This equation includes a surface force due to the electron dynamics in the exterior region of the cluster. In the subsequent parts of this chapter, the numerical results are presented. First, the focus is put on the SSVM with one representative electron state. The analysis of linear cluster excitations within the SSVM follows preliminary studies of [107]. This analysis is continued in Section 4.3, where a complete discussion of plasmon excitations is provided. Finally a detailed analysis of the surface plasmon damping mechanism is presented based on the dynamics of the electron density. As a major result, "surface scattering" is shown to lead to a conversion from surface plasmons to volume plasmons [81]. While Landau damping [15, 17] is related to a coupling of collective modes and single-particle excitations, the presented damping mechanism is associated with a coupling of two collective modes. In the last section 4.4, the description of cluster excitations is extended to the multistream model. Here, an ensemble of representative states is considered for the description of the electron system. As a reference example, small Na clusters are treated up to a radius of 1.2nm and 198 cluster electrons. Finally, the perturbation results of the simple SSVM are compared with corresponding results of the many-electron calculations for Na clusters and with previous results on the damping rate of the Mie plasmon.

4.1 Perturbation Theory

The present chapter provides an analysis of atomic cluster excitations in linear perturbation theory. In this section, the basic formalism of the perturbation theory is

derived. The perturbative description is based on a partial wave expansion of the wave functions and the self-consistent potential in terms of SH $Y_{lm}(\theta,\varphi)$ [108]. A short introduction to the SH is given in Subsection 4.1.1. In addition, important properties of the Wigner 3-j symbols [109] are summarized that are important for the perturbative formalism. In Subsection 4.1.2, the underlying equations 2.3.3 are linearized about the set of equilibrium functions, which were calculated in Chapter 3. Subsequently, the basic formalism of the perturbation theory is derived based on a partial wave expansion of the linearized equations. A complete set of wave functions for the radial parts of the perturbation in the corresponding self-consistent potential is obtained. Finally, the cluster multipole moments are expressed by the wave functions of the perturbation theory in Subsection 4.1.3.

4.1.1 Spherical Harmonics and Wigner 3-j Symbols

The SH $Y_{lm}(\theta,\varphi)$ [108] define a complete set of basis functions over the unit sphere

$$S_2 = \{\boldsymbol{r} \in \mathbb{R}^3 : \ |\boldsymbol{r}| = 1\}. \tag{4.1.1}$$

They are determined by the relation ($l \in \mathbb{N}_0$, $|m| \leq l$)

$$Y_{lm}(\theta,\varphi) = \sqrt{\frac{(2l+1)}{4\pi}\frac{(l-|m|)!}{(l+|m|)!}}\, P_l^{|m|}(\cos\theta)\, e^{im\varphi} \begin{cases} (-1)^m & m \geq 0 \\ 1 & m < 0 \end{cases}, \tag{4.1.2}$$

where the associated Legendre polynomials $P_l^m(x)$ ($0 \leq m \leq l$) are given by

$$P_l^m(x) = (1-x^2)^{\frac{m}{2}} \frac{d^m}{dx^m} P_l(x), \quad -1 \leq x \leq 1. \tag{4.1.3}$$

The functions $P_l^m(x)$ are related to Legendre polynomials $P_l(x)$, which read

$$P_l(x) = \frac{1}{2^l l!}\frac{d^l}{dx^l}(x^2-1)^l, \quad Y_{l0}(\theta) = \sqrt{\frac{2l+1}{4\pi}} P_l(\cos\theta). \tag{4.1.4}$$

A basic property of SH (4.1.2) is the orthogonality relation

$$\int_{S_2} Y_{lm}^*(\theta,\varphi)\, Y_{l'm'}(\theta,\varphi)\, d\Omega = \delta_{ll'}\delta_{mm'}. \tag{4.1.5}$$

Furthermore, they have the property

$$Y_{lm}^* = (-1)^m Y_{l(-m)}. \tag{4.1.6}$$

Since the SH define a complete set of basis functions, a scalar function $g(\boldsymbol{r})$ can be expanded as a linear combination of SH. By using (4.1.5), this expansion is given by

$$g(\boldsymbol{r}) = \sum_{l=0}^{\infty}\sum_{m=-l}^{l} g_{lm}(r) Y_{lm}(\theta,\varphi), \quad g_{lm}(r) = \int_{S_2} Y_{lm}^*(\theta,\varphi) g(\boldsymbol{r}) d\Omega. \tag{4.1.7}$$

In this representation, the functions g_{lm} depend on the radial distance $r = |\boldsymbol{r}|$.

In Subsection 4.1.2, one has to expand products of two SH in terms of SH. With (4.1.7), the corresponding expansion coefficients are defined by the expressions

$$Y_{l'm'}(\theta,\varphi)Y_{lm}(\theta,\varphi) = \sum_{\bar{l}=0}^{\infty} C_{l'm'\,lm\,\bar{l}}\, Y_{\bar{l}\,(m+m')}(\theta,\varphi), \tag{4.1.8a}$$

$$C_{l'm'\,lm\,\bar{l}} = \int\limits_{S_2} Y^{*}_{\bar{l}\,(m+m')}(\theta,\varphi)\, Y_{l'm'}(\theta,\varphi) Y_{lm}(\theta,\varphi)\, d\Omega. \tag{4.1.8b}$$

The coefficient $C_{l'm'\,lm\,\bar{l}} \in \mathbb{R}$ is nonvanishing only for certain values of $\bar{l}$ [110],

$$C_{l'm'\,lm\,\bar{l}} \neq 0 \;\Leftrightarrow\; \bar{l} \in M_{l'l}, \tag{4.1.9}$$

where the set $M_{l'l}$ is given by

$$M_{l'l} = \{|l'-l|, |l'-l|+2, |l'-l|+4, \ldots, l'+l\}. \tag{4.1.10}$$

This set contains $|M_{l'l}| = \min(l,l')+1$ elements. For the further discussion in Subsection 4.1.2, it is convenient to express the constants $C_{l'm'\,lm\,\bar{l}}$ by Wigner 3-j symbols [109]. The Wigner 3-j symbols are determined by integrals of products of three SH,

$$\begin{aligned} &\int Y_{l_1m_1}(\theta,\varphi)\, Y_{l_2m_2}(\theta,\varphi)\, Y_{l_3m_3}(\theta,\varphi) d\Omega \\ &= \sqrt{\frac{(2l_1+1)(2l_2+1)(2l_3+1)}{4\pi}} \begin{pmatrix} l_1 & l_2 & l_3 \\ 0 & 0 & 0 \end{pmatrix} \begin{pmatrix} l_1 & l_2 & l_3 \\ m_1 & m_2 & m_3 \end{pmatrix}. \end{aligned} \tag{4.1.11}$$

Based on this definition and by using (4.1.6), the expansion coefficients (4.1.8b) can be written as

$$\begin{aligned} C_{l_1m_1\,l_2m_2\,l_3} &= \sqrt{\frac{(2l_1+1)(2l_2+1)(2l_3+1)}{4\pi}} \\ \times(-1)^{m_1+m_2} &\begin{pmatrix} l_1 & l_2 & l_3 \\ 0 & 0 & 0 \end{pmatrix} \begin{pmatrix} l_1 & l_2 & l_3 \\ m_1 & m_2 & -m_1-m_2 \end{pmatrix}. \end{aligned} \tag{4.1.12}$$

In the following, several basic properties of Wigner 3-j symbols

$$\begin{pmatrix} l_1 & l_2 & l_3 \\ m_1 & m_2 & m_3 \end{pmatrix} \tag{4.1.13}$$

are introduced. First, it is noted that the Wigner 3-j symbols are only nonvanishing if the following selection rules are fulfilled:

$$m_1 + m_2 + m_3 = 0, \tag{4.1.14a}$$

$$|l_1 - l_2| \leq l_3 \leq l_1 + l_2. \tag{4.1.14b}$$

The elements (4.1.13) have certain symmetry properties. For example, they are in-

variant under any even perturbation of the columns,

$$\begin{pmatrix} l_1 & l_2 & l_3 \\ m_1 & m_2 & m_3 \end{pmatrix} = \begin{pmatrix} l_2 & l_3 & l_1 \\ m_2 & m_3 & m_1 \end{pmatrix} = \begin{pmatrix} l_3 & l_1 & l_2 \\ m_3 & m_1 & m_2 \end{pmatrix}, \tag{4.1.15a}$$

$$\begin{pmatrix} l_1 & l_2 & l_3 \\ m & -m & 0 \end{pmatrix} = \begin{pmatrix} l_1 & l_2 & l_3 \\ -m & m & 0 \end{pmatrix}. \tag{4.1.15b}$$

A further important property is the orthogonality relation

$$(2l_3+1) \sum_{m_1=-l_1}^{l_1} \sum_{m_2=-l_2}^{l_2} \begin{pmatrix} l_1 & l_2 & l_3 \\ m_1 & m_2 & m_3 \end{pmatrix} \begin{pmatrix} l_1 & l_2 & l_3' \\ m_1 & m_2 & m_3' \end{pmatrix} = \delta_{l_3 l_{3'}} \delta_{m_3 m_{3'}}. \tag{4.1.16}$$

of two elements. General formulas for Wigner 3-j symbols are rather complicated. However, for $m_1 = m_2 = m_3 = 0$, the explicit formula ($2p = l_1 + l_2 + l_3$)

$$\begin{aligned} \begin{pmatrix} l_1 & l_2 & l_3 \\ 0 & 0 & 0 \end{pmatrix} = (-1)^p \sqrt{\frac{(2p-2l_1)!(2p-2l_2)!(2p-2l_3)!}{(2p+1)!}} \\ \times \frac{p!}{(p-l_1)!(p-l_2)!(p-l_3)!} \end{aligned} \tag{4.1.17}$$

can be obtained for l_3-values in the range (4.1.14b). Finally, it should be mentioned that the Wigner 3-j symbols can be written in terms of the well-known Clebsch-Gordan coefficients,

$$\begin{pmatrix} l_1 & l_2 & l_3 \\ m_1 & m_2 & m_3 \end{pmatrix} = \frac{(-1)^{l_1 - l_2 - m_3}}{\sqrt{2l_3+1}} \langle l_1 m_1 l_2 m_2 | l_3 (-m_3) \rangle. \tag{4.1.18}$$

4.1.2 Spherical Harmonic Expansion of the Linearized Equations

In the following, the linearized equations of the perturbation theory are derived. Since the electron system is considered to be close to the equilibrium state, each representative state $\varphi_k(\boldsymbol{r}, t)$can be characterized by a set of equilibrium quantum numbers $k = (nlm)$. In the perturbative description, the time-propagated single-particle states and the self-consistent potential are assumed to be of the form

$$\varphi_{nlm}(\boldsymbol{r}, t) = \left[\varphi^{(0)}_{nlm}(\boldsymbol{r}) + \varphi^{(1)}_{nlm}(\boldsymbol{r}, t)\right] e^{-i\epsilon_{nl}t}, \tag{4.1.19a}$$

$$\phi(\boldsymbol{r}, t) = \phi^{(0)}(r) + \phi^{(1)}(\boldsymbol{r}, t), \tag{4.1.19b}$$

$$n(\boldsymbol{r}, t) = n^{(0)}(r) + n^{(1)}(\boldsymbol{r}, t). \tag{4.1.19c}$$

The quantities with a superscript 1 describe small perturbations of the equilibrium quantities $\varphi^{(0)}_{nlm}$, $\phi^{(0)}$ and $n^{(0)}$, which were calculated in section 3. It is noted that the time-dependent phase in (4.1.19a) is related to the time evolution of the unperturbed system. It is split off in order to provide stability of the numerical scheme, which is used for the solution of the linearized theory.

In the next step, the equations (2.3.3) are linearized with respect to the perturbations $\varphi^{(1)}_{nlm}$ and $\phi^{(1)}$. Then, the time evolution of the perturbed wave functions $\varphi^{(1)}_{nlm}$ is

governed by the linearized Schrödinger-Poisson system

$$i\partial_t \varphi^{(1)}_{nlm} = \left[H^{(0)} - \epsilon_{nl}\right] \varphi^{(1)}_{nlm} - \left[\phi_{ext} + \phi^{(1)}\right] \varphi^{(0)}_{nlm}, \tag{4.1.20a}$$

$$\Delta\phi^{(1)} = n^{(1)} = \sum_{l=0}^{l_{max}} \sum_{m=-l}^{l} \sum_{n=1}^{N_l} 2w\, \Re\left\{\varphi^{(0)\,*}_{nlm}\, \varphi^{(1)}_{nlm}\right\}, \tag{4.1.20b}$$

where $H^{(0)}$ denotes the equilibrium Hamiltonian as defined in (3.2.1a). In this chapter, the focus is put on azimuthally symmetric excitations of the electron system. An elementary excitation in a given sector l' is defined by

$$n^{(1)} = n^{(1)}_{l'}(r,t) Y_{l'0}(\theta), \tag{4.1.21a}$$

$$\phi^{(1)} = h_{l'}(r,t) Y_{l'0}(\theta), \tag{4.1.21b}$$

$$\phi_{ext} = -\nu_{l'}(r,t)\, Y_{l'0}(\theta). \tag{4.1.21c}$$

The study of these elementary excitations allows for an isolated treatment of the multipole excitations of the electron system. In particular, a perturbation with $l' = 1$ is related to the dipole motion of the electron system, while the sector $l' = 2$ corresponds to the quadrupole dynamics.

The perturbation theory is set up with a partial wave expansion of the perturbed wave functions $\varphi^{(1)}_{nlm}$ in terms of SH. Since azimuthally symmetric perturbations (4.1.21) do not couple to the z-component of the angular momentum, the expansion of $\varphi^{(1)}_{nlm}$ can be restricted to partial waves with quantum number m,

$$\varphi^{(1)}_{nlm}(\boldsymbol{r},t) = \sum_{\bar{l}=0}^{\infty} g_{nlm\,\bar{l}}\,(r,t)\, Y_{\bar{l}m}(\theta,\phi). \tag{4.1.22}$$

In the following, it is shown that in this expansion only a finite number of partial waves has to be taken into account in order to describe azimuthally symmetric excitations of the form 4.1.21.

The first step of the perturbation theory consists of an expansion of the inhomogeneous part of the Schrödinger equation (4.1.20a) as a linear combination of SH. Here, the general expansion (4.1.8) of a product of two SH in terms of SH has to be taken into account. By introducing the perturbations (4.1.21), the equilibrium wave function (3.2.5) and the product rule (4.1.8), one obtains

$$\begin{aligned} &- \left(\phi_{ext} + \phi^{(1)}\right) \varphi^{(0)}_{nlm} \\ &= \left(\nu_{l'} - h_{l'}\right) R_{nl}\, Y_{l'0}\, Y_{lm} \\ &= \left(\nu_{l'} - h_{l'}\right) R_{nl} \sum_{\bar{l}\in M_{l'l}} C_{l'0\,lm\,\bar{l}}\, Y_{\bar{l}m}. \end{aligned} \tag{4.1.23}$$

In the next step, the expansion (4.1.22) of the wave function is introduced in (4.1.20a). By taking into account the orthogonality relations (4.1.5) and (3.2.9), one ends up with independent, radial equations for the functions $g_{nlm\,\bar{l}}\,(r,t)$,

$$i\partial_t\, g_{nlm\,\bar{l}} = \left[-\frac{1}{2}\Delta_{\bar{l}} - \phi^{(0)} - \epsilon_{nl}\right]\, g_{nlm\,\bar{l}} + R_{nl}\, \left[\nu_{l'} - h_{l'}\right] C_{l'0\,lm\,\bar{l}}\,. \tag{4.1.24}$$

Now, one has to distinguish the two cases $\bar{l} \notin M_{l'l}$ and $\bar{l} \in M_{l'l}$. By making use of the selection rule (4.1.9), the equation of motion for the radial wave functions $g_{nlm\,\bar{l}}$ with $\bar{l} \notin M_{l'l}$ reads

$$i\partial_t\, g_{nlm\,\bar{l}} = \left[-\frac{1}{2}\Delta_{\bar{l}} - \phi^{(0)} - \epsilon_{nl}\right]\, g_{nlm\,\bar{l}}. \tag{4.1.25}$$

It can be shown that wave functions with $\bar{l} \notin M_{l'l}$ do not couple to the sector l' of the electron density. The corresponding proof is rather technical and is therefore moved to Appendix A.2.1. Based on this insight, one has to choose the initial condition $g_{nlm\,\bar{l}}(r,0) = 0$ for $\bar{l} \notin M_{l'l}$. Then, according to (4.1.24), the solution for $t > 0$ reads $g_{nlm\,\bar{l}}(r,t) = 0$. In conclusion, partial waves with $\bar{l} \notin M_{l'l}$ can be excluded in the expansion (4.1.22).

Now, the case $\bar{l} \in M_{l'l}$ is considered. One recognizes that the m-dependence of the inhomogeneity in (4.1.24) is only generated by the constant $C_{l'0\,lm\,\bar{l}}$. In conclusion, solutions of (4.1.24) for fixed values of l and n and different m-values differ from one another only by the constant factor $C_{l'0\,lm\,\bar{l}}$. Finally, the m-dependence can be removed by introducing radial wave functions $g_{nl\,\bar{l}}(r,t)$,

$$g_{nlm\,\bar{l}}(r,t) = g_{nl\,\bar{l}}(r,t)\, C_{l'0\,lm\,\bar{l}}. \tag{4.1.26}$$

Then, the resulting Schrödinger equation for the m-independent wave function reads

$$i\partial_t\, g_{nl\,\bar{l}} = \left[-\frac{1}{2}\Delta_{\bar{l}} - \phi^{(0)} - \epsilon_{nl}\right]\, g_{nl\,\bar{l}} + R_{nl}\left(\nu_{l'} - h_{l'}\right). \tag{4.1.27}$$

So far, it has been demonstrated that elementary excitations (4.1.21) are associated with wave functions of the form

$$\varphi^{(1)}_{nlm}(\boldsymbol{r},t) = \sum_{\bar{l}\in M_{l'l}} g_{nl\,\bar{l}}(r,t)\, C_{l'0\,lm\,\bar{l}}\, Y_{\bar{l}m}(\theta,\phi). \tag{4.1.28}$$

Since the set $M_{l'l}$ contains $\min(l,l')+1$, the time evolution of a single-electron perturbation $\varphi^{(1)}_{nlm}$ is determined by $\min(l,l')+1$ radial wave functions $g_{nl\,\bar{l}}$, which are independent of the quantum number m. Now, this result is used for the linearization of Poisson's equation (4.1.20b).

The expansion of the linearized density in terms of SH is derived by introducing the equilibrium states $\varphi^{(0)}_{nlm}$ as defined in (3.2.5) and the expansion (4.1.28) of the perturbed wave functions,

$$\begin{aligned}
n^{(1)} &= \sum_{l,n,m}\sum_{\bar{l}\in M_{l'l}} 2w\,\Re\{\, Y^*_{lm}\, Y_{\bar{l}m} R^*_{nl}\, g_{nl\,\bar{l}}\, C_{l'0\,lm\,\bar{l}}\} \\
&\overset{(4.1.6)}{=} \sum_{l,n,m}\sum_{\bar{l}\in M_{l'l}} 2w\,\Re\{\, Y_{l(-m)}\, Y_{\bar{l}m}\, R^*_{nl}\, g_{nl\,\bar{l}}\, C_{l'0\,lm\,\bar{l}}\}\,(-1)^m \\
&\overset{(4.1.8)}{=} \sum_{l,n}\sum_{\bar{l}\in M_{l'l}}\sum_{l''\in M_{\bar{l}l}} 2w\,\Re\{R^*_{nl}\, g_{nl\,\bar{l}}\}\underbrace{\sum_m (-1)^m C_{l(-m)\,\bar{l}m\,l''} C_{l'0\,lm\,\bar{l}}}_{\equiv\, D_{l''\,l'\,\bar{l}\,l}} Y_{l''0}.
\end{aligned} \tag{4.1.29}$$

The four-component coupling constant $D_{l''\,l'\,\bar{l}\,l}$ can be evaluated analytically by using the definition of the Wigner 3-j symbols and their properties as defined in subsec-

tion 4.1.1. First, the relation (4.1.12) is taken into account to express the expansion coefficients C by Wigner 3-j symbols,

$$\begin{aligned} D_{l''\,l'\,\bar{l}\,l} &= \sum_{m=-l}^{l} (-1)^m C_{l(-m)\,\bar{l}m\,l''} C_{l'0\,lm\,\bar{l}} \\ &= \sum_{m=-l}^{l} \frac{(2l+1)(2\bar{l}+1)\sqrt{(2l'+1)(2l''+1)}}{4\pi} \\ &\quad \times \begin{pmatrix} l & \bar{l} & l' \\ 0 & 0 & 0 \end{pmatrix} \begin{pmatrix} l & \bar{l} & l' \\ m & -m & 0 \end{pmatrix} \begin{pmatrix} l & \bar{l} & l'' \\ 0 & 0 & 0 \end{pmatrix} \begin{pmatrix} l & \bar{l} & l'' \\ m & -m & 0 \end{pmatrix}. \end{aligned} \tag{4.1.30}$$

Here, the symmetry properties (4.1.15) were used to rearrange the Wigner 3-j symbols. In the last step, the orthogonality relation (4.1.16) is considered to evaluate the remaining m-sum. Since the selection rule (4.1.14) holds, the orthogonality relation can be alternatively written in the form

$$(2l_3+1) \sum_{m_1=-l_1}^{l_1} \begin{pmatrix} l_1 & l_2 & l_3 \\ m_1 & -m_1-m_3 & m_3 \end{pmatrix} \begin{pmatrix} l_1 & l_2 & l_3' \\ m_1 & -m_1-m_3 & m_3 \end{pmatrix} = \delta_{l_3 l_{3'}}. \tag{4.1.31}$$

This relation can be directly applied to (4.1.30), which yields

$$D_{l''\,l'\,\bar{l}\,l} = \frac{(2l+1)(2\bar{l}+1)}{4\pi} \begin{pmatrix} l & \bar{l} & l' \\ 0 & 0 & 0 \end{pmatrix}^2 \delta_{l''\,l'} \equiv D_{l'\,\bar{l}\,l}\, \delta_{l''\,l'}. \tag{4.1.32}$$

The analytical result for the remaining Wigner 3-j symbol with $m_1 = m_2 = m_3 = 0$ is given in (4.1.17). Finally, the three-component coupling constants $D_{l'\,\bar{l}\,l}$ read

$$\begin{aligned} D_{l'\,\bar{l}\,l} &= \frac{(2l+1)(2\bar{l}+1)}{4\pi} \frac{(L-2l)!(L-2l')!(L-2\bar{l})!}{(L+1)!} \\ &\quad \times \left(\frac{(L/2)!}{(L/2-l)!(L/2-l')!(L/2-\bar{l})!} \right)^2, \end{aligned} \tag{4.1.33}$$

where $L = l + l' + \bar{l}$. With this result, the linearized density (4.1.29) reads

$$n^{(1)} = n_{l'}^{(1)} Y_{l'0}, \quad n_{l'}^{(1)} = \sum_{n,l} \sum_{\bar{l} \in M_{l'l}} 2w D_{l'\,\bar{l}\,l}\, \Re\left\{ R_{nl}^*\, g_{nl\,\bar{l}} \right\}. \tag{4.1.34}$$

This result shows explicitly that the wave functions (4.1.28) are sufficient to describe azimuthally symmetric perturbations in sector l'.

Altogether, by using (4.1.21b), (4.1.34) and (4.1.27), the basic equations of the perturbation theory for the radial parts $g_{nl\,\bar{l}}$ and $h_{l'}$ of the wave functions and the self-consistent potential read

$$i\partial_t\, g_{nl\,\bar{l}} = H^{(0)}_{nl\,\bar{l}}\, g_{nl\,\bar{l}} + R_{nl}\,(\nu_{l'} - h_{l'})\,, \tag{4.1.35a}$$

$$\Delta_{l'}\, h_{l'} = n^{(1)}_{l'} = \sum_{l=0}^{l_{max}} \sum_{n=1}^{N_l} \sum_{\bar{l}\in M_{l'l}} 2w D_{l'\,\bar{l}\,l}\, \Re\{R^*_{nl}\, g_{nl\,\bar{l}}\}\,, \tag{4.1.35b}$$

where the equilibrium Hamiltonian $H^{(0)}_{nl\,\bar{l}}$ is given by

$$H^{(0)}_{nl\,\bar{l}} = -\frac{1}{2}\Delta_{\bar{l}} - \phi^{(0)} - \epsilon_{nl}, \quad \Delta_l = \Delta_r - \frac{l(l+1)}{r^2}. \tag{4.1.36}$$

For a given perturbation of the form (4.1.21) in sector l', the system (4.1.35) has to be solved for every subshell with equilibrium quantum numbers n and l and every corresponding partial wave with quantum number $\bar{l} \in M_{l'l}$. Since there are N_l different n-values for a given angular momentum l, the linear theory requires the time propagation of in total

$$N_p = \sum_{l=0}^{l_{max}} N_l\Big(\min(l, l') + 1\Big) \tag{4.1.37}$$

radial wave functions $g_{nl\,\bar{l}}$ based on time-dependent Schrödinger equations in one dimension. The time propagation of the wave functions is done by the Crank-Nicolson finite-difference method [95, 96] on a radial grid. The potential $h_{l'}$ is calculated on the same grid by using central differences [97] and LU decomposition [98]. The Wigner 3-j symbols are taken from the *GNU Scientific Library* [111].

4.1.3 Multipole Moments

In order to study the surface plasmon resonance, cluster multipole moments are considered in sections 4.3 and 4.4. For the numerical evaluation of their time evolution, the multipole moments have to be expressed in terms of the wave functions $g_{nl\,\bar{l}}(r,t)$ of the perturbation theory by introducing the partial wave expansion (4.1.34) of the electron density.

To study dipole excitations ($l' = 1$), the focus is put on the c.m. In dimensional (superscript *) and dimensionless form, it is given by ($V_{ion} = (4/3)\pi R^3$)

$$\boldsymbol{R}^\star(t^\star) = \frac{1}{N_e}\int_{\mathbb{R}^3} n^\star(\boldsymbol{r}^\star, t^\star)\, \boldsymbol{r}^\star\, d^3r^\star, \tag{4.1.38a}$$

$$\boldsymbol{R}(t) = \frac{1}{V_{ion}}\int_{\mathbb{R}^3} n(\boldsymbol{r}, t)\, \boldsymbol{r}\, d^3r, \tag{4.1.38b}$$

where n is the electron density. In this chapter, azimuthally symmetric excitations are treated. Therefore, only the z-component $Z(t)$ of the c.m. is nonzero. By using the relation

$$z = r\cos(\theta) = r\sqrt{\frac{4\pi}{3}}Y_{10}(\theta) \tag{4.1.39}$$

and the plasma units of Table 2.3.1, the dimensionless c.m. $Z(t)$ can be evaluated according to the following equation ($V_{ion} = (4/3)\pi R^3$):

$$\begin{aligned} Z(t) &= \frac{1}{V_{ion}} \int\limits_{\mathbb{R}^3} n^{(1)}(\boldsymbol{r},t)\, z d^3r = \frac{1}{V_{ion}} \sqrt{\frac{4\pi}{3}} \int\limits_0^\infty n_1^{(1)}(r,t)\, r^3 dr \\ &= \frac{1}{V_{ion}} \sqrt{\frac{16\pi}{3}} w \sum_{l,n} \sum_{\bar{l}\in M_{1l}} D_{1\,\bar{l}\,l} \int\limits_0^\infty \Re\left\{R^*_{nl}\, g_{nl\,\bar{l}}\right\} r^3 dr. \end{aligned} \tag{4.1.40}$$

Beyond dipole excitations, quadrupole excitations ($l' = 2$) are studied based on the element Q_{33} of the quadrupole tensor,

$$Q^\star_{33}(t^\star) = \int\limits_{\mathbb{R}^3} \rho^\star(\boldsymbol{r}^\star, t^\star) \left(2z^2 - x^2 - y^2\right)^\star d^3r^\star, \quad \rho^\star = -e\, n^\star, \tag{4.1.41a}$$

$$Q_{33}(t) = -\int\limits_{\mathbb{R}^3} n(\boldsymbol{r},t) \left(2z^2 - x^2 - y^2\right) d^3r. \tag{4.1.41b}$$

By using the relation

$$\begin{aligned} 2z^2 - x^2 - y^2 &= r^2 \left(2\cos(\theta)^2 - \sin(\theta)^2 \left(\cos(\varphi)^2 + \sin(\varphi)^2\right)\right) \\ &= r^2 \left(3\cos(\theta)^2 - 1\right) = \sqrt{\frac{16\pi}{5}} r^2\, Y_{20}(\theta), \end{aligned} \tag{4.1.42}$$

the dimensionless quadrupole moment Q_{33} can be calculated as follows:

$$\begin{aligned} Q_{33}(t) &= -\int\limits_{\mathbb{R}^3} n^{(1)}(\boldsymbol{r},t)\, (2z^2 - x^2 - y^2) d^3r = -\sqrt{\frac{16\pi}{5}} \int\limits_0^\infty n_2^{(1)}(r,t)\, r^4 dr \\ &= -\sqrt{\frac{64\pi}{3}} w \sum_{l,n} \sum_{\bar{l}\in M_{2l}} D_{2\,\bar{l}\,l} \int\limits_0^\infty \Re\left\{R^*_{nl}\, g_{nl\,\bar{l}}\right\} r^4 dr. \end{aligned} \tag{4.1.43}$$

4.2 Equation of Motion of the Center of Mass

For the analysis of the Mie plasmon with $l' = 1$, it turns out to be instructive to derive an equation of motion for the c.m. The resulting equation can be used to gain information about how the plasmon dynamics is affected by the details of the equilibrium density and in particular by electrons that are located outside the ion sphere in the equilibrium state. It is noted that in this section the time propagation of the electron states is not limited to the linear regime. By using (4.1.38b), the c.m. can be expressed in terms of the single-particle states $\varphi_k(\boldsymbol{r},t)$,

$$\boldsymbol{R}(t) = \frac{1}{V_{ion}} \int\limits_{\mathbb{R}^3} n(\boldsymbol{r},t)\, \boldsymbol{r}\, d^3r = \frac{w}{V_{ion}} \sum_{k=1}^{N_s} \langle \boldsymbol{r} \rangle_k(t), \quad \langle \boldsymbol{r} \rangle_k \equiv \langle \varphi_k(t) | \boldsymbol{r} | \varphi_k(t) \rangle, \tag{4.2.1}$$

where the electron density of (2.3.3b) was introduced. According to Ehrenfest's theorem, the spatial expectation value of the k-th representative state fulfills the equation of motion

$$\frac{d^2}{dt^2}\langle \boldsymbol{r}\rangle_k = \langle \nabla\phi\rangle_k, \tag{4.2.2}$$

where the total potential ϕ reads

$$\phi(\boldsymbol{r},t) = \phi_{int}(\boldsymbol{r},t) + \phi_{ext}(\boldsymbol{r},t). \tag{4.2.3}$$

Here, ϕ_{int} is the potential that is generated by the electrons and the ions. For the further evaluation, it is convenient to write ϕ_{int} as a sum of the single-particle contributions $\phi_k(\boldsymbol{r},t)$ of the electrons and the ion potential $\phi_{ion}(r)$,

$$\begin{aligned} \phi &= \sum_{k=1}^{N_s}\phi_k + \phi_{ion} + \phi_{ext}, \quad \Delta\phi_k = |\varphi_k|^2, \\ \phi_{ion} &= \begin{cases} -\frac{1}{6}(r^2 - 3R^2), & r < R, \\ \frac{R^3}{3r}, & r > R. \end{cases} \end{aligned} \tag{4.2.4}$$

In the following, an external laser field in dipole approximation is introduced that is polarized along the z-axis. Then, the external potential reads $\phi_{ext} = -E(t)z$.

By taking the second derivative of $\boldsymbol{R}(t)$ and by using (4.2.2), one obtains the following relation

$$\begin{gathered} \ddot{\boldsymbol{R}} = \boldsymbol{F}_{ext} + \boldsymbol{F}_{ion} + \boldsymbol{F}_{ee}, \\ \boldsymbol{F}_{ion} = \sum_{k=1}^{N_s}\langle\nabla\phi_{ion}\rangle_k\,, \quad \boldsymbol{F}_{ee} = \sum_{k=1}^{N_s}\sum_{j=1}^{N_s}\langle\nabla\phi_j\rangle_k\,, \quad \boldsymbol{F}_{ext} = -E(t)\,\boldsymbol{e}_z\,. \end{gathered} \tag{4.2.5}$$

In the following, it is shown that $\boldsymbol{F}_{ee} = 0$. For the proof, Green's second identity is used, which is given by

$$\int_V (\alpha\Delta\beta - \beta\Delta\alpha)dV = \int_{\partial V}(\alpha\nabla\beta - \beta\nabla\alpha)\cdot d\boldsymbol{\mathcal{F}}. \tag{4.2.6}$$

Here $\alpha(\boldsymbol{r})$ and $\beta(\boldsymbol{r})$ denote two scalar functions and ∂V the boundary of region V. Furthermore, the relation

$$\int_V (\beta\nabla\alpha + \alpha\nabla\beta)dV = \int_V \nabla(\alpha\beta)dV = \int_{\partial V}\alpha\beta\, d\boldsymbol{\mathcal{F}} \tag{4.2.7}$$

will be used. With these two relations, the expectation value $\langle\nabla\phi_j\rangle_k$ can be rewritten as follows:

$$\begin{aligned} \langle\nabla\phi_j\rangle_k &= \int_{\mathbb{R}^3}(\nabla\phi_j)|\varphi_k|^2dV \overset{(4.2.4)}{=} \int_{\mathbb{R}^3}(\nabla\phi_j)\Delta\phi_k dV \overset{(4.2.7)}{=} -\int_{\mathbb{R}^3}\phi_j\Delta(\nabla\phi_k)dV \\ &\overset{(4.2.6)}{=} -\int_{\mathbb{R}^3}\Delta\phi_j(\nabla\phi_k)dV = -\langle\nabla\phi_k\rangle_j. \end{aligned} \tag{4.2.8}$$

Here, the boundary condition $\varphi_k \to 0$ for $r \to \infty$ was imposed to omit the surface integrals in (4.2.6) and (4.2.7). It is noted that the relation (4.2.8) is the quantum-mechanical analog of Newton's third law. In particular, for $k = j$, one obtains $\langle \nabla \phi_k \rangle_k = 0$. With (4.2.8), the force $\boldsymbol{F_{ee}}$ can be written as

$$\boldsymbol{F_{ee}} = \sum_{k=1}^{N} \sum_{j=1}^{N} \langle \nabla \phi_j \rangle_k = - \sum_{k=1}^{N} \sum_{j=1}^{N} \langle \nabla \phi_k \rangle_j = -\boldsymbol{F}_{ee}. \tag{4.2.9}$$

This result gives $\boldsymbol{F}_{ee} = 0$. In the next step, the electric field of the ions is rewritten as

$$\begin{aligned} \nabla \phi_{ion} &= \begin{cases} -\frac{1}{3}\boldsymbol{r}, & r < R, \\ -\frac{1}{3}\frac{R^3}{r^3}\boldsymbol{r}, & r > R, \end{cases} \\ &= -\frac{1}{3}\boldsymbol{r} + \begin{cases} 0, & r < R, \\ \frac{1}{3}\boldsymbol{r}\left(1 - \frac{R^3}{r^3}\right), & r > R. \end{cases} \end{aligned} \tag{4.2.10}$$

This relation is introduced in (4.2.5). By using the definition (4.2.1), the final equation of motion of the c.m. reads

$$\ddot{\boldsymbol{R}} + \omega_M^2 \boldsymbol{R} = \boldsymbol{F}_{ext} + \boldsymbol{F}_{sc}, \tag{4.2.11a}$$

$$\boldsymbol{F}_{sc}(t) = \frac{w}{V_{ion}} \sum_{k=1}^{N_s} \langle \varphi_k(t) | \boldsymbol{f}_{sc} | \varphi_k(t) \rangle, \tag{4.2.11b}$$

$$\boldsymbol{f}_{sc}(\boldsymbol{r}) = \omega_M^2 \boldsymbol{r} \left(1 - \frac{R^3}{r^3}\right) \theta(r - R). \tag{4.2.11c}$$

Here, the Mie frequency $\omega_M = 1/\sqrt{3}$ in plasma units was introduced.

The motion of the c.m. corresponds to that of a harmonic oscillator with an additional force that is determined by the ensemble average of the operator $\boldsymbol{f}_{sc}$. This operator contributes only outside the ion sphere and takes into account the surface effects of the dynamics. The surface force $\boldsymbol{F}_{sc}$ in (4.2.11) can be written in terms of the spill-out density

$$n_{out}(\boldsymbol{r}, t) = n(\boldsymbol{r}, t)\, \theta(r - R) \tag{4.2.12}$$

of the electron system,

$$\boldsymbol{F}_{sc} = w \sum_{k=1}^{N_s} \frac{\langle \varphi_k | \boldsymbol{F}_{sc} | \varphi_k \rangle}{\langle \varphi_k | \varphi_k \rangle} = \frac{1}{V_{ion}} \int_{\mathbb{R}^3} n_{out}\, \boldsymbol{f}_{sc}\, d^3 r. \tag{4.2.13}$$

In this chapter, linear perturbations are considered. In order to get a more precise interpretation of the surface force in this regime, $\boldsymbol{F}_{sc}$ is evaluated up to linear order by introducing the partial wave expansion (4.1.34) of the linearized density,

$$\begin{aligned} \boldsymbol{F}_{sc}^{(1)}(t) = \sqrt{\frac{16\pi}{3}} \omega_M^2 \sum_{l=0}^{l_{max}} \sum_{n=1}^{N_l} \sum_{\bar{l} \in M_{1l}} w D_{1\bar{l}l} \\ \times \int_R^\infty \Re \left\{ R_{nl}^*(r)\, g_{nl\bar{l}}(r, t) \right\} \left(r^3 - R^3\right) dr = F_{sc}^z(t)\, \boldsymbol{e}_z. \end{aligned} \tag{4.2.14}$$

This formula can be used to calculate the surface force based on the time-propagated wave functions $g_{nl\bar{l}}$.

Relation (4.2.14) shows explicitly that only spill-out electrons with

$$\varphi_k^{(0)}\,\theta(r-R) \neq 0 \tag{4.2.15}$$

contribute to $\boldsymbol{F}_{sc}$. This means that only electrons with a finite probability of being located outside the ion sphere in the equilibrium state will affect the harmonic motion of the c.m. For an electron system with equilibrium density $n^{(0)}$, the fraction of spill-out electrons in the equilibrium state is defined by

$$f_{out} = \frac{N_{out}}{N_e} = \frac{1}{V_{ion}} \int\limits_{\mathbb{R}^3} n_{out}^{(0)}(r)\, d^3r. \tag{4.2.16}$$

This value quantifies the relevance of surface effects for the Mie plasmon.

In the following, the individual contributions of electronic subshells to f_{out} are discussed for the reference Na cluster with radius $R = 10.8$. By writing the equilibrium density

$$n^{(0)}(r) = \sum_{l=0}^{l_{max}} \sum_{n=1}^{N_l} n_{nl}^{(0)}(r) \tag{4.2.17}$$

as a sum of subshell densities, the subshell-resolved fraction of spill-out electrons can be analyzed. Figure 4.2.1 shows the subshell-resolved fraction of spill-out electrons as a function of the subshell number. For easier reference, the subshells are numbered starting from one with the quantum numbers $n = 1, l = 0$. Then, for each value of n, the subshells are numbered from $l = 0$ up to the maximum l-value for a given n-value (see Table 3.3.1).

In the case of subshell 1, the contribution to f_{out} is almost zero. Therefore, this subshell is almost completely bound to the interior region of the cluster. For increasing values of l and a given value of n, the figure illustrates that f_{out} increases monotoneously. This behavior quantifies the tendency that electrons with high l-values are located closer to the cluster surface due to the influence of the centrifugal barrier $V_{cf}(r) = l(l+1)/(2r^2)$. In conclusion, the function profile exhibits local maxima at the maximum l-value for a given n-value. It is also visible that f_{out} increases as a function of n for a fixed l. This is related to the additional radial nodes of the wave functions with $n > 1$.

As demonstrated by this section, the spill-out density determines the surface effects of the Mie plasmon. Therefore, the detailed electron distribution inside the cluster may not be so relevant for the motion of the c.m. In conclusion, an accurate description of the plasmon dynamics requires a proper description of the density spill out. It was shown in Section 3.4 that the SSVM leads to a rather good description of the spill-out density in the equilibrium state compared with the multistream model. In this sense, the SSVM can be seen as a good starting point for the analysis of the Mie plasmon.

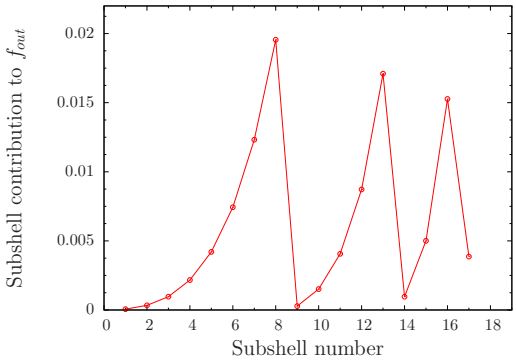

Figure 4.2.1: Subshell-resolved fraction of spill-out electrons (Na cluster, $N_e = 198$, $R = 10.8$). Each value describes the contribution of a single subshell to the total fraction f_{out} of spill-out electrons (see text for details). The subshells are numbered as shown in Table 3.3.1.

4.3 Single-State Description

In this section, the electron dynamics is studied in the SSVM based on the perturbation theory described in Section 4.1. In this framework, the time evolution of the electron system in a single sector l' of the density perturbation is represented by a single wave function $g_{00\,l'}(r,t)$ $(\min(0,l')+1=1)$. The advantage of the SSVM arises from the fact that the numerical effort can be reduced drastically. This simplification is especially helpful when it comes to parameter studies, where one has to calculate a large number of cluster equilibria over a wide range of cluster sizes.

In Subsection 4.3.1, the focus is put on the surface plasmon resonance that is associated with a perturbation of the electron density that is located near the cluster surface. For the analysis of the Mie plasmon, the c.m. motion of the electron system is analyzed based on the time-propagated wave function. By studying the time dependence of the c.m. oscillation, one can calculate the resonance frequency and damping rate of the Mie plasmon and also for higher multipole excitations.

In Subsection 4.3.2, the focus is put on volume plasmons that correspond to perturbations of the electron density in the interior region of the cluster. This analysis is based on a Fourier analysis of the time-dependent density fluctuations inside the cluster.

The last Subsection 4.3.3 provides a detailed analysis of the surface plasmon damping mechanism within the SSVM in the quantum-size regime.

4.3.1 Surface Plasmon Resonance

In this subsection, the surface plasmon resonance is investigated in the framework of the SSVM. For comparison, the well-known theoretical results for the free multipole oscillations of a homogeneous sphere with dielectric function $\epsilon(\omega) = 1 - \omega_p^2/\omega^2$ and

radius R are briefly reviewed [8]. The electrostatic boundary value problem leads to the potential perturbations (complex representation)

$$\phi_{l'}(\boldsymbol{r},t) = A\,Y_{l'0}(\theta)\,e^{-i\omega_{l'}t}\begin{cases}\left(\frac{r}{R}\right)^{l'}, & r<R,\\ \left(\frac{R}{r}\right)^{l'+1}, & r>R,\end{cases} \tag{4.3.1}$$

where $A \in \mathbb{C}$ is the amplitude of the perturbation and

$$\omega_{l'} = \sqrt{\frac{l'}{2l'+1}} \tag{4.3.2}$$

the resonance frequency.

Dipole Oscillation

Now, the perturbation results are presented for the dipole order $l' = 1$. To excite free dipole oscillations, the following initial condition has been imposed. The equilibrium density is shifted uniformly along the z-axis by a small displacement δ. Up to linear order in the parameter δ, this yields a perturbation that is proportional to Y_{10},

$$\begin{aligned} n(\boldsymbol{r},0) &= n^{(0)}(\boldsymbol{r}-\delta\,\boldsymbol{e}_z) = |\varphi_{100}^{(0)}|^2(\boldsymbol{r}-\delta\,\boldsymbol{e}_z) = n^{(0)}(r) - 2\delta\,\Re\{(\partial_z\,\varphi_{100}^{(0)})\,\varphi_{100}^{(0)\,*}\} \\ &= n^{(0)}(r) \underbrace{-2\delta\,\Re\{(\partial_r\,\varphi_{100}^{(0)})\,\varphi_{100}^{(0)\,*}\}\sqrt{\frac{4\pi}{3}}Y_{10}}_{n^{(1)}}, \end{aligned} \tag{4.3.3}$$

with

$$\frac{\partial z}{\partial r} = \frac{z}{r} = \cos(\theta) = \sqrt{\frac{4\pi}{3}}Y_{10}(\theta). \tag{4.3.4}$$

By comparing the initial condition for the density with the partial wave expansion of the density perturbation (4.1.34), the displacement corresponds to the initial wave function ($D_{110} = 1/4\pi$)

$$g_{10\,1}(r,0) = -\sqrt{\frac{4\pi}{3}}\,\delta\,\partial_r\,R_{10}(r). \tag{4.3.5}$$

Figure 4.3.1 shows the time evolution of Z for an initial displacement of $\delta = 0.1$ calculated from (4.1.40). One can confirm that the motion of the c.m. corresponds to that of a damped harmonic oscillator with frequency ω and damping rate γ for clusters that are not too small. As visible in Fig. 4.3.1, the damping effect is more pronounced for the smaller cluster. In this case, the spill-out of the electron density in the equilibrium state is significant (see Fig. 3.4.1). The plasmon parameters γ and ω can be calculated by a fit using the model function

$$f(t) = f_0\cos(\omega t)e^{-\gamma t}, \tag{4.3.6}$$

which yields the values $\gamma = 0.104$ and $\omega = 0.561$ for $R = 10$ and $\gamma = 0.009$ and $\omega = 0.577$ for $R = 100$. The frequency of the resonance is significantly redshifted [101–103] with respect to the Mie value $\omega_M = 1/\sqrt{3} \approx 0.5773$ for the smaller cluster with $R = 10$. The result of the larger cluster is close to ω_M.

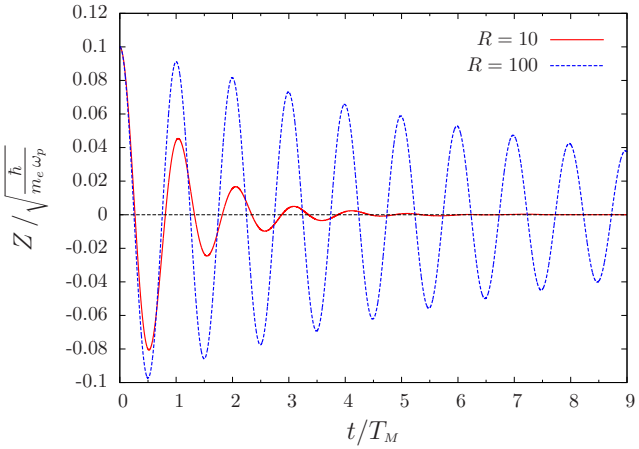

Figure 4.3.1: Time evolution of the center of mass (c.m.) $Z(t)$ for two cluster radii $R = 10$ and $R = 100$ (T_M: Mie period). At $t = 0$, the equilibrium distribution of the electrons is shifted homogeneously along the z-axis ($\delta = 0.1$). One recognizes the decay of the c.m. It is shown that the damping of the c.m. is more pronounced for the smaller cluster where the spill-out effect of the electron density becomes decisive.

The previous result indicates that the surface force $\boldsymbol{F}_{sc}$ in the equation of motion (4.2.11) and the related density spill-out gives rise to an exponential damping of the Mie plasmon, where $\boldsymbol{F}_{sc}$ acts as a friction force $\boldsymbol{F}_{fr}(t)$ that is proportional to the velocity $\dot{\boldsymbol{R}}(t)$ of the c.m.,

$$\boldsymbol{F}_{fr}(t) = -2\gamma\dot{\boldsymbol{R}}(t). \tag{4.3.7}$$

To test whether the simulation results are consistent with (4.2.11), $\boldsymbol{F}_{sc}$ is numerically evaluated with (4.2.14) and the time-propagted wave function. Figure 4.3.2 shows the z-component F_{sc}^z as a function of time for a cluster with $R = 30$ and an initial displacement parameter of $\delta = 1$. The result is compared with a friction force calculated from (4.3.7), where the damping rate $\gamma = 0.032$ is extracted from the c.m. motion. Since the velocity of the c.m. vanishes at $t = 0$ (rigid shift of the equilibrium density), both quantities are zero, initially. It is visible that especially after a few Mie periods both quantities are in very good agreement. This result shows that for moderately large clusters the surface force can be represented to a good approximation by a friction force acting on the c.m.

Quadrupole Oscillation

So far, dipole excitations were considered. Now, the focus is put on higher multipole excitations with $l' > 1$ in order to investigate the dependence of the plasmon damping rate on the multipole order. For the excitation of higher order multipole moments, an external point charge q is considered that is placed at position $\boldsymbol{r}' = r'\boldsymbol{e}_z$ on the positive part of the z-axis with $r' > 0$ at initial time $t = 0$. The distance between the cluster and the charge is considered to be sufficiently large ($r < r'$) such that the potential of

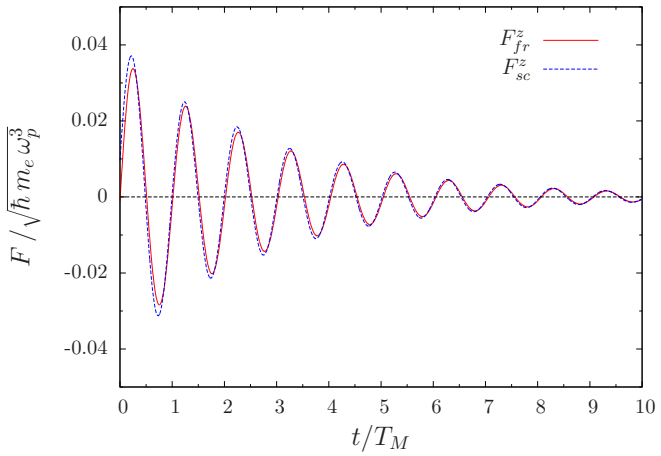

Figure 4.3.2: Component F^z_{sc} of the surface force $\boldsymbol{F}_{sc}$ (see 4.2.14) as a function time ($R = 30$, $\delta = 0.1$). The result is compared with a Stokes-like friction force $F^z_{fr}(t) = -2\gamma\dot{Z}(t)$ that is calculated by the damping rate $\gamma = 0.032$ of the Mie plasmon and the velocity $\dot{Z}$ of the c.m. It is visible that F^z_{sc} can be represented to a good approximation by the friction force F^z_{fr}.

the external charge can be decomposed as [8]

$$\begin{aligned} \phi_{ext}(\boldsymbol{r}) = \frac{q}{|\boldsymbol{r}-\boldsymbol{r}'|} &= -\sum_{l'=0}^{\infty} \nu_{l'}(r)\, Y_{l'0}(\theta), \\ \nu_{l'} &= -\sqrt{\frac{4\pi}{2l'+1}}\,\frac{q}{r'}\left(\frac{r}{r'}\right)^{l'}. \end{aligned} \tag{4.3.8}$$

Now, the response of the multipole orders $l' = 1$ and $l' = 2$ to the external perturbation is analyzed. Figure 4.3.3 shows the time evolution of the c.m. ($l' = 1$) and the quadrupole moment Q_{33} ($l' = 2$) for the parameters $R = 20$, $q = 500$ and $r' = 2R = 40$. The charge q is chosen sufficiently large to generate large numerical values of Q_{33}. At time $t = 0$, the electrons are in the equilibrium state and all multipole moments vanish. Due to the external perturbation, the multipole moments start oscillating around the asymptotic values $Z(\infty)/R = 0.55$ and $Q_{33}(\infty)/(QR^2) = 0.062$ that are approached for $t \to \infty$, where $Q = -V_{ion}$ is the total charge of the electrons in plasma units. This oscillation is damped and one can extract the plasmon parameters by a fit using the model function

$$f(t) = a - (a\cos(\omega t) + b\sin(\omega t))\, e^{-\gamma t}, \quad a = f(\infty), \tag{4.3.9}$$

which gives $\gamma = 0.076$ and $\omega = 0.630$ for the quadrupole mode and parameters $\gamma = 0.048$ and $\omega = 0.570$ for the dipole mode. The classical frequency of the quadrupole mode is given by $w_2 = \sqrt{2/5} = 0.6324$. This result indicates that the damping rate of the surface plasmon increases as a function of the mode number l'. Up to now, cluster radii $R \gtrsim 10$ were treated. For these radii, the fraction f_{out} of spill-out electrons in the equilibrium state is smaller than 10%. In particular, the surface force for $l' = 1$ was found to behave like a Stokes-like friction force on the c.m.

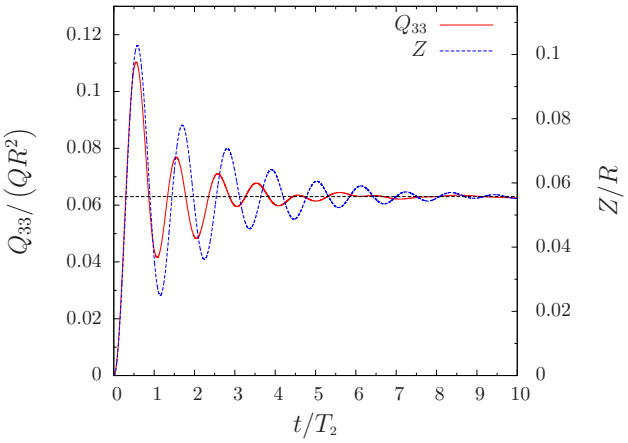

Figure 4.3.3: Time evolution of multipole moments ($R = 20$) following an excitation by a point charge $q = 500$ that is placed on the positive z-axis at distance $r' = 40$ from the origin. The time is measured in units of the classical period $T_2 = 2\pi/\omega_2$ of the quadrupole resonance. The figure shows the center of mass $Z(t)$ ($l' = 1$) and the element $Q_{33}(t)$ ($l' = 2$) of the quadrupole tensor. It is visible that the damping rate of the quadrupole moment is larger than that of the center of mass.

Small Clusters

In the following, smaller clusters with $R \lesssim 10$ are treated. In particular, calculations were performed for a cluster radius $R = 5$ with otherwise identical parameters as in the previous case. For this cluster size, f_{out} is given by 0.19.

In Fig. 4.3.4, the evolution of Q_{33} is shown for two cluster radii $R = 5$ and $R = 10$. In addition, for $R = 5$, the contributions of electrons are shown that are located in and outside the ion sphere. The sum of both contributions yields the total quadrupole moment Q_{33}. For $R = 10$, a strongly damped oscillation on the timescale of T_2 is visible that vanishes already after a few periods. In addition, one can see a slowly varying oscillation that is much more weakly damped. To analyze the emergence of the secondary oscillation in more detail, the Fourier transform of Q_{33} is introduced. Throughout this thesis, the Fourier transform $\tilde{g}(\omega)$ of a time-dependent function $g(t)$ is calculated based on the relation

$$\tilde{g}(\omega) = \frac{1}{t^*} \int_0^{t^*} e^{i\omega t} g(t) dt, \tag{4.3.10}$$

where t^* is the final time of wave propagation.

The inset plot in Fig. 4.3.4 shows the Fourier transform $\tilde{Q}_{33}(\omega)$. For $R = 10$, one can clearly recognize two resonances. The right maximum of $\tilde{Q}_{33}$ appears close to the classical frequency ω_2 of the surface plasmon resonance. The left maximum is associated with the residual oscillations of Q_{33} that are weakly damped. For the smaller cluster of radius $R = 5$, $\tilde{Q}_{33}$ exhibits only a single resonance well below ω_2. To understand the origin of the low-frequency oscillation in more detail, it turned out

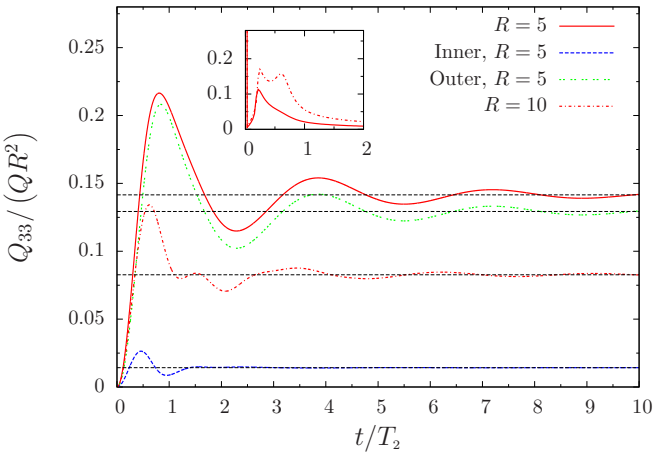

Figure 4.3.4: Motion of the quadrupole moment $Q_{33}(t)$ for two cluster radii R and the parameters in Fig. 4.3.3. The inset plot shows the corresponding Fourier transform $\tilde{Q}_{33}(\omega)$ (y-axis) measured in units of QR^2 (Q: Total electron charge) as a function of ω/ω_p (x-axis). The figure also shows the contributions of inner and outer electrons to the total quadrupole moment Q_{33} for $R = 5$. For small clusters, the quadrupole oscillation becomes dominated by outer electrons, which oscillate with a frequency smaller than the frequency $w_2 = 2\pi/T_2 = \sqrt{2/5}$ that is classically predicted.

to be instructive to analyze the contributions of outer and inner electrons separately. Fig. 4.3.4 shows that the contribution of inner electrons is quite small. It oscillates with a frequency close to ω_2 and vanishes already after a single period. One can see that the motion of the total quadrupole moment is dominated by outer electrons. Their contribution performs a damped harmonic oscillation around the corresponding asymptotic value, where the damping rate is much smaller than that of the inner electrons. A fit (see (4.3.9)) yields the resonance parameters $\gamma = 0.025$ and $\omega = 0.181 = 0.29\omega_2$. The value of γ is close to that obtained for a larger cluster of radius $R = 60$ ($f_{out} = 0.016$), where the motion of Q_{33} is mainly determined by inner electrons due to the small fraction of spill-out electrons.

The redshift of the resonance frequency ω with repect to ω_2 can be explained as follows: In the jellium model, the restoring force generated by the ions increases linearly with the radial distance inside the ion sphere. Outside the cluster, it decays Coulomb-like. Therefore, electrons that are located outside the ion sphere feel a restoring force that decreases as a function of the radial distance r. As the radius R decreases, f_{out} increases (see Fig. 3.4.1) and the number of electrons that feel a weaker restoring force than electrons inside the cluster increases. This leads to a reduction of the resonance frequency with respect to ω_2.

Finally, the results of this subsection can be summarized as follows: In the case of moderately large clusters with f_{out} being smaller than roughly 10%, the spill-out electrons act as a small perturbation to the plasmon dynamics both for the dipole and the quadrupole mode. In this regime, the surface force corresponds to a Stokes-like friction force acting on the multipole moments. This leads to an exponential decay of the multipole moments with damping constant γ, where the quadrupole mode relaxes faster.

The resonance frequencies are redshifted with respect to their classical reference values $\omega_{l'}$. When f_{out} becomes larger than 10%, the motion becomes significantly influenced by electrons which are located far outside the cluster due to the increasing influence of the spill-out effect for decreasing cluster sizes. These electrons feel a restoring force that is strongly reduced with respect to the restoring force at the cluster surface. This leads to low-frequency oscillations of the multipole moments which become dominant as the cluster size tends to zero.

4.3.2 Volume Plasmon Resonance

The last subsection has been devoted to the treatment of surface plasmons. These excitations are associated with a surface polarization of the cluster charges. In the following section, a second type of cluster excitations is considered, the so-called volume plasmons. Volume plasmons are basic excitations of the cluster density in the interior region of the cluster. While surface plasmons couple to an external light wave, volume plasmons are not accessible by light due to its transverse nature. However, they can be excited for example via inelastic scattering of fast electrons [71, 72] and measured by electron energy loss spectroscopy [73]. In contrast to surface plasmons, these excitations couple only weakly to the multipole moments of the cluster. Volume plasmons are of basic importance for the interpretation of the surface plasmon damping mechanism. Therefore, this subsection is intended to characterize volume plasmons in more detail. First, volume plasmons within a homogeneous sphere are reviewed. These apply to large cluster radii where surface effects are negligible. Subsequently, numerical results are stated which have been obtained in [107]. These results are used for the further analysis in Subsection 4.3.3.

To derive the characteristics of volume plasmons, consider again the full Vlasov-Poisson system (2.3.3) within the SSVM. By using the Euler representation

$$\varphi_{100}(\boldsymbol{r},t) = A(\boldsymbol{r},t)\, e^{iS(\boldsymbol{r},t)}, \quad \boldsymbol{v} = \nabla S, \quad n = A^2, \tag{4.3.11}$$

of the SSVM wave function, the Vlasov Poisson system can be transformed into the following equivalent Madelung equations for the density $n(\boldsymbol{r},t)$, the velocity field $\boldsymbol{v}(\boldsymbol{r},t)$ and the self-consistent potential $\phi(\boldsymbol{r},t)$ [112]:

$$\partial_t\, n + \nabla\cdot(n\boldsymbol{v}) = 0, \tag{4.3.12a}$$

$$\partial_t\, \boldsymbol{v} + (\boldsymbol{v}\cdot\nabla)\boldsymbol{v} = -\nabla U, \quad U = -\phi - \frac{1}{2}\frac{\Delta\sqrt{n}}{\sqrt{n}}, \tag{4.3.12b}$$

$$\Delta\phi = n - \theta(R-r). \tag{4.3.12c}$$

Equations (4.3.12) correspond to quantum Euler equations. The second term of the hydrodynamic potential $U(\boldsymbol{r},t)$ is a purely quantum-mechanical potential known as Bohm potential.

Now, a small perturbation of the equilibrium is considered with

$$\begin{aligned} n(\boldsymbol{r},t) &= n^{(0)}(r) + n^{(1)}(\boldsymbol{r},t), \\ \boldsymbol{v}(\boldsymbol{r},t) &= \boldsymbol{v}^{(1)}(\boldsymbol{r},t), \quad \boldsymbol{v}^{(0)} = 0, \\ \phi(\boldsymbol{r},t) &= \phi^{(0)}(r) + \phi^{(1)}(\boldsymbol{r},t). \end{aligned} \tag{4.3.13}$$

The velocity field vanishes in the equilibrium state since $S^{(0)}(t) = -i\epsilon_{10}t$ is spatially homogeneous. Here, ϵ_{10} is the eigenvalue of the SSVM.

Based on this ansatz, the equations (4.3.12) can be linearized with respect to the perturbations. First, the potential U is linearized, which gives

$$U = \underbrace{-\phi^{(0)} - \frac{1}{2}\frac{\Delta\sqrt{n^{(0)}}}{\sqrt{n^{(0)}}}}_{\epsilon_{10}} - \phi^{(1)} - \frac{1}{4\sqrt{n^{(0)}}}\Delta\frac{n^{(1)}}{\sqrt{n^{(0)}}} = U^{(0)} + U^{(1)}. \tag{4.3.14}$$

For clusters of finite size, the perturbation $U^{(1)}$ explicitly depends on the equilibrium density $n^{(0)}$. This dependency is of particular importance for the damping mechanism of the surface plasmon and is discussed in more detail in Section (4.3.3). However, to obtain a reference result for volume plasmons in the limit of large clusters, the equilibrium density can be approximated as $n^{(0)} = \theta(R - r)$ (see Section 3.4). Then, for $r < R$, the potential $U^{(1)}$ reads

$$U^{(1)} = -\phi^{(1)} - \frac{1}{4}\Delta n^{(1)} \tag{4.3.15}$$

and the linearized Madelung equations are given by

$$\partial t\, n^{(1)} + \nabla \cdot \boldsymbol{v}^{(1)} = 0, \tag{4.3.16a}$$

$$\partial t\, \boldsymbol{v}^{(1)} - \nabla\phi^{(1)} - \frac{1}{4}\nabla(\Delta n^{(1)}) = 0, \tag{4.3.16b}$$

$$\Delta\phi^{(1)} = n^{(1)}. \tag{4.3.16c}$$

These equations can be combined to obtain the following equation for the density perturbation:

$$(1 + \partial_t^2)n^{(1)} + \frac{1}{4}\Delta^2\, n^{(1)} = 0. \tag{4.3.17}$$

Azimuthally symmetric and regular solutions to this equations are of the form (complex representation)

$$n^{(1)}_{nl'}(\boldsymbol{r}, t) = Ae^{-i\omega t} j_l(kr)Y_{l0}(\Omega), \quad \omega^2 = 1 + \frac{1}{4}k^4, \quad A \in \mathbb{C}. \tag{4.3.18}$$

Here, $j_{l'}$ denotes the l'-th spherical Bessel function of the first kind. For $R \to \infty$, the fraction of spill-out electrons vanishes. The corresponding boundary condition $n^{(1)}_{nl'}(R, t) = 0$ leads to a quantization of the possible wavenumbers,

$$k_{nl'} = \frac{x_{nl'}}{R}, \quad j_{l'}(x_{nl'}) = 0, \quad n = 1, 2, 3, \dots\ . \tag{4.3.19}$$

Here, the number n counts the zeros of the l'-th spherical Bessel function. This result shows that volume plasmons exist for each multipole order l'. Furthermore, they can be classified by the number of radial nodes inside the cluster since a volume plasmon with mode number n has $n - 1$ radial nodes inside the cluster.

Volume plasmons in clusters of finite size were treated in [107] based on the present SSVM. In this framework, the resonance frequencies and damping rates of volume plasmons were extracted based on a Fourier analysis of the density perturbation in

n	1	2	3	4	5	6	7	8	9	10
ω_{n1}	1.007	1.008	1.02	1.06	1.12	1.20	1.30	1.43	1.59	1.77
γ_{n1}	0.0054	0.0047	0.01	0.02	0.03	0.05	0.08	0.1	0.13	0.15

Table 4.3.1: Damping rates γ_{n1} and resonance frequencies ω_{n1} of volume plasmons $(l' = 1, R = 20)$ taken from [107].

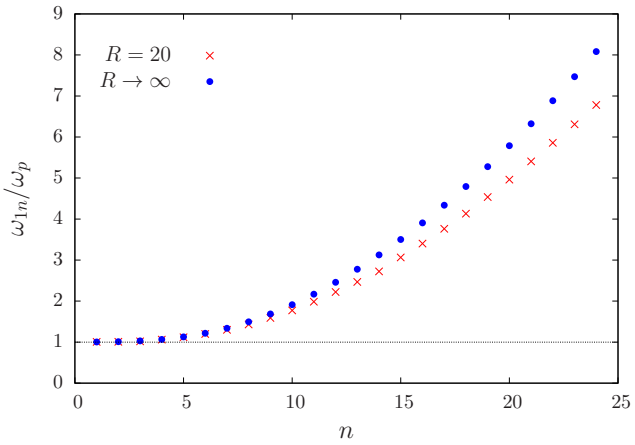

Figure 4.3.5: Resonance frequencies ω_{n1} of volume plasmons $(l' = 1)$. The figure shows the numerical results for a cluster radius $R = 20$ as well as the analytical results (4.3.18) in the limit of large clusters.

the interior region of the cluster. Corresponding results for $l' = 1$ are given in Table 4.3.1 and in Fig. 4.3.5. Volume plasmons corresponding to large values of n are strongly damped, while the resonance frequency is redshifted. It was found that both the damping rate and the redshift of the resonance frequency increases with increasing values of n. However, the damping rates associated with $n = 1$ and $n = 2$ are quite small and of the same order of magnitude as the numerical error. Furthermore, the corresponding resonance frequencies are close the analytical results (see (4.3.18)) in the large cluster limit.

4.3.3 Analysis of the Surface Plasmon Damping Mechanism

In this subsection, the damping mechanism of the Mie plasmon is analyzed in more detail. This analysis is divided into two parts: First, the focus is put on the question which interaction is responsible for the plasmon decay. Is it the electron-electron interaction or is it the electron-ion interaction? Secondly, it is investigated to which type of excitation the energy is transferred that is associated with the surface plasmon resonance.

Single Electron State Bound to a Homogeneously Charged Sphere

To answer the first question, several test calculations where performed. According to (4.2.13), the surface force acting on the c.m. can be fully expressed in terms of the spill-

out density. This fact raises the question, whether an overlap of the electron density with the exterior region of the ion sphere is already sufficient to observe a decay of the c.m. For this purpose, the reference example of an electron state is considered that is bound to a homogeneously charged sphere with radius R. This situation corresponds to the SSVM, but without taking into account the electron-electron interaction. Then, the electron state only interacts with the following ion potential:

$$\phi^{(0)}(\boldsymbol{r}) = \begin{cases} \frac{1}{6}\left(3R^2 - r^2\right), & r \leq R, \\ \frac{V_{ion}}{4\pi r}, & r \geq R, \end{cases} \qquad V_{ion} = \frac{4}{3}\pi R^3. \tag{4.3.20}$$

Inside the sphere, the electron sees a harmonic oscillator with frequency $\omega_M = 1/\sqrt{3}$. Outside the sphere, the potential is Coulomb-like.

For $R \gg 1$, the ground state corresponding to (4.3.20) tends to that of a harmonic oscillator since it is localized near the center of the sphere. As R becomes of the order of one, the ground state gets influenced by the surface of the sphere and the spill-out of the wave function can be observed. Since the spill-out effect can be controlled by the parameter R, this simple reference example is considered to demonstrate the effect of the density spill-out on the c.m. motion if the electron-electron interaction is switched off.

For the further analysis, the ground state $\varphi^{(0)}$ of the potential (4.3.20) was calculated numerically for several small values of R by considering the relaxation method described in Section 3.1. Now, the problem to be discussed is the time evolution of the c.m. as the ground state $\varphi^{(0)}$ is shifted out of the equilibrium position a distance of δ along the z-axis,

$$\varphi(\boldsymbol{r}, 0) = \varphi^{(0)}(\boldsymbol{r} - \delta \boldsymbol{e}_z). \tag{4.3.21}$$

In the limit $R \to \infty$, the initial state $\varphi(\boldsymbol{r}, 0)$ is a coherent state since $\varphi^{(0)}$ is the ground state of a harmonic oscillator. Then, the time-propagated wave function gives rise to a harmonic c.m. oscillation with a frequency of ω_M. Now, the situation is considered where R is of the order of one so that $\varphi^{(0)}$ is affected by the surface.

Figure 4.3.6 shows results for the time evolution of the z-component of the c.m. For the larger sphere, the motion of the c.m. is close to that of a harmonic oscillator with a frequency of ω that is slightly redshifted with respect to ω_M. The harmonic motion is driven by the superposition of the ground state and the first excited state which enters the expansion of the initial wave function due to the displacement. For the smaller sphere, the motion becomes nonharmonic since more excited contribute to the initial wave function. The dominant frequency $\omega \approx 0.5\,\omega_M$ of the motion is even more redshifted with respect to ω_M since the ground state energy is shifted towards zero. However, this simple reference shows that the c.m. does not undergo relaxation for the small parameters of δ considered. In conclusion, the density spill-out itself is not sufficient to describe a decay of the c.m in the linear regime.

The main difference between the above reference system and the SSVM is the electron-electron interaction. Due to the fact that the plasmon decay is present within the SSVM as demonstrated in Subsection 4.3.1, one can conclude that the damping mechanism must be closely related to the electron-electron interaction which is incorporated

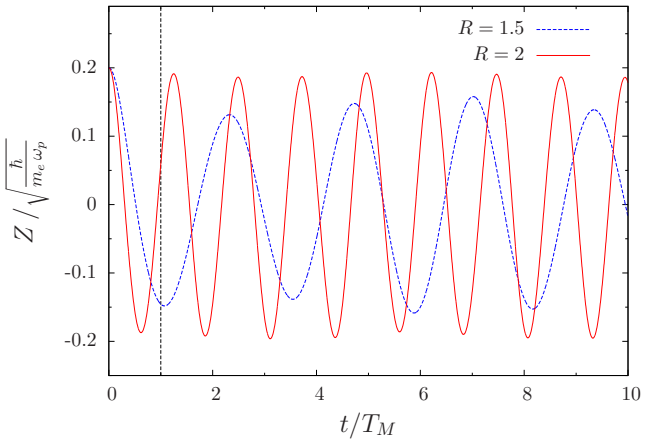

Figure 4.3.6: One electron state bound to a homogeneously charged sphere of radius R (single-state Vlasov model without electron-electron interaction). The figure shows the time evolution of the center of mass (c.m.) $Z(t)$ for two radii $R = 1.5$ and $R = 2$. At $t = 0$, the ground state is shifted homogeneously along the z-axis ($\delta = 0.2$). One recognizes the redshift of the resonance frequency due to the spill-out effect of the ground state. It is shown that the linear motion of the c.m. is not damped if the electron-electron interaction is switched off in the single-state Vlasov model.

by the electron-electron interaction part of the self-consistent potential ϕ within the present Vlasov approach. As visible in Figure 3.4.1, the self-consistent equilibrium potential $\phi^{(0)}$ exhibits a surface inhomogeneity due to the electron density overshoot at the cluster surface. Commonly, all damping processes relying on the interaction of the cluster electrons with the surface are summarized as "surface scattering" [13]. Since both the plasmon damping rate and the surface potential vanish for $R \to \infty$, it appears within the Vlasov approach that the decay is driven by the interaction with the surface inhomogeneity of the self-consistent electron-electron interaction potential.

Energy Consideration

After having treated the simple reference example of an electron state bound to a homogeneously charged sphere, the focus is put again on the SSVM. The decay of the c.m. is associated with an energy loss of the collective electron motion. Since the treatment of small cluster excitations by linear perturbation theory neglects ionization effects [19], the energy must be transferred to electrons that are still bound to the cluster. In particular, it remains the question to which cluster excitations the energy of the surface plasmon is transferred. In the following, the focus is put on this question starting with an energy consideration.

The full Vlasov theory (2.3.3) conserves the average total energy per electron

$$E = \langle T \rangle + \langle V \rangle, \qquad V = -\phi_{ion} - \frac{1}{2}\phi_{ee} \tag{4.3.22}$$

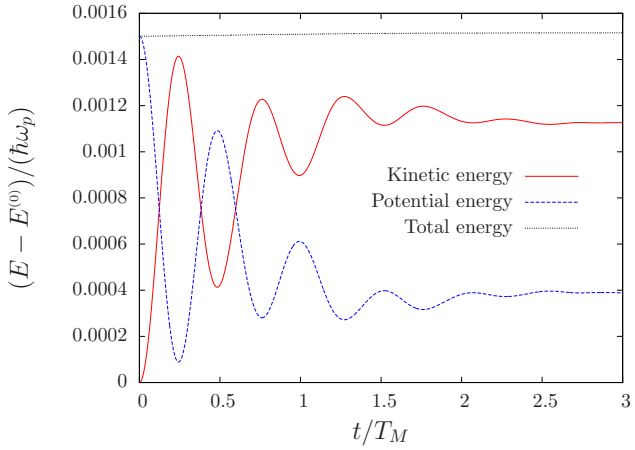

Figure 4.3.7: Average kinetic and potential energy per electron as a function of time ($R = 10$, $\delta = 0.1$). The energies are measured with respect their corresponding equilibrium values $E^{(0)}$. It is shown that the plasmon excitation energy $V(0) - V^{(0)}$ is partitioned into kinetic and potential energies in the course of time. At the end of the simulation time, both quantities become almost stationary. In addition, the total energy is plotted to demonstrate the energy conservation of the present approach.

if no external field is present ($\phi_{ext} = 0$). Here, ϕ_{ion} is the electrostatic potential of the ions given by (4.3.20) and ϕ_{ee} the electron-electron interaction part of the self-consistent potential. The factor 1/2 has to be taken into account in order to avoid double counting of the electron-electron interaction energy. As demonstrated in appendix A.2.2, linear perturbation theory is not sufficient to describe the energy transfer between potential and kinetic energies consistently. Therefore, in order to study the time evolution of kinetic and potential energy, corresponding calculations have been performed based on the nonlinear Vlasov-Poisson code introduced in Chapter (7), which solves the nonlinear Vlasov-Poisson system (2.3.3) in cylindrical coordinates.

Now, the partition of the plasmon excitation energy into kinetic and potential energy is studied as a function of time for the Mie plasmon. Again, the initial excitation of the c.m. is generated by a rigid shift (4.3.21) of the equilibrium distribution. Figure 4.3.7 shows the time evolution of the kinetic and potential energies per electron for a cluster radius of $R = 10$ and a displacement parameter of $\delta = 0.1$. The corresponding motion of the c.m. is given in Fig. 4.3.1. At initial time $t = 0$, the perturbation of the potential energy is nonzero since the electrons gain potential energy in the field of the ions due to the initial displacement. In contrast, the kinetic energy is not affected by the displacement since the form of the wave function is not modified. As the system evolves in time, both energies oscillate with half of the Mie period. Here, local maxima of the kinetic energy correspond to zero crossings of the c.m. The oscillating components of the energies are associated with the collective electron motion. They are damped since the c.m. $Z(t)$ and its velocity $\dot{Z}(t)$ vanish for large times. Both energies tend to constant values at the end of the calculation. This result indicates that the excitation energy is contained in fluctuations of the electron system.

Time Evolution of the Density Perturbation

In the following, the residual cluster excitations are characterized in more detail. For this purpose, the focus is put on the dynamics of the electron density. Figure 4.3.8 illustrates the time evolution of the density perturbation $n^{(1)}(\boldsymbol{r}, t)$ for the simulation parameters $R = 30$ and $\delta = 1$. Plot 4.3.8a shows snapshots of $n^{(1)}(x, z, t)$ in the xz-plane during the first two Mie periods ($y = 0$). In addition, to resolve the dynamics properly, it turned out to be instructive to study the perturbation $n^{(1)}(z, t)$ along the z-axis. This result is given in Figure 4.3.8b. By using the representation (4.1.19c) of the density in linear perturbation theory, both quantities can be calculated based on the radial part $n_1^{(1)}(r, t)$ of the density perturbation ($l' = 1$) according to the following formula:

$$n^{(1)}(x, z, t) = n_1^{(1)}\left(\sqrt{x^2 + z^2}, t\right) Y_{10}\left(\frac{z}{\sqrt{x^2 + z^2}}\right). \tag{4.3.23}$$

At the beginning of the simulation, the density perturbation is located near the cluster poles. This is due to the fact that the equilibrium density $n^{(0)}$ is almost uniform inside the cluster. Therefore, a rigid shift of the equilibrium density distribution does not produce a finite value of $n^{(1)}$ in the interior region of the sphere. Furthermore, one recognizes a density overshoot at the north pole since the electron system is shifted in the positive z-direction.

As the system evolves in time, one recognizes an oscillatory behavior of the density at the cluster surface on the timescale of the Mie period T_M. This oscillations is related to the collective electron oscillation relative to the ion sphere. After each half period of the oscillation, particle streams are emitted from the cluster surface which move into the cluster. These streams partially result from a reflection of the electrons at the cluster surface as is visible, e.g., at the end of the first half period when the electron system moves in the negative z-direction. At time $t \approx T_M/2$, one can see that the density overshoot generated by incoming electrons at the lower cluster boundary splits into two streams. The stream that propagates in the positive z-direction is associated with electrons that are reflected at the cluster surface, while the transmitted stream moves in the negative z-direction and leaves the ion sphere.

In total, the waves propagating from the surface into the interior region of the cluster form a density profile that is close to that of a standing wave inside the cluster. The standing density wave is characterized by a certain number of nodes and anti-nodes of the local density amplitude, where the relative phase of density oscillations at two distinct points on the axis does not change. The standing wave pattern can be clearly identified in Fig. 4.3.8a. Red horizontal lines correspond to the nodes of the standing wave. Along these lines, the position is fixed and the density perturbation vanishes. Due to the symmetry of the density with respect to $z = 0$, there are two anti-nodes corresponding to the largest density amplitude, which are located close to the cluster center at $z \approx \pm 0.1R$.

Spatial Fourier Transform of the Density Perturbation

In the following, the residual standing wave pattern is characterized in more detail. For this purpose, the spatial Fourier transform $\tilde{n}^{(1)}(\boldsymbol{k}, t)$ of the density perturbation is

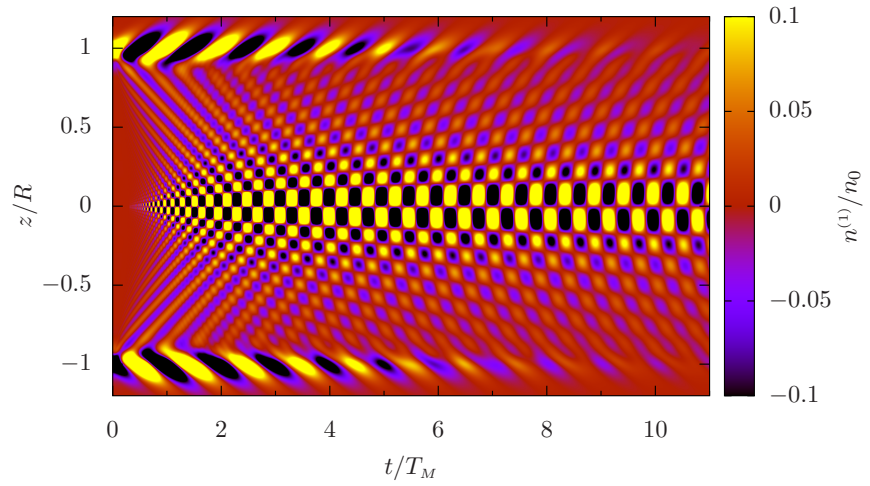

(a)

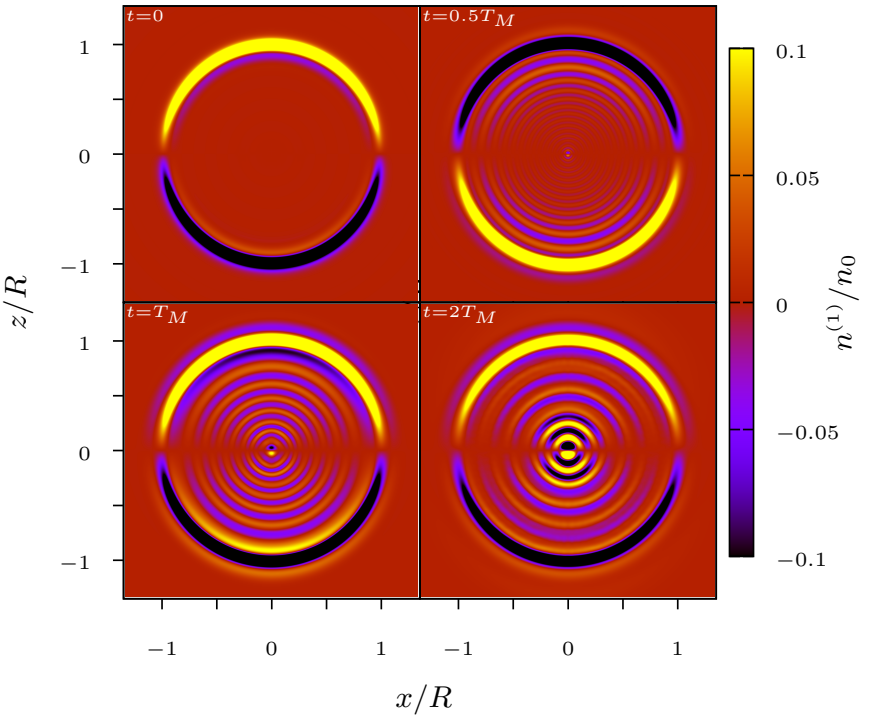

(b)

Figure 4.3.8: Time evolution of the density perturbation $n^{(1)}(\boldsymbol{r}, t)$ ($R = 30$, $\delta = 1$). (a) Density perturbation $n^{(1)}(z, t)$ along the z-axis ($x = y = 0$). (b) Snapshots of the density perturbation $n^{(1)}(x, z, t)$ in the xz-plane. The plots demonstrate the conversion of the Mie plasmon into volume modes by surface scattering [81].

calculated, which is defined by

$$\tilde{n}^{(1)}(\boldsymbol{k},t) = \frac{1}{\sqrt{2\pi}^3}\int\limits_{\mathbb{R}^3} n^{(1)}(\boldsymbol{r},t)e^{-i\boldsymbol{k}\cdot\boldsymbol{r}}d^3r, \tag{4.3.24a}$$

$$n^{(1)}(\boldsymbol{r},t) = \frac{1}{\sqrt{2\pi}^3}\int\limits_{\mathbb{R}^3} \tilde{n}^{(1)}(\boldsymbol{k},t)e^{i\boldsymbol{k}\cdot\boldsymbol{r}}d^3k. \tag{4.3.24b}$$

To evaluate (4.3.24a) based on the representation $n^{(1)}(\boldsymbol{r},t) = n_{l'}^{(1)}(r,t)Y_{l'0}(\theta)$ of the density in linear perturbation theory, the following spherical harmonic expansion of a plane wave $e^{-i\boldsymbol{k}\cdot\boldsymbol{r}}$ is introduced [8]:

$$e^{-i\boldsymbol{k}\cdot\boldsymbol{r}} = \sum_{l=0}^{\infty}\sqrt{4\pi(2l+1)}(-i)^l j_l(kr)Y_{l0}(\cos(\gamma)), \tag{4.3.25a}$$

$$Y_{l0}(\cos(\gamma)) = \sum_{m=-l}^{l}\sqrt{\frac{4\pi}{2l+1}}Y_{lm}^*(\Omega_r)Y_{lm}(\Omega_k). \tag{4.3.25b}$$

Here, j_l is a spherical Bessel function of the first kind and γ the angle between $\boldsymbol{k}$ and $\boldsymbol{r}$. Furthermore, $\Omega_r = (\theta_r, \varphi_r)$ and $\Omega_k = (\theta_k, \varphi_k)$ are the angles of $\boldsymbol{r}$ and $\boldsymbol{k}$ in spherical coordinates. By introducing the relations (4.3.25) in (4.3.24), the orthogonality relation (4.1.5) of the SH can be used to obtain the following representations of the Fourier transform

$$\tilde{n}^{(1)}(\boldsymbol{k},t) = Y_{l'0}(\Omega_k)\sqrt{\frac{2}{\pi}}(-i)^{l'}\int\limits_0^{\infty} j_{l'}(kr)\, n_{l'}^{(1)}(r,t)\, r^2\, dr. \tag{4.3.26}$$

and the density perturbation

$$n^{(1)}(\boldsymbol{r},t) = n_{l'}^{(1)}(r,t)Y_{l'0}(\Omega), \quad n_{l'}^{(1)}(r,t) = \int\limits_0^{\infty} j_{l'}(kr)\, \tilde{n}_{l'}^{(1)}(k,t)\, k^2\, dk, \tag{4.3.27a}$$

$$\tilde{n}_{l'}^{(1)}(k,t) \equiv \frac{2}{\pi}\int\limits_0^{\infty} j_{l'}(kr)\, n_{l'}^{(1)}(r,t)r^2dr. \tag{4.3.27b}$$

Relation (4.3.27a) expresses the radial part $n_{l'}^{(1)}(r,t)$ as a linear combination of spherical bessel functions $j_{l'}(kr)$ with expansion coefficients $\tilde{n}_{l'}^{(1)}(k,t)$. The advantage of this representation arises from the fact that it allows for a comparison between the residual cluster excitations shown in Fig. 4.3.8a and volume plasmons. Here, it is taken into account that the density profiles of volume plasmons are characterized by spherical bessel functions in the limit $R \to \infty$ (see Section 4.3.2). Then, the Fourier transform $\tilde{n}_{l'}^{(1)}$ of a volume plasmon with mode numbers n and l' is of the form $\tilde{n}_{l'}^{(1)} \sim \delta(k - k_{nl'})/k^2$. For a finite-sized cluster, the corresponding Fourier transform $\tilde{n}_{l'}^{(1)}$ is expected to be broadened around the value $k = k_{nl'}$ since the surface potential leads to a coupling of different wave numbers k in the representation of the density.

Now, the Fourier transform (4.3.27) is used to study the residual cluster excitations. In particular, the focus is put on the time evolution of the Fourier transform $\tilde{n}_1^{(1)}$ ($l' = 1$) which corresponds to the parameters in Fig. 4.3.8a. More precisely, it is investigated

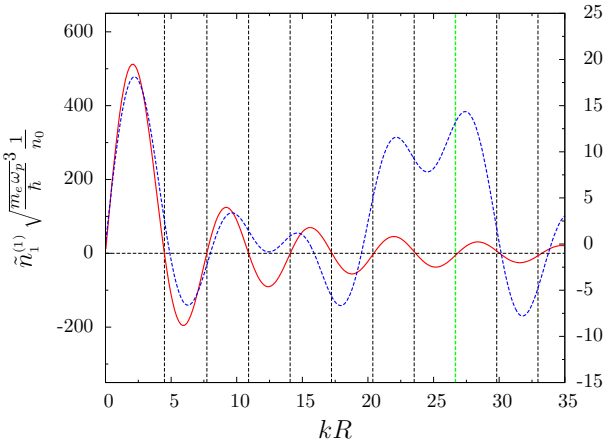

Figure 4.3.9: Spatial Fourier transform of the density perturbation $n^{(1)}(\boldsymbol{r},t) = n_1^{(1)}(r,t)Y_{10}(\theta)$ for the parameters in Fig. 4.3.8. The figure shows the Fourier transform $\tilde{n}_1^{(1)}(k,t)$ of the radial part (see 4.3.27) at times $t=0$ (red curve, left scale) and $t = 10T_M$ (blue curve, right scale). Dashed vertical lines at $kR = x_{1n}$ $(n = 1, 2\ldots)$ indicate the zeros x_{1n} of the spherical Bessel function $j_1(kR)$. The figure shows that the decay of the Mie plasmon is accompanied by an excitation of a volume plasmon with mode number $n = 8$ (green line) corresponding to $n-1 = 7$ radial nodes of the density profile.

how the function profile of $\tilde{n}_1^{(1)}(k,t)$ varies as a function of time. Figure 4.3.9 shows the Fourier transform $\tilde{n}_1^{(1)}$ as a function of the wave number k at initial time $t = 0$ and after ten Mie periods.

In order to comprehend the behavior of the result at $t = 0$ qualitatively, the Fourier transform is evaluated for a large cluster where the spatial density perturbation can be approximated by a δ-function, $n_1^{(1)}(r,0) \sim \delta(R-r)$. In this case, the Fourier transform (4.3.27b) is proportional to $j_1(kR)$. Therefore, the numerical result for $\tilde{n}_1^{(1)}(k,0)$ in Fig. 4.3.9 exhibits zeros for values of kR that are close to zeros of the first spherical Bessel function.

After ten Mie periods, the function profile of $\tilde{n}_1^{(1)}$ has changed significantly. At this time, the c.m. has dropped to 3.3% of its initial value. It is visible that the function $\tilde{n}_1^{(1)}$ is now nonzero at several k-values with $kR = x_{n1}$. In particular, large function values can be observed for $n = 8$ and $n = 7$. This observation is in agreement with the density plot 4.3.8a. By focusing the vertical line associated with $t/T_M = 10$, one can count a number of nodes on the positive z-axis comparable to these two values. As highlighted in Fig. 4.3.9 by a green dashed line, the function $\tilde{n}_1^{(1)}$ exhibits a local maximum close to $kR = x_{8,1}$, which is related to a large contribution of the wave number $k = x_{8,1}/R$ to the density $n^{(1)}$. Most notably, by considering the wave numbers $k = x_{n1}/R$ as a measure of volume plasmons for finite-sized systems, this result demonstrates that the decay of the c.m. is accompanied by an excitation of volume plasmons [81]. In particular, at $t = 10T_M$, the largest contribution is given by a volume plasmon with mode number $n = 8$ and seven radial nodes. For the cluster size $R = 30$ considered, this volume plasmon is more weakly damped compared with the corresponding mode

for a cluster radius $R = 20$ (see Table 4.3.1).

As mentioned above, the density perturbation at $t = 0$ is located close to the cluster surface. The excitation of volume plasmons during the decay of the c.m. is associated with a transfer of the density perturbation into the interior region of the cluster (see Fig. 4.3.8b). This transfer can be understood in terms of the hydrodynamic potential $U(\boldsymbol{r}, t)$ that enters the Madelung equations (4.3.12). In linearized form $U^{(1)}$, it is given in (4.3.14). For a finite-sized system, $\sqrt{n^{(0)}}$ is spatially inhomogeneous in a small region ϵ around the surface due to the spill-out effect. Therefore the hydrodynamic force $-\nabla U$ contains a surface force proportional to $\nabla n^{(0)}$, which is only nonzero in the surface region ϵ. This force leads to a radial flow of the density away from the surface region. The coupling of surface and volume modes can also be understood on the basis of the Fourier components $\tilde{n}_1^{(1)}(k, t)$ in the following way: For $R \to \infty$, The denominator $\sqrt{n^{(0)}}$ in (4.3.14) is spatially homogeneous. Therefore the components $\tilde{n}_1^{(1)}$ are independent for different values of k and of the form $\tilde{n}_{l'}^{(1)} \sim \delta(k - k_{nl'})/k^2$. In this limit, surface and volume modes exist independently. In a finite-sized system, the ratio $n^{(1)}/\sqrt{n^{(0)}}$ leads to a coupling of the components $\tilde{n}_{l'}^{(1)}$ for different values of k due to the inhomogeneity of $\sqrt{n^{(0)}}$.

Contribution of Volume Plasmons to the Center of Mass

So far, it has been demonstrated that the residual excitations following the decay of the Mie plasmon can be identified as volume plasmons. This result implies that the contribution of residual cluster excitations to the c.m. is small. Therefore, the following question is considered: Does the contribution of each individual volume plasmon to the c.m. vanish or is the decay driven by the superposition of all contributions? To answer this question, the following two quantities are introduced:

$$n_\kappa^{(1)}(r, t) \equiv \int_0^\kappa j_1(kr)\tilde{n}_1^{(1)}(k, t)k^2 dk, \quad Z_\kappa(t) \equiv \frac{1}{V_{ion}}\sqrt{\frac{4\pi}{3}}\int_0^\infty n_\kappa^{(1)}(r, t)r^3 dr. \tag{4.3.28}$$

By definition, the function $n_\kappa^{(1)}$ corresponds to a reduced density which represents the contributions of all wave numbers k to the total density perturbation (4.3.27a) up to a maximum value of κ. Then, Z_κ is the reduced c.m. which results from the definition (4.1.40) of the c.m by introducing the reduced density $n_\kappa^{(1)}$. The full quantities can be recovered in the limit

$$n_1^{(1)}(r, t) = \lim_{\kappa\to\infty} n_\kappa^{(1)}(r, t), \quad Z(t) = \lim_{\kappa\to\infty} Z_\kappa(t). \tag{4.3.29}$$

The advantage of the reduced quantities (4.3.28) arises from the fact that volume plasmons can be selected via the parameter κ. In particular, by studying the reduced c.m. $Z_\kappa(t)$ as a function of κ, one can identify the contribution of each volume plasmon to the c.m. $Z(t)$.

Figure 4.3.10 shows the reduced c.m. $Z_\kappa(t)$ at time $t = 10T_M$ again for the situation demonstrated in Fig. 4.3.8a. Starting at $\kappa = 0$, one recognizes a rapid increase of the function in the regime of small κ-values. Then, as κ increases further, the function

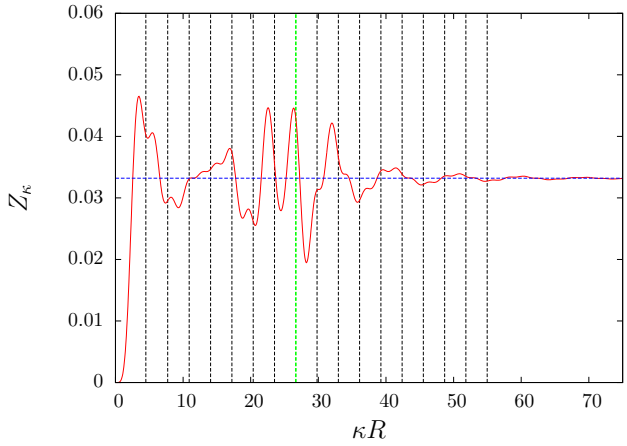

Figure 4.3.10: Reduced center of mass $Z_\kappa(t)$ at time $t = 10T_M$ (see (4.3.28)). Results are shown for the parameters in Fig. 4.3.8. The function Z_κ is plotted against the cutoff wave number κ, which corresponds to the highest wave number taken into account in the Fourier representation (4.3.27a) of the density perturbation ($l' = 1$). Dashed vertical lines (black) are associated with the zeros of the spherical Bessel function $j_1(\kappa R)$. The dashed horizontal line (blue) denotes the center of mass $Z(t)$ at time $t = 10T_M$. The oscillatory behavior of Z_κ indicates that the contributions of volume plasmons to the center of mass add destructively.

starts ocillating around the asymptotic value Z_∞. In particular, a strong oscillatory behavior can be observed in the κR-range between 20 and 30. As visible in Fig. 4.3.9, there is a strong signal of volume plasmons with seven and eight radial nodes in this parameter regime. The oscillation of Z_κ especially between 20 and 30 indicates that the contributions of volume plasmons to the c.m. add destructively rather than that they vanish independently. Therefore, as a whole, they do not contribute to the c.m. For large values of κ, the oscillatary behavior becomes small and the function approaches the value of the c.m. coordinate $Z(t)$.

Finally, the above result can also be described more quantitatively. By taking into account the asymptotic property

$$r = 3 \lim_{k\to 0} \frac{d}{dk} j_1(kr) \tag{4.3.30}$$

of the Bessel function j_1, the c.m. can be rewritten as

$$\begin{aligned} Z(t) &= \sqrt{\frac{4\pi}{3}} \frac{1}{V_{ion}} \int_0^\infty n_1^{(1)}(r,t)\, r^3\, dr \\ &= \sqrt{\frac{4\pi}{3}} \frac{1}{V_{ion}} 3 \lim_{k\to 0} \frac{d}{dk} \int_0^\infty j_1(kr)\, n_1^{(1)}(r,t)\, r^2\, dr \\ &= \sqrt{3\pi^3} \frac{1}{V_{ion}} \lim_{k\to 0} \frac{d}{dk}\, \tilde{n}_1^{(1)}(k,t). \end{aligned} \tag{4.3.31}$$

In the last step, the definition of the Fourier transform (4.3.27b) was used. The representation (4.3.31) of the c.m. states that the c.m. is merely determined by the slope of the Fourier transform $\tilde{n}_1^{(1)}$ at $k = 0$. This result is consistent with the behavior of $Z_\kappa(t)$ in Fig. 4.3.10 since the value $Z(t)$ is largely determined by the increase of $Z_\kappa(t)$ in the range of small κ-values. Therefore, higher wave numbers k in the representation of the density $n_1^{(1)}$ do not contribute to the c.m.

4.4 Multistream Na Cluster

In the last subsection, the electron dynamics was studied based one the SSVM with a single representative electron state. Now, the linear perturbation theory is applied to multistream equilibria with more than one representative state. Here, the main focus is put on the multistream Na clusters, which were introduced in Section 3.3. The electron configurations and radii of these clusters are given in Appendix A.1. The largest cluster has a radius of $R = 10.8$ (1.2nm) and contains 198 electrons. According to (4.1.35), the treatment of this cluster in linear perturbation theory requires a time propagation of $N_p = 30$ radial wave functions.

The first subsection (4.4.1) is aimed to present numerical results for the cluster dynamics of multistream clusters. Here, the fundamental cluster excitations of the multistream description are characterized in more detail. In the last section, it has been discussed within the SSVM that the damping mechanism of the Mie plasmon can be explained by a conversion of the surface plasmon into volume plasmons. Now, it is investigated in how far the damping mechanism of the Mie plasmon is affected by the presence of multiple electron states in the description of the cluster electrons. Finally, Subsection 4.4.2 focuses on the plasmon damping rate of the Mie plasmon. It is intended to compare results of the SSVM and the multistream model. Further comparison is made with previous work on the plasmon damping rate.

4.4.1 Perturbation Results

In this subsection, perturbation results are demonstrated for multistream Na clusters. Here, the main focus is put on the dipole order $l' = 1$ of the cluster dynamics. First, the initial conditions of the present simulations are described.

For the excitation of the cluster, the electron system is given an average momentum $\langle \boldsymbol{p} \rangle = p\boldsymbol{e}_z$ at the beginning of the simulation. This situation can be achieved by the following initial condition for the wave functions [50, 113]:

$$\varphi_{nlm}(\boldsymbol{r}, 0) = \varphi^{(0)}_{nlm}(\boldsymbol{r}) e^{ipz} \approx \varphi^{(0)}_{nlm}(\boldsymbol{r}) + \underbrace{ipz\varphi^{(0)}_{nlm}(\boldsymbol{r})}_{\varphi^{(1)}_{nlm}}. \tag{4.4.1}$$

Then, the initial conditions $g_{nl\bar{l}}(r, 0)$ for the radial wave functions of the perturbation theory can be deduced based on (4.3.4) and the partial wave expansion described in

Subsection (4.1.2),

$$\varphi^{(1)}_{nlm}(\boldsymbol{r},0) = \sum_{\bar{l}\in M_{1l}} g_{nl\,\bar{l}}(r,0)\, C_{10\,lm\,\bar{l}}\, Y_{\bar{l}m}(\theta), \quad g_{nl\,\bar{l}}(r,0) = \sqrt{\frac{4\pi}{3}} ipr R_{nl}(r). \tag{4.4.2}$$

Dipole Spectrum

Now, the c.m. motion is discussed exemplarily for a cluster with 198 electrons ($R = 10.8$). For the further analysis, it is instructive to introduce the subshell contributions $Z_{nl}(t)$ to the c.m., which are generated by all electrons of a given subshell with quantum numbers n and l. Then, the c.m. $Z(t)$ can be written in the form

$$Z(t) = \sum_{l=0}^{l_{max}} \sum_{n=0}^{N_l} Z_{nl}(t). \tag{4.4.3}$$

Figure (4.4.1) shows the motion of the c.m. in the time and frequency domain for an initial momentum $p = 1$. In addition, results for Z_{23} and Z_{24} are illustrated.

In Figure 4.4.1a, the decay of the Mie plasmon is observed, in close accordance with the SSVM result (see Subsection 4.3.1). It is visible that the decay is almost exponential over roughly three Mie periods when $Z(t)$ reaches a local minimum. The corresponding displacement indicates the redshift of the Mie oscillation frequency. After three Mie periods, one can observe slow oscillations of the c.m. that are nearly undamped over a few tens of Mie periods. More precisely, the amplitude of the residual oscillation is approximately one percent of the maximum displacement at $t \approx 0.25 T_M$.

To identify the frequency of the slowly varying component, the Fourier transform $\tilde{Z}(\omega)$ of the c.m. is considered. The absolute value of the Fourier transform is plotted in (4.4.1b). First of all, one recognizes a broad resonance with a maximum slightly below ω_M. This maximum is associated with the Mie plasmon. While the width of the Mie resonance is in qualitative agreement with the corresponding result of the SSVM, one recognizes a landscape of maxima and minima below ω_M that are not present within the SSVM. At small frequencies, a plateau is visible that is superimposed by a few smaller resonances followed by a rather sharp and pronounced maximum at $\omega \approx 0.1$. This resonance is associated with the nearly undamped low-frequency oscillation of the c.m. following the decay of the Mie plasmon.

In order to understand the structure of the oscillator strength $|\tilde{Z}|(\omega)$ below ω_M, now the focus is put on the subshell contributions $Z_{nl}(t)$ that are also plotted in Figure (4.4.1a) for the 2f and 2g electrons. During the first three Mie periods, one can observe damped oscillations of Z_{nl} on the timescale of the Mie period. This signature is associated with the collective electron motion characterized by a phase-coherent oscillation of all electrons. Besides the collective component, one can see nearly undamped low-frequency oscillations of the functions Z_{nl}. The corresponding amplitudes are of the same order of magnitude as the maximum displacements of the collective oscillations. This is contrast to the behavior of the c.m. which shows only a weak low-frequency component of oscillation after the decay of the Mie plasmon. Therefore, one can

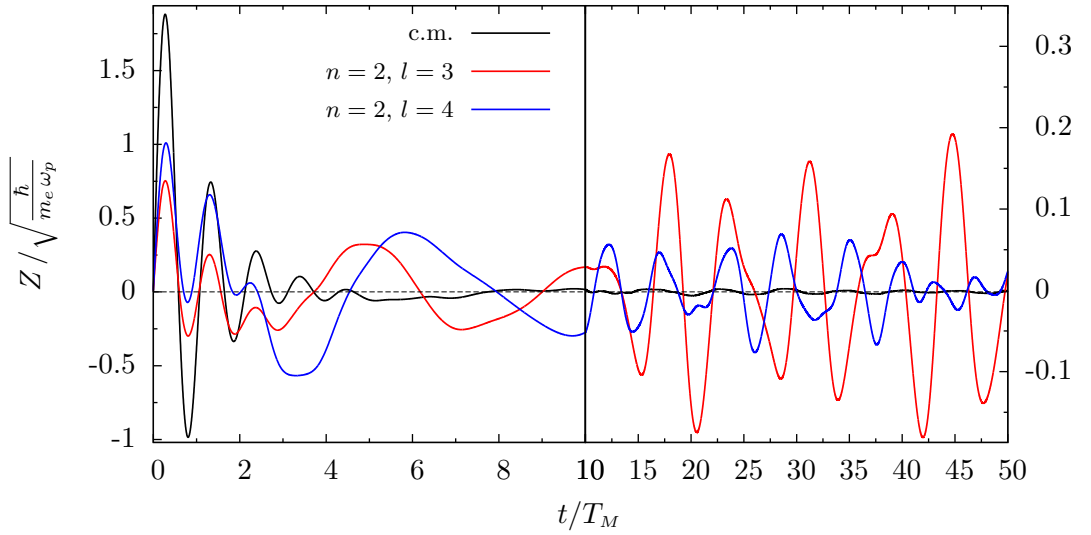

(a)

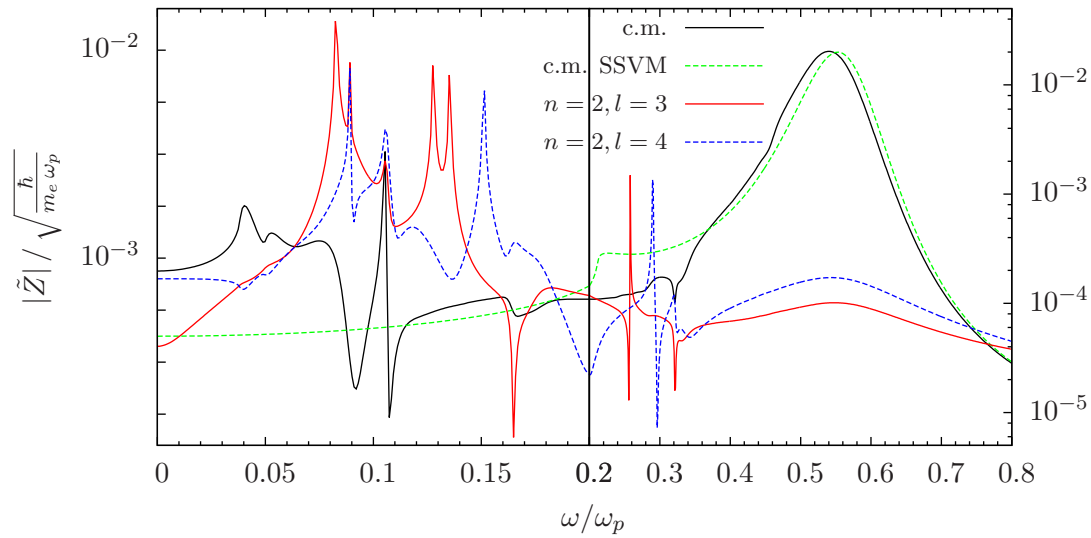

(b)

Figure 4.4.1: Motion of the center of mass (c.m.) following an impulsive excitation with initial momentum $p = 1$ (Na cluster, $N_e = 198$, $R = 10.8$). 4.4.1a The c.m. $Z(t)$ (left scale) and corresponding subshell contributions $Z_{nl}(t)$ (right scale) in the time domain. 4.4.1b Corresponding functions $\tilde{Z}(\omega)$ (left scale) and $\tilde{Z}_{nl}(\omega)$ (right logarithmic scale) in the frequency domain. The result of the single-state Vlasov model (SSVM) is indicated. In 4.4.1a, one can recognize the decay of the Mie plasmon and residual oscillations of the subshell contributions that are associated with dipole transitions of the single-particle states [15, 16]. In 4.4.1b, a broad maximum of $\tilde{Z}(\omega)$ close to $\omega_M \approx 0.577$ (plasma units) is visible, which is associated with the Mie plasmon. The frequencies of the residual subshell oscillations lie below ω_M and the resonance curve of the c.m. exhibits a low-frequency maximum at $\omega \approx 0.1$.

conclude that the majority of functions Z_{nl} add destructively in the representation (4.4.3) of the c.m. for $t \gg T_M$.

Figure 4.4.1b shows the corresponding subshell oscillator strengths $|\tilde{Z}_{nl}|(\omega)$. For each subshell, one can observe a number of pronounced peaks below ω_M next to the broad resonance of the collective oscillation. These peaks are associated with the low-frequency oscillations of Z_{nl} for $t \gg T_M$. One can recognize that the oscillator strengths $|\tilde{Z}_{23}|$ and $|\tilde{Z}_{24}|$ meet at $\omega \approx 0.09$, where they form resonances of almost equal height and width. For this frequency, the author has convinced that the values $\tilde{Z}_{23}$ and $\tilde{Z}_{24}$ have opposite signs. Therefore, the superposition of both contributions does not lead to a signature of the frequency $\omega \approx 0.09$ in the total oscillator strength $|\tilde{Z}_{nl}|$ and the resonances of $|\tilde{Z}_{23}|$ and $|\tilde{Z}_{24}|$ are associated with a non-collective excitation of the 2f and 2g electrons. This excitation is characterized by an oppositely-phased oscillation of the subshell dipole moments with almost equal amplitudes. By using Table (3.3.2), the corresponding frequency can be identified with the transition frequency $\omega_t = \epsilon_{24} - \epsilon_{23} = 0.0890$ of the two subshells with eigenvalues $\epsilon_{24} = -0.0885$ and $\epsilon_{23} = -0.1775$. In the present framework of linear perturbation theory, the self-consistent potential $\phi^{(1)} \sim Y_{10}$ is dipole-like. In this sense, the non-collective excitation of the 2f and 2g electrons is associated with dipole transitions ($\Delta l = \pm 1$) of these electron states [15, 16].

In Fig. 4.4.1b, one can recognize additional resonances of $|\tilde{Z}_{24}|$ and $|\tilde{Z}_{23}|$ that cannot be explained by transitions between the two considered subshells. These additional frequencies in the motion of Z_{24} and Z_{23} are partially related to transitions between the single-particle states of the 2f and 2g subshell and states of different subshells. In particular, the resonance of $|\tilde{Z}_{24}|$ at $\omega \approx 0.15$ can be referred to a dipole transition 2g $\leftrightarrow$ 1h with a transition frequency of $\omega_t = \epsilon_{24} - \epsilon_{15} = 0.1511$, where $\epsilon_{15} = -0.2396$. Most notably, Fig. 4.4.1b shows a further maximum of the subshell-resolved dipole strengths at the same position $\omega = 0.1055$ for both considered subshells. This maximum cannot be understood in terms of a dipole transition in which the two considered subshells are involved. By comparing this value of ω with the energy eigenvalues of Table (3.3.2), one comes to the conclusion that ω is associated with the frequency $\omega_t = 0.1052$ of the transition 3p $\leftrightarrow$ 4s. Since the two subshells of Fig. 4.4.1 are not involved in this transition, the corresponding transition frequency $\omega_t = 0.1052$ can only enter the motion of Z_{24} and Z_{23} via the interaction of the electron states with the self-consistent potential $\phi^{(1)}$. Therefore, the subshell resonance at $\omega = 0.1055$ must be related to an increased influence of the electron-electron interaction between the 2f and 2g states and states that are involved in the transition 3p $\leftrightarrow$ 4s.

Low-Frequency Resonance of the Center of Mass

So far, it has been demonstrated that the low-frequency resonance of the c.m. at $\omega = 0.1055$ is accompanied by resonances of the subshell oscillator strengths $|\tilde{Z}_{nl}|$ for 2f and 2g states. The author has confirmed that the functions $|\tilde{Z}_{nl}|$ exhibit similar resonances close to $\omega = 0.1055$ for all other subshells. Therefore, it remains the question whether the resonance of the c.m. at frequency ω is generated either by a constructive interference of all subshell contributions $\tilde{Z}_{nl}$ or by a large contribution of a single subshell.

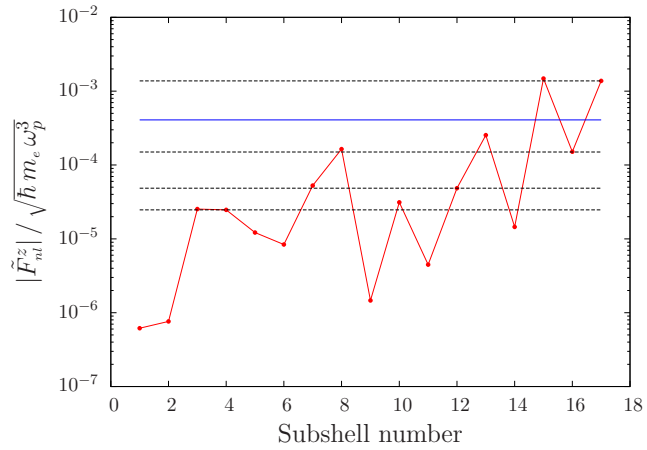

Figure 4.4.2: Subshell-resolved surface force $\tilde{F}^z_{nl}(\omega)$ in the frequency domain (Na cluster, $N_e = 198$, $R = 10.8$). The plot shows the absolute values $|\tilde{F}^z_{nl}|$ at the low-frequency resonance point $\omega = 0.1055$ of the center of mass (see Fig. 4.4.1b). The subshells are numbered as shown in Table 3.3.1. Horizontal black lines indicate subshell pairs whose surface forces $\tilde{F}^z_{nl}$ add almost destructively at the resonance point. The horizontal blue line indicates the value $|\tilde{F}^z_{sc}|(\omega)$ of the total surface force. It is demonstrated that the main contribution to the resonance is generated by an unscreened contribution of the 2g electrons.

In order to answer this question, the linearized surface force $\boldsymbol{F}^{(1)}_{sc}$ (see (4.2.14)) is evaluated for the c.m. motion demonstrated in Fig. 4.4.1. As discussed in Section 4.2, $\boldsymbol{F}^{(1)}_{sc}$ determines the c.m. motion via the equation of motion

$$\ddot{\boldsymbol{R}} + \omega_M^2 \boldsymbol{R} = \boldsymbol{F}^{(1)}_{sc}. \tag{4.4.4}$$

According to this equation, the low-frequency maximum of the c.m. resonance curve at $\omega = 0.1055$ must be related to a strong contribution of $\boldsymbol{F}^{(1)}_{sc}$ at this specific frequency.

To resolve the surface effects of individual subshells, it is instructive to write $\boldsymbol{F}^{(1)}_{sc}$ as a sum of subshell contributions,

$$\boldsymbol{F}^{(1)}_{sc}(t) = F^z_{sc}(t)\boldsymbol{e}_z, \qquad F^z_{sc}(t) = \sum_{l=0}^{l_{max}} \sum_{n=0}^{N_l} F^z_{nl}(t)\boldsymbol{e}_z. \tag{4.4.5}$$

Then, the functions $F^z_{nl}(t)$ describe all surface effects of the c.m. motion related to the subshell with quantum numbers n and l. Now, the focus is put on the resonance point $\omega = 0.1055$ by considering the Fourier transform $\tilde{F}^z_{nl}(\omega)$ at this frequency. Figure 4.4.2 shows the absolute values $|\tilde{F}^z_{nl}(\omega)|$ for all subshells of the electron system.

It can be seen that subshells 15 (3p) and 17 (4s) give rise to large values of $|\tilde{F}^z_{nl}|$ driven by the resonant dipole transition between the corresponding electron states ($\omega_t = 0.1052$) at the considered frequency. The next lower value stems from an isolated contribution of subshell 13 (2g). As shown in Fig. 4.2.1, this subshell contains the second largest fraction of spill-out electrons. Moreover, it is indicated that several subshells form pairs of almost equal strength $|\tilde{F}^z_{nl}|$. For example, the horizontal line at

$|\tilde{F}^z_{nl}| \approx 2.5 \cdot 10^{-5}$ is related to the contributions of the 1d (subshell 3) and 1f (subshell 4) states. Most notably, there are additional pairs that refer to subshells which differ in the quantum number l by $|\Delta l| > 1$. In particular, subshells 7 (1i) and 12 (2f) both yield a strength of $|\tilde{F}^z_{nl}| \approx 5 \cdot 10^{-5}$, while subshells 7 (1j) and 16 (3d) give rise to values $|\tilde{F}^z_{nl}| \approx 5 \cdot 10^{-4}$. By looking at the real and imaginary parts of $\tilde{F}^z_{nl}$, one can confirm that all subshell pairs oscillate with almost opposite phase. This result shows that the surface effects of several subshells are almost completely screened by other subshells. As mentioned above, this screening is in general not related to resonant dipole transitions between the states of the subshell pairs.

In conclusion, by summing the subshell contributions $\tilde{F}^z_{nl}$ of a single pair, the pair contribution to the total surface force is much smaller than the values $|\tilde{F}^z_{nl}|$. This observation leads to the conclusion that the Fourier transform $\tilde{F}^z_{sc}(\omega)$ of the total surface force is dominated by a large unscreened contribution $\tilde{F}^z_{24}$ of the $2g$ electrons that is close to $\tilde{F}^z_{sc}$ (see Fig. 4.4.2). The remaining part of $\tilde{F}^z_{sc}$ is determined by the residual pair contribution of the resonant dipole transition 3p $\leftrightarrow$ 4s. Based on this insight concerning the surface force, one can state more precisely that the low-frequency resonance of the of c.m. at $\omega \approx 0.1$ is driven by the electron-electron interaction induced coupling of the 2g surface states to the resonant transition 3p $\leftrightarrow$ 4s.

Time Evolution of the Density Perturbation

In the following, the decay of the Mie plasmon is studied on the basis of the electron density. Within the SSVM description of Section 4.3, it was demonstrated that the plasmon decay is accompanied by a conversion of the Mie plasmon into volume plasmons. Now, it is discussed in how far this picture is affected by the presence of multiple ensemble states within the present multistream model. For this purpose, the focus is put on the time evolution of the density perturbation $n^{(1)}(z,t)$ along the z-axis (see (4.3.23)) that corresponds to the c.m. motion shown in Fig. 4.4.1. In addition, the Fourier transform $\tilde{n}^{(1)}(z,\omega)$ is considered to spatially localize different types of cluster excitations. It can be obtained by performing a Fourier transform of the time-dependent density perturbation at each position on the z-axis.

To resolve the effect of multistream equilibria on the plasmon decay properly, similar calculations were performed for various values of N_s smaller than $N_s = 99$ (Na configuration) by keeping the radius fixed. The results are plotted in Fig. 4.4.3. As in Fig. 4.3.8, the damped oscillation of the surface density is associated with the decay of the Mie plasmon. The spatial localization of the surface plasmon can be clearly identified by the pronounced maximum of the Fourier transform $|\tilde{n}^{(1)}|$ close to the cluster poles ($|z| = R$) at $\omega = \omega_M$. For $N_s = 9$, one can recognizes a residual density oscillation in the interior region of the ion sphere on the timescale of the plasma period $T_p = 2\pi/\omega_p$. This oscillation is nearly undamped. The corresponding Fourier transform demonstrates the residual excitation of volume plasmons above ω_p. By looking at the vertical line associated with the red maximum at $\omega \approx \omega_p$, it is visible that the motion of the density is dominated by a volume plasmon with one spatial node on the positive z-axis. Besides the dominant contribution of volume plasmons, one can see minor signatures of single-particle excitations below ω_M that are also located well

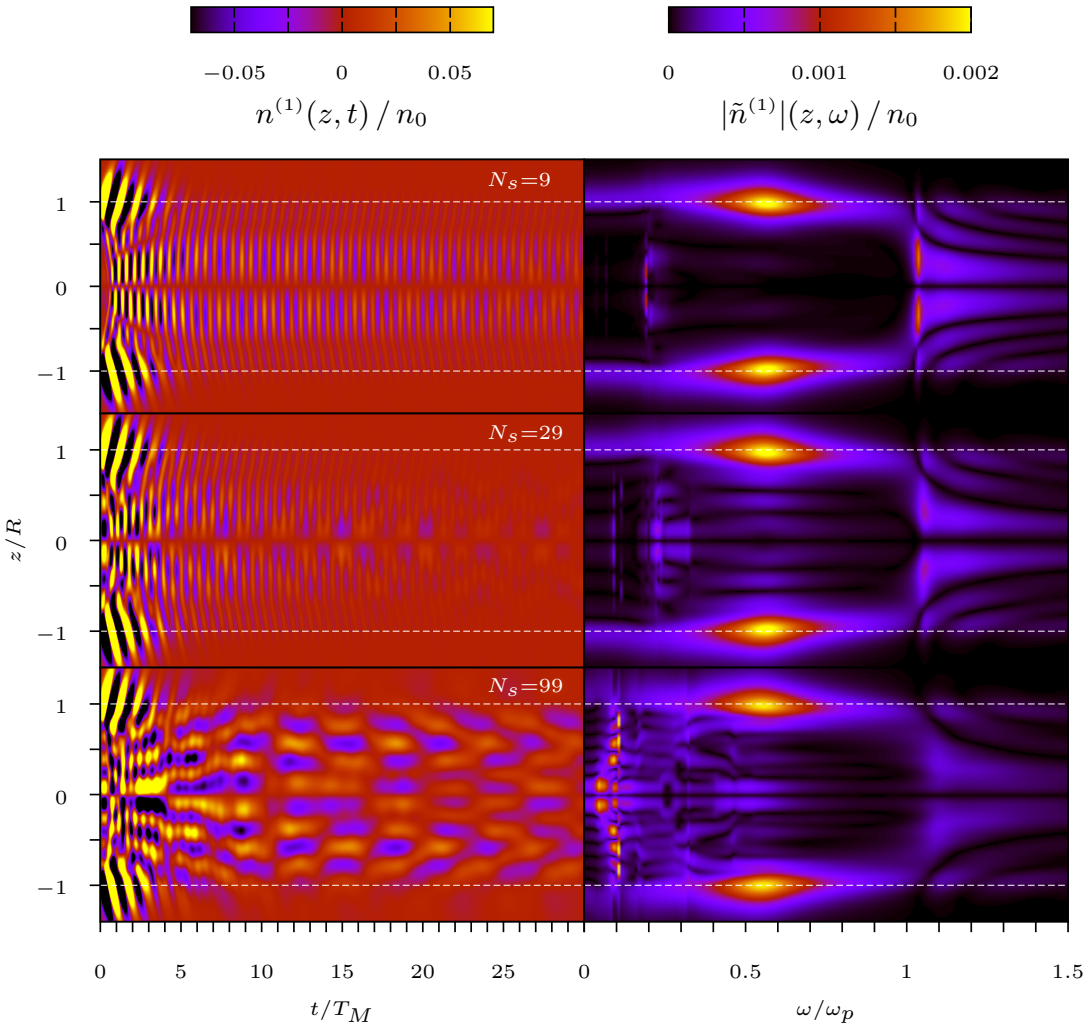

Figure 4.4.3: Time evolution of the electron density following an impulsive excitation with initial momentum $p = 1$ ($R = 10.8$). The plots on the left illustrate the density perturbation $n^{(1)}(z,t)$ along the z-axis for various numbers of representative states up to a number of $N_s = 99$. This value of N_s correponds to the number of spatial wave functions in a Na cluster with 198 electrons. The calculation with $N_s = 99$ refers to the c.m. motion shown in Fig. 4.4.1. On the right, the absolute value of the temporal Fourier transform $\tilde{n}^{(1)}(z,\omega)$ is plotted. For $N_s = 9$, it shown that surface scattering leads to a conversion of the Mie plasmon into volume plasmons which oscillate with a frequency close to ω_p. These collective excitations are nearly undamped for $N_s = 9$. By increasing N_s, it is demonstrated that single-particle excitations ($\omega < \omega_M$) contribute to the evolution of the electron density, which refer to dipole transitions of single-particle states with $\Delta l = \pm 1$. The residual volume plasmons are damped by these excitations. This result shows the growing influence of Landau damping [15, 16] for increasing values of N_s.

inside the cluster. Therefore, these low-frequency oscillations do not couple directly to the surface force and the c.m.

By increasing the value of N_s up to $N_s = 27$, the equilibrium density becomes more and more inhomogeneous inside the cluster. The displacement of the electron system during the first quarter of the initial Mie oscillation already couples to the internal electron density. This behavior is only weakly pronounced in the case $N_s = 9$ since the equilibrium density is still quite homogeneous as in the SSVM. In the course of time, one can see oscillations on the timescale of T_p, again associated with the volume plasmon resonance. However, in contrast to the SSVM density, one can observe a damping of residual volume plasmons in the time domain. The decay of the volume plasmon is accompanied by a reduction of the Fourier amplitude close to ω_p. In addition, one can observe an increased number of low-frequency maxima of $|\tilde{n}^{(1)}|$.

For $N_s = 99$, the volume plasmon resonance gets even more suppressed and one can observe a strong signal of weakly damped single-particle excitations. The energy transfer between a collective excitation and single-particle excitations is known as Landau damping. Landau damping of plasma waves is a well-known damping mechanism in classical [114] and quantum plasmas [17, 115] of infinite extent. Furthermore, it has been studied for clusters [15, 16] in the framework of TDLDA.

For $N_s = 99$, a clear signature of single-particle excitations can be observed at $\omega \approx 0.1$. The coupling of the corresponding single-particle excitation to the c.m. has been discussed above by considering the subshell-resolved surface force. This coupling can be viewed also on the basis of the electron density shown in Fig. 4.4.3. For small values of N_s, the single-particle excitations with transition frequencies ω_t are located deep in the interior region of the cluster. In this case, the corresponding density profiles $\tilde{n}^{(1)}(z, \omega_t)$ do not overlap with the region $r > R$. Therefore, the surface force is not influenced by the frequencies ω_t. As N_s gets larger, the density profiles $\tilde{n}^{(1)}(z, \omega_t)$ are more and more shifted towards the cluster surface (see Figure). For $N_s = 99$, it is visible that the density profile corresponding to $\omega \approx 0.1$ is located near the surface. In this sense, the coupling to the surface force leads to a signature of the frequency $\omega \approx 0.1$ in the resonance curve 4.4.1b of the c.m.

To summarize, it can be said that the inclusion of multiple ensemble states within the multistream model leads to a modification of the mode conversion process (see Subsection 4.3.3). For small numbers of representative states, the equilibrium density is almost homogeneous inside the cluster and mode conversion from the Mie plasmon to volume plasmons is visible. The residual volume plasmons are nearly undamped. By increasing the number of representative states, volume plasmons interact with the subshell-induced inhomogeneity of the equilibrium density inside the cluster. As a result, they are damped by single-particle excitations. In this framework, Landau damping appears as a secondary process of the Mie-plasmon decay. In the following subsection, it is intended to investigate more quantitatively in how far this secondary process influences the damping rate of the Mie plasmon.

4.4.2 Comparison of Multistream and Single-State Vlasov Model

This subsection is intended to compare perturbation results of the multistream model for Na configurations with those of the SSVM. In particular, the focus is put on the damping rate γ of the Mie plasmon as a function of the cluster radius. For this reason, SSVM results for the size-dependence of γ are taken up again, which where calculated in [107] by the author of this thesis. These results are also interpreted in more detail based on the insights of Subsections 4.3.3 and 4.4.1 concerning the damping mechanism. Finally, the SSVM and multistream results for γ are compared with previous results on the plasmon damping rate.

In [107], the size dependence of the resonance frequency ω and the damping rate γ of the Mie plasmon was calculated for cluster radii up to $R = 260$. By considering a typical solid density of $n_0 = 10^{23}\,\mathrm{cm}^{-3}$, cluster radii up to 21nm are treated in this range. Figure 4.4.4 shows results for γ and ω as a function of R both for the dipole and the quadrupole mode (SSVM). The results demonstrate the increase of γ and the increasing redshift of ω for descreasing cluster sizes due to the growing influence of the spill-out effect (see Fig. 4.3.3). In particular, 25% of the electrons are located outside the ion sphere for the smallest cluster of radius $R = 4$. For large values of R, quantum-size effects become small and the plasmon parameters approach their classical reference values of $\omega = \omega_{l'} = \sqrt{l'/(2l'+1)}$ and $\gamma = 0$ [8].

In the following, the SSVM results for the plasmon parameters are compared with corresponding multistream results for Na clusters. For this purpose, the plasmon parameters were calculated for four differently sized Na clusters with up to 198 electrons as characterized in Appendix A.1. The plasmon dynamics of the largest cluster has been studied in Subsection 4.4.1. For the Mie oscillation, the plasmon parameters were extracted with the help of a fitting procedure by studying the exponential decay of the Mie plasmon that follows an impulsive excitation (see Fig. 4.4.1). The resulting data points are also plotted in Fig. 4.4.4.

Most notably, Fig. 4.4.4a demonstrates that the data points of the Na clusters fit rather accurately to the data points of the SSVM. This is the case both for the dipole and the quadrupole mode. Although the electronic details of the Na clusters are completely neglected within the SSVM, this result indicates that the properties of the surface plasmon resonance within the multistream model can be described to a good approximation by only a single representative electron state. In the previous subsection, it has been demonstrated in the framework of the multistream model that the decay of the Mie plasmon results in an excitation of volume plasmons (mode conversion) [81]. These collective excitations turned out to be damped by single-particle excitations (Landau damping) [15]. Since the Landau mechanism is not present within the SSVM (due to the lack of multiple single-particle states), the close agreement of the damping rates indicates that mode conversion is the driving process of the surface plasmon decay.

In Section (4.2), it was demonstrated that the surface effects of the Mie plasmon can be fully expressed in terms of a surface force $\boldsymbol{F}_{sc}(t)$ that enters the equation of motion of the c.m. In particular, it was shown that $\boldsymbol{F}_{sc}$ can be written in terms of the spill-out density of the electrons. Therefore, the close agreement between the equilibrium

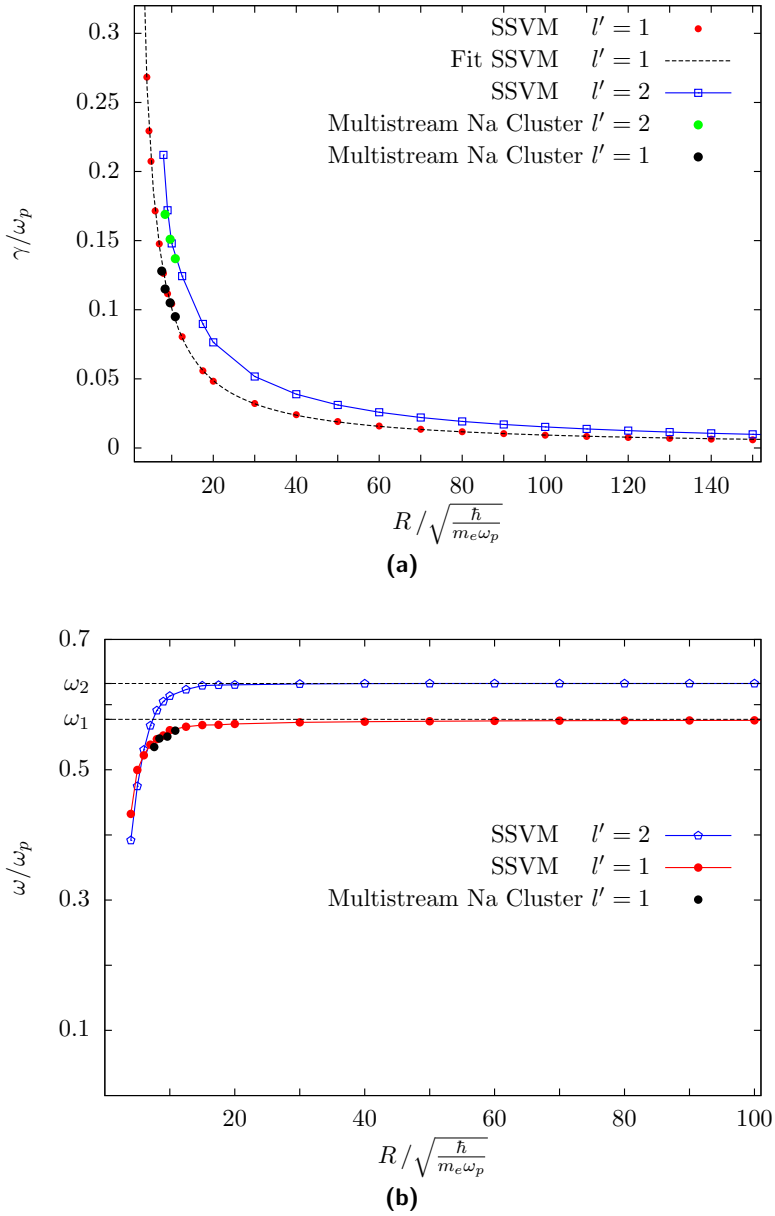

Figure 4.4.4: Damping rates γ (a) and resonance frequencies ω (b) of surface plasmons for the dipole ($l' = 1$) and quadrupole ($l' = 2$) order. Results are plotted for the single-state Vlasov model (SSVM) and for many-electron equilibria of Na clusters with up to 198 electrons as a function of the cluster radius R. Data points of the SSVM are taken from [107]. The electron configurations of the Na clusters can be found in Appendix A.1. The SSVM results for γ are fitted to the inverse power laws $\gamma(R) = 0.96/R^{0.99}$ for the dipole mode and $\gamma(R) = 1.54/R^{0.99}$ for the quadrupole mode. It is demonstrated that the data points of the Na clusters are close to the results of the SSVM.

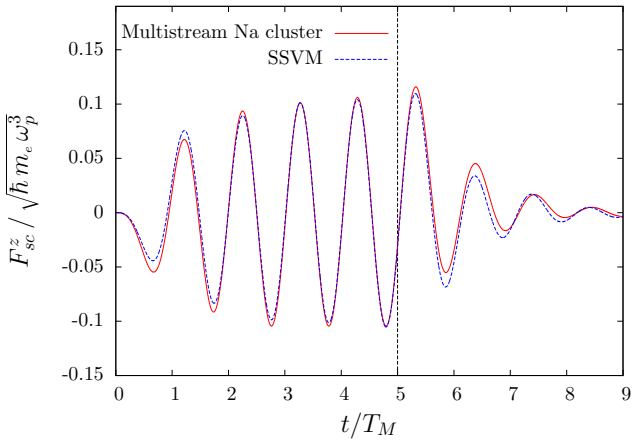

Figure 4.4.5: Component $F^z_{sc}(t)$ of the linearized surface force $\boldsymbol{F}^{(1)}_{sc}(t)$ as a function of time. The electron system is excited resonantly by a laser field in dipole approximation that is switched off after five laser cycles ($\omega = \omega_M$, $\mathcal{E}_0 = 0.1$). The switch-off point is indicated by a dashed vertical line. The force F^z_{sc} is shown for the single-state Vlasov model (SSVM) and for a multistream Na cluster ($R = 10.8$ and 198). Both results are in good qualitative agreement, which reflects the close agreement between the plasmon damping rate of the SSVM and the multistream model.

spill-out densities of the SSVM and the multistream model (see Fig. 3.4.2) was seen as a motivation to study plasmon excitations within the SSVM. By using the insight that the damping rates of both models deviate only slightly, it is instructive to analyze whether the close agreement between the damping rates can also be understood on the basis of the surface force. For this purpose, the time evolution of the linearized surface force $\boldsymbol{F}^{(1)}_{sc}(t)$ is calculated exemplarily for the SSVM and the largest Na cluster with 198 electrons.

For the reference calculation, the excitation of the Mie plasmon is considered to be driven by a monochromatic laser field $\boldsymbol{\mathcal{E}}(t)$ in dipole approximation, which is polarized along the z-axis. Then, the external potential reads

$$\begin{aligned} &\phi_{ext}(\boldsymbol{r},t) = -\boldsymbol{\mathcal{E}}(t)\cdot\boldsymbol{r} = -\nu_1(r,t)Y_{10}(\theta), \\ &\boldsymbol{\mathcal{E}}(t) = \mathcal{E}_0 \sin(\omega t)\boldsymbol{e}_z, \quad \nu_1(r,t) = r\sqrt{\frac{4\pi}{3}}\mathcal{E}_0 \sin(\omega t). \end{aligned} \tag{4.4.6}$$

The electron system is resonantly excited ($\omega = \omega_M$) at a field strength of $\mathcal{E}_0 = 0.1$. To study the decay of the Mie plasmon, the laser is switched off instantaneously after five laser cycles $T = 2\pi/\omega$. Figure 4.4.5 shows the result for the z-component of $\boldsymbol{F}^{(1)}_{sc}$ calculated with equation (4.2.14). Prior to the interaction with the laser, the electron system is in the equilibrium state. Therefore, F^z_{sc} vanishes at $t = 0$. As the laser is switched on, the c.m. starts oscillating and F^z_{sc} builds up. It is visible that both results are quite close after a few laser cycles. Also after the switch-off of the laser, both curves are in good qualitative agreement. Since the surface force quantifies the surface effects of the c.m. motion, one may expect a close agreement between the plasmon damping rate of the multistream model and the SSVM.

l	α	β
1	0.96	0.99
2	1.54	0.99

(a) γ

α	β
0.95	1.00

(b) f_{out}

Table 4.4.1: Size dependence of the damping rate γ and the fraction f_{out} of spill-out electrons. The table shows fit parameters which have been obtained based on the model function (4.4.7).

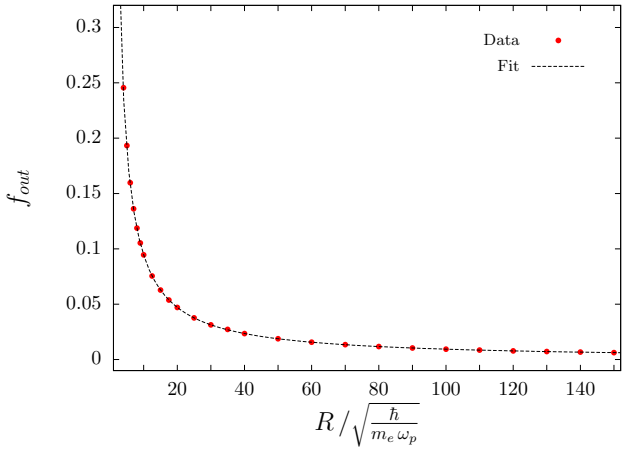

Figure 4.4.6: Size-dependent fraction f_{out} of spill-out electrons in the equilibrium state (Single-state Vlasov model). The data points are fitted to the inverse power law $f_{out}(R) = 0.95/R$. It is shown that f_{out} exhibits a $1/R$-dependence similar to the plasmon damping rate.

Finally, the focus is put on the size dependence of the damping rate. In [107], the data points of the SSVM were fitted to a model function of the form

$$\gamma(R) = \frac{\alpha}{R^{\beta}}, \tag{4.4.7}$$

which is also plotted in Fig. 4.4.4a for the Mie plasmon. The resulting fit parameters α and β are shown in Table 4.4.1a. The value of $\beta \approx 1$ indicates a $1/R$-dependence of the damping rate [24, 43, 44, 100, 105], which is closely related to the surface-to-volume ratio of the ion sphere.

In Subsection (4.3.3), it was demonstrated that the plasmon decay arises due to the spill-out induced surface inhomogeneity of electron density at the cluster surface. To analyze the relation between γ and the fraction f_{out} of spill-out electrons in the equilibrium state, f_{out} is plotted against R in Fig. 4.4.6 (SSVM). The plot indicates a size dependence of f_{out} similar to γ. Therefore, the data points are fitted to the same model function (4.4.7), which yields the fit parameters given in Table 4.4.1b. Since f_{out} shows the same scaling with the inverse cluster radius, the size dependence of γ can be directly linked to that of f_{out}. Moreover, one recognizes that the fit parameters of the Mie plasmon are very close to those of f_{out}. Therefore, both quantities are almost equal in dimensionless units and one can state the following simple relation between

the damping rate $\gamma^\star$ in dimensional units and f_{out}:

$$\gamma^\star \approx \omega_p \, f_{out}. \tag{4.4.8}$$

Now, comparison is made with previous work on the plasmon damping rate. For this purpose, the power law (4.4.7) for γ is transformed into dimensional units (see Table 2.3.1), which gives ($\beta \approx 1$)

$$\gamma^\star = a \, \frac{v_{pl}}{R^\star}, \quad a = \frac{\alpha}{\sqrt{2}}. \tag{4.4.9}$$

Here, $v_{pl} = \sqrt{2\hbar\omega_p/m_e}$ is the plasma velocity and $R^\star$ the cluster radius in dimensional units. By using the definition of ω_p, this relation can be alternatively be written in terms of the density parameter n_0,

$$\gamma^\star = a' \, \frac{\left(\frac{n_0}{10^{23}\mathrm{cm}^{-3}}\right)^{\frac{1}{4}}}{\left(\frac{R^\star}{1\mathrm{nm}}\right)} \mathrm{fs}^{-1}, \quad a' \approx 1.44\alpha, \tag{4.4.10}$$

with parameters $a' = 1.38$ for the Mie plasmon and $a' = 2.21$ for the quadrupole mode. It was demonstrated in this subsection that the SSVM results and the multistream results for γ are rather close. Therefore, the power law (4.4.9) of the SSVM can be seen as a proper starting point for the comparison with previous results on the damping rate.

For this purpose, it is noted that the present result for $\gamma^\star$ scales with v_{pl}. In the literature, $\gamma^\star$ is commonly expressed by the Fermi velocity $v_F = (3\pi^2 n_0)^{1/3}\hbar/m_e$ [100]. Therefore, both velocities are compared by considering their ratio

$$\frac{v_{pl}}{v_F} = 1.22\left(\frac{n_0}{10^{23}\mathrm{cm}^{-3}}\right)^{-1/12}. \tag{4.4.11}$$

This ratio has been evaluated for typical densities n_0 within the range $10^{22}\mathrm{cm}^{-3} < n_0 < 10^{23}\mathrm{cm}^{-3}$, which gives values between 1.48 and 1.22. In conclusion, the present Vlasov result differs slightly from a scaling with v_F over the range of typical densities. In particular, for Na, the relation between plasma and Fermi velocity is given by $v_{pl} = 1.36 v_F$.

In order to compare the damping rate (4.4.9) with corresponding results in the literature, the damping rate is transformed into an expression (4.0.1) for the plasmon linewidth Γ by using the relation $\Gamma = 2\gamma^\star$. Then, the Vlasov result for the linewidth and the A-parameter of the Mie plasmon reads

$$\Gamma = A\frac{v_F}{R}, \qquad A = \frac{2 \cdot 0.96}{\sqrt{2} \cdot 1.36} = 1.85. \tag{4.4.12}$$

The A-parameter is roughly seven times larger than both the TDLDA result $A \approx 0.28$ [105] (for free isolated clusters) and the experimental result $A = 0.25$ [23, 24]. In order to understand the discrepancy of the present A-parameter from these previous results, two approaches were considered. First, the author made certain that the deviation is not related to numerical errors. For this reason, the author has reproduced the A-parameter (4.4.12) by using the full nonlinearized Vlasov-Poisson code that will be

introduced in Chapter 7. Secondly, the focus has been put on the question whether the discrepancy can be explained by the lack of exchange and correlation effects within the Vlasov model. Therefore, the author has performed cluster simulations including the exchange-correlation potential of Gunnarson and Lundqvist [90]. The corresponding equilibrium density for the largest Na cluster considered with 198 electrons is plotted in Fig. 3.4.2.

By using the general form (3.4.1) of the exchange-correlation potential and the plasma units of Na (see Table 2.3.2), the linearized exchange-correlation potential for Na reads

$$\phi_{xc}^{(1)}(\boldsymbol{r},t) = \frac{1}{3} n^{(0)}(r)^{-2/3} \left[0.705 + 0.439 \, \frac{1}{1 + 2.848 \, n^{(0)}(r)^{1/3}} \right] n^{(1)}(\boldsymbol{r},t). \qquad (4.4.13)$$

For the reference simulations, this potential was added to the self-consistent potential $\phi^{(1)}$ in (4.1.20a). The simulation of the Na cluster with 198 electrons has lead to a damping rate of $\gamma = 0.017$ for the Mie plasmon. This value is much smaller than both the multistream result $\gamma = 0.095$ and the SSVM result $\gamma = 0.088$. To compare the reduced value of γ with the reference results [23, 24, 105], γ can be transformed into an A-parameter of $A = 0.33$. Obviously, this numerical value is much closer to the experimental value of $A = 0.25$ and the TDLDA result $A \approx 0.28$. Therefore, it is concluded that exchange and correlation effects play an important role for the quantitative description of the damping rate in Na clusters. In general agreement with this observation, the fraction of spill-out electrons in the equilibrium state is model-dependent. While the multistream model yields a value of $f_{out} = 0.1$, the inclusion of exchange-correlation corrections leads to $f_{out} = 0.064$. However, the deviation of the two damping rates by roughly a factor seven cannot simply be explained quantitatively by the reduction of f_{out}. Therefore, it would be instructive to apply the multistream model and the SSVM to clusters of higher density. For high electron densities, the exchange interaction is expected to become less decisive [92, 116].

Summary

In this chapter, linear electrostatic excitations of quantum-sized clusters have been treated in the multistream model and in the SSVM. In the framework of the SSVM, the damping of the Mie plasmon can be explained by a mode conversion process [81] from surface to volume plasmons due to surface scattering. The conversion process is closely related to the surface inhomogeneity of the electron-electron interaction potential.

Increasing the number of representative states in the multistream approach, it has been shown that the residual volume plasmons are damped by single-particle excitations (Landau damping) due to the interaction of the plasmon with the subshell-induced inhomogeneity of the electron density inside the cluster. In this framework, Landau damping appears as a secondary process of the Mie-plasmon decay.

Reference calculations for simple metal clusters have been performed with complete electron configurations of Na clusters. The plasmon damping rate of the dipole (Mie plasmon) and quadrupole mode shows good quantitative agreement with the damping

rate obtained within the SSVM. This result indicates the importance of mode conversion for the plasmon decay. The damping rate shows a characteristic scaling with the inverse cluster radius. In addition, the resonance frequency is redshifted with respect to the Mie frequency especially for small clusters. By further including exchange-correlation corrections, close agreement of the damping rate coefficient with previous experimental and numerical results can be achieved.

Chapter 5

Linear Theory of Electromagnetic Cluster Excitations

In the previous chapter, excitations of nanometer-sized clusters were treated within the electrostatic Vlasov model. Now, the Vlasov model is generalized to the EM regime with a full account to the EM radiation field by solving the corresponding Vlasov-Maxwell system for the SSVM (see Subsection 3.4) in linear perturbation theory. In this framework, both surface effects and radiative effects of the cluster dynamics are described in a self-consistent manner.

While classical PIC codes [60] and further approaches based on the Fourier transform [117] are well-established for the solution of the classical Vlasov-Maxwell system, the treatment of the quantum Vlasov-Maxwell system is a less covered topic, as pointed out in [118].

The present approach aims to describe the interaction of spherical clusters with an external plane EM wave on a quantum-mechanical basis. The first treatment of light scattering by spherical particles goes back to Mie [10] who considered the scattering of a plane EM wave by a dielectric sphere of radius R with a spatially-constant dielectric function $\epsilon(\omega)$. While Mie's theory is limited to homogeneous spheres with a sharp surface, the present treatment can be used to calculate absorption and scattering cross sections of clusters with an arbitrary radial density profile of the background ions. In particular, it is capable of describing collective effects of the laser-cluster interaction that are related to the spatial inhomogeneity of the electron density.

In Section 5.1, the theoretical background is viewed. Starting with an introduction to vector spherical harmonics (VSH) in Subsection 5.1.1, basic results of the Mie theory are summarized in Subsection 5.1.2. Subsequently, the basic equations of this chapter are formulated in Subsection 5.1.3 based on a partial wave expansion of the linearized Vlasov-Maxwell system in terms of VSH.

In Section 5.2, numerical results are presented. First, results are presented for a homogeneous ion sphere in Subsection 5.2.1. Here, comparison is made with corresponding results of Mie's theory. In Subsection 5.2.2, the present model is applied to clusters with a spatially inhomogeneous ion background. In this framework, resonance absorption of laser light is studied for spherical clusters with variable angles of incidence and light polarizations along the surface. Resonance absorption forms the dominant absorption mechanism in hot inhomogeneous plasmas. It is well-treated for plane surfaces and p-polarized light [74–76].

In the SSVM, the Vlasov-Maxwell system determines the time evolution of the representative state $\varphi(\boldsymbol{r},t)$, the self-consistent scalar potential $\phi(\boldsymbol{r},t)$ and the self-consistent vector potential $\boldsymbol{A}(\boldsymbol{r},t)$. In Lorenz gauge, it is given by

$$i\partial_t\varphi = \left[\frac{\Pi^2}{2} - \phi\right]\varphi, \tag{5.0.1a}$$

$$\left[\Delta - \frac{1}{c'^2}\partial_t^2\right]\boldsymbol{A} = \frac{1}{c'}\boldsymbol{j}, \quad \boldsymbol{j} = \Re\{\varphi^*\Pi\,\varphi\}, \tag{5.0.1b}$$

$$\left[\Delta - \frac{1}{c'^2}\partial_t^2\right]\phi = n, \quad n = |\varphi|^2 - n_{ion}, \tag{5.0.1c}$$

where $\boldsymbol{j}(\boldsymbol{r},t)$ is the probability current, $\boldsymbol{n}(\boldsymbol{r},t)$ the electron density and $n_{ion}(r)$ the ion density (measured in units of the density parameter n_0). Furthermore,

$$\Pi(\boldsymbol{r},t) = \left(-i\,\nabla + \frac{1}{c'}\boldsymbol{A}(\boldsymbol{r},t)\right), \quad c' = 208.61\left(\frac{n_0}{10^{23}/\mathrm{cm}^3}\right)^{-1/4} \tag{5.0.2}$$

is the momentum operator, c the speed of light and $c' = c/v_{pl}$ the speed of light measured in plasma units. The numerical results of this chapter are presented exemplarily for a typical density $n_0 = 10^{23}/\mathrm{cm}^3$, which corresponds to the dimensionless speed of light $c' = 208.61$.

5.1 Theoretical Background

5.1.1 Vector Spherical Harmonics

In this subsection, the VSH are introduced which define a complete set of vector functions over the unit sphere S_2. The VHS are used in this chapter to expand the vector potential $\boldsymbol{A}(\boldsymbol{r},t)$ of an EM field into a sum of partial waves. In the following, a brief overview over the basic properties of the VSH is given [119–121].

The VSH form an extension of the scalar SH $Y_{lm}(\Omega)$, where $\Omega = (\theta,\varphi)$. They are defined by the following expressions:

$$\boldsymbol{Y}_{lm}(\Omega) = \boldsymbol{e}_r Y_{lm}(\Omega), \qquad \boldsymbol{Y}^*_{lm} = (-1)^m \boldsymbol{Y}_{l,-m}, \tag{5.1.1a}$$

$$\boldsymbol{\Psi}_{lm}(\Omega) = r\nabla Y_{lm}(\Omega), \qquad \boldsymbol{\Psi}^*_{lm} = (-1)^m \boldsymbol{Y}_{l,-m}, \tag{5.1.1b}$$

$$\boldsymbol{\Phi}_{lm}(\Omega) = \boldsymbol{r}\times\nabla Y_{lm}(\Omega), \quad \boldsymbol{\Phi}^*_{lm} = (-1)^m \boldsymbol{Y}_{l,-m}. \tag{5.1.1c}$$

In (5.1.1a), the possible l-values are restricted to $l \in \mathbb{N}_0$, while the VHS (5.1.1b) and (5.1.1c) are defined for $l \in \mathbb{N}$. As for the scalar SH, the possible m-values range from $m = -l$ to $m = l$.

For given values of $l > 0$ and m, there are three orthonormal vector fields $\boldsymbol{Y}_{lm}$, $\boldsymbol{\Psi}_{lm}$ and $\boldsymbol{\Phi}_{lm}$. Here, the scalar product of two vector functions $\boldsymbol{V}(\Omega)$ and $\boldsymbol{W}(\Omega)$ is defined by

$$\langle \boldsymbol{V}|\boldsymbol{W}\rangle = \int_{S_2} \boldsymbol{V}^*(\Omega)\cdot\boldsymbol{W}(\Omega)\,d\Omega. \tag{5.1.2}$$

With this definition, the VSH fulfill the orthogonality relations

$$\langle \boldsymbol{\Psi}_{lm} | \boldsymbol{\Psi}_{l'm'} \rangle = \langle \boldsymbol{\Phi}_{lm} | \boldsymbol{\Phi}_{l'm'} \rangle = l(l+1)\delta_{ll'}\delta_{mm'}, \tag{5.1.3a}$$

$$\langle \boldsymbol{Y}_{lm} | \boldsymbol{Y}_{l'm'} \rangle = \delta_{ll'}\delta_{mm'}, \tag{5.1.3b}$$

$$\langle \boldsymbol{\Psi}_{lm} | \boldsymbol{\Phi}_{l'm'} \rangle = \langle \boldsymbol{\Psi}_{lm} | \boldsymbol{Y}_{l'm'} \rangle = \langle \boldsymbol{\Phi}_{lm} | \boldsymbol{Y}_{l'm'} \rangle = 0. \tag{5.1.3c}$$

Furthermore, they have the properties

$$\boldsymbol{Y}_{lm} \cdot \boldsymbol{\Psi}_{l'm'} = \boldsymbol{Y}_{lm} \cdot \boldsymbol{\Phi}_{l'm'} = 0. \tag{5.1.4}$$

In analogy with the spherical harmonic expansion of a scalar function, a vector field $\boldsymbol{f}(\boldsymbol{r})$ can be expanded in terms of the VHS (5.1.1),

$$\boldsymbol{f}(\boldsymbol{r}) = \sum_{l=0}^{\infty} \sum_{m=-l}^{l} f_{lm}^{(a)}(r)\boldsymbol{Y}_{lm}(\Omega) + f_{lm}^{(b)}(r)\boldsymbol{\Psi}_{lm}(\Omega) + f_{lm}^{(c)}(r)\boldsymbol{\Phi}_{lm}(\Omega), \tag{5.1.5}$$

where $\boldsymbol{\Psi}_{00} = \boldsymbol{\Phi}_{00} = 0$ by definition. By using the orthogonality relations (5.1.3), the radial functions $f_{lm}^{(a)}$, $f_{lm}^{(b)}$ and $f_{lm}^{(c)}$ are given by

$$f_{lm}^{(a)}(r) = \langle \boldsymbol{Y}_{lm} | \boldsymbol{f} \rangle, \quad f_{lm}^{(b)}(r) = \frac{1}{l(l+1)} \langle \boldsymbol{\Psi}_{lm} | \boldsymbol{f} \rangle, \quad f_{lm}^{(c)}(r) = \frac{1}{l(l+1)} \langle \boldsymbol{\Phi}_{lm} | \boldsymbol{f} \rangle. \tag{5.1.6}$$

The expansion (5.1.5) can be used to express the curl and divergence of $\boldsymbol{f}(\boldsymbol{r})$ by VSH and SH,

$$\mathrm{div}\boldsymbol{f}(\boldsymbol{r}) = \sum_{l=0}^{\infty} \sum_{m=-l}^{l} \left\{ \frac{1}{r^2} \frac{d}{dr} \left(r^2 f_{lm}^{(a)}(r) \right) - \frac{l(l+1)}{r} f_{lm}^{(b)}(r) \right\} Y_{lm}(\Omega), \tag{5.1.7a}$$

$$\mathrm{rot}\boldsymbol{f}(\boldsymbol{r}) = \sum_{l=0}^{\infty} \sum_{m=-l}^{l} \Bigg\{ - \frac{l(l+1)}{r} f_{lm}^{(c)}(r)\boldsymbol{Y}_{lm}(\Omega) - \frac{1}{r} \frac{d}{dr} \left(r f_{lm}^{(c)}(r) \right) \boldsymbol{\Psi}_{lm}(\Omega) \tag{5.1.7b}$$

$$+ \left(\frac{1}{r} \frac{d}{dr} \left(r f_{lm}^{(b)}(r) \right) - \frac{1}{r} f_{lm}^{(a)}(r) \right) \boldsymbol{\Phi}_{lm}(\Omega) \Bigg\}.$$

Furthermore, the gradient of a scalar function

$$g(\boldsymbol{r}) = \sum_{l=0}^{\infty} \sum_{m=-l}^{l} g_{lm}(r) Y_{lm}(\Omega) \tag{5.1.8}$$

can be expressed as follows:

$$\nabla g(\boldsymbol{r}) = \sum_{l=0}^{\infty} \sum_{m=-l}^{l} g_{lm}^{'}(r)\boldsymbol{Y}_{lm}(\Omega) + \frac{g_{lm}(r)}{r} \boldsymbol{\Psi}_{lm}(\Omega). \tag{5.1.9}$$

5.1.2 Mie Theory

In this subsection, the classical Mie theory is viewed [8, 10, 122]. *For the sake of clarity, quantities in this subsection are given in dimensional form.* The Mie theory treats the

scattering of a monochromatic EM plane wave by a dielectric sphere with a spatially-constant dielectric function $\epsilon(\omega)$. In the following, the electric field $\boldsymbol{E}_L(\boldsymbol{r},t)$ of the plane wave is considered to be polarized along the x-axis. In complex representation, $\boldsymbol{E}_L$ is given by

$$\boldsymbol{E}_L(\boldsymbol{r},t) = E_0 e^{i\mathbf{k}_0\cdot\mathbf{r}-i\omega t}\boldsymbol{e}_x, \quad c = \frac{\omega}{k_0}, \tag{5.1.10}$$

where c is the speed of light. Since the free charge density of the EM field is vanishing within the dielectric model, the EM field can be represented by a vector potential $\boldsymbol{A}(\boldsymbol{r},t) \sim \exp(i\omega t)$, which satisfies the wave equation

$$\Delta\boldsymbol{A} + k^2\boldsymbol{A} = 0, \quad k(\omega) = \begin{cases} k_0, & r > R \\ n(\omega)k_0, & r < R \end{cases}. \tag{5.1.11}$$

Here, $n(\omega) = \sqrt{\epsilon(\omega)}$ is the refractive index of the sphere of radius R. Solutions to (5.1.11) for $r < R$ and $r > R$ in spherical coordinates can be constructed based on the VSH, which were introduced in Subsection 5.1.1. The solution in the whole space can be obtained by applying the boundary conditions for the EM field at the surface of a dielectric medium [8]. Then, the result for the scattered fields $\boldsymbol{E}_{sc}(\boldsymbol{r},t)$ and $\boldsymbol{B}_{sc}(\boldsymbol{r},t)$ of the sphere in the exterior region reads

$$\boldsymbol{E}_{sc} = E_0 e^{-i\omega t}\sum_{l,\pm1} d_l \left(a_{l\pm}\, h_l^{(1)}(k_0 r)\boldsymbol{\Phi}_{l,\pm1} + \frac{1}{k_0} b_{l\pm}\, \nabla\times h_l^{(1)}(k_0 r)\boldsymbol{\Phi}_{l,\pm1} \right), \tag{5.1.12a}$$

$$\boldsymbol{B}_{sc} = -iE_0 e^{-i\omega t}\sum_{l,\pm1} d_l \left(b_{l\pm}\, h_l^{(1)}(k_0 r)\boldsymbol{\Phi}_{l,\pm1} + \frac{1}{k_0} a_{l\pm}\, \nabla\times h_l^{(1)}(k_0 r)\boldsymbol{\Phi}_{l,\pm1} \right), \tag{5.1.12b}$$

where $h_l^{(1)}$ are Hankel functions of the first kind and $d_l = i^{l-1}\sqrt{\pi(2l+1)/(l(l+1))}$. The following relations define the expansion coefficients of (5.1.12), where the variable $\rho = k_0 R$ is used:

$$a_{l\pm} = \frac{j_l(n\rho)\,[\rho j_l(\rho)]' - j_l(\rho)\,[n\rho j_l(n\rho)]'}{h_l^{(1)}(\rho)\,[n\rho j_l(n\rho)]' - j_l(n\rho)[\rho h_l^{(1)}(\rho)]'}, \tag{5.1.13a}$$

$$b_{l\pm} = \pm\left\{ \frac{n^2 j_l(n\rho)\,[\rho j_l(\rho)]' - j_l(\rho)\,[n\rho j_l(n\rho)]'}{h_l^{(1)}(\rho)\,[n\rho j_l(n\rho)]' - n^2 j_l(n\rho)[\rho h_l^{(1)}(\rho)]'} \right\}. \tag{5.1.13b}$$

The derivatives denoted by a prime are calculated with respect to the argument of the Hankel respectively the Bessel function.

The relations (5.1.13) can be used to calculate the optical properties of spherical particles [123]. In particular, plasmon resonances of electric type are determined by the zeros of the denominator of (5.1.13b),

$$h_l^{(1)}(\rho)\,[n\rho j_l(n\rho)]' - n^2 j_l(n\rho)[\rho h_l^{(1)}(\rho)]' = 0. \tag{5.1.14}$$

For a given dielectric function $\epsilon(\omega)$, (5.1.14) can be solved for the complex resonance frequency $\omega = \omega_r + i\omega_i$ with the help of a root-finding algorithm. Then, the damping rate γ of the resonance is given by $\gamma = -\omega_i$.

In this work, Mie's theory acts as a benchmark test for the comparison with the present

self-consistent SSVM calculations. For this purpose, a Drude model with

$$\epsilon(\omega) = 1 - \frac{\omega_p^2}{\omega^2 - 2i\nu(R)\omega} \tag{5.1.15}$$

is considered [124, 125]. Here, $\nu(R)$ is the collision frequency, which takes into account surface effects. For the reference calculations in this chapter, $\nu(R)$ is associated with the plasmon damping rate $\gamma_0(R)$ in the electrostatic regime (see Subsection 4.4.2), which takes into account the effect of surface scattering.

The Poynting vector $\boldsymbol{S}(\boldsymbol{r}, t)$ of an EM field reads

$$\boldsymbol{S} = \frac{c}{4\pi}(\boldsymbol{\mathcal{E}} \times \boldsymbol{\mathcal{B}}) \tag{5.1.16}$$

and describes the directional energy flux of the field, where $\boldsymbol{\mathcal{E}} = \Re\{\boldsymbol{E}\}$ and $\boldsymbol{\mathcal{B}} = \Re\{\boldsymbol{B}\}$ are the corresponding real fields. Based on the Poynting vector, one can calculate the scattering and absorption cross sections σ_{sc} of Mie's light-scattering problem,

$$\sigma_{sc} = \frac{\bar{P}_{sc}}{I_0}, \qquad \bar{P}_{sc} = \int\limits_{\partial V_{R'}} \bar{\boldsymbol{S}}_{sc}(\boldsymbol{r}) \cdot d\boldsymbol{\mathcal{F}}, \tag{5.1.17a}$$

$$\sigma_{abs} = \frac{\bar{P}_{abs}}{I_0}, \quad \bar{P}_{abs} = \int\limits_{\partial V_{R'}} \bar{\boldsymbol{S}}_{tot}(\boldsymbol{r}) \cdot d\boldsymbol{\mathcal{F}}, \tag{5.1.17b}$$

where $\bar{P}_{sc}$ and $\bar{P}_{abs}$ are the time-averaged scattered and absorbed powers with respect to the laser period $T = 2\pi/\omega$ and $I_0 = \frac{c}{8\pi}|E_0|^2$ the intensity of the incoming light wave. In (5.1.17), $\bar{\boldsymbol{S}}_{sc}$ is the time-averaged Poynting vector of the scattered field (5.1.12) and $\bar{\boldsymbol{S}}_{tot}$ that of the total field. Furthermore, $\partial V_{R'}$ is the surface of a sphere of radius $R' > R$.

By using the complex fields (5.1.12), one can calculate the time-averaged Poynting vector

$$\bar{\boldsymbol{S}}_{sc} = \frac{c}{8\pi}\,\Re\{\boldsymbol{E}_{sc} \times \boldsymbol{B}_{sc}^*\}. \tag{5.1.18}$$

This result can be introduced in (5.1.17), which finally yields the following expression:

$$\sigma_{sc} = \frac{2\pi}{k_0^2} \sum_l (2l+1)\left[|a_{l+}|^2 + |b_{l+}|^2\right]. \tag{5.1.19}$$

5.1.3 Perturbation Theory

In this chapter, linear cluster excitations are studied based on (5.0.1). In the following, the linearized functions with a superscript 1 describe small perturbations of the

equilibrium and are defined by the following ansatz:

$$\begin{aligned}
\varphi(\boldsymbol{r},t) &= e^{-i\epsilon_0 t}\left(\varphi^{(0)}(r)+\varphi^{(1)}(\boldsymbol{r},t)\right),\\
\phi(\boldsymbol{r},t) &= \phi^{(0)}(r)+\phi^{(1)}(\boldsymbol{r},t),\\
\boldsymbol{A}(\boldsymbol{r},t) &= \boldsymbol{A}^{(1)}(\boldsymbol{r},t) = \boldsymbol{A}_{int}(\boldsymbol{r},t)+\boldsymbol{A}_{ext}(\boldsymbol{r},t),\\
n(\boldsymbol{r},t) &= n^{(0)}(r)+n^{(1)}(\boldsymbol{r},t), \quad n^{(0)}=|\varphi^{(0)}|^2,\\
\boldsymbol{j}(\boldsymbol{r},t) &= \boldsymbol{j}^{(1)}(\boldsymbol{r},t).
\end{aligned} \tag{5.1.20}$$

The equilibrium quantities (with a superscript 0) are defined in Chapter 3. For later purpose, the vector potential is split into an internal part $\boldsymbol{A}_{int}$ and an external part $\boldsymbol{A}_{ext}$. Here, $\boldsymbol{A}_{int}$ takes into account the contribution of the internal charge and current densities to the total vector potential, while $\boldsymbol{A}_{ext}$ is associated with a source-free radiation field, which is considered in radiation gauge ($\boldsymbol{\phi}_{ext}=0, \nabla\cdot\boldsymbol{A}_{ext}=0$). By using the ansatz (5.1.20), the Vlasov-Maxwell system (5.0.1) can be linearized with respect to the perturbations, which yields the following linear system of equations:

$$i\partial_t\varphi^{(1)} = \left[-\frac{1}{2}\Delta-\phi^{(0)}\right]\varphi^{(1)} - \left(\frac{i}{c'}\boldsymbol{A}^{(1)}\cdot\nabla+\frac{i}{2c'}\nabla\cdot\boldsymbol{A}_{int}+\phi^{(1)}\right)\varphi^{(0)}, \tag{5.1.21a}$$

$$\left[\Delta-\frac{1}{c'^2}\partial_t^2\right]\boldsymbol{A}_{int} = \boldsymbol{j}^{(1)}, \quad \boldsymbol{j}^{(1)} = \frac{1}{c'}n^{(0)}\boldsymbol{A}^{(1)}+\Im\{\varphi^{(0)*}\nabla\varphi^{(1)}+\varphi^{(1)*}\nabla\varphi^{(0)}\}, \tag{5.1.21b}$$

$$\left[\Delta-\frac{1}{c'^2}\partial_t^2\right]\phi^{(1)} = n^{(1)}, \quad n^{(1)} = 2\Re\{\varphi^{(0)*}\varphi^{(1)}\}. \tag{5.1.21c}$$

At time $t=0$, the system is considered to be in the equilibrium state, $\varphi^{(1)}(\boldsymbol{r},0)=0$. For $t>0$, it is exposed to a plane EM wave with frequency ω (in analogy with Mie's theory), which is associated with an external laser field. The light wave travels along the z-axis and the corresponding electric field $\boldsymbol{\mathcal{E}}_{ext}$ is polarized along the x-axis,

$$\boldsymbol{\mathcal{E}}_{ext}(\boldsymbol{r},t) = \mathcal{E}_0\sin(kz-\omega t)(1-e^{-gt})\boldsymbol{e}_x. \tag{5.1.22}$$

For numerical reasons, the field is adiabatically switched on with a switch-on time of $1/g$. For the simulations of this chapter, a value of $g=0.2$ is chosen. In radiation gauge, the laser field is represented by a vector potential,

$$\boldsymbol{\mathcal{E}}_{ext} = -\frac{1}{c'}\partial_t\boldsymbol{A}_{ext}, \quad \boldsymbol{A}_{ext}(\boldsymbol{r},t) = A^+(t)e^{ikz}+A^-(t)e^{-ikz}, \quad A^- = (A^+)^*, \tag{5.1.23}$$

where

$$\begin{aligned}
A^+(t) &= -\frac{c'\mathcal{E}_0}{2i}\int_0^t (1-e^{-gt'})e^{-i\omega t'}\,dt'\\
&= \frac{\mathcal{E}_0}{2k}\Big((1-e^{-i\omega t})+\frac{\omega}{i\gamma-\omega}(1-e^{-(i\omega+g)t})\Big).
\end{aligned} \tag{5.1.24}$$

Here, the initial condition $\boldsymbol{A}_{ext}(\boldsymbol{r},0)=0$ is chosen. This choice is consistent with the radiation gauge, since one can always add a time-independent vector field to $\boldsymbol{A}_{ext}$, thereby leaving the fields invariant.

The linear system (5.1.21) can be transformed to a system of spatially one-dimensional equations with the help of a partial wave expansion. Scalar functions are expanded in

terms of SH, vector functions by VSH. For this purpose, $\boldsymbol{A}_{ext}$ has to be expanded in terms of VSH. The expansion of a vector plane wave in terms of VSH is given by [8]

$$\begin{aligned} e^{ikz}\boldsymbol{e}_x &= \sum_{l,\pm 1} d_l \left[j_l \boldsymbol{\Phi}_{l,\pm 1} \mp \left\{ \frac{l(l+1)}{kr} j_l \boldsymbol{Y}_{l,\pm 1} + \left(j_l' + \frac{j_l}{kr} \right) \boldsymbol{\Psi}_{l,\pm 1} \right\} \right], \\ d_l &= i^{l-1} \sqrt{\pi(2l+1)/(l(l+1))}. \end{aligned} \tag{5.1.25}$$

Here, $j_l(kr)$ are spherical Bessel functions of the first kind and j_l' the corresponding derivatives with respect to the argument kr. The expression (5.1.25) can be used to expand $\boldsymbol{A}_{ext}$ based on (5.1.23), which yields the following relation:

$$\boldsymbol{A}_{ext}(\boldsymbol{r},t) = \sum_{l,\pm 1} \tilde{A}^{(a)}_{l\pm}(r,t)\boldsymbol{Y}_{l,\pm 1}(\Omega) + \tilde{A}^{(b)}_{l\pm}(r,t)\boldsymbol{\Psi}_{l,\pm 1}(\Omega) + \tilde{A}^{(c)}_{l\pm}(r,t)\boldsymbol{\Phi}_{l,\pm 1}(\Omega), \tag{5.1.26a}$$

$$\tilde{A}^{(a)}_{l\pm}(r,t) = \mp \left(A^+(t) - (-1)^l A^-(t) \right) d_l \, l(l+1) \, j_l(kr)/(kr), \tag{5.1.26b}$$

$$\tilde{A}^{(b)}_{l\pm}(r,t) = \mp \left(A^+(t) - (-1)^l A^-(t) \right) d_l \, (j_l'(kr) + j_l(kr)/(kr)), \tag{5.1.26c}$$

$$\tilde{A}^{(c)}_{l\pm}(r,t) = \left(A^+(t) + (-1)^l A^-(t) \right) d_l \, j_l(kr). \tag{5.1.26d}$$

Since the possible m-values of this expansion are restricted to $m = \pm 1$, the linearized functions defined in (5.1.21) can be expanded in terms of SH and VSH with $m = \pm 1$,

$$\varphi^{(1)}(\boldsymbol{r},t) = \sum_{l,\pm 1} \varphi_{l\pm}(r,t) Y_{l,\pm 1}(\Omega), \tag{5.1.27a}$$

$$\phi^{(1)}(\boldsymbol{r},t) = \sum_{l,\pm 1} \phi_{l\pm}(r,t) Y_{l,\pm 1}(\Omega), \quad n^{(1)}(\boldsymbol{r},t) = \sum_{l,\pm 1} n_{l\pm}(r,t) Y_{l,\pm 1}(\Omega), \tag{5.1.27b}$$

$$\boldsymbol{A}_{int}(\boldsymbol{r},t) = \sum_{l,\pm 1} A^{(a)}_{l\pm}(r,t)\boldsymbol{Y}_{l,\pm 1}(\Omega) + A^{(b)}_{l\pm}(r,t)\boldsymbol{\Psi}_{l,\pm 1}(\Omega) + A^{(c)}_{l\pm}(r,t)\boldsymbol{\Phi}_{l,\pm 1}(\Omega), \tag{5.1.27c}$$

$$\boldsymbol{j}^{(1)}(\boldsymbol{r},t) = \sum_{l,\pm 1} j^{(a)}_{l\pm}(r,t)\boldsymbol{Y}_{l,\pm 1}(\Omega) + j^{(b)}_{l\pm}(r,t)\boldsymbol{\Psi}_{l,\pm 1}(\Omega) + j^{(c)}_{l\pm}(r,t)\boldsymbol{\Phi}_{l,\pm 1}(\Omega). \tag{5.1.27d}$$

This representation can be introduced in (5.1.21) to obtain a system of equations for the corresponding radial functions and a given value of l by using the orthogonality relations (5.1.3) and (4.1.5). For this purpose, one has to make use of further properties of the VSH, which were summarized in Subsection (5.1.1).

To evaluate the wave equation (5.1.21b) for $\boldsymbol{A}_{int}$, one has to apply the Laplacian on the vector potential (5.1.27c). The expansion of the result in terms of VSH is a problem that was not found to be discussed in common textbooks. Therefore, the corresponding calculations are carried out more detailed in Appendix A.3.1. Finally, one ends up with the following radial Schrödinger equation for the wave functions $\varphi_{l\pm}$:

$$\begin{aligned} i\partial_t \varphi_{l\pm} = \left[-\frac{1}{2}\Delta_l - \phi^{(0)} - \epsilon_0 \right] \varphi_{l\pm} - \varphi^{(0)} \phi_{l\pm} - \frac{i}{c'} \varphi^{(0)\prime} \left(A^{(a)}_{l\pm} + \tilde{A}^{(a)}_{l\pm} \right) \\ - \frac{i}{2c'} \varphi^{(0)} \left(A^{(a)\prime}_{l\pm} + \frac{2}{r} A^{(a)}_{l\pm} - \frac{l(l+1)}{r} A^{(b)}_{l\pm} \right) \end{aligned} \tag{5.1.28}$$

The self-consistent potentials $\phi_{l\pm}$, $A^{(a)}_{l\pm}$, $A^{(b)}_{l\pm}$ and $A^{(c)}_{l\pm}$ of the internal EM field are determined by a coupled system of radial wave equations,

$$\left(\Delta_r - \frac{l(l+1)}{r^2} - \frac{1}{c'^2}\partial_t^2\right)\phi_{l\pm} = n_{l\pm}, \tag{5.1.29a}$$

$$\left(\Delta_r - \frac{l(l+1)+2}{r^2} - \frac{1}{c'^2}\partial_t^2\right)A_{l\pm}^{(a)} + \frac{2l(l+1)}{r^2}A_{l\pm}^{(b)} = \frac{1}{c'}j_{l\pm}^{(a)}, \tag{5.1.29b}$$

$$\left(\Delta_r - \frac{l(l+1)}{r^2} - \frac{1}{c'^2}\partial_t^2\right)A_{l\pm}^{(b)} + \frac{2}{r^2}A_{l\pm}^{(a)} = \frac{1}{c'}j_{l\pm}^{(b)}, \tag{5.1.29c}$$

$$\left(\Delta_r - \frac{l(l+1)}{r^2} - \frac{1}{c'^2}\partial_t^2\right)A_{l\pm}^{(c)} = \frac{1}{c'}j_{l\pm}^{(c)}, \tag{5.1.29d}$$

where the sources are calculated based on the time-propagated wave functions $\varphi_{l\pm}$,

$$j_{l\pm}^{(a)} = \frac{1}{c'}n^{(0)}\left(A_{l\pm}^{(a)} + \tilde{A}_{l\pm}^{(a)}\right) + \frac{1}{2i}\Big[(\varphi^{(0)*}\varphi'_{l\pm} - \varphi^{(0)*'}\varphi_{l\pm}) \tag{5.1.30a}$$

$$- (\varphi^*_{l\mp}\,\varphi^{(0)'} - \varphi^{*'}_{l\mp}\,\varphi^{(0)})\Big], \tag{5.1.30b}$$

$$j_{l\pm}^{(b)} = \frac{1}{c'}n^{(0)}\left(A_{l\pm}^{(b)} + \tilde{A}_{l\pm}^{(b)}\right) + \left(\varphi^{(0)*}\varphi_{l\pm} + \varphi^{(0)}\varphi^*_{l\mp}\right)/r, \tag{5.1.30c}$$

$$j_{l\pm}^{(c)} = \frac{1}{c'}\left(A_{l\pm}^{(c)} + \tilde{A}_{l\pm}^{(c)}\right), \tag{5.1.30d}$$

$$n_{l\pm} = \left(\varphi^{(0)*}\varphi_{l\pm} - \varphi^{(0)}\varphi^*_{l\mp}\right). \tag{5.1.30e}$$

For the numerical evaluation, one has to choose a cut-off value l_{max}, which defines the highest propagated multipole order. Depending on the ratio R/λ, l_{max} has to be chosen sufficiently large in order to achieve convergence. Here, λ is the wavelength of the laser field. The limit $R/\lambda \to 0$ is associated with the dipole approximation where $l_{max} = 1$ is sufficient.

The time propagation of the wave functions $\varphi_{l\pm}$ is done by the Crank-Nicolson finite-difference method [95, 96] on a radial grid. The system of wave equations (5.1.29) is solved explicitly [126] on the same radial grid by using central differences [97] and radiation boundary conditions [127].

5.2 Perturbation Results

5.2.1 Homogeneous Ion Background

In this subsection, numerical results are presented for a homogeneous background of the ions, $n_{ion} = \theta(R-r)$. The corresponding ground state $\varphi^{(0)}$ was already considered for the electrostatic calculations in Section 4.3.

First, the result of a test calculation is presented, which was performed in order to test the correct propagation of the EM field outside the cluster based on the present numerical scheme. Here, comparison is made between the time-propagated internal

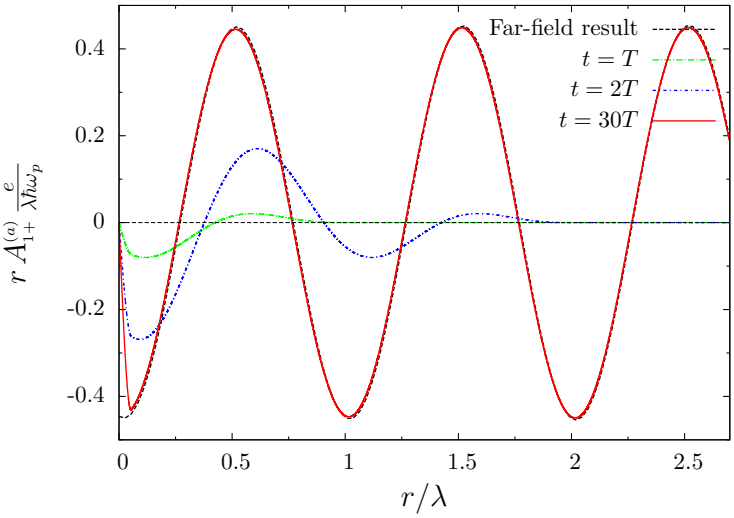

Figure 5.2.1: Component $A_{1+}^{(a)}(r,t)$ of the internal vector potential (5.1.27c) as a function of r measured in units of the laser wavelength $\lambda = 2\pi c'/\omega$. The simulation parameters are a cluster radius of $R = 100$ and a laser frequency of $\omega = 1/\sqrt{2}$. The numerical result is shown at different times of the laser-cluster interaction. In addition, the far-field result (5.2.2) is plotted. It is shown that the numerical result with radiation boundary conditions closely approaches the analytical far-field result of the radiated fields outside the cluster.

vector potential $\boldsymbol{A}_{int}(\boldsymbol{r},t)$ and the corresponding analytical solution $\boldsymbol{A}_f(\boldsymbol{r},t)$ in the far-field (f) regime $R \ll \lambda \ll r$. The latter result is given by [8]

$$\boldsymbol{A}_f(\boldsymbol{r},t) = \frac{1}{4\pi c' r}\dot{\boldsymbol{d}}(t - r/c) \tag{5.2.1}$$

and describes the dipole order of the vector potential ($l = 1$), where $\boldsymbol{d}(t)$ is the dipole moment of the internal charges. Due to the polarization the laser field, $\boldsymbol{d}$ is parallel to the x-axis, $\boldsymbol{d}(t) = d(t)\boldsymbol{e}_x$. For the comparison, $\boldsymbol{A}_f$ is expanded in terms of VSH,

$$\boldsymbol{e}_x = \sqrt{\frac{2\pi}{3}} \sum_{\pm 1} \mp \left(\boldsymbol{Y}_{1,\pm 1} + \boldsymbol{\Psi}_{1,\pm 1}\right), \tag{5.2.2a}$$

$$\boldsymbol{A}_f = \sum_{\pm 1} \left(A_{1\pm}^{(a)} \boldsymbol{Y}_{1,\pm 1} + A_{1\pm}^{(b)} \boldsymbol{\Psi}_{1,\pm 1}\right), \tag{5.2.2b}$$

$$A_{1\pm}^{(a)} = A_{1\pm}^{(b)} = \mp\sqrt{\frac{2\pi}{3}} \frac{1}{4\pi c' r} \dot{d}(t - r/c'). \tag{5.2.2c}$$

Figure 5.2.1 shows the numerical result for the component $A_{1+}^{(a)}(r,t)$ of the internal vector potential (5.1.27c) at different times t. The parameters of simulation are a cluster radius of $R = 100$ and a laser frequency of $\omega = 1/\sqrt{2}$.

As can be seen from the figure, the excitation of the internal charges by the laser field results in the formation of an EM wave, which propagates away from the cluster. The wavelengthλ of the emitted wave corresponds to that of the laser field. After the first

and the second laser cycle, it is shown that the propagation distances of the emitted wave are given by $\Delta r = \lambda$ for $t = T$ and $\Delta r = 2\lambda$ for $t = 2T$. At time $t = 30T$, the wave has already reached the boundary of the computational grid at $r = 2.7\lambda$. Due to the radiation boundary conditions of the numerical scheme, the wave passes through the boundary without being reflected. Comparison with the far-field result shows that both curves are in good agreement outside the cluster already close to the cluster boundary. In the present case, the ratio of the cluster radius and the laser wavelength is given by $R/\lambda \approx 0.05$. Therefore, retardation effects are less pronounced and $\boldsymbol{A}_f$ can accurately describe the dipole order of the internal field outside the cluster.

Next, it is demonstrated how scattering and absorption cross sections σ_{sc} and σ_{abs} can be extracted within the present self-consistent description. According to (5.1.17), the scattered and absorbed powers are given by surface integrals of the time-averaged internal and total Poynting vectors. For the numerical evaluation, the Poynting vector in plasma units (see Table 2.3.1) is introduced, which reads

$$\boldsymbol{S} = c' \boldsymbol{\mathcal{E}} \times \boldsymbol{\mathcal{B}}. \tag{5.2.3}$$

The solution to the surface integrals based on the partial wave expansion of the potentials ϕ and $\boldsymbol{A}$ is discussed in Appendix A.3.2. With this result, the energy fluxes through the surface of a sphere of radius $R' > R$ are given by

$$P_{sc}(t) = c' \sum_{l,\pm 1} l(l+1) \left\{ \left(\phi_{l\pm} + \frac{1}{c'} r \dot{A}^{(b)}_{l\pm} \right) \left(\partial_r \left(r A^{(b)}_{l\mp} \right) - A^{(a)}_{l\mp} \right) + \frac{1}{c'} \dot{A}^{(c)}_{l\pm} r \partial_r \left(r A^{(c)}_{l\mp} \right) \right\} \Bigg|_{r=R'}, \tag{5.2.4a}$$

$$P_{abs}(t) = c' \sum_{l,\pm 1} l(l+1) \left\{ \left(\phi_{l\pm} + \frac{1}{c'} r \dot{A}^{tot\,(b)}_{l\pm} \right) \left(\partial_r \left(r A^{tot\,(b)}_{l\mp} \right) - A^{tot\,(a)}_{l\mp} \right) + \frac{1}{c'} \dot{A}^{tot\,(c)}_{l\pm} r \partial_r \left(r A^{tot\,(c)}_{l\mp} \right) \right\} \Bigg|_{r=R'}. \tag{5.2.4b}$$

In (5.2.4a), one has to introduce the radial functions of $\boldsymbol{A}_{int}$ (see (5.1.27)), in (5.2.4a) those of the total vector potential $\boldsymbol{A}_{tot} = \boldsymbol{A}_{int} + \boldsymbol{A}_{ext}$. The expansion of $\boldsymbol{A}_{ext}$ is given in (5.1.26). For the calculation of σ_{sc} and σ_{abs}, the functions (5.2.4) have to be averaged with respect to the laser period.

Figure 5.2.2 shows the radiated power P_{sc} through the surface of an imaginary sphere of radius $R' = 1.1\lambda$. The power corresponds to the field calculation of Fig. 5.2.1. The plot shows that P_{sc} increases as the radiated field reaches the boundary of the sphere of radius R'. As the system evolves in time, the effect of the switch-on vanishes and P_{sc} oscillates around its time average $\bar{P}_{sc}$ with the double laser frequency 2ω. The numerical values of σ_{sc} and σ_{abs} can be calculated by studying the sequence

$$\sigma^{(n)}_{sc} = \frac{P^{(n)}_{sc}}{I_0}, \quad P^{(n)}_{sc} = \frac{1}{T} \int\limits_{(n-1)T}^{nT} P_{sc}(t)\, dt, \quad n = 1, 2, \ldots \quad . \tag{5.2.5}$$

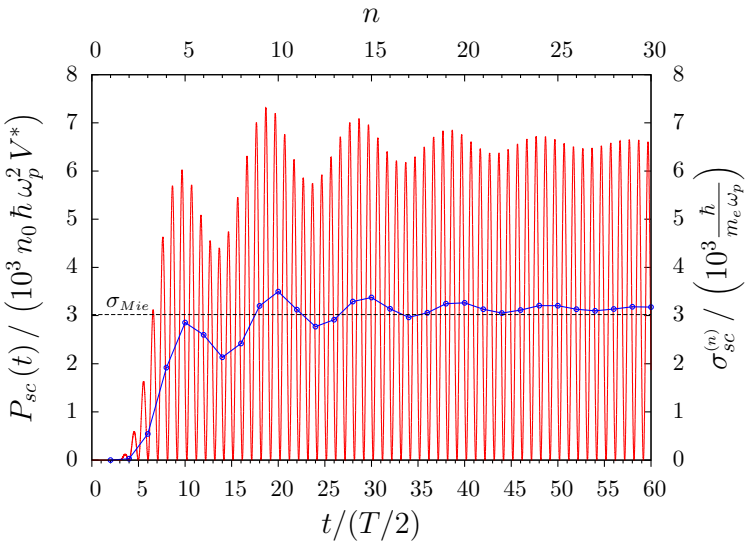

Figure 5.2.2: Scattered power $P_{sc}(t)$ (red, solid) through the surface of an imaginary sphere of radius $R' = 1.1\lambda$ as a function of time. Here, P_{sc} is measured in units of $n_0\hbar\omega_p^2 V^*$, where $V^* = (\hbar/(m_e\omega_p))^{(3/2)}$ is the plasma unit of volume. The power corresponds to the field calculation as demonstrated in Fig. 5.2.1. In addition, the sequence $\sigma_{sc}^{(n)} = P_{sc}^{(n)}/I_0$ is plotted (blue, dotted), where $P_{sc}^{(n)}$ is the time average of P_{sc} with respect to the n-th laser cycle. The horizontal line (black, dashed) indicates the Mie scattering cross section σ_{Mie} for the same cluster radius $R = 100$. For large n, $\sigma_{sc}^{(n)}$ converges to the scattering cross section σ_{sc}. It is shown that σ_{sc} is close to the Mie result.

Then, σ_{sc} and σ_{abs} are given by

$$\sigma_{sc} = \lim_{n\to\infty} \frac{P_{sc}^{(n)}}{I_0}, \quad \sigma_{abs} = \lim_{n\to\infty} \frac{P_{abs}^{(n)}}{I_0}. \tag{5.2.6}$$

The sequence $\sigma_{sc}^{(n)}$ is also plotted in Fig. 5.2.2. It is shown that $\sigma_{sc}^{(n)}$ approaches a limit σ_{sc} for large n. This limit is close to the corresponding Mie result σ_{Mie} calculated with (5.1.19), where the electrostatic plasmon damping rate is given by $\gamma_0 = 0.0096$ for the value of $R = 100$ under consideration. The relative deviation of the self-consistent result from the Mie result is given by approximately 5%. It is concluded that Mie's theory can describe the self-consistent jellium results in the regime of large clusters to a good approximation.

Now, the focus is put on the transition regime between small clusters where quantum-size effects dominate and large clusters where radiative effects become significant. For this purpose, the plasmon damping rate γ of the Mie plasmon is studied as a function of R. As in Chapter 4, the numerical values of γ within the SSVM are extracted by studying the exponential decay of the c.m. Here, the laser field is switched off at a certain time T_{off}. The result is shown in Fig. 5.2.3 together with the electrostatic result $\gamma_0(R)$ of Chapter 4. Additionally, the result of the Mie-Drude theory is plotted, which is calculated as described in Subsection 5.1.2.

It is visible that both the Vlasov-Maxwell and the Mie result (by construction) ap-

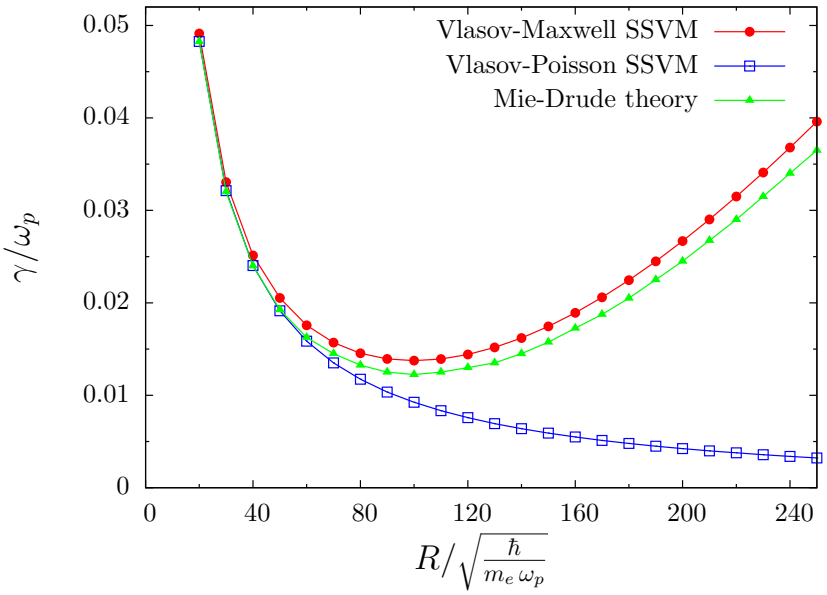

Figure 5.2.3: Damping rate γ of the Mie plasmon as a function of the cluster radius R. The figure shows the present results of the Vlasov-Maxwell theory. In addition, the corresponding electrostatic result of the Vlasov-Poisson theory is presented (see Subsection 4.4.2) as well as that of Mie's theory (see Subsection 5.1.2) evaluated with a Drude-like dielectric function $\epsilon(\nu, \omega)$. For the collision frequency ν, the electrostatic SSVM result is introduced. It is shown that the inclusion of retardation effects by the Vlasov-Maxwell theory leads to an increase of γ with respect to the electrostatic result for large cluster radii (radiation damping). The Mie result is in qualitative agreement with the Vlasov-Maxwell result in the transition regime between quantum-sized clusters and large clusters.

proach the electrostatic result for small clusters. For increasing values of R, the Vlasov-Maxwell value for γ deviates from the electrostatic result, which is due to the growing influence of radiation damping on the plasmon dynamics for large values of R [13, 14]. The interplay of surface effects and radiative effects leads to a local minimum of γ [60, 124] at $R \approx 100$ (8nm). For large clusters, the radiative decay dominates, which results in an increase of γ for $R \gtrsim 100$.

The performed calculations have shown that a reduction of n_0 yields a shift of the local minimum towards larger values of R, indicating a weaker influence of radiation damping for a fixed value of R. This observation can be explained qualitatively by the reduction of the Mie frequency ω_M for decreasing values of n_0. The radiated power of a Hertzian oscillating dipole is proportional to the fourth power of the oscillation frequency [8]. Since ω_M decreases as n_0 decreases, the radiated power is reduced. The reduction of the radiated power results in a slower conversion of the c.m. energy into radiant energy.

Finally, it is noted that the Mie-Drude result is in qualitative agreement with the Vlasov-Maxwell result in the transition regime between quantum-sized clusters and large clusters. In particular, it can reproduce the position of the local minimum rather

accurately. In the local minimum, the Mie-Drude value of γ deviates from that of the Vlasov-Maxwell theory by roughly 10%.

5.2.2 Inhomogeneous Ion Background

The propagation of an EM wave into a plasma is strongly influenced by the density of the plasma. The critical density n_{cr} defines the density at which the local plasma frequency $\omega_p(n_{cr})$ equals the frequency of the EM wave. As the plasma density exceeds the critical density, the wave cannot propagate inside the plasma and it is therefore reflected near the critical density. If the plasma density within the surface becomes inhomogeneous, the plasma can absorb EM field energy locally at the critical density. This absorption mechanism is associated with the excitation of electrostatic plasma waves at the critical density. For a plane surface and p-polarized light, the absorption coefficient depends on the density gradient length L_{cr} at the critical density and the angle of incidence of the incoming EM wave [76].

In this subsection, the previously mentioned absorption mechanism is investigated for spherical clusters with an inhomogeneous radial surface profile. For this purpose, the ion density is modeled by a Fermi function,

$$n_{ion}(r) = \frac{1}{1 + e^{((r-R)/\delta)}}. \tag{5.2.7}$$

The inhomogeneity scale length δ determines the smoothness of the surface profile.

To study the dynamics of the cluster based on the perturbation theory of Subsection 5.1.3, one has to calculate the equilibrium wave function $\varphi^{(0)}$ of the SSVM for the ion profile (5.2.7). For the values of R considered in this subsection, the corresponding equilibrium density $n^{(0)}$ is rather close to n_{ion}.

As in the previous subsection, the cluster is excited by an external plane electromagnetic wave, which travels along the z-axis. The results of this subsection are presented for a frequency of $\omega = 1/\sqrt{2}$, which corresponds to a wavelength $\lambda = 1853.66$ (149.3nm) in the ultraviolet (UV) regime. Laser wavelengths in the UV regime can be achieved e.g. by free-electron lasers [128] or excimer lasers [129]. The critical density of the light wave is determined by the relation $n_{cr} = \omega^2$ (plasma units), which gives $n_{cr} = 1/2$ for the above frequency. According to (5.2.7), this value of the density is achieved at a radial distance $r_{cr} = R$. It is mentioned that in this subsection the focus is put on the regime $\delta < R \lesssim \lambda$, which justifies the present EM treatment of the scattering problem.

Now, simulation results are presented for the laser-cluster interaction. To investigate the influence of the diffuse surface profile on the laser-driven cluster dynamics, the time evolution of the electron density is considered. Figure (5.2.4) shows snapshots of the density perturbation $n^{(1)}$ in the xz-plane for cluster parameters $R = 500$ (40.3nm) and $\delta = 40$ (3.2nm), where $R/\lambda = 0.27$. For better illustration, white circles are added to the snapshots to indicate the surface of an imaginary sphere on which the equilibrium density equals the critical density n_{cr} (critical surface). For the present simulation, $l_{max} = 4$ multipole orders have to be propagated in order to observe convergence of the numerical results.

First of all, one recognizes that the dynamics of $n^{(1)}$ takes place mainly in the underdense region $r \gtrsim R$ where $n^{(0)}$ is smaller than n_{cr}. At time $t = 2.7$, the system is still close to the equilibrium state. Due to the variation of the electric field inside the particle, one can observe a spatially inhomogeneous polarization pattern close to the critical density. In particular, at time $t = 5.4$, it is visible that in the region $x \lesssim -0.4$ where the electric field points in the positive x-direction, electrons are pushed in the negative x-direction, which yields a lack of electrons (inner blue arc) close to the upper half of the critical sphere. The opposite behavior of the surface polarization can be observed for $x \gtrsim -0.4$. Here the electric field vector points in the negative x-direction, which leads to a lack of electrons close to lower half of the critical surface.

The snapshots demonstrate that the density perturbations generated at the critical density travel away from the particle in form of a plasma wave. The wavelength of the wave becomes smaller in the course of time. The author has confirmed that for large times t a stationary wave pattern is generated that is characterized by a harmonic oscillation of the density perturbation $n^{(1)}$ with the laser frequency ω. The convergence behavior turns out to be strongly influenced by the inhomogeneity scale length δ. For the simulation results in Fig. 5.2.4, a stationary wave pattern is achieved after approximately 20 laser periods. In particular, at $t = 21.6$, a clear wave pattern can be observed around the critical surface.

It is noted that the behavior of the present plasma waves is different to that of volume plasmons in small quantum-sized clusters (see Subsection 4.3.3). While volume plasmons are located in the interior region of the cluster, the present plasma waves are generated at the critical density and propagate into the exterior region of the cluster.

In Fig. 5.2.4, it visible that the excitation of plasma waves is favored at the poles of the critical sphere. This is related to the fact that at these points the electric field vector of the light wave is parallel to the surface normal of the critical sphere. In contrast to that, one can see that the excitation of plasma waves is suppressed close to the points $(0, 0, -R)$ and $(0, 0, R)$ on the critical surface. Here, the electric field vector of the light wave is perpendicular to the surface normal of the critical sphere, which corresponds to normal light incidence where the light wave is completely reflected at the critical density [76].

To characterize the plasma waves of Fig. 5.2.4 in more detail, the focus is put on the internal EM field. In particular, their influence on the self-consistent fields $\phi(\boldsymbol{r}, t)$ and $\boldsymbol{A}_{int}(\boldsymbol{r}, t)$ is investigated. Within the present linearized description, the potentials are determined by radial functions $\phi_{l+}(r, t)$ and $A^{(a)}_{l+}(r, t)$ via the expansion (5.1.27). Several radial parts ϕ_{l+} and $A^{(a)}_{l+}$ are plotted in Fig. 5.2.5 for the previously presented simulation (see Fig. 5.2.4) at the end of the simulation time ($t = 25T$).

First, comparison is made between the numerical result of Fig. 5.2.5 for ϕ_{l+} and the analytical result (4.3.1) of Mie's theory in the limit of small cluster sizes. While ϕ_{1+} increases linearly for $r \ll R$ where the equilibrium density is almost homogeneous, ϕ_{2+} shows a quadratic dependence on the radial distance in accordance with (4.3.1). However, the behavior close to the critical density ($r \approx R$) is quite different. While approaching the critical density from the interior, one can observe a rapid increase of ϕ_{2+} and a drop of ϕ_{1+}. This rapid spatial variation with respect to r is associated with strong internal electric fields near the critical surface.

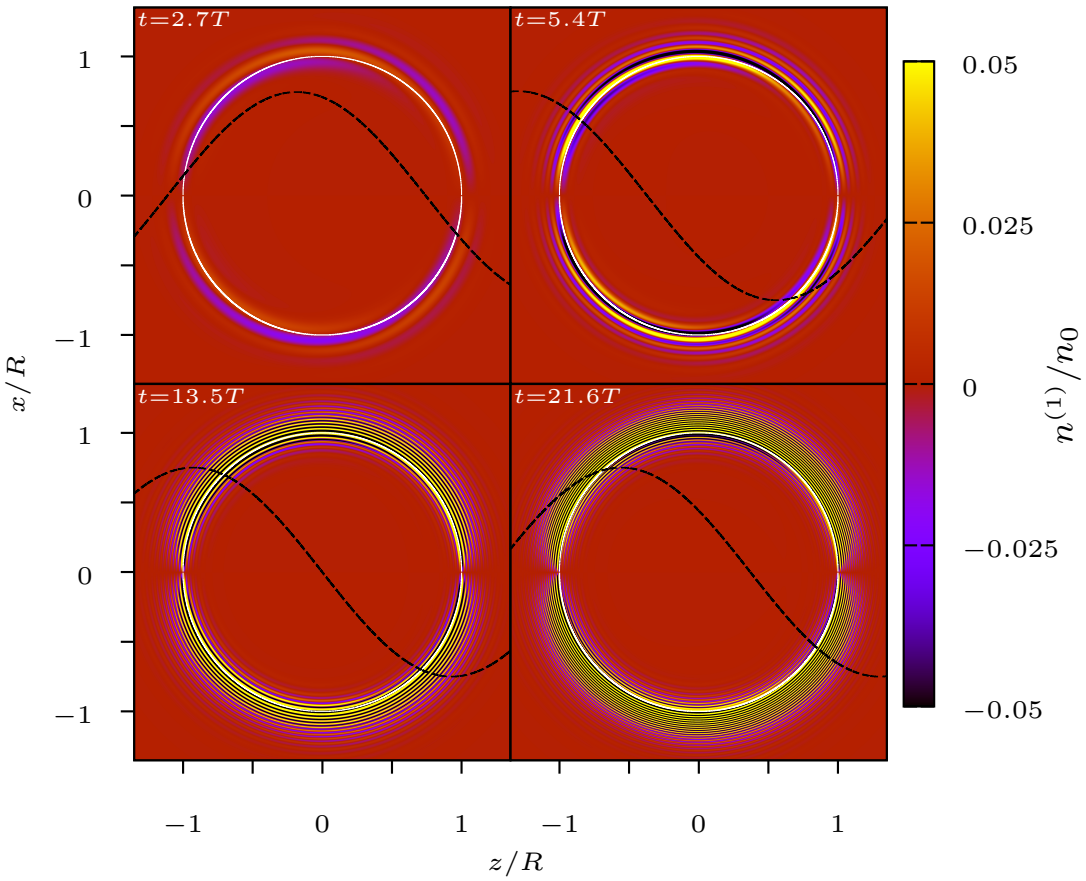

Figure 5.2.4: Density perturbation $n^{(1)}$ in the xz-plane as a function of time. The cluster ($R = 500$, $\delta = 40$, $n_0 = 10^{23}/\mathrm{cm}^3$) is irradiated by a linearly polarized plane electromagnetic wave at frequency $\omega = 1/\sqrt{2}$ with an electric field amplitude of $\mathcal{E}_0 = 0.1$. The plane wave travels along the z-axis and its electric field (5.1.22) is polarized along the x-axis (black dashed curve). The white circle indicates the surface of an imaginary sphere with radius $r_{cr} = R$ on which the equilibrium density equals the critical density n_{cr} of the laser. The figure illustrates that the interaction of the laser with the surface inhomogeneity leads to an excitation of plasma waves close to r_{cr}, which propagate into the underdense region with $n < n_{cr}$ away from the cluster.

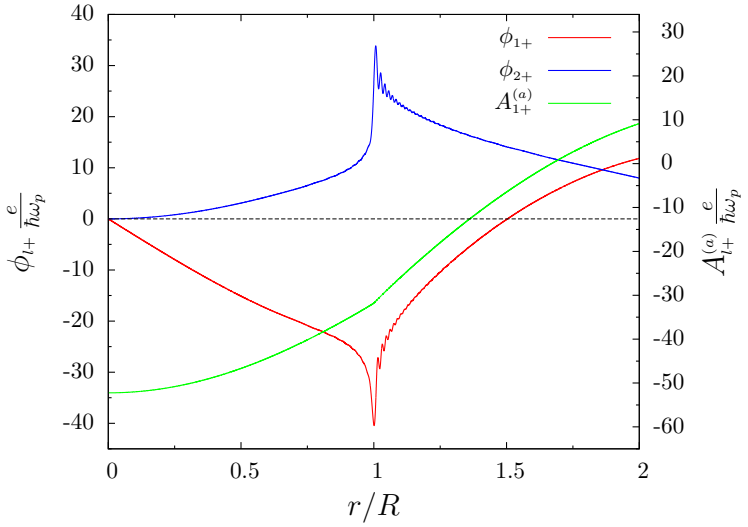

Figure 5.2.5: Radial parts $\phi_{l+}(r,t)$ and $A^{(a)}_{l+}(r,t)$ of the self-consistent potentials for $l=1$ and $l=2$ ($t=25T$). The radial parts define the scalar potential $\phi(\boldsymbol{r},t)$ and the vector potential $\boldsymbol{A}_{int}(\boldsymbol{r},t)$ of the internal EM field via the expansion (5.1.27). The self-consistent potentials are associated with the electron density shown in Fig. 5.2.4. It is demonstrated that the plasma waves generated at the critical density couple to the scalar potential $\phi(\boldsymbol{r},t)$.

Furthermore, oscillations of the radial functions are visible for $r \gtrsim R$. These oscillations are referred to the plasma waves illustrated Fig. 5.2.4 which vary spatially on the same length scale. It is noted that $A^{(a)}_{1+}$ shows a quite different behavior. Here, the function profile is smooth near the surface and shows no signature of the surface excitations. Since the plasma waves couple only to the electrostatic potential, it is concluded that they are purely electrostatic and in analogy with longitudinal electrostatic plasma waves in a homogeneous plasma, which are characterized by the zeros of the dielectric function [114].

The excitation of electrostatic plasma waves at the critical surface is associated with the absorption of laser field energy. In the following, it is investigated how this absorption mechanism depends on the inhomogeneity scale length δ and the radius R of the critical surface. Simulations were performed for cluster parameters of $R=500$ (40.3nm) and $R=1000$ (80.6nm) as a function of the parameter δ. In the latter case, the diameter $D=2R$ is slightly larger than the laser wavelength ($R/\lambda=0.54$) and one has to propagate $l_{max}=7$ multipole orders for convergence of the numerical results. Figure 5.2.6 shows the results for the total scattering efficiency $Q_{sc}=\sigma_{sc}/(\pi R^2)$ and the total absorption efficiency $Q_{abs}=\sigma_{sc}/(\pi R^2)$ as a function of δ. The cross sections can be calculated with (5.2.4) and the procedure described in Subsection 5.2.1. In this way, Q_{sc} and Q_{abs} can be written as a sum over all multipole contributions $Q^{(l)}_{sc}$ and $Q^{(l)}_{sc}$,

$$Q_{sc}=\sum_{l=0}^{\infty}Q^{(l)}_{sc}, \qquad Q_{abs}=\sum_{l=0}^{\infty}Q^{(l)}_{abs}. \tag{5.2.8}$$

Several multipole contributions are also plotted in Fig. 5.2.6 for $R=500$.

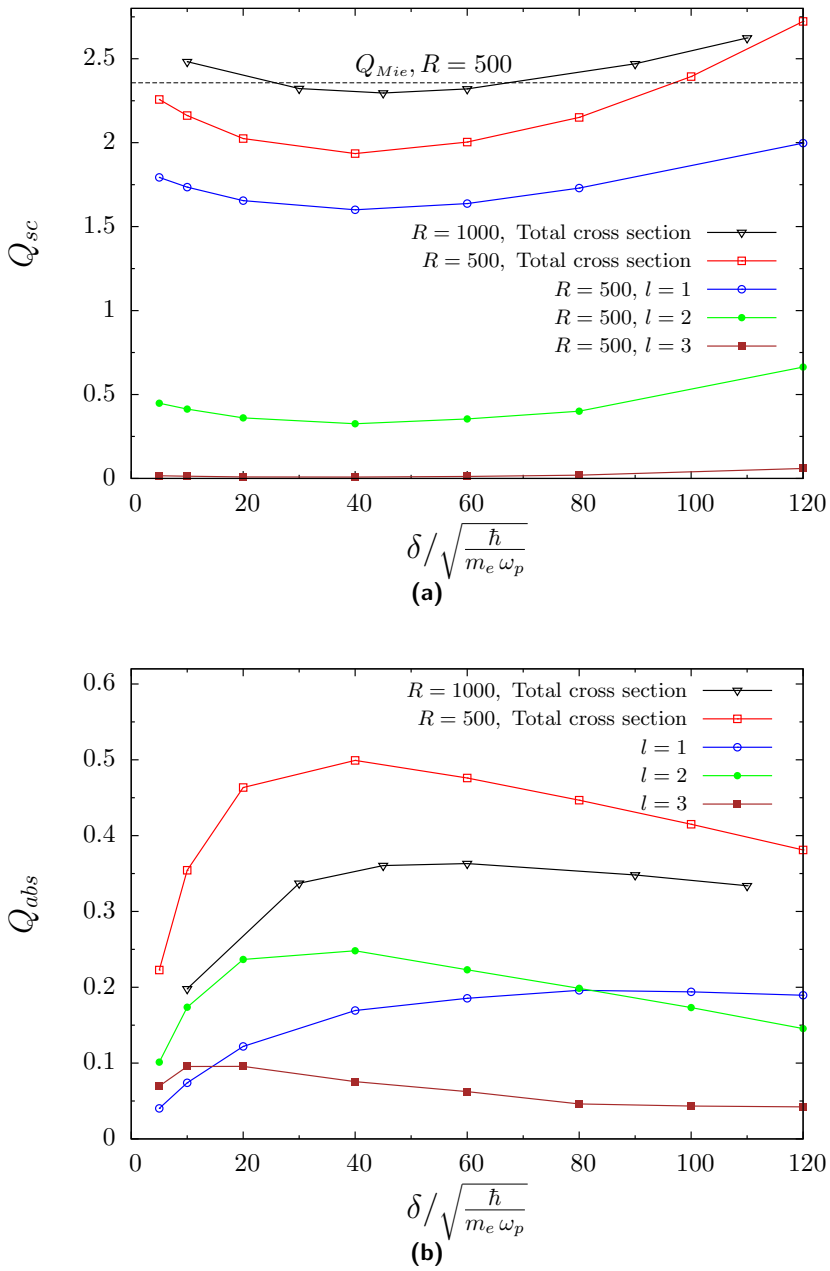

Figure 5.2.6: (a) Scattering efficiency Q_{sc} and (b) absorption efficiency Q_{abs} as a function of the inhomogeneity scale length δ of the ion density (5.2.7). The total cross sections are shown for two radii $R = 500$ (40.3nm) and $R = 1000$ (80.6nm). In addition, several multipole contributions $Q_{sc}^{(l)}$ and $Q_{abs}^{(l)}$ are plotted for $R = 500$. The laser frequency of $\omega = 1/\sqrt{2}$ corresponds to a wavelength of $\lambda = 1853.66$ (149.3nm). A dashed horizontal line indicates the total scattering cross section of the Mie theory ($R = 500$) evaluated with the dielectric function of a free electron gas. The figure illustrates that the total absorption cross section for $R = 500$ exhibits a local maximum at $\delta \approx 40$, while the scattering cross section has a local minimum at the same value of δ. By increasing the particle size, the resonance curve gets broadened and a reduction of Q_{abs} at the local maximum can be observed.

First, the results for $R = 500$ are discussed. For $\delta \to 0$, it is visible that Q_{abs} tends to zero, while Q_{sc} approaches the value Q_{Mie} of Mie's theory. This behavior is consistent with results of the previous subsection, since the limit $\delta \to 0$ corresponds the jellium description. For this case, it was demonstrated that the Mie theory gives rise to a good approximation of the self-consistent result for the scattering cross section. Moreover, since quantum-size effects are small ($\gamma_0 \approx 0$) for the considered value of R in the limit $\delta \to 0$, the incoming laser energy is totally reflected by the cluster ($Q_{abs} = 0$).

As the parameter δ is increased, Q_{abs} increases as well up to a local maximum at $\delta \approx 40$ with $Q_{abs} \approx 0.5$. Here, the ratio δ/R is roughly 10%. For larger values of δ, Q_{abs} decreases almost linearly between $\delta = 60$ and $\delta = 120$. Besides the maximum of Q_{abs}, Figure 5.2.6b also shows that the multipole contributions $Q_{abs}^{(l)}$ exhibit individual local maxima, where the maximum becomes rather broad in the case $l = 1$. Based on the rapid increase of $Q_{abs}^{(2)}$ for small values of δ, one can conclude that the resonance of Q_{abs} is largely determined by the contribution of multipole order $l = 2$.

In comparison with Q_{abs}, the scattering efficiency shows an opposite behavior. First, Q_{sc} decreases to a local minimum at $\delta \approx 40$. At this minimum, the value of Q_{sc} is reduced with respect to the Mie value Q_{Mie} by approximately 20%. Here, the deviation of Q_{sc} from Q_{Mie} is close to the corresponding value of Q_{abs}. For $\delta > 40$, Q_{sc} increases again and exceeds the value Q_{Mie} for $\delta \gtrsim 100$. Furthermore, it is noted that the qualitative behavior of the functions $Q_{sc}^{(l)}$ is quite similar for all values of l, where local minima at $\delta \approx 40$ can be observed for all multipole orders.

Summary

In this chapter, the linear scattering and absorption of a plane electromagnetic wave by spherical clusters has been studied on the basis of the EM SVVM for a cluster density $n_0 = 10^{23}/\mathrm{cm}^3$.

In the first step, a homogeneous ion background has been considered. The damping rate of the Mie plasmon increases for small values of R due to the increasing influence of surface scattering. For large R, the damping rate is dominated by radiation damping. The competition of both damping mechanisms leads to a local minimum of the damping rate at a cluster radius of approximately 8nm. It has been confirmed that the self-consistent results for the plasmon damping rate and the cross sections can be described to a good approximation by the Mie-Drude theory.

In the second step, resonance absorption has been investigated for an inhomogeneous ion background with a diffuse surface profile. In this framework, the well-known theory of resonance absorption has been generalized from plane to spherical surfaces with variable angles of incidence and light polarizations along the surface. By studying the absorption efficiency as a function of the inhomogeneity scale length, a local maximum has been found whose position and width depends on the cluster radius. The evolution of the electron density shows the generation of plasma waves close to the critical density which propagate into the exterior region of the cluster. They are accompanied by a rapid increase of the internal electric field at the critical density. The author has convinced that the plasma waves are purely electrostatic since they couple only to the self-consistent scalar potential.

Chapter 6

Nonlinear Electrostatic Model of a Thin Plasma Foil

This chapter summarizes parts of the results which were presented at the twenty fifth annual International Laser Physics Workshop (LPHYS'16) by the author of this thesis. These results have been pre-published in [82]. *Most of the passages in this chapter are quoted almost verbatim from this reference.*

In the previous two chapters, cluster excitations were treated in linear perturbation theory both in the electrostatic quantum-size regime and in the EM radiation-dominated regime. In Chapter 7, the electrostatic description of quantum-sized clusters is generalized to the nonlinear regime of cluster excitations. Since the nonlinear simulations in spherical geometry require rather long computation times, it turned out to be instructive to perform a pre-study by considering the corresponding problem for plane geometry in one spatial dimension (1d) [79]. This ansatz can be helpful in order to capture essential nonlinear processes with less numerical effort and to get an estimate on how the numerical parameters have to be chosen in the nonlinear regime.

The electron-ion system in 1d is associated with a plasma foil of width l. In this chapter, the interaction of thin plasma foils with an external laser field is investigated. The laser field is considered to be obliquely incident on the foil surfaces. The classical Brunel theory [77] describes the nonresonant collisionless energy absorption of a plane metal surface by electrons which are pulled into the vacuum and accelerated in the presence of the laser field. This mechanism dominates the absorption of laser energy if the metal has a sharp surface and an electron density well above the critical density. Within the linear description of the previous chapter, it was demonstrated for spherical particles that in this case the laser energy is completely scattered. In contrast to that, the Brunel mechanism is a nonlinear mechanism that is closely related to outer ionization [19]. Brunel's theory predicts a characteristic scaling $E_{abs} \sim \mathcal{E}_0^3$ of the absorbed energy with the electric field amplitude $\mathcal{E}_0$ of the laser. The corresponding mechanism has been analyzed classically for clusters [78] and for foils with two surfaces in the framework of a 1d capacitor model [80, 130]. However, if the foil thickness approaches the nanoscale, quantum-size effects of the absorption are expected to become relevant which refer to the spill-out effect of the electron density at the foil surface and which have not been treated so far. In this chapter, it is investigated how Brunel's scaling law is affected by quantum effects in thin plasma foils.

Now, the basic equations of this chapter are introduced. By considering the usual Vlasov-Poisson system (2.3.3) in 1d, it turned out that the relaxation method (see

Chapter 3) for the calculation of the electron equilibrium does only converge properly for $N_s = 1$ (SSVM). For a multistream description with $N_s > 1$, convergence could only be achieved by excluding the self-interaction term in (2.3.3b), which becomes a small perturbation for large values of N_s. Due to this fact, the multistream calculations of this chapter are performed without the self-interaction term. Then, each electron state sees an individual self-consistent potential $\phi_k(x,t)$ and the basic equations for N_s representative states $\varphi_k(x,t)$ in 1d read ($N_s > 1$)

$$i\partial_t \varphi_k = \left[-\partial_x^2 - \phi_k - \phi_{ext}\right] \varphi_k, \tag{6.0.1a}$$

$$\partial_x^2 \phi_k = \sum_{k' \neq k} w\,|\varphi_{k'}|^2 - \theta(l/2 - |x|), \tag{6.0.1b}$$

where ϕ_{ext} is an external laser potential in the dipole approximation and $w = 1/N_s$. In the dimensionless representation (6.0.1), the states φ_k are normalized to the length of the foil in plasma units, $\langle\varphi_k|\varphi_k\rangle = l$. It is noted that the system (6.0.1) corresponds to the well-known Hartree theory of an interacting electron system.

The SSVM for the representative state $\varphi(x,t)$ and the self-consistent potential $\phi(x,t)$ in 1d reads

$$i\partial_t \varphi = \left[-\partial_x^2 - \phi - \phi_{ext}\right] \varphi, \tag{6.0.2a}$$

$$\partial_x^2 \phi = |\varphi|^2 - \theta(l/2 - |x|). \tag{6.0.2b}$$

The time propagation of the wave functions is done by the Crank-Nicolson finite-difference method [95, 96] on a computational grid. The potentials are calculated on the same grid by using central differences [97] and LU decomposition [98].

In Section 6.1, the equilibrium states of the Hartree model and the SSVM are introduced. Subsequently, both models are compared in Section 6.2 by studying the dynamics of the foil in the presence of a laser field. Finally, the energy absorption of the foil is studied as a function of the laser field strength in Section 6.3.

6.1 Equilibrium States

The equilibrium states of (6.0.1) and (6.0.2) can be calculated with the help of a relaxation method by analogy with Chapter 3. Figure 6.1.1 shows the equilibrium densities

$$n^{(0)} = \sum_k w\,|\varphi_k^{(0)}|^2 \tag{6.1.1}$$

for a foil of thickness $l = 50$. Comparison is made between the SSVM and the Hartree model for different values of N_s. Furthermore, results for the self-consistent potentials $\phi_k^{(0)}$ in the equilibrium state are plotted in Fig. 6.1.2.

As depicted, the electron density within the Hartree model becomes homogeneous inside the foil as N_s is chosen sufficiently large. In this case, the equilibrium density is close to the corresponding SSVM result. For smaller values of N_s, the Hartree density shows pronounced local maxima. Each maximum is associated with the contribution of a representative state $\varphi_k^{(0)}$ to the total density, where the states $\varphi_k^{(0)}$ are strongly localized in contrast to the equilibrium state $\varphi^{(0)}$ of the SSVM.

The self-consistent potential of the SSVM exhibits two pronounced minima close to the foil surface, which generate the binding of the electrons. Within the Hartree model, each state sees an individual potential with a single local minimum around which it is centered. As one can see, the potential $\phi_k^{(0)}$ is a linear function of x far away from electron state k. This fact is related to the 1d nature of the underlying model. In 1d, a localized charge distribution $\rho(x)$ with total charge q generates a constant electric field $|\mathcal{E}| = |q|/2$ far away from the charge distribution. Since a Hartree state sees a charge distribution with total charge $q = l/N_s > 0$, an outgoing electron will be accelerated back to the foil. However, this effect of the 1d description becomes small if N_s is chosen sufficiently large.

For small values of l, the spill-out effect of the electron density becomes significant. Figure 6.1.3 shows the fraction f_{out} of spill-out electrons as a function of the foil thickness (SSVM calculation). For $l = 5$, 13% of the electrons are located outside the foil in the equilibrium state. For $l \gtrsim 5$, it is found that f_{out} scales with the inverse foil thickness. A fit to the data points with $l \gtrsim 5$ by using the model function $f_{out}(l) = \alpha/l^\beta$ yields the values $\alpha = 0.659$ and $\beta = 0.997$. This result can be compared with the three-dimensional cluster result of Subsection 4.4.2. By making the replacement $l = D$, where $D = 2R$ is the diameter of the corresponding cluster, one finds that f_{out} is three times smaller for a foil. The increase of f_{out} with the spatial dimension can be expected by considering the additional surfaces of a cubical volume.

As shown in Fig. 6.1.1a, the Hartree states $\varphi_k^{(0)}$ are localized states, which are centered around the corresponding spatial expectations values $\langle x \rangle_k$. To get a more precise interpretation of the states $\varphi_k^{(0)}$ and to compare the results with corresponding classical calculations, analytical solutions are calculated for $\varphi_k^{(0)}$ in the limit of small values of N_s such that $N_s/l \to 0$. Here, the overlap of the states $\varphi_k^{(0)}$ becomes small and the functions can be treated as well separated. Then, the potentials $\phi_k^{(0)}$ can be calculated with the help of the following consideration: Assume a symmetric charge distribution $\rho(x)$ with extension d and total charge q which is centered around a point $x = x'$,

$$\rho(x) = \begin{cases} 0, & |x - x'| > d/2, \\ \neq 0, & |x - x'| < d/2. \end{cases} \tag{6.1.2}$$

By choosing the gauge $\phi(x') = 0$, the potential $\phi(x)$ outside the charge distribution reads

$$\phi(x) = \begin{cases} \frac{1}{2}qx + C, & x < x' - d/2, \\ -\frac{1}{2}qx + C, & x > x' + d/2, \end{cases} \quad C \in \mathbb{R}. \tag{6.1.3}$$

By assuming that the state $\varphi_k^{(0)}$ is symmetric with respect to a certain point $x = x_k$

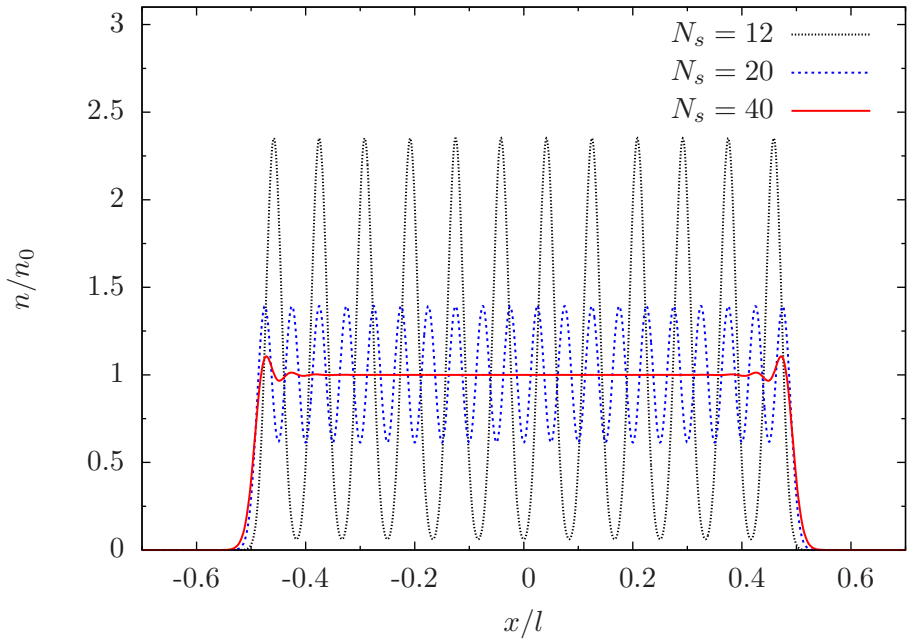

(a)

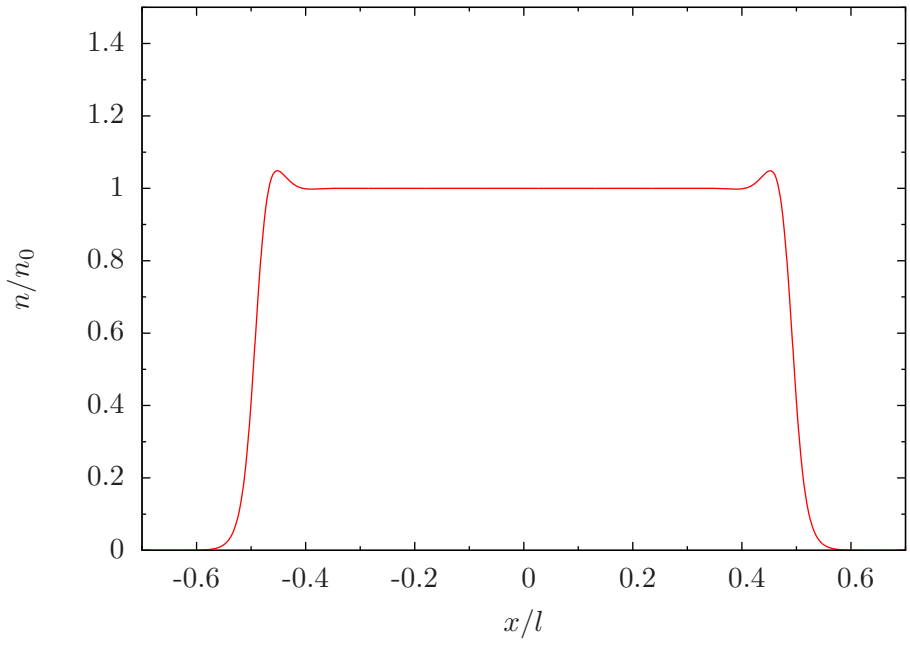

(b)

Figure 6.1.1: Equilibrium densities for a foil of thickness $l = 50$. Results are shown for (a) the Hartree model and (b) the single-state Vlasov model (SSVM). The Hartree results are shown for various values of N_s, where N_s is the number of electron states. It is shown that the Hartree result for the electron density is close to the SSVM result as the value of N_s is chosen sufficiently large.

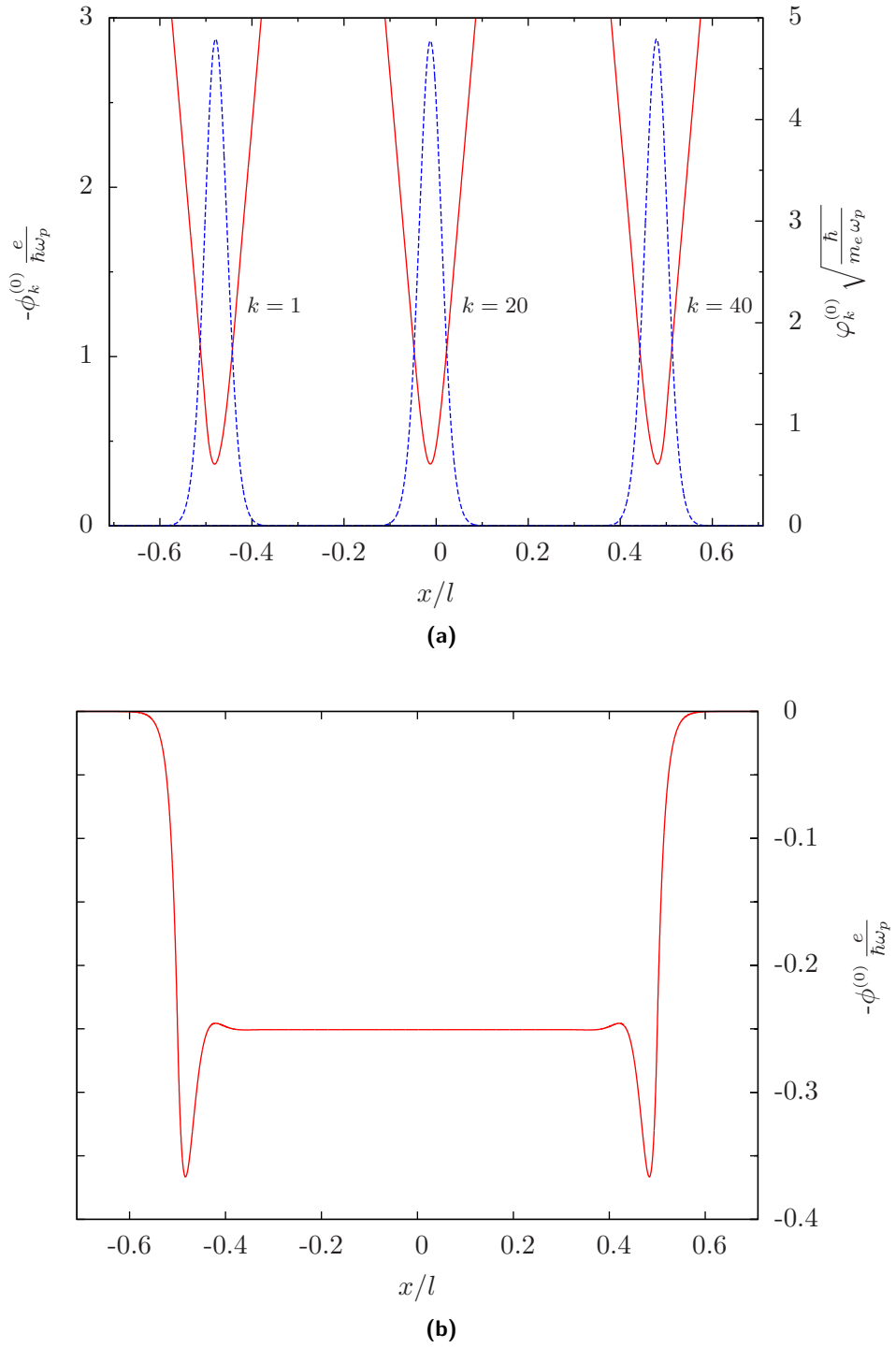

Figure 6.1.2: Self-consistent potentials in the equilibrium state for a foil of thickness $l = 50$. The results are shown for (a) the Hartree model with $N_s = 40$ representative states and (b) the single-state Vlasov model. In 6.1.2a, corresponding equilibrium wave functions $\varphi_k^{(0)}$ are plotted (dashed curves).

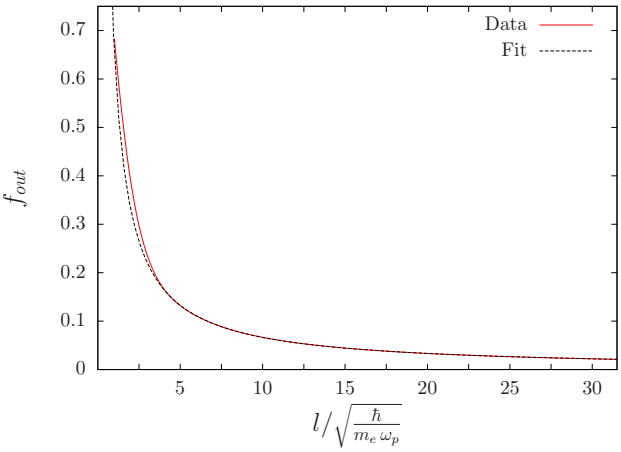

Figure 6.1.3: Fraction f_{out} of spill-out electrons as a function of the foil thickness l. The data points are fitted to the inverse power law $f_{out} = 0.659/l^{0.997}$.

and by using (6.1.3), the potential $\phi_k^{(0)}$ close to the point $x = x_k$ is given by

$$\begin{aligned}\phi_k^{(0)} &= \sum_{i=1}^{k-1} \frac{l}{2N_s} x - \sum_{i=k+1}^{N_s} \frac{l}{2N_s} x + (N_s - 1)C - \phi_{ion} \\ &= -l\frac{N_s - 2k + 1}{2N_s} x + (N_s - 1)C + \phi_{ion}.\end{aligned} \tag{6.1.4}$$

Here, it was used that each state contributes with a charge of $q = -l/N_s$ to the total charge of the electrons. In the considered limit $N_s/l \to 0$, all electron states are located inside the foil and the ion potential can be approximated by the corresponding potential inside the foil, $\phi_{ion} = -(1/2)x^2$. With the definitions

$$x_k = -l\frac{N_s - 2k + 1}{2N_s}, \quad D = (N_s - 1)C - \frac{1}{2}x_k, \tag{6.1.5}$$

the equilibrium potential (6.1.4) of electron state k reads

$$\phi_k^{(0)} = \frac{1}{2}(x - x_k)^2 + D. \tag{6.1.6}$$

In conclusion, each equilibrium state sees a shifted harmonic potential, which is centered around $x = x_k$. Therefore, the equilibrium functions $\varphi_k^{(0)}$ are coherent states which are separated by a distance of $l/N_s \gg 1$,

$$\varphi_k^{(0)}(x) = \frac{1}{\sqrt[4]{\pi}}\, e^{-(x-x_k)^2/2}. \tag{6.1.7}$$

This asymptotic result suggests that the Hartree model (6.0.1) can be interpreted as the quantum-mechanical analog of the classical particle model defined in [80], where the equation of motion of the point charge k has to be replaced by the Schrödinger equation for the wave function φ_k.

In the following, the plasma foil is exposed to a laser field. Before the interaction with the laser at $t = 0$, the electron system is considered to be in the equilibrium state.

6.2 Comparison of Hartree and Single-State Vlasov Model

The numerical calculation of the electron dynamics in the presence of strong laser fields requires on the one hand large spatial grids to account for fast electrons moving far away from the foil and on the other hand small numerical grid constants with respect to the time variable to resolve their dynamics. These requirements are already present in classical PIC calculations. Since the present quantum-mechanical description furthermore requires small spatial grid constants to resolve the spatial variation of the wave functions, calculations with large N_s become time-consuming for high laser intensities. Since one is interested in macroscopic quantities like the absorbed energy per electron, it is an instructive task to analyze two major questions. Does the dynamics of the electron system converge if the number of electron states N_s is chosen sufficiently large? If yes, is the SSVM capable of describing the main features of the energy absorption? In particular, the last point is of great interest since calculations within the SSVM are numerically feasible to perform calculations over a wide range of laser and foil parameters.

In order to investigate the above questions, test calculations were performed within the Hartree model for different values of N_s and the SSVM in the presence of a strong laser field compared with the electric field that is generated by the ions. In the following, a sine-square pulse with n laser cylces, frequency $\omega = 2\pi/T$ and pulse duration $\tau = nT$ is considered,

$$\phi_{ext}(x,t) = -x\mathcal{E}(t), \quad \mathcal{E}(t) = \mathcal{E}_0 \sin(\pi t/\tau)^2 \sin(\omega t). \tag{6.2.1}$$

The average total energy E_{tot} of the foil per electron is given by

$$\frac{E_{tot}}{N_e} = w \sum_{k=1}^{N_s} \frac{\langle\varphi_k|E_k|\varphi_k\rangle}{\langle\varphi_k|\varphi_k\rangle} + \frac{E_{ion}}{N_e}, \tag{6.2.2}$$

$$E_k = T + V_k, \quad T = -\frac{1}{2}\frac{\partial^2}{\partial x^2}, \quad V_k = -\phi_{ion} - \frac{1}{2}\phi_k^{(ee)}, \tag{6.2.3}$$

where E_{ion} is the potential energy of the ion system, which is a constant value within the present jellium approximation. The potential $\phi_k^{(ee)}$ is the electron-electron interaction part of the self-consistent potential, which is related to ϕ_k by the relation $\phi_k = \phi_{ion} + \phi_k^{(ee)}$. It is noted that the prefactor 1/2 in the definition of the potential energy V_k has to be taken into account in order to avoid double-counting of the electron-electron interaction energy.

For the following test calculations, a foil with $l = 10$ is considered. The calculations are performed over a wide range of N_s-values. Therefore, a sufficiently short single-cycle pulse ($n = 1$) with $\omega = 0.125$ and $\mathcal{E}_0/\mathcal{E}_{ion} = 40\%$ is chosen in order to make the calculations numerically feasible. Here, $\mathcal{E}_{ion} = l/2$ is the maximum field strength of the ions, which is achieved at the foil boundary. Figure 6.2.1 shows the dynamics of the c.m. $X(t)$ as a function of time, which is calculated based on the relation

$$X(t) = w \sum_{k=1}^{N_s} \frac{\langle\varphi_k|x|\varphi_k\rangle}{\langle\varphi_k|\varphi_k\rangle}. \tag{6.2.4}$$

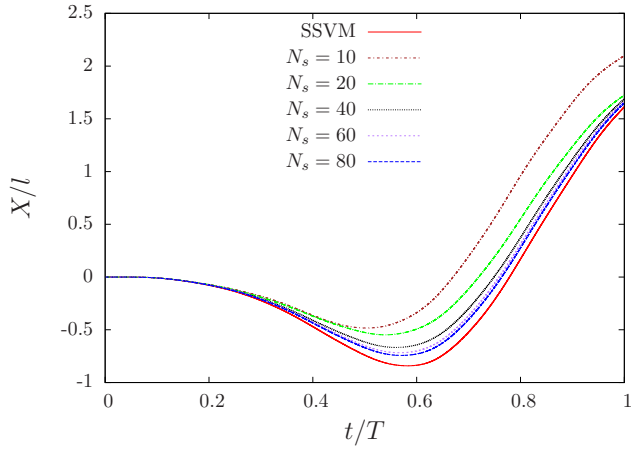

(a)

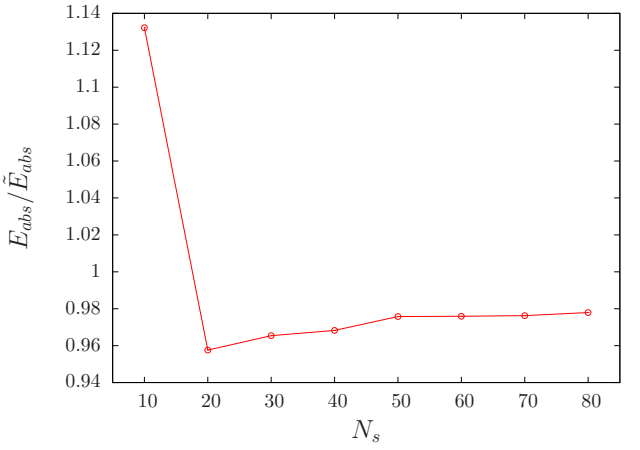

(b)

Figure 6.2.1: (a) Motion of the center of mass $X(t)$. (b) Absorbed energy E_{abs} (laser parameters: $n = 1$, $\omega = 0.125$, $\mathcal{E}_0/\mathcal{E}_{ion} = 40\%$). In (a), the results are shown for various numbers of electron states within the Hartree model. In addition, the result of the single-state Vlasov model (SSVM) is plotted. In (b), the absorbed energy is measured in units of the SSVM result $\tilde{E}_{abs}$. It can be seen that the Hartree results are close to the SSVM result for large values of N_s.

In addition, the absorbed energy per electron $E_{abs} = (\, E_{tot}(\tau) - E_{tot}(0)\,)/N_e$ is plotted against N_s. For the value of $\mathcal{E}_0$ considered, grid constants of $\Delta x \lesssim 0.01$ and $\Delta t \lesssim 0.001$ have to be chosen in order to observe convergence of the numerical solution. To avoid boundary effects driven by outgoing electrons, one has to choose a spatial grid with about 10^5 grid points.

Figure 6.2.1a shows that the electrons are pulled in the negative x-direction within the first half of the laser cycle where a large number of electrons leave the foil. Within the second half of the cycle, the electrons are accelerated back to the foil and gain enough energy to move through the foil. A large displacement of the electron system with respect to the equilibrium state can be observed at the end of the pulse. Since

the laser frequency is well below the resonance frequency $\omega_p = 1$ (plasma units), the large final displacement is related to the larger quiver amplitude of outgoing electrons, which feel a restoring force that differs from the harmonic restoring force inside the foil.

As depicted in Fig. 6.2.1b, the absorbed energy deviates from the SSVM result by more than 10% for the smallest value of $N_s = 10$ considered. In this case, the equilibrium densities look quite different within both descriptions (see Fig. 6.1.1). However, for $N_s > 10$, one can see that the deviation of the absorbed energy becomes less than 5% and varies only slightly over the range of N_s-values considered. For the largest value of $N_s = 80$, the Hartree result differs from the SSVM result by approximately 2%. Therefore, it is concluded that the SSVM captures the main features of the energy absorption to a good approximation for sufficiently high laser intensities.

6.3 Energy Absorption in the Presence of a Laser Field

In this section, the energy absorption of a thin foil is studied as a function of the field strength $\mathcal{E}_0$ of the laser. Brunel described the nonresonant electron dynamics at a single sharp metal surface by an ensemble of single-particle trajectories interacting via an electrostatic potential [77]. As a major result, it was found that the absorbed energy of the surface per electron can be written in the form

$$\frac{E_{abs}}{N_e} = \frac{1}{2}\,\eta\,\frac{\mathcal{E}_0^3}{\omega^2}\,\frac{1}{l}, \tag{6.3.1}$$

where η is a numerical constant which depends on the pulse duration τ. It should be noted that the result of Brunel as given in (6.3.1) corresponds to plasma units (see Table 2.3.1), where the length dependence is due to these units. The corresponding absorption mechanism, known as vacuum heating, has been analyzed classically for a foil with two sharp surfaces [80]. It was found that the absorbed energy can be represented by a scaling law similar to (6.3.1), but with a different numerical value for η. From a classical point of view, the characteristic scaling of the absorbed energy with the third power of $\mathcal{E}_0$ can be motivated based on the assumption that the energy absorption is mainly driven by electrons which leave the foil. Since the quantum-mechanical results of this chapter are compared with the classical results of Brunel, the main points are shortly summarized. For the estimation of the absorbed energy, the c.m. motion is approximated by the equation of motion without surface effects,

$$\ddot{X} + X = -\mathcal{E}(t). \tag{6.3.2}$$

In the nonresonant limit $\omega \ll 1$, the solution reads $X(t) = -\mathcal{E}(t)$, with a maximum displacement of $X_0 = \mathcal{E}_0$. Since the equilibrium density is spatially homogeneous within the classical description, the maximum number N_{out} of electrons leaving the foil over one laser cycle is given by

$$N_{out} = n_0 X_0^\star = \frac{N_e}{l}\mathcal{E}_0, \tag{6.3.3}$$

where $X_0^\star$ is the maximum discplacement in dimensional units and n_0 the density of the electrons at the surface. Electrons which are pulled into the vacuum are accelerated by the laser field and gain an amount of energy proportional to the mean quiver energy $U_p \sim \mathcal{E}_0^2$ of a free electron in a laser field, known as ponderomotive potential. With this consideration, the absorbed energy exhibits a scaling of the form $E_{abs} \sim N_{out} U_p \sim \mathcal{E}_0^3$.

In the following, it is investigated how the energy absorption of a thin foil depends on $\mathcal{E}_0$. Due to the fact that the cycle-averaged absorbed energy is not expected to vary significantly during the main part of the pulse [80], a single-cycle pulse is chosen with frequency $\omega = 0.125$.

Figure 6.3.1 shows the absorbed energy per electron as a function of $\mathcal{E}_0$ for two foils of thickness $l = 5$ and $l = 50$ on a double-logarithmic scale. For $l = 5$, one can clearly identify two ranges of $\mathcal{E}_0$-values where E_{abs} can be represented by scaling laws $E_{abs}/N_e = \alpha\, \mathcal{E}_0^\beta$. The first range covers $\mathcal{E}_0$-values up to $\mathcal{E}_0/\mathcal{E}_{ion} \approx 0.2$, while the second range covers $\mathcal{E}_0$-values larger than this reference value. A fit to the data points yields the parameters $\alpha = 5.65$, $\beta = 3.33$ for the first range and $\alpha = 5.13$, $\beta = 2.98$ for the second range. The resulting fit functions are also indicated in Fig. 6.3.1.

This behavior of E_{abs} is much less pronounced for $l = 50$. Here, two scaling regimes can be identified as well. However, the crossover point is shifted to a much smaller value of $\mathcal{E}_0/\mathcal{E}_{ion} \approx 0.02$ in comparison to $l = 5$. A fit yields the values $\alpha = 0.43$, $\beta = 3.15$ for the first range and $\alpha = 0.4$, $\beta = 3.07$ for the second range.

In summary, for sufficiently large values of $\mathcal{E}_0$, the scaling behavior of E_{abs} is close to that predicted by Brunel's theory ($\beta = 3$) for both foils. However, for the smaller foil, a significant deviation from the classical behavior can be observed over a wide range of $\mathcal{E}_0$-values. Here, the scaling exponent is larger than $\beta = 3$. Since this effect is less pronounced for thick foils, it is concluded that the deviation must be referred to quantum-size effects in thin foils.

To investigate the emergence of the increased scaling exponent for $l = 5$, the focus is put on the number $N_{out}(t)$ of electrons which leave the foil during the laser-foil interaction. As a measure for the fraction of free electrons, the time-averaged fraction $\bar{f}_{out}$ of electrons is calculated which are located outside the foil over the pulse duration,

$$\bar{f}_{out} = \frac{1}{\tau} \int_0^\tau f_{out}(t)\, dt\,, \quad f_{out}(t) = 1 - \frac{1}{N_e} \int_{-\frac{l}{2}}^{\frac{l}{2}} n(x,t) dx, \tag{6.3.4}$$

where $f_{out}(t) = N_{out}(t)/N_e$.

Figure (6.3.2) shows the results for the two foils of thickness $l = 5$ and $l = 50$. In both cases, one clearly identifies a linear dependence of $\bar{f}_{out}$ on $\mathcal{E}_0$ for sufficiently large values of $\mathcal{E}_0$, by analogy with Brunel's classical consideration. For $l = 50$, the linear behavior between $\bar{f}_{out}$ and $\mathcal{E}_0$ can already be observed for $\mathcal{E}_0/\mathcal{E}_{ion} \gtrsim 0.06$, while it requires much stronger fields $\mathcal{E}_0/\mathcal{E}_{ion} \gtrsim 1$ for $l = 5$.

To investigate the increase of $\bar{f}_{out}$ in the range of small $\mathcal{E}_0$-values, a fit is performed to the data with $\mathcal{E}_0/\mathcal{E}_{ion} < 0.2$ by using the model function $\bar{f}_{out}(\mathcal{E}_0) = \alpha\, \mathcal{E}_0^\beta + \delta$.

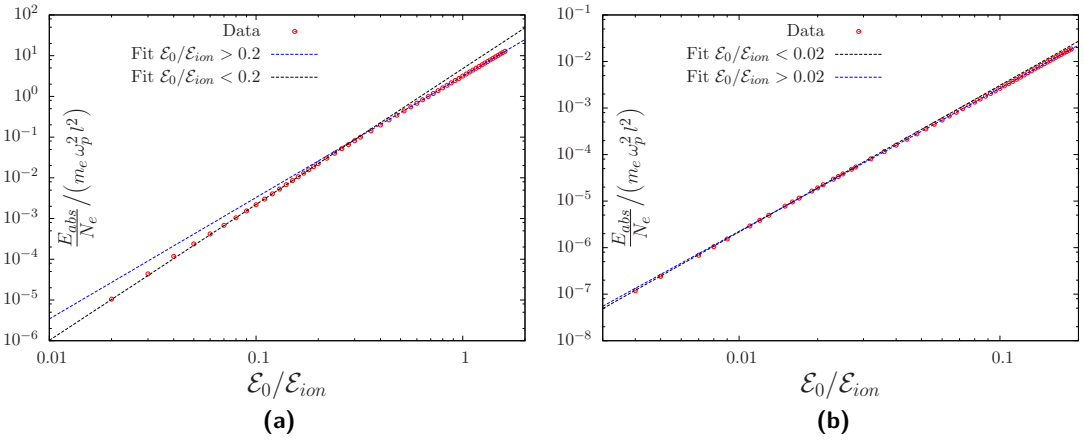

Figure 6.3.1: Absorbed energy per electron as a function of the laser field strength $\mathcal{E}_0$. Results are shown for two foils of thickness (a) $l = 5$ and (b) $l = 50$ (laser parameters: $n = 1$, $\omega = 0.125$). The numerical values of E_{abs} are measured in units of the electron-ion interaction energy $m_e\omega_p^2 l^2$ at the foil boundary. For $l = 5$, the data points are fitted to the power laws $E_{abs} = 5.65\,\mathcal{E}_0^{3.33}$ for $\mathcal{E}_0/\mathcal{E}_{ion} < 0.2$ and $E_{abs} = 5.13\,\mathcal{E}_0^{2.98}$ for $\mathcal{E}_0/\mathcal{E}_{ion} > 0.2$. The crossover point $\mathcal{E}_0/\mathcal{E}_{ion} = 0.2$ is shifted towards smaller values of $\mathcal{E}_0$ as l is increased.

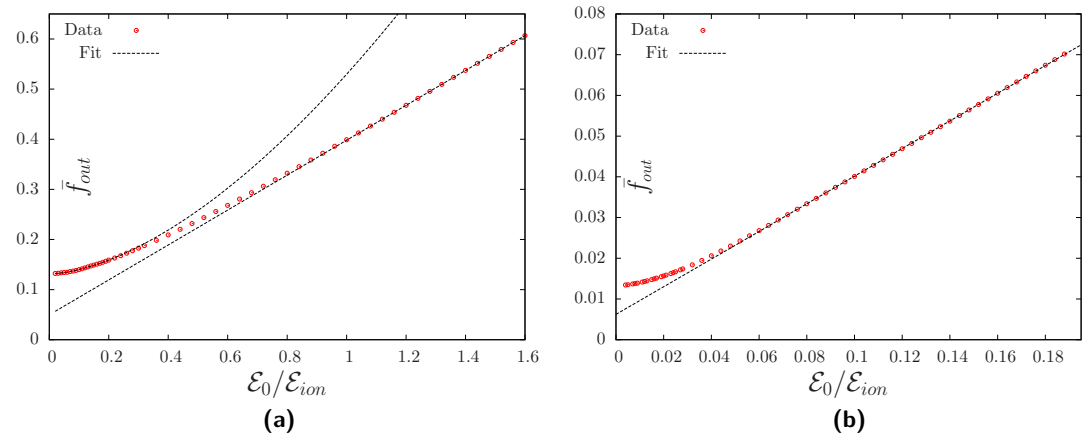

Figure 6.3.2: Cycle-averaged fraction $\bar{f}_{out}$ of electrons located outside the foil (laser parameters: $n = 1$, $\omega = 0.125$). Results are shown for two foils of thickness (a) $l = 5$ and (b) $l = 50$. In both cases, the data points are fitted to linear functions for large values of $\mathcal{E}_0$. For $l = 5$, data points with $\mathcal{E}_0/\mathcal{E}_{ion} < 0.2$ are fitted to the power law $\bar{f}_{out} = 0.088\,\mathcal{E}_0^{1.65} + 0.13$. It is shown that the scaling exponent of $\bar{f}_{out}$ is larger than one for thin foils and moderately large field strengths.

The fit yields the values $\alpha = 0.088$, $\beta = 1.65$, $\delta = 0.13$ and is also indicated in Fig. 6.3.2a. Here, δ corresponds to the fraction of spill-out electrons in the equilibrium state. This result indicates that $\bar{f}_{out}$ grows more rapidly for moderately large values of $\mathcal{E}_0$ in comparison to the linear behavior for large $\mathcal{E}_0$-values. Within Brunel's theory, N_{out} is considered to be a linear function of $\mathcal{E}_0$. In this sense, the increased scaling exponent of E_{abs} for $\mathcal{E}_0/\mathcal{E}_{ion} \lesssim 0.2$ can be explained by the fact that N_{out} has a larger scaling exponent.

The differing behavior of $\bar{f}_{out}$ for thin foils can be understood in terms of the surface profile of the equilibrium density. By decreasing the value of l, the transition region of the equilibrium density shown in Fig. 6.1.1b is broadened. Now, consider a shift of the equilibrium distribution by an amount ξ along the x-axis, where $N_{out}(\xi)$ is the number of electrons which leave the foil due to the displacement. In the classical case, one has $N_{out} \sim \xi$ due to the homogeneity of the equilibrium density inside the foil. If the electron density is broadened at the surface, the Taylor expansion of $N_{out}(\xi)$ also contains higher orders of ξ. However, if the displacement is chosen sufficiently large such that the inhomogeneous part of the equilibrium density is already located outside the foil, the density distribution becomes again homogeneous at the foil boundary and a further increase $d\xi$ generates a number of outgoing electrons $dN_{out} \sim d\xi$.

After having gained more insight into the quantum effects of the energy absorption for moderately large values of $\mathcal{E}_0$, comparison is made between the extracted scaling law (see Fig. 6.3.1)

$$\frac{E_{abs}}{N_e} = a(l)\,\mathcal{E}_0^b \tag{6.3.5}$$

for large values of $\mathcal{E}_0$ ($b \approx 3$) and the classical foil result of [80]. The authors find a scaling law similar to the result (6.3.1) of Brunel, with a numerical constant of $\eta = 8.75$ for a laser pulse with a duration of $n = 10$ laser cycles. The corresponding value for a single-cycle pulse is given by $\eta = 0.875$, assuming that the result of [80] scales linearly with n. For the comparison with the scaling law of this chapter, the a-parameter of (6.3.1) is evaluated by introducing the present laser frequency of $\omega = 0.125$ and the numerical constant $\eta = 0.875$ for a single-cycle pulse, which yields the classical reference result

$$a(l) = \frac{\eta}{2}\frac{1}{\omega^2}\frac{1}{l} = \frac{0.875}{2}\frac{1}{0.125^2}\frac{1}{l} = \frac{28}{l}. \tag{6.3.6}$$

In Fig. 6.3.3, numerical results for $a(l)$ are plotted as a function of l, which have been extracted as demonstrated in Fig. 6.3.1. For the comparison with (6.3.6), a model function $a(l) = \alpha/l^\beta$ is fitted to the data, which yields the fit parameters $\alpha = 30.1$ and $\beta = 1.09$. The fit function is also presented in Fig. 6.3.3. One can see that the found value of α is close to the value $\alpha = 28$ predicted classically. This demonstrates that for large values of $\mathcal{E}_0$ quantum effects of the absorption become small.

Summary

In this chapter, the nonlinear energy absorption of laser-driven foils has been studied in the framework of a Hartree model and the SSVM. It has been demonstrated that

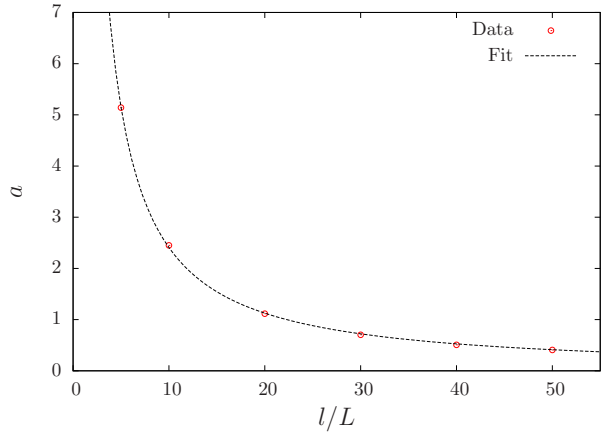

Figure 6.3.3: Scaling parameter a of the absorbed energy E_{abs} in the regime of large laser field strengths (see (6.3.5)). The results are plotted against the layer thickness l and are extracted as demonstrated in Fig. 6.3.1 for the same laser parameters. The data points are fitted to the inverse power law $a = 30.1/l^{1.09}$, where the prefactor 30.1 is close to the value 28 predicted by classical particle simulations.

the Hartree result for the absorbed energy converges to the corresponding SSVM result if the number of electron states is chosen sufficiently large.

By studying the absorbed energy as a function of the laser field strength, Brunel's scaling has been confirmed for thick foils or sufficiently large field strengths of the laser. In this regime, the coefficient of the energy absorption is in rather good agreement with previous results obtained from classical particle simulations. For thin foils and moderately large field strengths, the scaling exponent is increased. This can be explained by the fact that the scaling exponent of the number of outgoing electrons is larger than predicted by the classical Brunel theory due to the spill-out effect of the electron density.

Chapter 7

Nonlinear Theory of Electrostatic Cluster Excitations

In the previous chapter, the dynamics of small plasma foils has been studied in the nonlinear regime. The following chapter is again devoted to the treatment of clusters in spherical geometry. While the analysis of Chapter 4 has been limited to the linear regime of electrostatic cluster excitations, it is intended to generalize in the following chapter the description of azimuthally symmetric electrostatic cluster excitations to the nonlinear regime by solving the full nonlinear Vlasov-Poisson system (2.3.3).

In practice, cluster excitations beyond the linear regime can be generated e.g. by scattering of low-energetic charged ion beams in cluster media [49] or through the interaction of clusters with high-intensity laser fields [48]. An overview on major phenomena in the nonlinear response of metal clusters can be found in [18, 50, 51]. While the theoretical study of nonlinear phenomena in nanometer-sized clusters has been largely adressed in TDLDA [52, 54], PIC methods are well-established [55–61] for larger clusters where a classical treatment is reasonable.

The main goal of this chapter is to study in more detail the nonlinear evolution of free and laser-driven Mie oscillations within the multistream approach. In the following, the computational framework of this chapter is described in more detail. Prior to the external perturbation, the electron system is considered to be in the equilibrium state. Therefore, the initial wave functions $\varphi_k(\boldsymbol{r},0)$ are of the form (See Chapter 3)

$$\varphi_k(\boldsymbol{r},0) = R_{nl}(r)Y_{lm}(\theta,\varphi) \sim e^{im\varphi}. \tag{7.0.1}$$

Azimuthally symmetric excitations of the electron system do not couple the quantum number m of the time-propagated wave functions $\varphi_k(\boldsymbol{r},t)$. Therefore, they can be expressed in the form

$$\varphi_k(\boldsymbol{r},t) = \bar{\varphi}_k(z,\varrho,t)\, e^{im\varphi}, \tag{7.0.2}$$

where $\bar{\varphi}_k$ are φ-independent wave functions written in cylindrical coordinates. To express the Vlasov-Poisson system (2.3.3) in terms of these functions, the Laplacian in cylindrical coordinates is introduced,

$$\Delta = \Delta_{z,\varrho} + \frac{1}{\varrho^2}\frac{\partial^2}{\partial\varphi^2}, \quad \Delta_{z,\varrho} = \frac{1}{\varrho}\frac{\partial}{\partial\varrho} + \frac{\partial^2}{\partial\varrho^2} + \frac{\partial^2}{\partial z^2}. \tag{7.0.3}$$

Then, the resulting equations for the wave functions $\bar{\varphi}_k(z,\varrho,t)$ and the self-consistent potential $\phi(z,\varrho,t)$ in cylindrical coordinates read

$$i\partial_t \bar{\varphi}_k = \left[-\frac{1}{2}\Delta_{z,\varrho} - \phi_m - \phi_{ext} \right] \bar{\varphi}_k, \tag{7.0.4a}$$

$$\Delta_{z,\varrho}\,\phi = w \sum_{k=1}^{N_s} |\bar{\varphi}_k|^2 - \theta\left(R - \sqrt{\varrho^2 + z^2}\right). \tag{7.0.4b}$$

Here,

$$\phi_m = \phi - \frac{m^2}{2\varrho^2} \tag{7.0.5}$$

is a modified potential containing the m-dependent centrifugal barrier term. Due to the symmetry

$$\varphi^{(0)*}_{nlm} = (-1)^m \varphi^{(0)}_{nl(-m)}. \tag{7.0.6}$$

of the equilibrium wave functions and the fact that the Hamiltonian of (7.0.4a) depends only on $|m|$, it is sufficient to propagate wave functions with $m \geq 0$. Finally, one has to propagate

$$N_p = \sum_{l=0}^{l_{max}} N_l(l+1) \tag{7.0.7}$$

wave functions based on the two-dimensional Schrödinger equations (7.0.4a). Here, N_l is the number of distinct equilibrium states for given quantum numbers l and m. Parallely, one has to solve Poisson's equation (7.0.4b) in two dimensions. For the numerical evaluation of the underlying equations, the author has written an alternating direction implicit (ADI) simulation code [131]. The numerical scheme is described in more detail in Appendix A.4. For the simulation results presented in this chapter, a spatial grid with 2048 points in the z-direction and 1024 points in the ϱ-direction has been considered. An imaginary potential was added in the region close to the boundary of the computational grid in order to absorb outgoing wave packages [132]. Spatial grid constants $\Delta\varrho = \Delta z = 0.1$ are chosen together with a time step of $\Delta t = 0.025$ for the Schrödinger solver and a relaxation time step of $\Delta\tau = 1$ for the Poisson solver. The number of relaxation steps for the Poisson solver was set to $N = 5$. Convergence of the simulation results for these numerical parameters has been confirmed by the author.

In this chapter, calculations are presented for a Na cluster of radius $R = 9.57$ (1.1nm) and 138 electrons (see Appendix A.1). For this cluster size, one has to propagate $N_p = 41$ wave functions $\bar{\varphi}_{nlm}$. In Section 7.1, the free oscillation of the Mie plasmon is studied based on an impulsive excitation of the cluster equilibrium. Section 7.2 is devoted to the dynamics of the cluster electrons in the presence of femtosecond laser pulses.

7.1 Free Mie Oscillation

In this section, the focus is put on the free oscillation of the Mie plasmon in the non-linear regime. The corresponding problem for small perturbations of the equilibrium has been considered in Section (4.4) by linear perturbation theory. The excitation of

p	α
0.1	0.010
0.3	0.028
0.5	0.059

Table 7.1.1: Degree of ionization α for various initial momenta p.

the cluster is driven by an impulsive excitation with initial momentum $\langle \boldsymbol{p} \rangle = p\boldsymbol{e}_z$. The initial wave functions $\bar{\varphi}_{nlm}(\boldsymbol{r}, 0)$ read [50, 113]

$$\bar{\varphi}_{nlm}(\boldsymbol{r}, 0) = \bar{\varphi}^{(0)}_{nlm}(\boldsymbol{r}) e^{ipz}. \tag{7.1.1}$$

In the following, the dynamics of the Mie oscillation is studied based on the motion of the z-component $Z(t)$ of the c.m. (see 4.1.38b). For the further evaluation, it is convenient to introduce the c.m. contribution of electrons that are located in and outside an imaginary sphere of radius R'. They are calculated by the following relations:

$$Z^{<}_{R'}(t) = \int\limits_{\mathbb{R}^3} \theta(R' - r)\, n(\boldsymbol{r}, t)\, z\, d^3r, \quad Z^{>}_{R'}(t) = Z(t) - Z^{<}_{R'}(t). \tag{7.1.2}$$

Then, $Z^{<}_{R}$ describes the contribution of electrons which are located in the interior region of the ion sphere (inner electrons), while $Z^{>}_{R}$ refers to electrons which are located in the exterior region of the ion sphere (outer electrons).

In order to investigate the transition between the linear and nonlinear regime of the Mie oscillation, calculations were carried out for various initial momenta p. To measure the strength of the perturbation, the degree of ionization α is considered. In the following, it is defined as the ratio of the number $N_{out}(t_p)$ of electrons leaving the computational domain during the time t_p of wave propagation and the number $N_e(0)$ of electrons occupying the cluster in the equilibrium state,

$$x = \frac{N_{out}(t_p)}{N_e(0)} = 1 - \frac{N_e(t_p)}{N_e(0)}, \quad N_e(t) = \int\limits_{\substack{Comp.\\ domain}} n(\boldsymbol{r}, t)\, d^3r. \tag{7.1.3}$$

Depending on the p-parameter, one has to choose sufficiently large computation times t_p to account for delayed ionization [133]. Table 7.1.1 shows α-values for various initial momenta p considered in this section.

Dipole Oscillation

In the following, the simulation results are presented for the c.m. motion. In Fig. 7.1.1, one can see corresponding results for the evolution of the c.m. excited by different initial momenta. In order to capture the essential dynamics for the largest momentum, the electron states are propagated in time over approximately 150 Mie periods. For small perturbations ($p = 0.1$), the result is close to the corresponding curve obtained by linear perturbation theory over the first few Mie periods. This value of p corresponds to a value of $\alpha = 0.01$ for the degree of ionization, which is still small. Besides the

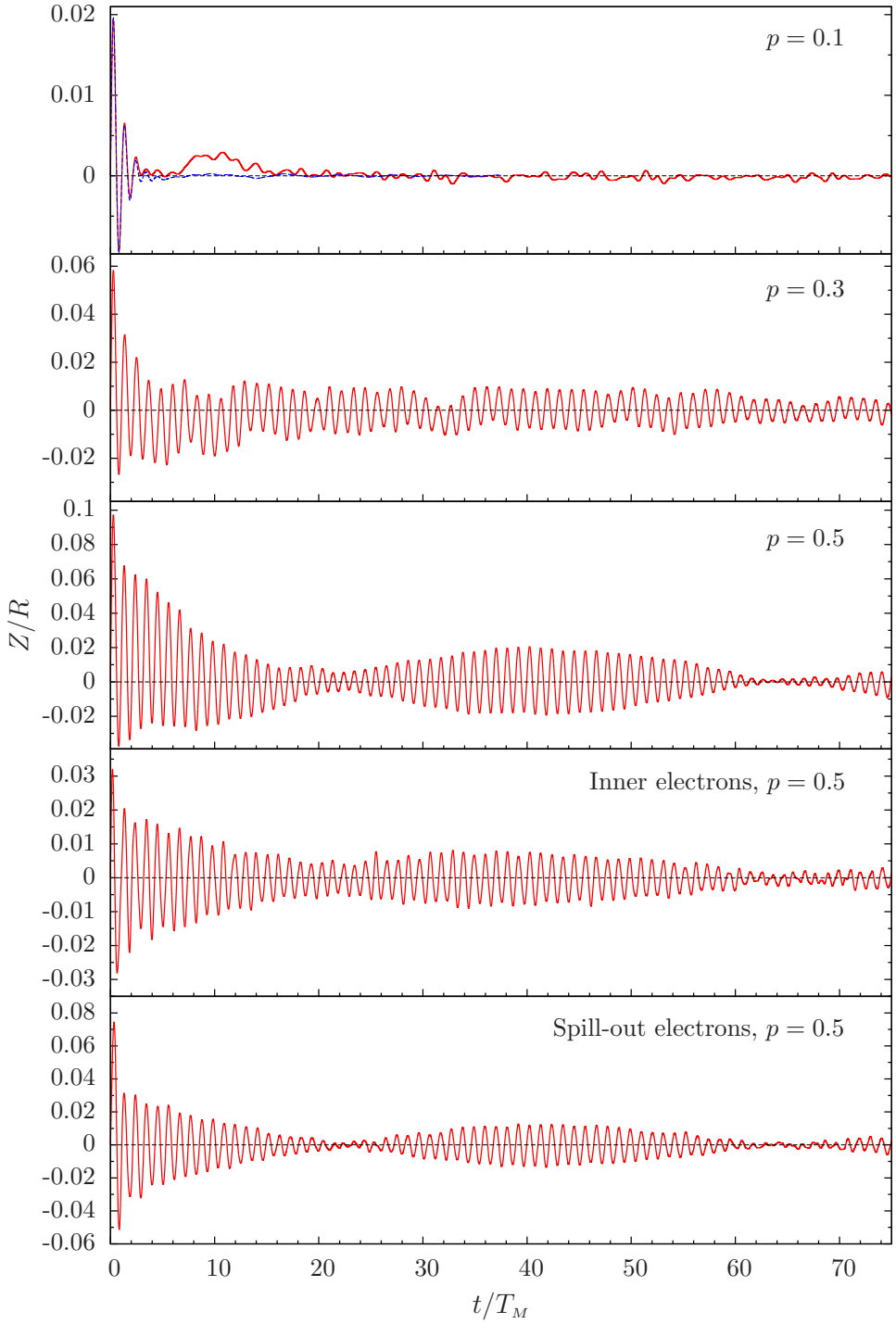

Figure 7.1.1: Motion of the z-component $Z(t)$ of the center of mass (c.m.) following an impulsive excitation with initial momenta $p = 0.1$, $p = 0.3$ and $p = 0.5$ (Na cluster, $N_e = 138$, $R = 9.57$). The three figures above show the c.m. motion (red, solid). For $p = 0.1$, the corresponding result obtained by linear perturbation theory (see Chapter 4) is plotted as well (blue, dashed). The two figures below show the c.m. contribution of electrons located inside the ion sphere and spill-out electrons located inside a spherical shell with inner radius R and outer radius $1.6R$. For $p = 0.1$, one recognizes that the motion of the c.m. is close to the linear result described to a good approximation by a damped harmonic oscillation. For larger values of p, the motion becomes nonharmonic and a beat-like behavior of the c.m. sets in (see text for details).

damped oscillation of the c.m. for $t \lesssim 3T_M$, one can see a subsequent increase of the nonlinear result in the range between $t = 8T_M$ and $t = 10T_M$. This increase is related to outgoing electron wave packets which move towards the boundary of the computational grid. These waves are absorbed by the imaginary potential, which leads to a decrease of the c.m. The residual oscillations of the c.m around $Z = 0$ are again related to oscillations of electrons which stay in the computational domain.

By increasing the initial momentum of the electrons to $p = 0.3$ ($\alpha = 0.028$), the relaxation of the c.m. motion becomes increasingly nonharmonic. Since the restoring force generated by the ions is nonharmonic in the exterior region of the ion sphere, this behavior indicates the growing influence of outer electrons on the motion of the c.m. In particular, the author has confirmed that the c.m. motion for $t \gtrsim 10T_M$ is largely driven by electrons which stay in the computational domain. In this range, one can observe oscillations on the timescale of T_M which are nearly undamped. The amplitude of these residual oscillations is roughly one order of magnitude larger than that observed for the smaller p-value $p = 0.1$.

In order to see how the behavior of the c.m. changes for even higher values of p, calculations were performed for a parameter of $p = 0.5$, where the degree of ionization is approximately 6%. First of all, one recognizes a rapid drop of the oscillation amplitude during the first Mie period. By studying the time dependence of the number of inner electrons, it becomes apparent that the outer ionization of the cluster takes place merely in this time interval (see Fig. 7.1.3). More precisely, one can confirm that roughly 3% of the electrons are removed from the interior region of the sphere during the first Mie period. Therefore, the initial drop of the oscillation amplitude reflects the growing influence of outer ionization [18, 19] on the plasmon relaxation for increasing values of p. Subsequent to the initial drop, the c.m. undergoes rather slow relaxation during roughly the first 22 Mie periods compared with the relaxation behavior for $p = 0.1$. Most notably, it is visible that the oscillation amplitude increases again for $t \gtrsim 22T_M$ until it reaches a local maximum at $t \approx 40T_M$. Subsequently, the amplitude decreases to a value close to zero at $t \approx 64T_M$. The author has convinced that the beat-like behavior of the c.m. continues over larger times, where the amplitude at the local maxima is slightly damped. By varying the size of the computational grid, it has been checked that the increase of the c.m. amplitude following the relaxation during the first 22 Mie periods is not related to electrons which reenter the cluster region due to a reflection at the boundary of the grid.

Dipole Spectrum

To resolve the frequencies contained in the c.m. motion $Z(t)$, the Fourier transform $\tilde{Z}(\omega)$ has been calculated. Figure 7.1.2 shows the oscillator strengths $|\tilde{Z}|(\omega)$ for the p-values considered in Fig. 7.1.1. The Mie resonance for $p = 0.1$ is rather broad, which is due to the strong surface-induced damping in the regime of small cluster excitations. In addition, a wide spectrum of low-frequency peaks can be observed which are related to single-particle excitations (see Subsection 4.4.1). By increasing the initial momentum to $p = 0.3$, the Mie resonance becomes sharper with respect to the case $p = 0.1$. In addition, it is blueshifted towards the classical Mie frequency ω_M. To understand the blueshift of the resonance, the electron density at the cluster surface

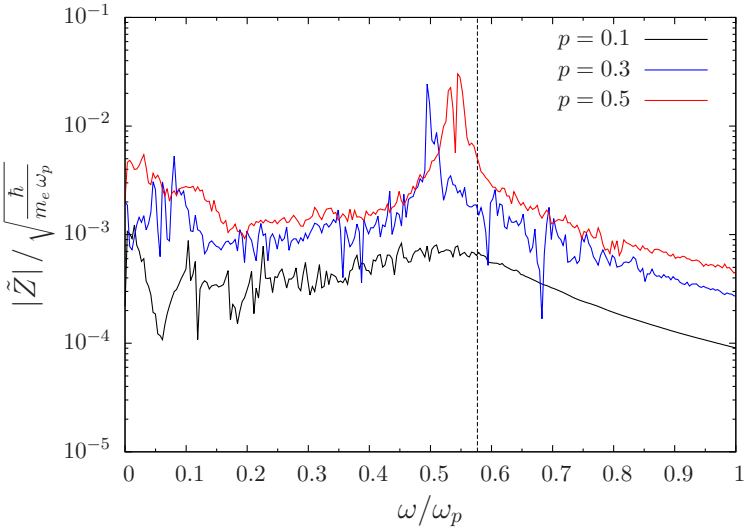

Figure 7.1.2: Fourier transform $\tilde{Z}(\omega)$ of the center of mass (c.m.) $Z(t)$. The figure shows the oscillator strengths $|\tilde{Z}|(\omega)$ corresponding to the results in Fig. 7.1.1. It is shown that the resonance of the Mie plasmon is shifted towards the classical Mie frequency ω_M (vertical dashed line) for increasing values of p and that the width of the resonance is reduced with respect to the case $p = 0.1$. For $p = 0.5$, the Mie resonance splits into two closely adjacent peaks of almost equal height.

has been studied as a function of time. This analysis shows that the outer ionization of the cluster during the first Mie period results in a uniform shift of the time-averaged density at the cluster surface towards smaller values compared with the equilibrium density. In particular, for $p = 0.5$, one finds that the density at the cluster northpole oscillates around a value $n \approx 0.3$, which corresponds to a reduction of the density by 25% with respect to the equilibrium density $n^{(0)} \approx 0.4$ at the cluster surface. Since outer ionization leads to a reduction of the total electron charge inside the ion sphere, the reduction of the electron density at the surface reflects the effect that electron states in charged clusters are bound stronger to the interior region of the ion sphere [134]. Therefore, surface scattering is less pronounced compared to the linear regime of cluster excitations.

By looking at the oscillator strength for $p = 0.5$, one can see that the blueshift becomes even more pronounced. Furthermore, one can observe a splitting of the Mie resonance into two closely adjacent peaks of almost equal height. Therefore, the beat-like behavior of the c.m. can be represented by a superposition of two oscillations with almost equal strength and frequency. Since the resonance frequencies are rather close, the envelope of the c.m. in Fig. 7.1.1 oscillates with a frequency much smaller than ω_M. In the following, the splitting of the Mie resonance for $p = 0.5$ is characterized in more detail.

First, the question has been considered whether the beating effect of the c.m. can be related to a different oscillatory behavior of inner electrons and spill-out electrons. According to (7.1.2), the contribution of inner electrons is given by $Z_R^<$. Since the spill-out electrons are largely located inside a spherical shell with inner radius R and outer

radius R', their contribution is determined by $Z^{<}_{R'} - Z^{<}_{R}$. Here, a radius of $R' = 1.6R$ turned out to be sufficient to describe the main contribution of spill-out electrons. The c.m. contributions of both subsystems are plotted in Fig. 7.1.1.

Subsequent to the initial drop, both functions oscillate in phase and decay on the same timescale over roughly 14 Mie periods. Around the local minimum of the c.m. oscillation amplitude, the functions move out of phase and the contribution of spill-out electrons is close to zero. In this intermediate stage, the displacement of the c.m. is largely determined by the contribution of inner electrons. One can verify that the decay of both functions in the range between $t = T_M$ and $t = 14T_M$ can be represented to a good approximation by a damped harmonic oscillation of the form

$$f(t) = (a\sin(\omega t) + b\cos(\omega t))\exp(-\gamma t). \tag{7.1.4}$$

By fitting the model function to the data points of the inner electrons, a damping rate of $\gamma = 0.007$ can be extracted. This value is roughly one order of magnitude smaller than the damping rate $\gamma = 0.105$ of linear plasmon excitations (see Fig. 7.1.2). Besides the simultaneous relaxation during the first 22 Mie periods, it becomes apparent that both functions exhibit a beat-like behavior similar to the total c.m. In this sense, the behavior of the c.m. cannot be explained by the motion of one of the two subsystems.

Time Evolution of the Density Perturbation

After having discussed the spectrum of the c.m. motion, the focus is now put on the time evolution of the density perturbation $n^{(1)}(\boldsymbol{r}, t) = n(\boldsymbol{r}, t) - n^{(0)}(r)$. Figure 7.1.3a shows the evolution of $n^{(1)}$ along the z-axis for an initial momentum $p = 0.5$. The colorbar range is chosen to illustrate the dynamics close to the cluster surface. At the cluster poles ($z = \pm R$), one recognizes an oscillation of the electron density which is associated with the Mie plasmon. During the first Mie period, one recognizes emissions of two pronounced electron wave packets at the north and southpole, which leave the cluster region. These bunches are responsible for the fast decrease of the number of inner electrons during the first Mie period, as mentioned above. Further wave packets are emitted after roughly each half Mie period until the c.m. has decreased sufficiently. As a result of the outer ionization, the density at the cluster surface is reduced (see above) and an electron cloud is formed outside the ion sphere. The reduction of the time averaged density at the surface with respect to the equilibrium density is visible by the blue discolorization of the plot close to the cluster poles.

Around the first local minimum of the c.m. oscillation amplitude at $t \approx 22T_M$, one recognizes that the density perturbation becomes nearly stationary at the cluster surface. In this intermediate stage of the dynamics, the effect of surface crossing of electron wave packets is less pronounced. As the oscillation amplitude builds up again, the situation at the cluster surface changes again. In particular, around the local maximum of the oscillation amplitude at $t \approx 41T_M$, an enhanced surface crossing of electron wave packets is visible, which indicates that the subsequent increase of the of c.m. is accompanied by an expansion of the electron system along z-axis. This behavior is clearly visible in Fig. 7.1.3c, which shows a snapshot of the electron density in the xz-plane at $t = 41.3T_M$. It is visible that the emission of electron wave packets merely

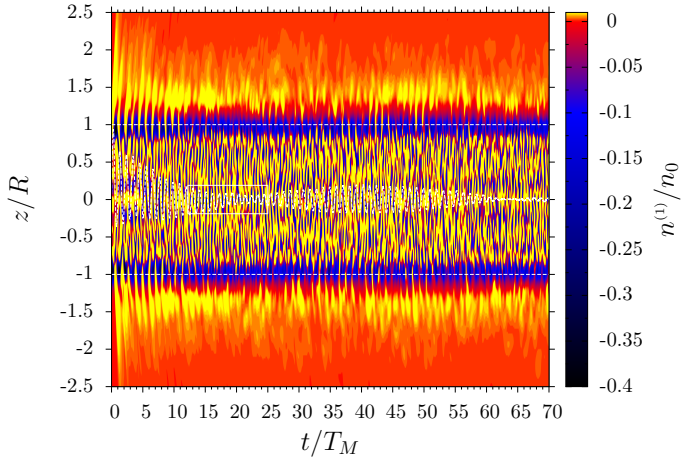

(a)

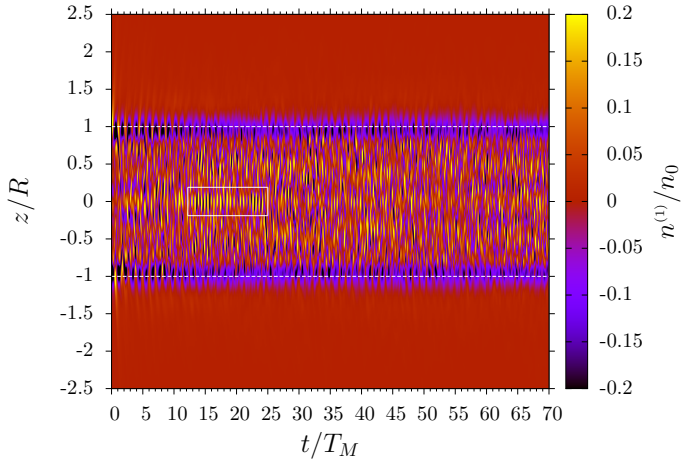

(b)

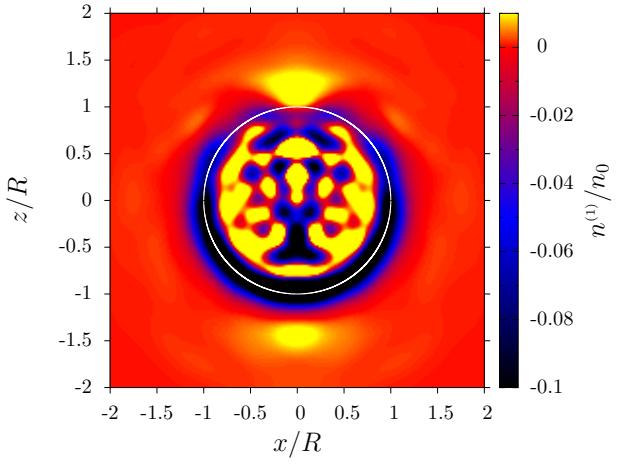

(c)

Figure 7.1.3: Density perturbation following an impulsive excitation with initial momentum $p = 0.5$ (Na cluster, $R = 9.57$, $N_e = 138$). (a),(b) Time evolution of the density perturbation $n^{(1)}(z,t)$ along the z-axis (different colorbar ranges). In (a), the motion of the c.m $Z(t)$ is indicated by a dashed white line (left scale). For better visibility, the values of Z are multiplied by R. (c) Snapshot of the density perturbation in the xz-plane ($t = 41.3T_M$). Different colorbar ranges are chosen to illustrate the dynamics both at the cluster surface and in the interior region of the ion sphere.

takes place close to the cluster poles and that their propagation is aligned along the z-axis. Before discussing the dynamics of the external electron cloud in more detail, the focus is put on the electron density inside the cluster.

Figure 7.1.3b shows the time evolution of the density perturbation on a different colorbar range to illustrate the dynamics inside the cluster. During the initial decrease of the c.m., one recognizes the generation of density oscillations near the cluster center. For $t \gtrsim 12$, it is visible that these oscillations become increasingly spread over the whole z-axis. The author has convinced that the timescale of the density oscillations is given by the plasma period $T_p = 2\pi/\omega_p$. In particular, in the range between $t = 12$ and $t = 25$ where the c.m. has already decreased significantly, one can see pronounced oscillations of the density at the center of the cluster (white rectangle). By studying their amplitude in this time interval, one finds that it reaches its maximum value $n^{(1)} \approx 0.5$ very close to the first local minimum of the c.m. oscillation amplitude ($t \approx 22T_M$). This large value of the density perturbation corresponds to half the density of the background ions. As the c.m. increases again, the pronounced oscillation of the density at the center of the cluster vanishes and the density fluctuations are spread over the whole z-axis.

This behavior of the density inside the cluster is quite different to the corresponding dynamics in the linear regime. In Section 5.2, it has been demonstrated for a slightly larger cluster of radius $R = 10.8$ (see Fig. 4.4.3) that volume modes with resonance frequencies close to the plasma frequency are damped by single-particle excitations due to the interaction with the subshell-induced inhomogeneity of the equilibrium density inside the cluster. Therefore, single-particle excitations with resonance frequencies well below the plasma frequency dominate the long-time behavior of the density in the linear regime. In contrast to that, the present nonlinear treatment for $p = 0.5$ shows the generation of spatially localized density fluctuations on the timescale of the plasma period, which are spread over the interior region of the ion sphere. In this regime, Landau damping of volume modes seems to play a minor role which is also visible by the resonance curve of the c.m. in Fig. 7.1.2. Here, the low-frequency peaks associated with single-particle excitations become less pronounced for the largest p-value considered.

Quadrupole Oscillation

After having focused the dynamics of the electron density inside the cluster, attention is paid to the electron dynamics in the exterior region of the cluster subsequent to the first local minimum of the c.m. oscillation amplitude. As mentioned above, the enhanced surface crossing of electron wave packets at $t \approx 41T_M$ (see Figures 7.1.3a and 7.1.3c) indicates an expansion of the cluster electrons along the z-axis close to the first local maximum of the oscillation amplitude. In order to capture the shape of the electron distribution as a function of time, the motion of the quadrupole moment Q_{33} has been studied, which is defined in (4.1.41b). Figure 7.1.4 shows the motion of Q_{33} for the parameters $p = 0.3$ and $p = 0.5$. In the following, the motion is discussed for $p = 0.5$. At $t = 0$, the electron system is in the ground state, which is associated with a spherically symmetric electron density. Therefore, all multipole moments vanish prior the impulsive excitation. Figure (7.1.1) shows that Q_{33} increases monotoneously

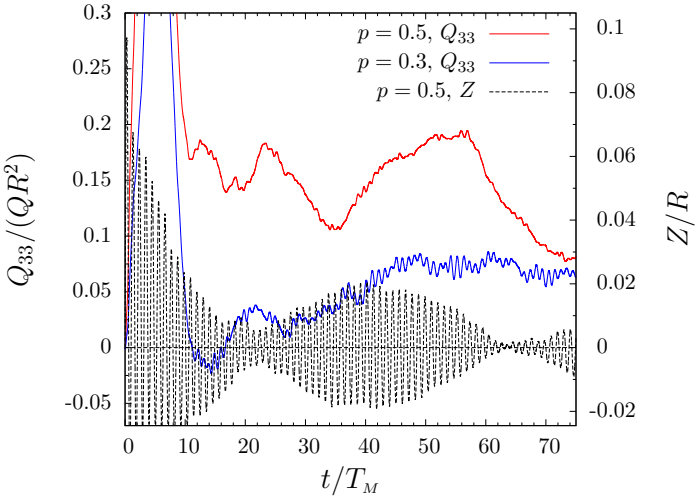

Figure 7.1.4: Motion of the quadrupole moment Q_{33} following an impulsive excitation with initial momenta $p = 0.3$ and $p = 0.5$ (Na cluster, $R = 9.57$, $N_e = 138$). The quadrupole moment is measured in units of QR^2, where Q is the total electron charge. In addition, the motion of the center of mass $Z(t)$ is plotted ($p = 0.5$). It is shown that the quadrupole moment for $p = 0.5$ is shifted towards positive values and that it oscillates on the same timescale as the envelope of the center of mass.

for $t \lesssim 5T_M$. This increase is driven by the outer ionization of the cluster during the first few Mie periods, which results in electron wave packets moving towards the boundary of the computational grid. At $t \approx 5T_M$, the wave front reaches the boundary and outgoing waves are absorbed leading to a decrease of Q_{33}. The motion of Q_{33} for $t \gtrsim 10T_M$ largely represents the contribution of electrons which stay inside the computational grid. Here, one recognizes that Q_{33} is shifted towards positive values over the time interval considered. This behavior indicates that the distribution of electrons is stretched along the z-axis subsequent to the initial excitation. To illustrate this, a snapshot of the density perturbation is plotted in Fig. 7.1.5 for $t = 23T_M$. Here, the c.m. oscillation amplitude is near its first local minimum. First of all, one recognizes the formation of an electron cloud outside the cluster. It is visible that the shape of the density is rather close to that of a spheroid. This shows that the electron distribution is elongated along the z-direction with respect to the spherically symmetric equilibrium distribution.

Besides the shift of Q_{33} towards positive values, Fig. (7.1.1) illustrates that Q_{33} oscillates around a value of approximately $0.15QR^2$. The oscillatory behavior of Q_{33} indicates the vibration of the external electron cloud shown in Fig. 7.1.5. Most notably, it is visible that local maxima of the c.m. oscillation amplitude appear close to local minima of Q_{33} and vice versa. In particular, in the range $t \gtrsim 20T_M$ where the beat-like behavior of the c.m. sets in, one can see that the oscillation period of Q_{33} is close to the period of the c.m. envelope. This observation shows the coupling between the collective dipole oscillation of the cluster electrons and the quadrupole oscillation of the external electron cloud. Since nonvanishing values of Q_{33} are accompanied by an energy gain of the quadrupole order of the self-consistent field, the almost oppositely phased oscillations of Q_{33} and the c.m. oscillation amplitude describe a periodic

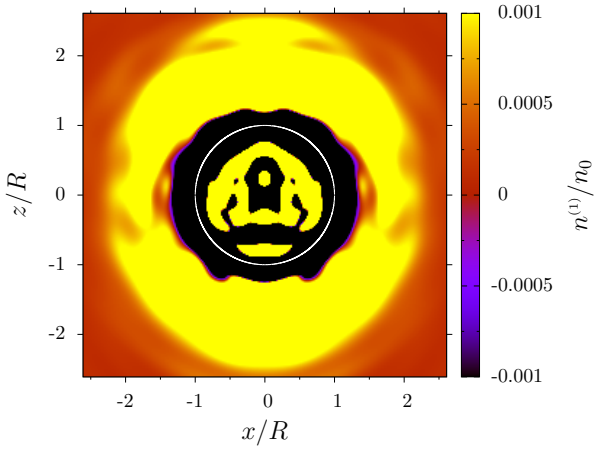

Figure 7.1.5: Snapshot of the density perturbation in the xz-plane ($t = 23T_M$) for an initial momentum $p = 0.5$ (Na cluster, $R = 9.57$, $N_e = 138$). The time considered is associated with the second local maximum of the quadrupole oscillation (see Fig. 7.1.4), where the oscillation amplitude of the center of mass is small. It is visible that an electron cloud is formed outside the cluster, which appears as a result of the initial perturbation. The shape of the density is stretched along the z-axis corresponding to a positive quadrupole moment Q_{33}.

energy transfer between the collective dipole oscillation of the cluster electrons and the quadrupole field of the external electrons. This transition leads to an additional broadening of the Mie resonance (see Fig. 7.1.3) for $p = 0.5$ compared with the resonance for $p = 0.3$. In the latter case, the oscillatory deformation effect is less pronounced which is visible by the corresponding quadrupole motion shown in Fig. 7.1.4. In contrast to the case $p = 0.5$, Q_{33} is close to zero at $t \approx 10T_M$ and increases rather slowly over time interval considered. The corresponding c.m. oscillation shown in Fig. 7.1.1 does not exhibit beats.

Finally, it is concluded that the beat-like behavior of the c.m. and the corresponding splitting of the Mie resonance is driven by a coupling of the cluster quadrupole and dipole degrees of freedom. On the basis of the multipole expansion of the density and the self-consistent potential, this coupling can be viewed by the product $n_1\phi_2 \sim Y_{10}Y_{20}$ of the dipole order of the density and the quadrupole order of the self-consistent potential. By expanding the product, it becomes apparent that the coupling leads to a contribution in the dipole sector. Since $\phi_2 = \mathcal{O}(p^2)$ and $n_1 = \mathcal{O}(p)$, the dipole-quadrupole interaction is a third-order effect for which the consistent propagation of higher multipole orders of the self-consistent potential is necessary.

It is noted that the splitting of the Mie resonance into several peaks is a well-known effect in small deformed metal clusters with a nonspherical ion background. More precisely, it has been anaylzed for Na clusters consisting of up to 40 atoms with a deformed jellium background [38, 39]. Calculations with a more precise account to the ionic structure have been performed for Mg clusters [40] consisting of up to 11 atoms. For small deformed clusters, the splitting of the Mie resonance is a linear effect which stems from the coupling of the surface plasmon to higher multipole orders of the

equilibrium potential. In conclusion, the splitting cannot be observed for spherically symmetric clusters in linear order perturbation. However, the present nonlinear treatment of spherically symmetric clusters with more than 100 electrons has shown that deformation effects can also arise dynamically. Here, the splitting of the resonance appears as a higher order effect due to the interaction of the Mie plasmon with the quadrupole field induced by the electron cloud exterior to the cluster region. Moreover, the present calculations have shown that deformation splitting can contribute significantly to the width of the surface plasmon even for larger clusters. This is in contrast to the linear regime where it has been pointed out [135] that Landau damping should be decisive for clusters consisting of more than 50 atoms. In particular, it has been demonstrated that single-particle excitations play a minor role for the plasmon relaxation in the nonlinear regime and that residual density fluctuations on the timescale of the plasma period dominate the long-time behavior of the electron density in the interior region of the cluster.

7.2 Laser-Driven Cluster Dynamics

This section is devoted to the nonlinear dynamics of electrons in clusters irradiated by a laser field. In the linear treatment of Chapter 4, it has been demonstrated that surface excitations can couple to volume excitations via the surface inhomogeneity of the self-consistent potential. Now, the emergence of laser-driven volume excitations is discussed in the nonlinear regime where they are strongly interacting.

For this purpose, a laser field in dipole approximation is introduced that is considered to be polarized along the z-axis. The laser field is modeled by a sine-square pulse with N laser cycles, frequency $\omega = 2\pi/T$ and pulse duration $\tau = NT$,

$$\phi_{ext}(\boldsymbol{r},t) = -\mathcal{E}_{\scriptscriptstyle L}(t)z, \quad \mathcal{E}_{\scriptscriptstyle L}(t) = \mathcal{E}_0 \sin(\omega t)\sin^2(\pi t/\tau). \tag{7.2.1}$$

Calculations were performed in the nonresonant regime by using a five-cycle pulse with a laser period of 3.5fs ($\omega/\omega_p = 0.2$) and peak intensities up to $1.4 \times 10^{14}\mathrm{W/cm}^2$.

In the following, the dynamics of the cluster electrons is discussed based on the evolution of the electron density for the largest peak intensity $1.4 \times 10^{14}\mathrm{W/cm}^2$. For this intensity, the degree of ionization is given by approximately 38%. Figure 7.2.1 shows snapshots of the density perturbation $n^{(1)}$ in the xz-plane taken at various times of the laser-cluster interaction. In addition, to resolve the dynamics properly, the evolution of $n^{(1)}$ along the z-axis is shown in Fig. 7.2.2a. For better interpretation, two additional quantities are considered. On the one hand the single-particle momentum distribution function

$$f_p(\boldsymbol{p}) = \frac{w}{V_{ion}} \sum_{k=1}^{N_s} |\tilde{\varphi}_k|^2(\boldsymbol{p}), \quad \tilde{\varphi}_k(\boldsymbol{p}) = \frac{1}{\sqrt{2\pi}^3} \int\limits_{\mathbb{R}^3} e^{-i\boldsymbol{p}\cdot\boldsymbol{r}} \varphi_k(\boldsymbol{r})\, d^3r \tag{7.2.2}$$

and on the other hand the total electric field

$$\mathcal{E}(\boldsymbol{r},t) = \mathcal{E}_{int}(\boldsymbol{r},t) + \mathcal{E}_{\scriptscriptstyle L}(\boldsymbol{r},t), \quad \mathcal{E}_{int} = -\nabla\phi. \tag{7.2.3}$$

The evolution of both quantities is shown in figures 7.2.2b and 7.2.2c.

In the second half of the initial laser cycle, $\mathcal{E}_L$ is negative and the electron system is accelerated in the positive z-direction. This is visible by the increase of $f_p^{(1)}$ for positive momenta p_z. At time $t = 0.76T$, $\mathcal{E}_L$ is close to its first local minimum. The corresponding snapshot shows that the electron system is shifted towards the positive z-direction, which leads to a density overshoot close on the upper half of the cluster surface. Furthermore, one recognizes the excitation of a volume plasmon in the interior region of the sphere. At this stage, the amplitude of the laser field strength is still small. The volume plasmon is generated through the interaction of the cluster electrons with the surface in the first laser cycle (see Subsection 4.3.3). Moreover, Fig. 7.2.2c shows that the laser field is screened inside the cluster during the initial build-up of the laser field when the $\mathcal{E}_L$ is still small.

The next snapshot at $t = 0.92T$ shows the generation of a plasma wave at the lower half of the cluster surface, which propagates into the cluster and which is guided by the surface [60, 61]. In contrast to volume plasmons in the linear regime, these volume excitations appear in the nonlinear stage of the laser-cluster interaction when the laser field strength has become sufficiently large. Fig. 7.2.2a shows that the wave is generated close to the first minimum of $\mathcal{E}_L$. The acceleration of the wave through the cluster is visibly by the orange and blue streams in Fig. 7.2.2a, which originate from $z \approx -R$ and which represent the wave crests and troughs. Since $\mathcal{E}_L$ changes its sign during the wave propagation through the cluster, the wave is deaccelerated at the beginning of the second laser cycle. As it reaches the upper half of the sphere, the electron system is already shifted in the negative z-direction and the wave breaks (snapshot $t = 1.11T$).

As $\mathcal{E}_L$ builds up to its second maximum at $t = 1.25T$, a second wave is produced on the upper half of the surface (snapshot $t = 1.27T$) whose amplitude is larger than that of the previous wave and which is accompanied by an excitation of the total electric field inside the cluster. Based on the evolution of the total electric field, it becomes apparent that the wave is produced at the surface region when the laser field is maximally enhanced by the internal polarization field [53, 60, 61]. The polarization field at $t = 1.25T$ is generated through the shift of the electron distribution towards the negative z-direction, which gives rise to an excess of ions on the upper half of the cluster surface. Therefore, the present plasma waves appear as a result of an enhanced acceleration of the surface electrons by the laser-induced polarization field.

In Fig. 7.2.2a, one recognizes that the secondary wave is generated slightly before the maximum of the laser field. It can be accelerated through the cluster rather effectively since the wave travels fast enough to reach the lower boundary of the cluster before $\mathcal{E}_L$ changes its sign. As a result, the wave gains enough energy such that the leading wave packet (first yellow stream originating from $z = R$) can leave the cluster region at time $t \approx 1.5T$, while the secondary wave crest is reflected at the lower cluster boundary. The density snapshot at $t = 1.59T$ shows that the outgoing electrons leave the cluster in form of a wave packet that is localized near the z-axis. This behavior will be discussed below in more detail.

In momentum space (see Fig. 7.2.2b), particles that cross the surface are associated with the yellow stream that penetrates the region $p_z < -1$. The corresponding turning

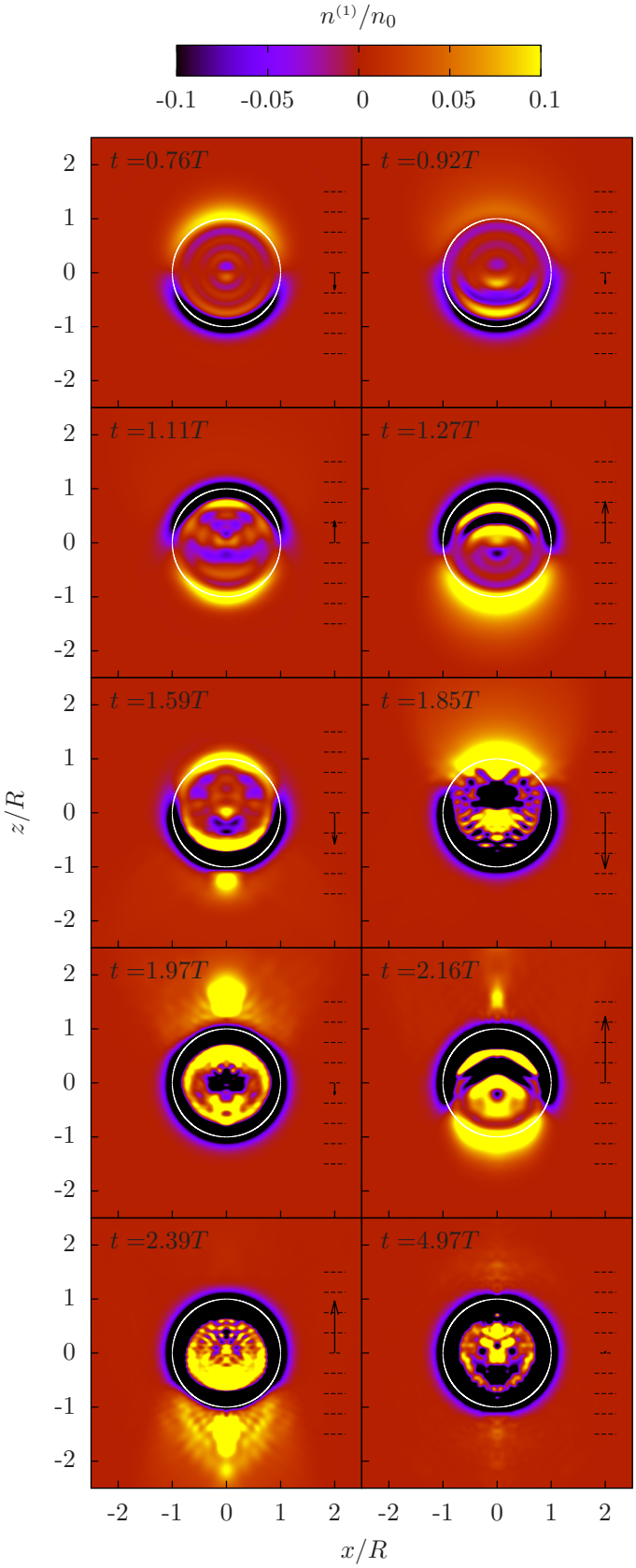

Figure 7.2.1: Snapshots of the density perturbation $n^{(1)}$ in the xz-plane (Na cluster, $R = 9.57$, $N_e = 138$). The cluster is irradiated by a five-cycle laser pulse (see (7.2.1)) with laser period 3.5fs and peak intensity $1.4 \times 10^{14}\mathrm{W/cm}^2$. The laser field vector $\boldsymbol{\mathcal{E}}_L(t)$ measured in units of the peak electric field $\mathcal{E}_0$ is indicated at each specific time t.

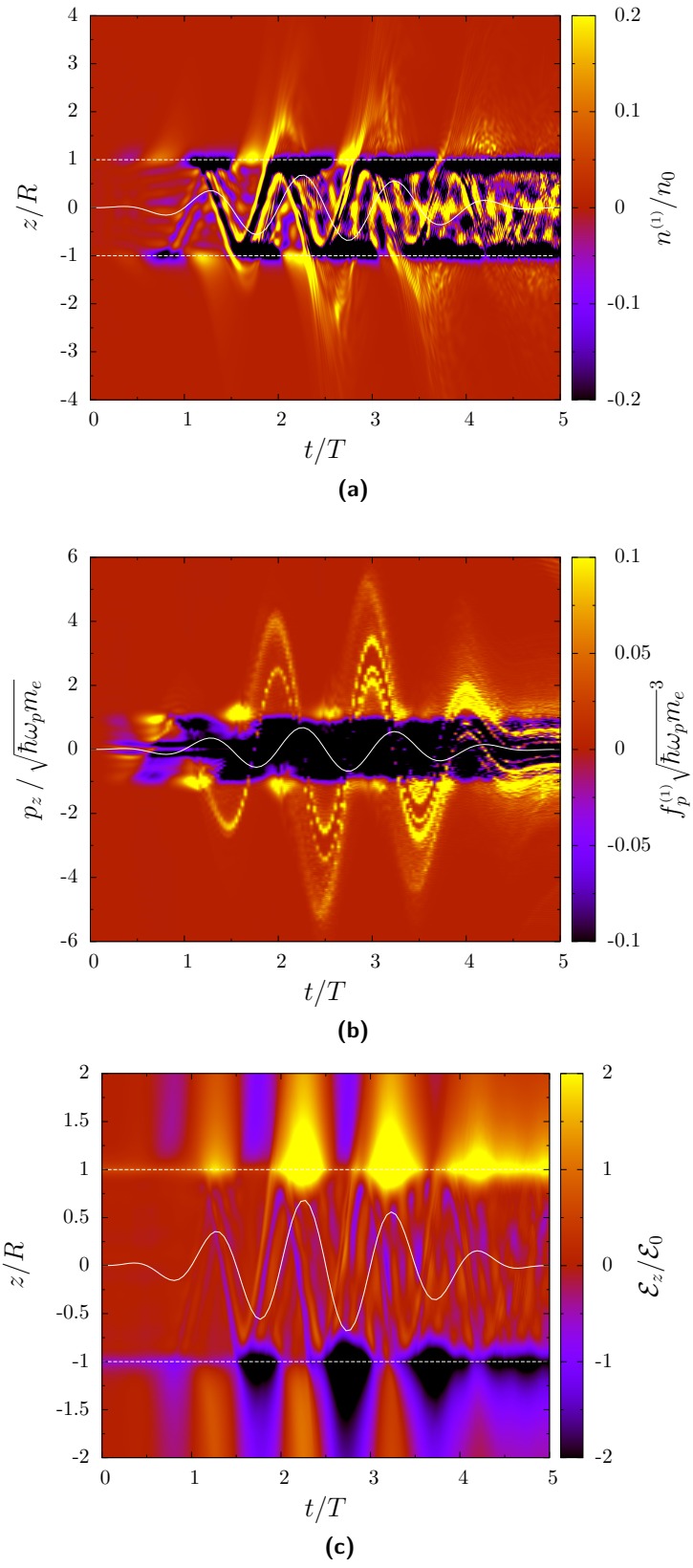

Figure 7.2.2: Time evolution of (a) the density perturbation $n^{(1)}$ along the z-axis, (b) the perturbation $f_p^{(1)}$ of the single-particle momentum distribution function for momenta $\boldsymbol{p} = p_z \boldsymbol{e}_z$ and (c) the total electric field $\boldsymbol{\mathcal{E}} = \mathcal{E}_z \boldsymbol{e}_z$ along the z-axis. Here, $\mathcal{E}_z$ is measured in units of the peak laser field $\mathcal{E}_0$. The results correspond to the parameters in Fig. 7.2.1.

point at $t \approx 1.5T$ indicates that a fraction of these outgoing electrons is accelerated back towards the cluster in the second half of the second laser cycle, which is also visible in the density plot 7.2.2a. Electrons that recombine with the cluster interfere with the plasma wave that is produced close to the second minimum of $\mathcal{E}_L$ at $t = 1.75T$. This interference results in spatial variations of the electron density on the Angstrom scale, which is visible in the snapshot at $t = 1.85T$.

Subsequently, a second wave packet is emitted (snapshot $t = 1.97T$) at the upper half of the surface that moves away from the cluster. As the previously emitted packet, it is focused along the z-axis [136]. Furthermore, it contains two groups of electrons that can be identified in the momentum distribution function shown in Fig. 7.2.2b. On the one hand those electrons that are related to the plasma wave produced at the lower half of the cluster surface at $t \approx 1.75T$ and on the other hand those electrons that have been emitted at $t \approx 1.5T$ and reaccelerated through the cluster.

The subsequent snapshot at $t = 2.17T$ shows an electron wave packet close to the upper half of the surface. This packet corresponds to electrons that are accelerated back towards the cluster. It contains less electrons than the packet that has been emitted at $t \approx 2T$. The lacking electrons have gained enough energy to leave the computational grid. Based on the total electric field in Fig. 7.2.2c, one can see that the recombining electrons are accelerated in a strongly enhanced electric field at the surface due to the large internal polarization field in the peak of the laser. It is noted that the maximum field enhancement is achieved close to the maximum of the laser field at $t = 3.25T$ with an electric field enhancement factor of approximately four. Moreover, the present snapshot shows the generation of a third plasma wave that is accelerated towards the lower half of the cluster surface followed by the emission of a further wave packet (snapshot $t = 2.39T$). As a result, a third group of electrons appears in the momentum distribution function next to the two groups that have been emitted and accelerated through the cluster in the previous laser cycle. This shows that the laser-cluster interaction and the related production of plasma waves at the cluster surface leads to a formation of distinct electron groups that are characterized by maxima in the momentum distribution function.

As an important aspect of the cluster dynamics, Fig. 7.2.2a shows that the dynamics of the electron density inside the cluster becomes faster in the course of time especially in the second half of the pulse. The origin of this increased dynamics becomes apparent as one focuses the recombination of electrons at times $t \approx 1.75T$ and $t \approx 2.25T$. In Fig. 7.2.2a, it is visible that the recombination and the related interference of internal plasma waves and recombining wave packets leads to a faster dynamics of the electron density inside the cluster. This behavior becomes even more pronounced as more outgoing electron wave packets recombine with the cluster. At the end of the laser pulse, the electron dynamics inside the cluster is characterized by density oscillations on the timescale of a few tens of attoseconds with peak electron densities of the double ion density n_0. It is mentioned that attosecond density fluctuations have been observed recently in microscopic PIC simulations of the resonant laser-cluster interaction by using larger noble gas clusters of radius 30nm [60, 61].

At the end of the laser pulse (snapshot $t = 4.97T$), it is visible that the electron density at the cluster surface is strongly reduced with respect to the equilibrium density. Here,

the cluster electrons are largely localized in the interior region of the sphere and the density spillout vanishes. As a result, the internal electric field at the cluster surface is enhanced with respect to the electric field in the equilibrium state (see Fig. 7.2.2c) due to the excess of ions at the cluster boundary. The reduction of the electron density at the cluster surface is related the relatively large degree of ionization of 38% for the present laser intensity. The remaining electrons of the charged cluster are bound closer to the cluster center [134].

To conclude the present discussion of the cluster dynamics, attention is paid again on the outer ionization dynamics of the cluster. As demonstrated above, the emission of electrons at the cluster surface is closely related to the dynamics of internal plasma waves in the presence of the laser field and the polarization field of the cluster. In particular, enhanced emission of electrons at the cluster surface can be observed when these waves reach the boundary of the cluster (see Fig. 7.2.2a). As a main feature of outer ionization, the emission is favored close to the cluster poles. To see how this behavior emerges from the propagation of the present plasma waves, it is instructive to focus the behavior when they reach the cluster surface. In particular, the two density snapshots at $t = 1.85T$ and $t = 1.97T$ in Fig. 7.2.1 show that the incoming wave is strongly focused onto the z-axis, which creates an enhanced electric field at the north pole (see Fig. 7.2.2c). Note the increase of $\mathcal{E}_z$ as the wave reaches the north pole before the laser field induces the polarization field. The enhanced emission of electrons at the cluster poles through focusing of plasma waves in spherical clusters appears quite similar to "plasmoemission" from two counter-propagating plasmon excitations at a flat metal surface [137].

After having discussed the dynamics of the cluster electrons, finally attention is paid to the local field enhancement at the cluster surface due to the laser-induced polarization field of the cluster. In order to quantify the field enhancement, the maximum field strength $\mathcal{E}_{max}$ of the total electric field on the z-axis is considered that is observed during the laser-cluster interaction. In particular, the dependence of $\mathcal{E}_{max}$ on the peak laser field strength $\mathcal{E}_0$ is briefly described. In Fig. 7.2.3, $\mathcal{E}_{max}$ is plotted against $\mathcal{E}_0$ for the same laser parameters as for the previous simulation and peak intensities between 10^{12} and $1.4 \times 10^{14}\mathrm{W/cm}^2$.

For small values of $\mathcal{E}_0$, it is visible that $\mathcal{E}_{max}$ is mainly determined by maximum electric field $\mathcal{E}^{(0)}_{max}$ in the equilibrium state. As $\mathcal{E}_0$ increases, $\mathcal{E}_{max}$ increases as well due to influence of the laser field and the induced polarization field at the cluster surface.

As $\mathcal{E}_0$ becomes of the same order of magnitude as $\mathcal{E}^{(0)}_{max}$, one can observe a transition in the behavior of $\mathcal{E}_{max}$ at $\mathcal{E}_0/\mathcal{E}^{(0)}_{max} \approx 0.5$, which corresponds to a peak intensity of roughly $10^{13}\mathrm{W/cm}^2$. The author has fitted a linear function

$$\frac{\mathcal{E}_{max}}{\mathcal{E}^{(0)}_{max}} = a\frac{\mathcal{E}_0}{\mathcal{E}^{(0)}_{max}} + b \tag{7.2.4}$$

to the data points with $\mathcal{E}_0/\mathcal{E}^{(0)}_{max} > 0.5$ (see Fig. 7.2.3), which leads to a good description of $\mathcal{E}_{max}$ in the regime of laser field strengths considered.

The fit yields the parameters $b = 1.56$ and $a = 3.05$. As a result, the laser field is enhanced by a factor three for sufficiently large values of $\mathcal{E}_0$. The linear dependence

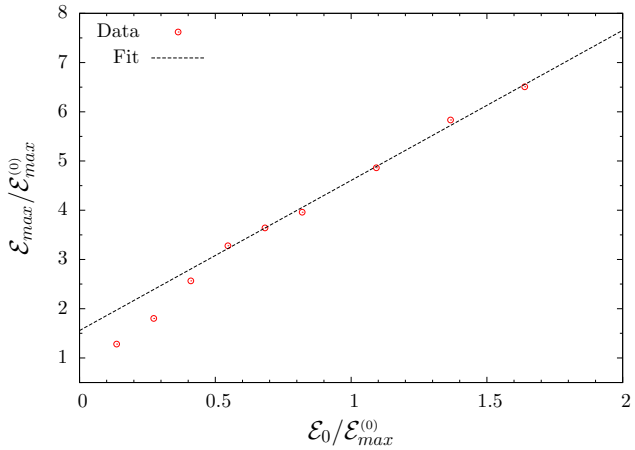

Figure 7.2.3: Maximum field strength $\mathcal{E}_{max}$ of the total electric field on the z-axis during the laser-cluster interaction (Na cluster, $R = 9.57$, $N_e = 138$). The cluster is irradiated by a five-cycle laser pulse (see (7.2.1)) with laser period 3.5fs and peak intensities between 10^{12} and 1.4×10^{14}W/cm^2. The results are plotted against the peak electric field $\mathcal{E}_0$ of the laser. In the figure, electric fields are measured in units of the maximum electric field $\mathcal{E}^{(0)}_{max}$ in the equilibrium state. A linear function is fitted to the data points with $\mathcal{E}_0/\mathcal{E}^{(0)}_{max} > 0.5$.

between $\mathcal{E}_{max}$ and $\mathcal{E}_0$ can be motivated by the following consideration: For large field strengths of the laser, outer ionization leads a reduction of the electron density at the surface (see Fig. 7.2.1, snapshot $t = 1.97T$) during the laser-cluster interaction. Therefore, internal electrons largely see a linear restoring force generated by the ion background. In conclusion, the displacement of the internal electrons and the corresponding polarization field should be roughly proportional to $\mathcal{E}_0$.

Chapter 8

Conclusions and Outlook

In the present work, the dynamics of cluster electrons in metallic atomic clusters was studied by means of the quantum Vlasov theory for the single-particle density operator. In this framework, the cluster electrons were treated as an ideal quantum plasma, thereby neglecting exchange and correlation effects. Through a discretization of the single-particle density operator, the Vlasov model was transformed into a quantum-mechanical multistream model, which describes the cluster electrons by a finite set of representative single-particle wave functions interacting via a self-consistent potential. The Vlasov model was treated by theoretical and numerical methods in the linear and nonlinear regime of free and laser-driven cluster excitations with particular attention to nanometer-sized clusters where quantum-size effects of the electron dynamics become important.

In Chapter 3, cluster equilibria were calculated. Here, the SSVM was introduced, which corresponds to a reduced Vlasov model with one representative state. It is found that the equilibrium of the SSVM can rather accurately describe the spill-out region of the electron density in multistream Na clusters, which is decisive for the dynamics of the Mie plasmon. The multistream results were calculated with complete electron configurations. Further comparison was made with previous DFT results for Na clusters. These results were reproduced by taking into account exchange and correlation effects in LDA.

In Chapter 4, linear electrostatic cluster excitations were treated in the multistream model and in the SSVM by performing a partial wave expansion of the linearized Vlasov-Poisson system in terms of SH. First, the dynamics of the Mie plasmon was studied in the SSVM. It is found that the spill-out-induced surface inhomogeneity of the self-consistent potential gives rise to a decay of the Mie plasmon. The corresponding damping mechanism can be explained by a mode conversion process from surface to volume plasmons. In particular, it corresponds to an energy transfer between two collective excitations of the electron system. The emergence of volume plasmons during the decay of the Mie plasmon was studied based on a spatial Fourier transform of the residual excitations of the electron density. Increasing the number of representative states in the multistream approach, it is shown that the residual volume plasmons are damped by single-particle excitations (Landau damping) due to the interaction of the plasmon with the subshell-induced inhomogeneity of the electron density inside the cluster. In this framework, Landau damping appears as a secondary process of the Mie-plasmon decay. Multistream calculations were performed for specific Na clusters up to a cluster radius of 1.2nm, where the largest cluster contains 198 electrons. The

plasmon damping rate shows good quantitative agreement with the damping rate obtained by the SSVM. Since the SSVM takes into account only collective excitations, the close agreement of the damping rates indicates the importance of mode conversion for the decay of the Mie plasmon. The damping rate shows a characteristic scaling with the inverse cluster radius, which is closely related to the surface-to-volume ratio of the ion sphere. In addition, the resonance frequency is redshifted with respect to the Mie frequency especially for small clusters. The damping rate coefficient of the multistream approach deviates from previous experimental and numerical results, which can be attributed to the lack of exchange and correlation effects in the underlying model. By further including exchange-correlation corrections in LDA, close agreement can be achieved with previous results. The linear calculations can be performed rather efficiently through the partial wave expansion of the wave functions and the self-consistent potential. Therefore, the full inclusion of the background ions within the present self-consistent treatment would be numerically feasible, thereby extending the jellium model to more realistic ion distributions. Furthermore, a treatment of clusters with an embedding material is desireable.

In Chapter 5, linear EM cluster excitations were treated in the SSVM. For this purpose, VSH were introduced to expand the linearized Vlasov-Maxwell system for clusters irradiated by a plane EM wave. While the SSVM neglects the single-particle properties of the cluster, it is able to account both for surface and radiative effects of the cluster dynamics in a self-consistent manner. In the first step, the cluster response was calculated for a homogeneous ion background. For large clusters, the damping rate of the Mie plasmon increases due to the increasing influence of radiation damping. For small clusters, the damping rate of the electrostatic treatment can be reproduced. In the intermediate regime of cluster sizes, the damping rate exhibits a local minimum, which is a well-known feature of the plasmon damping rate. It emerges due to the competition of surface and radiative effects. The results for the plasmon damping rate and the scattering cross sections were compared with corresponding results of the Mie-Drude theory. It is found that the results of the EM SSVM can be described to a good approximation by the Mie-Drude theory. In the second step, clusters with a diffuse surface profile were treated, thereby paying attention to cluster radii larger than 40nm and incoming light in the UV regime. By studying the absorption cross section as a function of the inhomogeneity scale length of the ion profile, a local maximum is found whose position and width depends on the cluster radius. The evolution of the electron density shows the generation of plasma waves close to the critical density, which propagate into the exterior region of the cluster. They are accompanied by a rapid increase of the internal electric field at the critical density. The author convinced that the plasma waves are purely electrostatic since they couple only to the self-consistent scalar potential. In this framework, the well-known theory of resonance absorption is generalized from plane to spherical surfaces with variable angles of incidence and light polarizations along the surface. As an improvement of the EM SSVM, it would be desireable to treat the EM multistream model with multiple electron states. In this framework, also single-particle excitations would be included in the EM description. From a technical point of view, the linear treatment of the EM multistream model requires the calculation of the partial wave expansion of products of VSH in terms of SH, which is a problem that is not discussed in common textbooks.

As a preparatory study for nonlinear electrostatic cluster excitations, the nonlinear

laser-driven dynamics of thin foils was investigated in Chapter 6 with an emphasis on the nonresonant collisionless absorption of laser light (Brunel mechanism). By studying the absorbed energy as a function of the laser field strength, Brunel's scaling is confirmed for thick foils or sufficiently large field strengths of the laser. In this regime, the coefficient of the energy absorption is in rather good agreement with previous results obtained from classical particle simulations. For thin foils and moderately large field strengths, the scaling exponent is increased. This can be explained by the fact that the scaling exponent of the number of outgoing electrons is larger than predicted by the classical Brunel theory due to the spill-out effect of the electron density.

Nonlinear electrostatic cluster excitations were investigated in Chapter 7 for spherical Na clusters of radius 1.1nm. First, the nonlinear Mie oscillation was studied based on an impulsive excitation of the cluster. For moderate perturbations, the resonance position of the Mie plasmon is blueshifted with respect to the linear result. In addition, the plasmon linewidth decreases. For sufficiently large perturbations, dynamical deformation effects are observed, which lead to a splitting of the Mie resonance. This splitting can be explained by a coupling of the cluster dipole moment to the quadrupole field induced by the electron cloud exterior to the cluster region. In contrast to the linear regime where the long-time behavior of the cluster dynamics is determined by single-particle excitations, the residual excitations in the strongly nonlinear regime are characterized by local density fluctuations on the timescale of the plasma period. Secondly, the electron dynamics was studied for clusters irradiated by five-cycle femtosecond laser pulses with peak intensities up to approximately $10^{14}\mathrm{W/cm}^2$ and a laser period of 3.5fs. It is found that the dynamics in the interior region of the cluster is strongly influenced by plasma waves that are generated at the cluster surface in the presence of strong laser-induced polarization fields. They are accelerated through the cluster by the laser field. Enhanced outer ionization can be observed when plasma waves reach the cluster surface. As a main feature, the emission of electron wave packets is favored at the cluster poles. This behavior is accompanied by a focusing of the incoming plasma waves onto the polarization axis of the laser. Furthermore, the interference of internal plasma waves and recombining electron wave packets leads to fast density oscillation on the attosecond scale. In the future, it would be instructive to analyze in more detail how the present plasma-wave propagation and enhanced outer ionization at the cluster poles depends on the laser frequency and the pulse duration. In particular, the evaluation of the energy distribution function would give rise to more insight into the kinetic energies of the emitted electrons. In addition, the present nonlinear Vlasov-Poisson code could be used to investigate the dynamics of nonspherical clusters with a rotational axis of symmetry.

Finally, it is mentioned that a proper inclusion of correlation effects in the description of the cluster electrons is desirable, which could be achieved e.g. through the quantum Boltzmann equation. Furthermore, exchange effects could be included in a systematic way by the Hartree-Fock method.

Appendix

A.1 Appendix to Chapter 2

Table A.1.1: Electron configurations of Na clusters

l	N_l
0	2
1	2
2	2
3	1
4	1

$R = 7.56$, $N_e = 68$

l	N_l
0	3
1	2
2	2
3	1
4	1
5	1

$R = 8.36$, $N_e = 92$

l	N_l
0	3
1	3
2	2
3	2
4	1
5	1
6	1

$R = 9.57$, $N_e = 138$

l	N_l
0	4
1	3
2	3
3	2
4	2
5	1
6	1
7	1

$R = 10.8$, $N_e = 198$

A.2 Appendix to Chapter 4

A.2.1 Completeness of the Partial Wave Expansion

In order to describe perturbations of the electron density in a single sector l' of the electron density,

$$n^{(1)} = n^{(1)}_{l''}(r,t)Y_{l'0}(\theta), \tag{A.2.1}$$

it is shown that partial waves with quantum numbers $\bar{l} \notin M_{l'l}$ have to be excluded in the expansion (4.1.22) of the linearized wave function $\varphi^{(1)}_{nlm}$. To proof the assertion, an ansatz

$$\varphi^{(1)}_{nlm}(\boldsymbol{r},t) = \sum_{\bar{l}\notin M_{l'l}} g_{nlm\,\bar{l}}\,(r,t)\,Y_{\bar{l}m}(\theta,\phi) \tag{A.2.2}$$

is chosen. In the following, it is demonstrated that wave functions of this form couple to sectors $l'' \neq l'$ of $n^{(1)}$.

With the definition (4.1.20b) of $n^{(1)}$, the contribution of electron stream (nlm) to $n^{(1)}$ is determined by the product $\varphi^{(0)\,*}_{nlm}\,\varphi^{(1)}_{nlm}$. Therefore, the partial wave expansion of this product is investigated based on the ansatz (A.2.2),

$$\varphi^{(0)\,*}_{nlm}\,\varphi^{(1)}_{nlm} = \sum_{\bar{l}\notin M_{l'l}} \sum_{l''\in M_{\bar{l}l}} R^{*}_{nl}\, g_{nlm\,\bar{l}}\,(-1)^{m} C_{l(-m)\,\bar{l}m\,l''} Y_{l''0}. \tag{A.2.3}$$

Here, the steps have been followed, which were introduced in (4.1.29). From (A.2.3) it is clear that one has to analyze the possible values of l'', which are generated by the double sum. The set of possible l''-values for fixed values of l and l' is given by

$$\left\{ l'' \in \mathbb{N}_0 \,:\, l'' \in M_{\bar{l}l} \,\wedge\, \bar{l} \in \overline{M}_{l'l} \right\}. \tag{A.2.4}$$

Here, the set $\overline{M}_{l'l} = \{\bar{l} \in \mathbb{N}_0 : \bar{l} \notin M_{l'l}\}$ defines the complement of $M_{l'l}$. In the following, one has to proof that the value l' is not contained in the set (A.2.4). Therefore, it is convenient to rewrite the set $M_{l'l}$ (see (4.1.10)),

$$M_{l'l} = \left\{ \bar{l} \in \mathbb{N}_0 \,:\, \bar{l} = |l-l'| + 2n\,,\; n \in \mathbb{Z} \,:\, n \geq 0 \,\vee\, n \,\leq \min(l,l') \right\}. \tag{A.2.5}$$

Then, $\overline{M}_{l'l}$ can be written in the form

$$\overline{M}_{l'l} = A_1 \cup A_2, \tag{A.2.6a}$$

$$A_1 = \left\{ \bar{l} \in \mathbb{N}_0 \,:\, \bar{l} = |l-l'| + 2n + 1\,,\; n \in \mathbb{Z} \right\}, \tag{A.2.6b}$$

$$A_2 = \left\{ \bar{l} \in \mathbb{N}_0 \,:\, \bar{l} = |l-l'| + 2n\,,\; n \in \mathbb{Z} \,:\, n < 0 \,\vee\, n > \min(l,l') \right\}. \tag{A.2.6c}$$

Now, it will be discussed seperatly, which values of l'' are generated in (A.2.4) for $\bar{l} \in A_1$ respectively $\bar{l} \in A_2$. For the discussion, the two relations (A.2.6b) and (A.2.5) will be combined.

First, the case $\bar{l} \in A_1$ is considered. Then, the possible l''-values read

$$\begin{gathered} l'' = ||l-l'| + 2n + 1 - l| + 2m, \quad n \in \mathbb{Z}, \\ 0 \leq m \leq \min(|l-l'| + 2n + 1, l). \end{gathered} \tag{A.2.7}$$

In the present case, one can conclude that every value of l'' can be written in the form $l'' = \pm l' + k$, where k is an odd number. In conclusion, one obtains $l'' \neq l'$ for $\bar{l} \in A_1$.

Now, the focus is put on the case $\bar{l} \in A_2$. Here, all values of l'' can be written in the form

$$\begin{gathered} l'' = ||l-l'| + 2n - l| + 2m, \quad n < 0 \,\vee\, n > \min(l,l'), \\ 0 \leq m \leq \min(|l-l'| + 2n, l). \end{gathered} \tag{A.2.8}$$

For the further analysis, the two cases $l \geq l'$ and $l < l'$ have to be distinguished. If

$l \geq l'$, one gets

$$\begin{gathered} l'' = |-l'+2n|+2m, \quad n<0 \vee n>l', \\ 0 \leq m \leq \min(l-l'+2n, l). \end{gathered} \tag{A.2.9}$$

For $l < l'$, (A.2.8) yields

$$\begin{gathered} l'' = |l'-2l+2n|+2m, \quad n<0 \vee n>l, \\ 0 \leq m \leq \min(l'-l+2n, l). \end{gathered} \tag{A.2.10}$$

In summary, all values of l'' for $\bar{l} \in A_2$ can be summarized as follows,

$$\begin{aligned} l'' = & \begin{cases} l'-2n+2m, & l \geq l', \quad n<0, \quad 0 \leq m \leq l-l'+2n \\ -l'+2n+2m, & l \geq l', \quad n>l', \quad 0 \leq m \leq l \\ |l'-2l+2n|+2m, & l<l', \quad n<0, \quad 0 \leq m \leq \min(l'-l+2n, l) \\ l'-2l+2n+2m, & l<l', \quad n>l, \quad 0 \leq m \leq l \end{cases} \\ & \begin{cases} >l', & l \geq l', \quad n<0, \quad 0 \leq m \leq l-l'+2n \\ >l', & l \geq l', \quad n>l', \quad 0 \leq m \leq l \\ <l', & l<l', \quad n<0, \quad 0 \leq m \leq \min(l'-l+2n, l) \\ >l', & l<l', \quad n>l, \quad 0 \leq m \leq l \quad . \end{cases} \end{aligned} \tag{A.2.11}$$

In the case $l < l'$ and $n < 0$, the upper bound was estimated according to

$$\begin{aligned} & |l'-2l+2n|+2m \\ = & \max(l'-l+2n, l) - \min(l'-l+2n, l) + 2m \\ \leq & \max(l'-l+2n, l) + \min(l'-l+2n, l) \\ = & l'+2n < l', \end{aligned} \tag{A.2.12}$$

where the restrictions $m \leq \min(l'-l+2n, l)$ and $n < 0$ were taken into account. The estimation in (A.2.11) shows that the set (A.2.4) does not contain the number l'. In conclusion, wave functions with a partial wave expansion (A.2.2) do not have to be taken into account in order to describe density perturbations of the form (A.2.1).

A.2.2 Energy Absorption in Linear Perturbation Theory

In the following, it is shown that the first-order perturbation theory is not sufficient to describe the energy absoprtion of the cluster in the presence of an external field $\phi_{ext}(\boldsymbol{r}) \sim Y_{l'0}(\Omega)$. The energy operator of the Vlasov theory is defined by

$$E = \frac{p^2}{2} - \frac{1}{2}\phi_{ee} - \phi_{ion}. \tag{A.2.13}$$

Here, ϕ_{ee} is the self-consistent potential of the electron-electron interaction and ϕ_{ion} the potential of the ions. In particular, it will be demonstrated that the expectation value $\langle E \rangle$ vanishes in linear perturbation theory. Up to linear order in the perturbation, $\langle E \rangle$

reads

$$\begin{aligned}\langle E\rangle &= \sum_{l,m,n}\langle\varphi_{nlm}|E|\varphi_{nlm}\rangle \\ &= E^{(0)} + \sum_{l,m,n} 2\Re\langle\varphi^{(0)}_{nlm}|E_0|\varphi^{(1)}_{nlm}\rangle - \frac{1}{2}\langle\varphi^{(0)}_{nlm}|\phi^{(1)}|\varphi^{(0)}_{nlm}\rangle.\end{aligned} \tag{A.2.14}$$

Here, the energy operator E_0 in the equilibrium state was introduced, which is evaluated with the equilibrium potential $\phi^{(0)}_{ee}$ and which is spherically symmetric. Due to the spherical symmetry of E_0, the following proportionality holds:

$$\begin{aligned}\sum_m\langle\varphi^{(0)}_{nlm}|E_0|\varphi^{(1)}_{nlm}\rangle &\sim \sum_m\sum_{\bar{l}\in M_{l'l}} C_{l'0\,lm\,\bar{l}}\int_\Omega Y^*_{lm}Y_{\bar{l}m}d\Omega \\ &= \sum_m C_{l'0\,lm\,l} = \int_\Omega Y_{l'0}\underbrace{\sum_m |Y_{lm}|^2}_{=\text{const}}\,d\Omega \sim \delta_{l'0}.\end{aligned} \tag{A.2.15}$$

Here, the expansion (4.1.28) of the linearized wave function was introduced. Furthermore, the expectation value of $\phi^{(1)}(\boldsymbol{r}) \sim Y_{l'0}(\Omega)$ with respect to the equilibrium wave functions in (A.2.14) can be evaluated as follows:

$$\sum_m\langle\varphi^{(0)}_{nlm}|\phi^{(1)}|\varphi^{(0)}_{nlm}\rangle \sim \int_\Omega Y_{l'0}\underbrace{\sum_m |Y_{lm}|^2}_{=\text{const}}\,d\Omega \sim \delta_{l'0}. \tag{A.2.16}$$

Since the external perturbation is nonspherical ($l' \neq 0$), all linear terms in (A.2.14) vanish. The quadratic terms in (A.2.14), which are generated by the linearized wave functions, are not sufficient to describe the energy absoprtion consistently up to second order, since the second-order wave functions give rise to further second-order contributions to the absorbed energy.

A.3 Appendix to Chapter 5

A.3.1 Action of the Laplace Operator on a Vector Function

For the solution to the wave equation of the vector potential $\boldsymbol{A}$, one has to evaluate the action of the Laplacian on $\boldsymbol{A}$, which is represented by the following expansion in terms of VSH ($\Omega = (\theta, \varphi)$):

$$\boldsymbol{A}(\boldsymbol{r},t) = \sum_{l,m} A^{(1)}_{lm}(r,t)\boldsymbol{Y}_{lm}(\Omega) + A^{(2)}_{lm}(r,t)\boldsymbol{\Psi}_{lm}(\Omega) + A^{(3)}_{lm}(r,t)\boldsymbol{\Phi}_{lm}(\Omega). \tag{A.3.1}$$

For reasons of clarity, the Einstein summation convention is used in this section. The following relations are frequently used for the calculation of $\Delta\boldsymbol{A}$ in addition to the

definition (5.1.1) of the VSH:

$$\Delta(fg) = \Delta f + \Delta g + 2\nabla f \cdot \nabla g, \tag{A.3.2a}$$

$$\nabla m(r) \cdot \nabla n(\Omega) = 0, \tag{A.3.2b}$$

$$\boldsymbol{e}_r \times \nabla\big(m(r)n(\Omega)\big) = m(r)\boldsymbol{e}_r \times \nabla n(\Omega). \tag{A.3.2c}$$

Here, $f(\boldsymbol{r})$, $g(\boldsymbol{r})$, $m(r)$ and $n(\Omega)$ are scalar functions.

In the following, the action of the Laplacian on different partial waves of (A.3.1) is calculated separately. First, the focus is put on partial waves associated with $\boldsymbol{Y}_{lm}$.

$$\Delta(A^{(1)}_{lm}\boldsymbol{Y}_{lm})_i = (\boldsymbol{Y}_{lm})_i \Delta A^{(1)}_{lm} + A^{(1)}_{lm}\Delta(\boldsymbol{Y}_{lm})_i + 2\underbrace{\nabla A^{(1)}_{lm} \cdot \nabla(\boldsymbol{Y}_{lm})_i}_{=0}\,, \tag{A.3.3a}$$

$$\Delta(\boldsymbol{Y}_{lm})_i = Y_{lm}\Delta(e_r)_i + (e_r)_i \Delta Y_{lm} + 2\nabla(e_r)_i \cdot \nabla Y_{lm}\,, \tag{A.3.3b}$$

$$\begin{aligned}
\Delta(e_r)_i &= \Delta\frac{r_i}{r} = \sum_{k=1}^{3}\partial_k^2\frac{r_i}{r} \\
&= \sum_{k=1}^{3}\partial_k\left(\frac{\delta_{ik}}{r} - \frac{r_i r_k}{r^3}\right) \\
&= \sum_{k=1}^{3}\left(-\frac{\delta_{ik}}{r^2}\frac{r_k}{r} - \frac{1}{r^3}(\delta_{ik}r_k + r_i) + \frac{3r_i r_k}{r^4}\frac{r_k}{r}\right) \\
&= -\frac{r_i}{r^3} - \frac{4r_i}{r^3} + \frac{3r_i}{r^3}\underbrace{\sum_{k=1}^{3}\frac{r_k^2}{r^2}}_{=1} = -\frac{2r_i}{r^3}\,,
\end{aligned} \tag{A.3.3c}$$

$$\begin{aligned}
\nabla(\boldsymbol{e}_r)_i \cdot \nabla Y_{lm} &= \left(\partial_k\frac{r_i}{r}\right)(\cdot\partial_k Y_{lm}) \\
&= \left(\frac{\delta_{ik}}{r} - \frac{r_i}{r^2}\frac{r_k}{r}\right)(\partial_k Y_{lm}) \\
&= \frac{\partial_i Y_{lm}}{r} - \frac{r_i}{r^3}\underbrace{\boldsymbol{r}\cdot\nabla Y_{lm}}_{=0} = \frac{\partial_i Y_{lm}}{r}\,,
\end{aligned} \tag{A.3.3d}$$

$$\Delta(A^{(1)}_{lm}\boldsymbol{Y}_{lm}) = \boldsymbol{Y}_{lm}\left(\Delta_r - \frac{1}{r^2}\Big(l(l+1)+2\Big)\right)A^{(1)}_{lm} + \frac{2}{r^2}\boldsymbol{\Psi}_{lm}\,. \tag{A.3.3e}$$

Now, the focus is put on partial waves corresponding to the VSH $\boldsymbol{Y}_{lm}$. By using the relations

$$[\Delta, r] = \frac{2}{r} + 2\partial_r, \quad \left(\frac{2}{r} + 2\partial_r\right)\nabla Y_{lm} = 0, \tag{A.3.4}$$

one gets

$$\Delta(A_{lm}^{(2)}\boldsymbol{\Psi}_{lm})_i = (\boldsymbol{\Psi}_{lm})_i \Delta A_{lm}^{(2)} + A_{lm}^{(2)} \Delta(\boldsymbol{\Psi}_{lm})_i + 2\underbrace{\nabla A_{lm}^{(2)} \cdot \nabla(\boldsymbol{\Psi}_{lm})_i}_{=0} , \tag{A.3.5a}$$

$$\begin{aligned} \Delta\boldsymbol{\Psi}_{lm} &= \Delta r \nabla Y_{lm} = r\nabla\Delta Y_{lm} = r\nabla\left(-\frac{l(l+1)}{r^2}\right) Y_{lm} \\ &= -r\left(-\frac{2l(l+1)}{r^3}(\nabla r) + \frac{l(l+1)}{r^2}\nabla\right) Y_{lm} \\ &= \frac{2l(l+1)}{r^2}\boldsymbol{Y}_{lm} - \frac{l(l+1)}{r^2}\boldsymbol{\Psi}_{lm} , \end{aligned} \tag{A.3.5b}$$

$$\Delta(A_{lm}^{(2)}\boldsymbol{\Psi}_{lm}) = \boldsymbol{\Psi}_{lm}\left(\Delta_r - \frac{l(l+1)}{r^2}\right) A_{lm}^{(2)} + \boldsymbol{Y}_{lm}\frac{2l(l+1)}{r^2} A_{lm}^{(2)} . \tag{A.3.5c}$$

Finally, the action of the Laplace operator on the solenoidal part of (A.3.1) associated with the vector fields $\boldsymbol{\Phi}_{lm}$ is left.

$$\Delta(A_{lm}^{(3)}\boldsymbol{\Phi}_{lm})_i = (\boldsymbol{\Phi}_{lm})_i \Delta A_{lm}^{(3)} + A_{lm}^{(3)} \Delta(\boldsymbol{\Phi}_{lm})_i + 2\underbrace{\nabla A_{lm}^{(3)} \cdot \nabla(\boldsymbol{\Phi}_{lm})_i}_{=0} , \tag{A.3.6a}$$

$$\begin{aligned} \Delta(\boldsymbol{\Phi}_{lm})_i &= \sum_{n=1}^{3} \partial_n^2 \epsilon_{ijk} r_j \partial_k Y_{lm} \\ &= \sum_{n=1}^{3} \epsilon_{ijk}\Big(\underbrace{\partial_n^2 r_j}_{=0} + r_j \partial_k \partial_n^2 Y_{lm} + 2\underbrace{(\partial_n r_j)}_{\delta_{nj}}(\partial_n \partial_k Y_{lm})\Big) \\ &= 2\underbrace{\epsilon_{ijk}\partial_j \partial_k}_{=0} Y_{lm} + \sum_{n=1}^{3} \epsilon_{ijk} r_j \partial_k \partial_n^2 Y_{lm} \\ &= (\boldsymbol{r} \times \nabla \Delta Y_{lm})_i = -\frac{l(l+1)}{r^2}(\boldsymbol{\Phi}_{lm})_i , \end{aligned} \tag{A.3.6b}$$

$$\Delta(A_{lm}^{(3)}\boldsymbol{\Phi}_{lm}) = \boldsymbol{\Phi}_{lm}\left(\Delta_r - \frac{l(l+1)}{r^2}\right) A_{lm}^{(3)} . \tag{A.3.6c}$$

In summary, one ends up with the following expansion of $\Delta\boldsymbol{A}$ in terms of VSH:

$$\begin{aligned} \Delta\boldsymbol{A} = \sum_{l,m} \quad & \boldsymbol{Y}_{lm}\left(\Big(\Delta_r - \frac{l(l+1)+2}{r^2}\Big) A_{lm}^{(1)} + \frac{2l(l+1)}{r^2} A_{lm}^{(2)}\right) \\ & + \boldsymbol{\Psi}_{lm}\left(\Big(\Delta_r - \frac{l(l+1)}{r^2}\Big) A_{lm}^{(2)} + \frac{2}{r^2} A_{lm}^{(1)}\right) \\ & + \boldsymbol{\Phi}_{lm}\left(\Delta_r - \frac{l(l+1)}{r^2}\right) A_{lm}^{(3)}. \end{aligned} \tag{A.3.7}$$

A.3.2 Calculation of Scattering and Absorption Cross Sections

For the calculation of the scattering and absorption cross sections, one has to calculate the surface integral

$$P = \int\limits_{\partial V_{R'}} \boldsymbol{S} \cdot d\boldsymbol{\mathcal{F}}, \quad d\boldsymbol{\mathcal{F}} = R'^2 d\Omega \boldsymbol{e}_r, \tag{A.3.8}$$

where $\partial V_{R'}$ is the surface of a sphere of radius $R' \gg R$ and $\boldsymbol{S}(\boldsymbol{r}, \boldsymbol{t})$ the Poynting vector of an EM field, which is represented by the potentials

$$\phi(\boldsymbol{r}, t) = \sum_{l,m} \phi_{lm}(r, t) Y_{lm}(\Omega), \tag{A.3.9a}$$

$$\boldsymbol{A}(\boldsymbol{r}, t) = \sum_{l,m} A^{(a)}_{lm}(r, t) \boldsymbol{Y}_{lm}(\Omega) + A^{(b)}_{lm}(r, t) \boldsymbol{\Psi}_{lm}(\Omega) + A^{(c)}_{lm}(r, t) \boldsymbol{\Phi}_{lm}(\Omega). \tag{A.3.9b}$$

To determine $\boldsymbol{S}$, one has to calculate the corresponding electric and magnetic field by using the relations (5.1.7a) and (5.1.7b),

$$\begin{aligned} \boldsymbol{\mathcal{E}}(\boldsymbol{r}, t) &= -\nabla\phi(\boldsymbol{r}, t) - \frac{1}{c'}\partial_t \boldsymbol{A}(\boldsymbol{r}, t) \\ &= -\sum_{lm} \left(\phi'_{lm} + \frac{1}{c'} \dot{A}^{(a)}_{lm} \right) \boldsymbol{Y}_{lm} + \left(\frac{\phi_{lm}}{r} + \frac{1}{c'} \dot{A}^{(b)}_{lm} \right) \boldsymbol{\Psi}_{lm} \\ &\qquad + \frac{1}{c'} \dot{A}^{(c)}_{lm} \boldsymbol{\Phi}_{lm}(\Omega), \end{aligned} \tag{A.3.10a}$$

$$\begin{aligned} \boldsymbol{\mathcal{B}}(\boldsymbol{r}, t) &= \nabla \times \boldsymbol{A}(\boldsymbol{r}, t) \\ &= -\sum_{lm} \frac{l(l+1)}{r} A^{(c)}_{lm} \boldsymbol{Y}_{lm} + \frac{1}{r} \partial_r (r A^{(c)}_{lm}) \boldsymbol{\Psi}_{lm} \\ &\qquad + \frac{1}{r} \left(A^{(a)}_{lm} - \partial_r (r A^{(b)}_{lm}) \right) \boldsymbol{\Phi}_{lm}. \end{aligned} \tag{A.3.10b}$$

By inserting the Poynting vector (measured in units of $n_0 \hbar \omega_p^2 l^*$)

$$\boldsymbol{S} = c' \boldsymbol{\mathcal{E}} \times \boldsymbol{\mathcal{B}} \tag{A.3.11}$$

in (A.3.8) together with the fields (A.3.10), one has to evaluate the following integrals with the help of the definition (5.1.1) and the orthogonality relations (5.1.3) of the VSH:

a)

$$\int\limits_{S_2} (\boldsymbol{\Phi}_{lm} \times \boldsymbol{\Phi}_{l'm'}) \cdot \boldsymbol{e}_r \; d\Omega = \int\limits_{S_2} \underbrace{(\boldsymbol{e}_r \times \boldsymbol{\Phi}_{lm})}_{-\boldsymbol{\Psi}_{lm}} \cdot \boldsymbol{\Phi}_{l'm'} \; d\Omega = 0, \tag{A.3.12}$$

$$(\boldsymbol{e}_r \times \boldsymbol{\Phi}_{lm}) = \boldsymbol{e}_r \times (\boldsymbol{e}_r \times \boldsymbol{\Psi}_{lm}) = \boldsymbol{e}_r (\boldsymbol{e}_r \cdot \boldsymbol{\Psi}_{lm}) - (\boldsymbol{e}_r \cdot \boldsymbol{e}_r) \boldsymbol{\Psi}_{lm} = -\boldsymbol{\Psi}_{lm},$$

b)

$$\int\limits_{S_2} (\boldsymbol{\Psi}_{lm} \times \boldsymbol{\Psi}_{l'm'}) \cdot \boldsymbol{e}_r \; d\Omega = \int\limits_{S_2} \underbrace{(\boldsymbol{e}_r \times \boldsymbol{\Psi}_{lm})}_{\boldsymbol{\Phi}_{lm}} \cdot \boldsymbol{\Psi}_{l'm'} \; d\Omega = 0, \tag{A.3.13}$$

c)

$$\begin{aligned} \int\limits_{S_2} (\boldsymbol{\Psi}_{lm} \times \boldsymbol{\Phi}_{l'm'}) \cdot \boldsymbol{e}_r \; d\Omega &= \int\limits_{S_2} \underbrace{(\boldsymbol{e}_r \times \boldsymbol{\Psi}_{lm})}_{\boldsymbol{\Phi}_{lm}} \cdot \boldsymbol{\Phi}_{l'm'} \; d\Omega = 0 \\ &= \int\limits_{S_2} \boldsymbol{\Phi}_{lm} \cdot \boldsymbol{\Phi}_{l'm'} \; d\Omega \\ &= (-1)^m \int\limits_{S_2} \boldsymbol{\Phi}^*_{l,-m} \cdot \boldsymbol{\Phi}_{l'm'} \; d\Omega \\ &= \delta_{ll'} \, \delta_{-m,m'} \, (-1)^m \, l(l+1). \end{aligned} \tag{A.3.14}$$

It is noted that any contribution of the fields to (A.3.8) involving the vector function $\boldsymbol{Y}_{lm}$ vanishes, since $\boldsymbol{Y}_{lm}$ is parallel to the normal vector $\boldsymbol{e}_r$. With the obtained relation (A.3.14), one can perform the surface integral (A.3.8), which gives

$$\begin{aligned} P = c' \sum_{lm} (-1)^{m+1} \, l(l+1) \Bigg\{ &\left(\phi_{lm} + \frac{1}{c'} r \dot{A}^{(b)}_{lm} \right) \left(\partial_r \left(r A^{(b)}_{l,-m} \right) - A^{(a)}_{l,-m} \right) \\ &+ \frac{1}{c'} \dot{A}^{(c)}_{lm} r \partial_r \left(r A^{(c)}_{l,-m} \right) \Bigg\} \Bigg|_{r=R'} . \end{aligned} \tag{A.3.15}$$

A.4 Appendix to Chapter 7

A.4.1 Relaxation Method for Poisson's Equation

In Chapter 7, the numerical solution of Poisson's equation

$$\Delta \phi(\boldsymbol{r}) = -\rho(\boldsymbol{r}) \tag{A.4.1}$$

is performed on the basis of a relaxation method. In this framework, $\phi(\boldsymbol{r})$ is calculated by alternatively solving the following inhomogeneous heat conduction equation for the auxiliary potential $\phi'(\boldsymbol{r}, \tau)$:

$$\partial_\tau \phi'(\boldsymbol{r}, \tau) = \Delta \phi'(\boldsymbol{r}, \tau) + \rho(\boldsymbol{r}) \tag{A.4.2}$$

By introducing the spatial Fourier representation

$$g(\boldsymbol{r}) = \frac{1}{\sqrt{2\pi}^3} \int\limits_{\mathbb{R}^3} \tilde{g}(\boldsymbol{k}) e^{i\boldsymbol{k}\cdot\boldsymbol{r}} d^3k \tag{A.4.3}$$

of a functiong $g(\boldsymbol{r})$, it can be shown that $\phi'(\boldsymbol{r},\tau)$ converges to $\phi(\boldsymbol{r})$ in the limit $\tau \to \infty$. In Fourier space, equations (A.4.2) and (A.4.1) read

$$\partial_t \tilde{\phi}'(\boldsymbol{k},\tau) = -k^2 \tilde{\phi}'(\boldsymbol{k},\tau) + \tilde{\rho}(\boldsymbol{k}), \tag{A.4.4a}$$

$$k^2 \tilde{\phi}(\boldsymbol{k}) = -\tilde{\rho}(\boldsymbol{k}). \tag{A.4.4b}$$

The general solution to (A.4.4a) reads

$$\phi'(\boldsymbol{k},\tau) = A e^{-k^2\tau} + \frac{1}{k^2}\tilde{\rho}(\boldsymbol{k}), \quad A \in \mathbb{R}. \tag{A.4.5}$$

Then, by taking into account (A.4.4b), the following limit can be deduced:

$$\lim_{\tau\to\infty} \tilde{\phi}'(\boldsymbol{k},\tau) = \frac{1}{k^2}\,\tilde{\rho}(\boldsymbol{k}) = \tilde{\phi}(\boldsymbol{k}) \tag{A.4.6}$$

Therefore, $\phi'(\boldsymbol{r},\tau)$ converges to $\phi(\boldsymbol{r})$ for large values of τ. Finally, it is noted that τ is only an auxiliary variable which should not be confused with the physical time t.

In Appendix (A.4.2), it is demonstrated how equation (A.4.2) can be solved numerically for azimuthally symmetric charge distributions $\rho(z,\varrho)$ in cylindrical coordinates. For this purpose, one has to specify the boundary values of $\phi(z,\varrho)$ at the boundary of the computational grid. In particular, these values can be approximated by the following multipole expansion of $\phi(\boldsymbol{r})$ truncated at the mutipole order:

$$\phi(\boldsymbol{r}) = \frac{Q}{4\pi r} + \frac{\boldsymbol{p}\cdot\boldsymbol{r}}{4\pi r^3} + \frac{1}{2}\,\frac{\boldsymbol{r}^T\cdot\boldsymbol{Q}\cdot\boldsymbol{r}}{4\pi r^5}. \tag{A.4.7}$$

The dipole moment $\boldsymbol{p}$ and the quadrupole tensor Q_{ij} read

$$\boldsymbol{p} = \int_{\mathbb{R}^3} \rho(\boldsymbol{r})\,\boldsymbol{r}\,d^3r, \quad Q_{ij} = \int_{\mathbb{R}^3} (3r_ir_j - r^2\delta_{ij})\,\rho(\boldsymbol{r})\,d^3r. \tag{A.4.8}$$

By taking into account the symmetry of ρ, the multipole moments have the properties $\boldsymbol{p} \sim \boldsymbol{e}_z$ and $Q_{ij} \sim \delta_{ij}$. Therefore, the multipole expansion of $\phi(z,\varrho)$ in cylindrical coordinates is given by

$$\begin{aligned}
\phi(z,\varrho) &= \frac{Q}{4\pi r} + \frac{p_z\,z}{4\pi r^3} + \frac{1}{2}\,\frac{Q_{33}\,z^2 + Q_{11}\,\varrho^2}{r^5}, \quad r = \sqrt{z^2+\varrho^2},\\
p_z &= 2\pi \int_0^\infty\int_{-\infty}^\infty \rho(z,\varrho)\,z\,\varrho\,d\varrho\,dz,\\
Q_{11} &= Q_{22} = \pi \int_0^\infty\int_{-\infty}^\infty \varrho\,(\varrho^2 - 2z^2)\,\rho(z,\varrho)\,d\varrho\,dz,\\
Q_{33} &= 2\pi \int_0^\infty\int_{-\infty}^\infty \varrho\,(2z^2 - \varrho^2)\,\rho(z,\varrho)\,d\varrho\,dz.
\end{aligned} \tag{A.4.9}$$

A.4.2 Alternating Direction Implicit Scheme

In this section, the numerical solution of the two-dimensional Vlasov-Poisson system (7.0.4) in cylindrical coordinates is described. The numerical method is based on an alternating direction implicit (ADI) finite difference scheme [131]. It has been demonstrated in Appendix A.4.1 that the solution of Poisson's equation can be alternatively obtained by solving the heat conduction equation (A.4.2). In order to provide a compact numerical scheme both for the Schrödinger equation (7.0.4a) and the heat conduction equation (A.4.2), both equations are written in the compact form ($K \in \mathbb{C}$, $\beta \in \mathbb{R}$): (7.0.4)

$$K\frac{\partial}{\partial t}\psi(\boldsymbol{r},t) = H(\boldsymbol{r},t)\psi(\boldsymbol{r},t) + f(\boldsymbol{r},t), \quad H(\boldsymbol{r},t) = \beta\Delta_{z,\varrho} + \frac{m^2}{2\varrho^2} + V_z(\boldsymbol{r},t). \quad \text{(A.4.10)}$$

In this representation, the Schrödinger equation (7.0.4a) can be recovered by making the replacement $K = i$, $\beta = -1/2$, $f = 0$, $\psi = \bar{\varphi}_{nlm}$ and $V_z = -\phi$, where ϕ is the self-consistent potential. Furthermore, equation (A.4.2) for the auxiliary potential ϕ' can be obtained by making the replacement $K = 1$, $m = 0$, $V_z = 0$, $f = \rho$ and $\psi = \phi'$.

For the further discussion, the Hamiltonian is written in the following form:

$$H = H_\varrho + H_z, \quad \text{(A.4.11a)}$$

$$H_z = \beta\partial_z^2 + V_z(z,\varrho,t), \quad \text{(A.4.11b)}$$

$$H_\varrho = \beta(\partial^2\varrho + \varrho^{-1}\partial_\varrho) + V_\varrho, \quad V_\varrho(\varrho) = \frac{m^2}{2\varrho^2}. \quad \text{(A.4.11c)}$$

ADI Propagator

The time-propagation of ψ based on (A.4.10) can be performed numerically by a discretization of the time derivative. For this purpose, a time grid

$$t_n = n\Delta t, \quad n = 1, 2, \ldots, N \quad \text{(A.4.12)}$$

is introduced. In particular, to achieve global second-order accuracy of the numerical solution with respect to the time step Δt, the centered derivative of ψ is introduced,

$$K\frac{\psi^{n+1} - \psi^n}{\Delta t} = \frac{1}{2}H^{n+\frac{1}{2}}(\psi^{n+1} + \psi^n) + f^{n+\frac{1}{2}}. \quad \text{(A.4.13)}$$

Here, H has to be evaluated at the intermediate grid point $t_{n+1/2} = t_n + \Delta t/2$. This gives the following implicit Crank-Nicolson scheme [95]:

$$(2K - \Delta t H^{n+\frac{1}{2}})\psi^{n+1} = (2K + \Delta t H^{n+\frac{1}{2}})\psi^n + 2\Delta t f^{n+\frac{1}{2}}. \quad \text{(A.4.14)}$$

The ADI method is based on a splitting of the operators which act on the wave functions ψ^n and ψ^{n+1},

$$\begin{aligned} 2K \pm \Delta t H &= 2K \pm \Delta t H_\varrho \pm \Delta t H_z \\ &= \frac{1}{2K}[(2K \pm \Delta t H_\varrho)(2K \pm \Delta t H_z) - \Delta t^2 H_\varrho H_z]. \end{aligned} \quad \text{(A.4.15)}$$

The last term of second-order in Δt can be omitted. Then, (A.4.14) can be transformed into the ADI scheme

$$\begin{aligned} R^+ Z^+ \psi^{n+1} &= R^- Z^- \psi^n + \bar{f}^{n+\frac{1}{2}}, \\ R^+ &= K\alpha_\varrho - 2\Delta\varrho^2 H_\varrho, \\ R^- &= -K\alpha_\varrho - 2\Delta\varrho^2 H_\varrho, \\ Z^+ &= K\alpha_z - 2\Delta z^2 H_z^{n+1/2}, \\ Z^- &= -K\alpha_z - 2\Delta z^2 H_z^{n+1/2}, \\ \bar{f} &= \alpha_\varrho\, \alpha_z\, K\, \Delta t\, f, \end{aligned} \tag{A.4.16}$$

which can be used to propagate the function ψ^n at time t_n over one time step Δt. Here,

$$\alpha_\varrho = \frac{4\Delta\varrho^2}{\Delta t}, \quad \alpha_z = \frac{4\Delta z^2}{\Delta t} \tag{A.4.17}$$

are numerical constants including the spatial grid constants Δz and $\Delta\varrho$ of the computational grid.

Spatial Discretization of the Hamiltonian

In order to discretize the operators H_z and H_ϱ in (A.4.16), a spatial grid is introduced,

$$\begin{aligned} \varrho_j &= (j-0.5)\Delta\varrho, \quad j = 1, 2 \ldots, J\,, \\ z_k &= -z_{max} + (k-1)\Delta z, \quad k = 1, 2, \ldots, 2K\,, \\ \psi^n_{k,j} &= \psi(z_k, \varrho_j, t_n). \end{aligned} \tag{A.4.18}$$

If the edge coordinates z_{max} and ϱ_{max} of the computational grid are fixed (in addition to the number of grid points $2K$ and J), the grid constants are determined by

$$\begin{aligned} \Delta\varrho &= \frac{\varrho_{max}}{J - 1/2}, \\ \Delta z &= \frac{2z_{max}}{2K-1}. \end{aligned} \tag{A.4.19}$$

The action of the operators H_z and H_ϱ on the wave function can be calculated up to second-order accuracy in $\Delta\varrho$ and Δz by the following central difference formulas for the spatial derivatives ($\varrho_{j\pm1/2} = \varrho_j \pm \Delta\varrho/2$):

$$\begin{aligned} \Delta z(\partial_z\psi)_k &= \psi_{k+1} - \psi_{k-1}, \\ \Delta z^2(\partial_z^2\psi)_k &= \psi_{k+1} + \psi_{k-1} - 2\psi_k, \\ \Delta\varrho^2\left(\varrho^{-1}\partial_\varrho\psi + \partial_\varrho^2\psi\right)_j &= \psi_{j+1} + \psi_{j-1} - 2\psi_j + \frac{\Delta\varrho}{2\varrho_j}(\psi_{j+1} - \psi_{j-1}) \\ &= \frac{\varrho_{j+1/2}}{\varrho_j}\psi_{j+1} + \frac{\varrho_{j-1/2}}{\varrho_j}\psi_{j-1} - 2\psi_j. \end{aligned} \tag{A.4.20}$$

These expressions can be used to write the operators $R^{\pm}$ and $Z^{\pm}$ in discretized form

$$\begin{aligned}(R^{\pm}\psi)^n_{k,j} &= a_{\varrho,j}\,\psi^n_{k,j-1} + b^{\pm}_{\varrho,j}\,\psi^n_{k,j} + c_{\varrho,j}\,\psi^n_{k,j+1}, \\ a_{\varrho,j} &= -2\beta\frac{\varrho_{j-1/2}}{\varrho_j}, \\ c_{\varrho,j} &= -2\beta\frac{\varrho_{j+1/2}}{\varrho_j}, \\ b^{\pm}_{\varrho,j} &= \pm K\alpha_{\varrho} + 4\beta - 2\Delta\varrho^2 V_{\varrho,j},\end{aligned} \tag{A.4.21a}$$

$$\begin{aligned}(Z^{\pm}\psi)^n_{k,j} &= a_{z,k}\,\psi^n_{k-1,j} + b^{\pm}_{z,k}\,\psi^n_{k,j} + c_{z,k}\,\psi^n_{k+1,j}, \\ a_{z,k} &= -2\beta, \\ c_{z,k} &= -2\beta, \\ b^{+}_{z,k} &= K\alpha_z + 4\beta - 2\Delta z^2 V^{n+1/2}_{z,k}, \\ b^{-}_{z,k} &= -K\alpha_z + 4\beta - 2\Delta z^2 V^{n+1/2}_{z,k},\end{aligned} \tag{A.4.21b}$$

where $R^{\pm}$ and $Z^{\pm}$ become tridiagonal matrices.

Boundary Conditions

In order to truncate the ADI scheme (A.4.16) based on the spatial discretization (A.4.21), one has to specify boundary values $\psi^{(b)}$ outside the computational grid at

$$\begin{aligned}z_0 &= -z_{2K+1}, \\ z_{2K+1} &= z_{max} + \Delta z, \\ \varrho_{J+1} &= \varrho_{max} + \Delta\varrho.\end{aligned} \tag{A.4.22}$$

Due to the fact that $a_{\varrho,1} = 0$, the scheme is automatically truncated at ϱ_1 By solving the Schrödinger equation, the wave functions can be set to zero, $\psi^{(b)} = \bar{\varphi}^{(b)}_{nlm} = 0$. This boundary condition requires a sufficiently large computational grid to account for outgoing parts of the wave functions. To solve the heat conduction equation for the auxiliary potential ϕ', the values $\psi^{(b)} = \phi'^{(b)}$ at time t_n are approximated by the multipole expansion (A.4.9) of the self-consistent potential ϕ up to the quadrupole term.

Based on the elementary boundary values $\psi^{(b)}$ and the relation (A.4.21), one can deduce the boundary values of the function $Z^{\pm}\psi^n$ at ϱ_{J+1},

$$\begin{aligned}&k = 1, \ldots, 2K: \\ &X^{(b)\pm}_k \equiv (Z^{\pm}\psi)_{k,J+1} = a_{z,k}\,\psi^{(b)}_{k-1,J+1} + b^{\pm,n}_{z,k}\,\psi^{(b)}_{k,J+1} + c_{z,k}\,\psi^{(b)}_{k+1,J+1}.\end{aligned} \tag{A.4.23}$$

Finally, the ADI scheme (A.4.16) can be solved for the function ψ^{n+1} by using LU decomposition [98] for the inversion of the tridiagonal matrices $Z^{\pm}$ and $R^{\pm}$ given in (A.4.21).

Numerical Algorithm

1. Multiplication by Z^- for $j = 1, \ldots, J$

$$
\begin{aligned}
Y_{k,j} &= Z^-_{kk'}\, \psi^n_{k',j}\,, \quad k = 2, \ldots, 2K-1 \\
\\
Y_{1,j} &= a_{z,1}\, \psi^{(b)}_{0,j} + b^-_{z,1}\, \psi^n_{1,j} + c_{z,1}\, \psi^n_{2,j}\,, \quad k = 1 \\
Y_{2K,j} &= a_{z,2K}\, \psi^n_{2K-1,j} + b^-_{z,2K}\, \psi^n_{2K,j} + c_{z,2K}\, \psi^{(b)}_{2K+1,j}\,, \quad k = 2K
\end{aligned}
\tag{A.4.24}
$$

2. Multiplication by R^- for $k = 1, \ldots, 2K$

$$
\begin{aligned}
Y'_{k,j} &= R^-_{jj'}\, Y_{k,j'}\,, \quad j = 2, \ldots, J-1 \\
\\
Y'_{k,1} &= b^-_{\varrho,1}\, Y_{1,j} + c_{\varrho,1}\, Y_{2,j}\,, \quad j = 1 \\
Y'_{k,J} &= a_{\varrho,J}\, Y_{k,J-1} + b^-_{\varrho,J}\, Y_{k,J} + c_{\varrho,J}\, X^{(b)-}_k\,, \quad j = J
\end{aligned}
\tag{A.4.25}
$$

3. Add inhomogeneity

$$
Y''_{k,j} = Y'_{k,j} + \bar{f}^{n+1/2}_{k,j}\,,
\tag{A.4.26}
$$

4. Inversion of R^+ for $k = 1, \ldots, 2K$

$$
\begin{aligned}
Y''_{k,j} &= R^+_{jj'} \bar{\psi}_{k,j'}, \quad j = 2, \ldots, J-1 \\
\\
Y''_{k,1} &= b^+_{\varrho,1}\, \bar{\psi}_{1,j} + c_{\varrho,1}\, \bar{\psi}_{2,j}, \quad j = 1 \\
Y''_{k,J} - c_{\varrho,J}\, X^{(b)+}_k &= a_{\varrho,J}\, \bar{\psi}_{k,J-1} + b^+_{\varrho,J}\, \bar{\psi}_{k,J}, \quad j = 2K
\end{aligned}
\tag{A.4.27}
$$

5. Inversion of Z^+ for $j = 1, \ldots, J$

$$
\begin{aligned}
\bar{\psi}_{k,j} &= Z^+_{kk'} \psi^{n+1}_{k',j}, \quad k = 2, \ldots, 2K-1 \\
\\
\bar{\psi}_{1,j} - a_{z,1}\, \psi^{(b)}_{0,j} &= b^+_{z,1}\, \psi^{n+1}_{1,j} + c_{z,1}\, \psi^{n+1}_{2,j}, \quad k = 1 \\
\bar{\psi}_{2K,j} - c_{z,2K}\, \psi^{(b)}_{2K+1,j} &= a_{z,2K}\, \psi^{n+1}_{2K-1,j} + b^+_{z,2K}\, \psi^{n+1}_{2K,j}, \quad k = 2K
\end{aligned}
\tag{A.4.28}
$$

Self-Consistent Propagation of the Vlasov-Poisson System

To propagate the representative states ψ^n at time t_n over a single time step Δt, one has to calculate the potential energy $V^{n+1/2}$ at the intermediate grid point. Therefore, the self-consistent potential ϕ has to be calculated at times $t_{n+1/2}$. Since the wave functions are calculated at the grid points t_n, one has to a proper approximation for

the charge density $\rho^{n+1/2}$. By discretizing the continuity equation for ρ with respect to the time variable, the following can be deduced with third-order accuracy:

$$\rho^{n+1/2} = \rho^{n-1/2} + \Delta t \, \mathrm{div} \boldsymbol{j}^n \tag{A.4.29}$$

Since the current density $\boldsymbol{j}^n$ can be calculated based on the wave functions ψ^n, this relation can be used to propagate the charge density on the intermediate grid. The scheme (A.4.29) can be truncated at $t_{1/2}$ by considering the fact that the electron system is in the equilibrium state at time $t = 0$. Therefore, one can set $\rho^{-1/2}$ equal to the equilibrium charge density $\rho^{(0)}$.

A.5 List of Abbreviations

SSVM	Single-state Vlasov model
PIC	Particle-in-cell
c.m.	Center of mass
EM	Electromagnetic
SH	Spherical harmonics
VSH	Vector spherical harmonics
DFT	Density functional theory
LDA	Local-density approximation
TDLDA	Time-dependent local-density approximation
RPA	Random-phase approximation

Bibliography

[1] O. F. Hagena, Z. Phys. D **4**, 291 (1987).

[2] J. Mattauch, H. Ewald, O. Hahn, and F. Strassmann, Z. Phys. **120**, 598 (1943).

[3] T. Ditmire, T. Donnelly, R. Falcone, and M. Perry, Phys. Rev. Lett. **75**, 3122 (1995).

[4] L. M. Chen, J. J. Park, K. H. Hong, I. W. Choi, J. L. Kim, J. Zhang, and C. Nam, Phys. Plasmas **9**, 3595 (2002).

[5] Y. Shao, T. Ditmire, J. Tisch, E. Springate, J. Marangos, and M. Hutchinson, Phys. Rev. Lett. **77**, 3343 (1996).

[6] E. Springate, N. Hay, J. W. G. Tisch, M. B. Mason, T. Ditmire, M. H. R. Hutchinson, and J. P. Marangos, Phys. Rev. A **61**, 063201 (2000).

[7] L. Köller, M. Schumacher, J. Köhn, S. Teuber, J. Tiggesbäumker, and K.-H. Meiwes-Broer, Phys. Rev. Lett. **82**, 3783 (1999).

[8] J. Jackson, *Classical Electrodynamics*, 2nd ed. (de Gruyter, 1975).

[9] F. R. S. Lord Rayleigh, Philos. Mag. **12**, 81 (1881).

[10] G. Mie, Ann. Phys. **330**, 377 (1908).

[11] L. Spitzer and R. Härm, Phys. Rev. **89**, 977 (1953).

[12] T. Fennel, G. F. Bertsch, and K.-H. Meiwes-Broer, Eur. Phys. J. **29**, 367 (2004).

[13] U. Kreibig and M. Vollmer, *Optical Properties of Metal Clusters*, Vol. 25 (Springer Science & Business Media, 2013).

[14] C. Sönnichsen, T. Franzl, T. Wilk, G. von Plessen, and J. Feldmann, New J. Phys. **4**, 93 (2002).

[15] W. Ekardt, Phys. Rev. B **31**, 6360 (1985).

[16] D. Bauer, F. Ceccherini, A. Macchi, and F. Cornolti, Phys. Rev. A **64**, 063203 (2001).

[17] W. Steffen and H.-J. Kull, Phys. Rev. E **93**, 033207 (2016).

[18] T. Fennel, K.-H. Meiwes-Broer, J. Tiggesbäumker, P.-G. Reinhard, P. M. Dinh, and E. Suraud, Rev. Mod. Phys. **82**, 1793 (2010).

[19] F. Greschik, L. Arndt, and H.-J. Kull, Europhys. Lett. **72**, 376 (2005).

[20] P. Mulser, M. Kanapathipillai, and D. H. H. Hoffmann, Phys. Rev. Lett. **95**, 103401 (2005).

[21] U. Kreibig, J. Phys. F: Met. Phys. **4**, 999 (1974).

[22] F. Megi, M. Belkacem, M. A. Bouchene, E. Suraud, and G. Zwicknagel, J. Phys. B: At. Mol. Opt. Phys. **36**, 273 (2003).

[23] H. Hövel, S. Fritz, A. Hilger, U. Kreibig, and M. Vollmer, Phys. Rev. B **48**, 18178 (1993).

[24] S. Berciaud, L. Cognet, P. Tamarat, and B. Lounis, Nano Lett. **5**, 515 (2005).

[25] J. Tiggesbäumker, L. Köller, K.-H. Meiwes-Broer, and A. Liebsch, Phys. Rev. A **48**, R1749 (1993).

[26] J. Euler, Z. Phys. **137**, 318 (1954).

[27] E. Coronado and G. C. Schatz, J. Chem. Phys. **119**, 3926 (2003).

[28] H.-J. Kull and A. El-Khawaldeh, *Classical Plasma Dynamics of Mie-Oscillations in Atomic Clusters*, J. Phys. Conf. Ser. (2018), accepted for publication.

[29] A. Kawabata and R. Kubo, J. Phys. Soc. Jpn. **21**, 1765 (1966).

[30] B. Delley and E. F. Steigmeier, Phys. Rev. B **47**, 1397 (1993).

[31] W. Ekardt, Phys. Rev. B **29**, 1558 (1984).

[32] M. S. Hansen and H. Nishioka, Z. Phys. D **28**, 73 (1993).

[33] L. H. Thomas, Math. Proc. Camb. Phil. Soc. **23**, 542–548 (1927).

[34] W. A. de Heer, Rev. Mod. Phys. **65**, 611 (1993).

[35] M. Brack, Rev. Mod. Phys. **65**, 677 (1993).

[36] W. D. Knight, W. A. de Heer, W. A. Saunders, K. Clemenger, M. Y. Chou, and M. L. Cohen, Chem. Phys. Lett. **134**, 1 (1987).

[37] W. D. Knight, K. Clemenger, W. A. de Heer, W. A. Saunders, M. Y. Chou, and M. L. Cohen, Phys. Rev. Lett. **52**, 2141 (1984).

[38] W. Ekardt and Z. Penzar, Phys. Rev. B **43**, 1322 (1991).

[39] T. Hirschmann, M. Brack, and J. Meyer, Ann. Phys. **506**, 336 (1994).

[40] I. A. Solov'yov, A. V. Solov'yov, and W. Greiner, J. Phys. B: At. Mol. Opt. Phys. **37**, L137 (2004).

[41] A. A. Lushnikov and A. J. Simonov, Z. Phys. **270**, 17 (1974).

[42] E. Zaremba and B. N. J. Persson, Phys. Rev. B **35**, 596 (1987).

[43] Y. E. Lozovik and V. N. Nishanov, Sov. Phys. Solid State **20**, 2111 (1978).

[44] D. B. T. Thoai and W. Ekardt, Solid State Commun. **41**, 687 (1982).

[45] W. Ekardt, Phys. Rev. Lett. **52**, 1925 (1984).

[46] W. Ekardt, Phys. Rev. B **32**, 1961 (1985).

[47] D. Strickland and G. Mourou, Opt. Commun. **56**, 219 (1985).

[48] T. Ditmire, J. W. G. Tisch, E. Springate, M. B. Mason, N. Hay, R. A. Smith, J. P. Marangos, and M. H. R. Hutchinson, Nature **386**, 54 (1997).

[49] F. Chandezon, C. Guet, B. A. Huber, D. Jalabert, M. Maurel, E. Monnand, C. Ristori, and J. C. Rocco, Phys. Rev. Lett. **74**, 3784 (1995).

[50] F. Calvayrac, P.-G. Reinhard, E. Suraud, and C. Ullrich, Phys. Rep. **337**, 493 (2000).

[51] C. Guet and L. Plagne, *Electron Dynamics in Metal Clusters* in *Theory of Atomic and Molecular Clusters*, Springer Series in Cluster Physics, edited by J. Jellinek (Springer, 1999) pp. 209–227.

[52] C. A. Ullrich, P.-G. Reinhard, and E. Suraud, J. Phys. B: At. Mol. Opt. Phys. **30**, 5043 (1997).

[53] P.-G. Reinhard and E. Suraud, Eur. Phys. J. D **3**, 175 (1998).

[54] F. Calvayrac, P.-G. Reinhard, and E. Suraud, Ann. Phys. **255**, 125 (1997).

[55] J. M. Dawson, Rev. Mod. Phys. **55**, 403 (1983).

[56] S. Pfalzner and P. Gibbon, *Many-Body Tree Methods in Physics* (Cambridge University Press, 2005).

[57] F. Greschik and H.-J. Kull, Laser Part. Beams **22**, 137 (2004).

[58] U. Saalmann and J.-M. Rost, Phys. Rev. Lett. **91**, 223401 (2003).

[59] M. Kundu and D. Bauer, Phys. Rev. Lett. **96**, 123401 (2006).

[60] C. Peltz, C. Varin, T. Brabec, and T. Fennel, New J. Phys. **14**, 065011 (2012).

[61] C. Varin, C. Peltz, T. Brabec, and T. Fennel, Phys. Rev. Lett. **108**, 175007 (2012).

[62] M. Winkel, *High-resolution Simulations of Strongly Coupled Coulomb Systems with a Parallel Tree Code*, Ph.D. thesis, RWTH Aachen University (2013).

[63] F. Haas, G. Manfredi, and M. Feix, Phys. Rev. E **62**, 2763 (2000).

[64] N. N. Bogolyubov and K. P. Gurov, J. Exp. Theor. Phys. **17**, 614 (1947).

[65] N. N. Bogolyubov, J. Exp. Theor. Phys. **16**, 691 (1946).

[66] J. Yvon, *La théorie statistique des fluides et l'équation d'état* (Hermann & Cie, 1935).

[67] J. G. Kirkwood, J. Chem. Phys. **14**, 180 (1946).

[68] J. G. Kirkwood, J. Chem. Phys. **15**, 72 (1947).

[69] M. Born and H. S. Green, Proc. Roy. Soc. A. **188**, 10 (1946).

[70] A. Schmidt-Bleker, W. Gassen, and H.-J. Kull, Europhys. Lett. **95**, 55003 (2011).

[71] V. B. Gildenburg, V. A. Kostin, and I. A. Pavlichenko, Phys. Plasmas **23**, 032120 (2016).

[72] L. G. Gerchikov, A. N. Ipatov, R. G. Polozkov, and A. V. Solov'yov, Phys. Rev. A **62**, 043201 (2000).

[73] Y. W. Wang, J. S. Kim, G. H. Kim, and K. S. Kim, Appl. Phys. Lett. **88**, 143106 (2006).

[74] N. G. Denisov, J. Exp. Theor. Phys. **4**, 544 (1957).

[75] W. L. Kruer, *The Physics of Laser Plasma Interactions* (Addison-Wesley Pub. Co. Inc., Reading, MA, 1988).

[76] H.-J. Kull, *Laserphysik: Physikalische Grundlagen des Laserlichts und seiner Wechselwirkung mit Materie* (de Gruyter, 2015).

[77] F. Brunel, Phys. Rev. Lett. **59**, 52 (1987).

[78] T. Taguchi, T. M. Antonsen, and H. M. Milchberg, Phys. Rev. Lett. **92**, 205003 (2004).

[79] H. M. Milchberg, S. J. McNaught, and E. Parra, Phys. Rev. E **64**, 056402 (2001).

[80] F. Greschik, L. Dimou, and H.-J. Kull, Laser Part. Beams **18**, 367 (2000).

[81] A. El-Khawaldeh and H.-J. Kull, Phys. Rev. A **95**, 043401 (2017).

[82] A. El-Khawaldeh and H.-J. Kull, J. Phys. Conf. Ser. **826**, 012011 (2017).

[83] E. A. Uehling and G. E. Uhlenbeck, Phys. Rev. **43**, 552 (1933).

[84] D. B. Boercker and J. W. Dufty, Ann. Phys. **119**, 43 (1979).

[85] D. Kremp, T. Bornath, M. Bonitz, and M. Schlanges, Phys. Rev. E **60**, 4725 (1999).

[86] G. Manfredi, Fields Inst. Commun. **46**, 263 (2005).

[87] M. V. Kuzelev and A. A. Rukhadze, Phys. Usp. **42**, 603 (1999).

[88] S. V. Vladimirov and Y. O. Tyshetskiy, Phys. Usp. **54**, 1243 (2011).

[89] S. E. Koonin, K. T. R. Davies, V. Maruhn-Rezwani, H. Feldmeier, S. J. Krieger, and J. W. Negele, Phys. Rev. C **15**, 1359 (1977).

[90] O. Gunnarsson and B. I. Lundqvist, Phys. Rev. B **13**, 4274 (1976).

[91] E. Runge and E. K. U. Gross, Phys. Rev. Lett. **52**, 997 (1984).

[92] N. W. Ashcroft and N. D. Mermin, *Solid State Physics* (Harcourt Brace College Publishers, 1976).

[93] A. Goldberg and J. L. Schwartz, J. Comput. Phys. **1**, 448 (1967).

[94] G. B. Arfken and H. J. Weber, *Mathematical methods for physicists*, 6th ed. (Academic Press, 2005) pp. 643–644.

[95] J. Crank and P. Nicolson, Math. Proc. Cambridge Philos. Soc. **43**, 50 (1947).

[96] A. Goldberg and J. L. Schwartz, J. Comput. Phys. **1**, 433 (1967).

[97] W. F. Ames, *Numerical Methods for Partial Differential Equations*, 3rd ed. (Academic press, 2014).

[98] H.-J. Kull, *Computational Physics*, Lecture Notes (2013).

[99] N. D. Lang and W. Kohn, Phys. Rev. B **1**, 4555 (1970).

[100] U. Kreibig and L. Genzel, Surf. Sci. **156**, 678 (1985).

[101] C. Bréchignac, P. Cahuzac, N. Kebaïli, J. Leygnier, and A. Sarfati, Phys. Rev. Lett. **68**, 3916 (1992).

[102] T. Reiners, C. Ellert, M. Schmidt, and H. Haberland, Phys. Rev. Lett. **74**, 1558 (1995).

[103] C. Bréchignac, P. Cahuzac, F. Carlier, M. de Frutos, and J. Leygnier, Chem. Phys. Lett. **189**, 28 (1992).

[104] K. Selby, M. Vollmer, J. Masui, V. Kresin, W. A. de Heer, and W. D. Knight, Z. Phys. D **12**, 477 (1989).

[105] R. C. Monreal, S. P. Apell, and T. J. Antosiewicz, Opt. Express **22**, 24994 (2014).

[106] H. Abe, W. Schulze, and B. Tesche, Chem. Phys. **47**, 95 (1980).

[107] A. El-Khawaldeh, *Quantum plasma model of atomic cluster excitations*, Master's thesis, RWTH Aachen University (2014).

[108] C. Cohen-Tannoudji, B. Diu, and F. Laloe, *Quantum Mechanics*, 2nd ed., Vol. 1 (de Gruyter, 1999) pp. 658–660.

[109] A. Messiah, *Quantum Mechanics*, Vol. 2 (North-Holland Publishing Co., Amsterdam, 1965) pp. 1057–1059.

[110] C. Cohen-Tannoudji, B. Diu, and F. Laloe, *Quantum Mechanics*, 2nd ed., Vol. 2 (de Gruyter, 1999) pp. 231–232.

[111] M. Galassi, *GNU Scientific Library Reference Manual*, 3rd ed.

[112] E. Madelung, Z. Phys. **40**, 322 (1927).

[113] K. Yabana and G. F. Bertsch, Phys. Rev. B **54**, 4484 (1996).

[114] R. J. Goldston and P. H. Rutherford, *Introduction to Plasma Physics* (CRC Press, 1995).

[115] J. Lindhard, Fys. Medd. Dan. Vid. Selsk **28**, 57 (1954).

[116] M. Gell-Mann and K. A. Brueckner, Phys. Rev. **106**, 364 (1957).

[117] B. Eliasson, Transp. Theory Stat. Phys. **39**, 387 (2010).

[118] F. Haas, ArXiv: 1210.0261 [physics.plasm-ph] , 6 (2012).

[119] W. Cassing and H. van Hees, *Mathematische Methoden für Physiker*, Lecture Notes (2014).

[120] R. G. Barrera, G. Estevez, and J. Giraldo, Eur. J. Phys. **6**, 287 (1985).

[121] E. Hill, Am. J. Phys. **22**, 211 (1954).

[122] J. A. Stratton, *Electromagnetic Theory* (McGraw-Hill Book Company, 1941).

[123] W. Hergert and T. Wriedt, *The Mie Theory: Basics and Applications* (Springer, 2012).

[124] K. Kolwas and A. Derkachova, J. Quant. Spectrosc. Radiat. Transf. **114**, 45 (2013).

[125] P. Drude, Ann. Phys. **306**, 566 (1900).

[126] R. Courant, K. Friedrichs, and H. Lewy, Ann. Math. **100**, 32 (1928).

[127] A. Bayliss and E. Turkel, Comm. Pure Appl. Math. **33**, 707 (1980).

[128] J. M. Madey, J. Appl. Phys. **42**, 1906 (1971).

[129] N. G. Basov, V. A. Danilychev, Y. M. Popov, and D. D. Khodkevich, J. Exp. Theor. Phys. Lett. **12**, 329 (1970).

[130] D. W. Forslund, J. M. Kindel, K. Lee, and E. L. Lindman, Phys. Rev. Lett. **36**, 35 (1976).

[131] D. W. Peaceman and H. H. Rachford, Jr, J. Soc. Ind. Appl. Math. **3**, 28 (1955).

[132] D. Neuhauser and M. Baer, J. Chem. Phys. **90**, 4351 (1989).

[133] S. E. Kooi and A. W. Castleman Jr, J. Chem. Phys. **108**, 8864 (1998).

[134] M. Zapata Herrera, J. Aizpurua, A. K. Kazansky, and A. G. Borisov, Langmuir **32**, 2829 (2016).

[135] V. O. Nesterenko, W. Kleinig, and P.-G. Reinhard, Eur. Phys. J. D **19**, 57 (2002).

[136] T. Fennel, T. Döppner, J. Passig, C. Schaal, J. Tiggesbäumker, and K.-H. Meiwes-Broer, Phys. Rev. Lett. **98**, 143401 (2007).

[137] D. Podbiel, P. Kahl, A. Makris, B. Frank, S. Sindermann, T. J. Davis, H. Giessen, M. H.-v. Hoegen, and F.-J. Meyer zu Heringdorf, Nano Lett. **17**, 6569 (2017).

Acknowledgments

I would like to express my sincere gratitude to my advisor Prof. Dr. Hans-Jörg Kull for his all-time support, the interesting conversations and the opportunity to present my research at various conferences.

I also want to thank Prof. Dr. Dieter Bauer for the preparation of the second opinion.

Finally, a special word of thanks to my parents who supported me both morally and financially throughout my studies.